ENGINEERING RESEARCH PAPERS

GECE AKADEMİ

Kitap Adı : Engineering Research Papers

İmtiyaz Sahibi : Gece Kitaplığı

Genel Yayın Yönetmeni : Doç. Dr. Atilla ATİK

Kapak&İç Tasarım : Tuğçe GÖKÇE

Sosyal Medya : Arzu ÇUHACIOĞLU

Yayına Hazırlama : Gece Akademi Dizgi Birimi

Yayıncı Sertifika No : 15476

Matbaa Sertifika No : 42539

Matbaa Adı : GeceAkademi

ISBN : 978-625-7958-55-4

Editörler :Dr. Öğr.Üyesi Abdurahman GÜNDAY

Prof. Dr. Erol PEHLİVAN

Dr. Öğr. Üyesi Mehmet Recep MİNAZ

GECE AKADEMİ

Gece Publishing

ABD Adres/ USA Address: 387 Park Avenue South, 5th Floor, New York, 10016, USA

Telefon/Phone: +1 347 355 10 70

Gece Akademi

Türkiye Adres/Turkey Address: Kocatepe Mah. Mithatpaşa Cad. 44/C Çankaya, Ankara, TR

Telefon/Phone: +90 312 431 34 84 - +90 555 888 24 26

ENGINEERING RESEARCH PAPERS

GECE AKADEMİ

CONTENTS

ENHANCED DECOLORIZATION OF MALACHITE GREEN AND METHYLENE BLUE BY GREEN SYNTHESIS OF FUNCTIONAL NANOSCALE ZERO-VALENT IRON DOPPED PAPPUS OF TRAGOPOGON DUBIUS WILDFLOWERS

CHAPTER

1

Şerife PARLAYICI[1]
Erol PEHLİVAN[2]

[1] Assoc. Prof. Dr. Department of Chemical Engineering, Konya Technical University, Campus, 42079, Konya, Turkey.
[2] Prof. Dr. Department of Chemical Engineering, Konya Technical University, Campus, 42079, Konya, Turkey

1. INTRODUCTION

Industrial activities are seriously threatening clean water resources. Especially, industrial wastewaters include dyes, which are seen as hazardous contaminants (Abdel-Ghani et al., 2007). Wastewaters dump without treatment from the sector, resulting in a substantial rise in dyes in soil, surface and groundwater resources. Dyes cause significant environmental problems due to their toxic effects on aquatic life and decreases light permeability and photosynthetic activity in aquatic life.

Methylene blue (MB) is a cationic color that is commonly used for dyeing cotton, silk, paper, wood and in medical applications (El-Moselhy and Kamal, 2018). MB known to cause blindness, vomiting, cyanosis respiratory distress, irritation to eyes and skin, mental confusion, and abdominal illnesses (Bedin et al., 2018; Khan et al., 2015). MB can induce chemical and biological changes in the human and animal organisms, resulting in cancer and mutations (Yang et al., 2016; Reddy et al., 2016). One of the most commonly used dyes is malachite green (MG), a cationic dye, which is used for dyeing silk, wool, leather, cotton and paper. It is also used as a fungicide in aquaculture and fishing. However, MG is environmentally persistent and toxic to aquatic medium and terrestrial animals (Srivastava et al., 2004). For these reasons, it is compulsory to remove MB and MG from wastewaters. Wastewater produced from pollution sources should be treated before discharging to the environment and lowered below the permissible levels of pollution according to different water norms. Many methods have been developed for the removal of dyes from wastewater such as advanced photocatalytic degradation (Zhang et al., 2019), flocculation-coagulation (Liang et al., 2014), membrane filtration (Wang et al., 2019a), ion exchange (Labanda et al., 2011) and adsorption (Wang et al., 2019b). Researchers have searched for an alternative and cheap but effective methods instead of expensive systems. Many of these methods are not highly preferred in the industry because the traditional methods can lead to high operating costs of the treatment process and the need for secondary treatment. The adsorption method is one of the commonly used methods for the removal of dye from the aqueous solutions because they are economically more suitable than other processes and provide good quality treatment. Natural products are used as adsorbents due to their low cost and environmental friendliness (Andrzejewska et al., 2004). nZVI⊙TDWp has not been studied as an adsorbent for dyes in literature.

Nanoscale zero-valent iron (nZVI) has obtained increased attention due to its high activity, big surface area and high reactivity and eco-friendliness (Chen et al., 2018). As an efficient reduction agent with a big surface area and elevated reactivity, nZVI has been used in latest years to remove a range of colors (Yu et al., 2019; Mehrabi et al., 2019). Iron nanoparticles, however, are easily aggregated and oxidized and lose reactivity in water or air, limiting their further application to remediate the environment (Li et al., 2018). Recent studies have shown that the removal efficiency of toxic materials can be improved using zeolite, Fe_3O_4, filter paper; graphene oxide, carbon materials and many other materials (Chen et al., 2018; Yu et al., 2019; Mehrabi et al., 2019). These supporting materials prevent nZVI from agglomeration, thereby prolonging the activity of the particles.

The objectives of this study were to synthesize nZVI⊙TDWp and to apply them for decolouring of MG and MB in the prepared solution. TDWp is not poisonous, cheap and environmentally friendly biomaterials. In the adsorption experiment, nZVI⊙TDWp was used and its performance was compared by changing factors such as the initial dye concentration, pH of the solution, contact time and the amount of adsorbent. A model on the isotherm studies was tried for MG and MB adsorption. The characteristics of nZVI⊙TDWp were conducted before and after treatment using FT-IR. The present study focuses on reducing the concentration of MG and MB by using nZVI⊙TDWp. All experiments were carried out in a batch process with the synthetic effluents at ambient conditions. It was concluded that nZVI⊙TDWp can find many applications to remove MG and MB from industrial wastewater or polluted streams.

2. EXPERIMENTAL

2.1. Materials and Instruments

Tragopogon Dubius Wildflowers pappus (TDWp) was obtained from Konya-Selcuklu region of Turkey. The chemicals used in the experiments were obtained from Merck Company in analytical purity and $NaBH_4$, $FeCl_3.6H_2O$, NaOH, HCl, MG and MB were purchased from Across Organics. Orion 900S2 Model pH meter, a thermo explicit shaker of GFL 3033 model, and IKAMAG- RO15 model magnetic stirrer were used for a simple adjustment of pH and mixing the solutions. The FT-IR spectra for nZVI⊙TDWp and dye loaded-nZVI⊙TDWp were recorded with Bruker-Platinum ATR-vertex 70 (Germany) between 500-4000 cm^{-1} wavenumbers at a resolution of 4 cm^{-1} using an attenuated total reflection (ATR) accessory. SEM (SEM, Nova Nano SEM 200) is from FEI Company and the samples were covered with a gold layer. The remaining MG and MB in the solution phase after decantation were measured by using a UV-Visible Spectrophotometer (Shimadzu UV-1700).

2.2. Preparation of nZVI⊙TDWp

TDWp was washed with distilled water to remove any adhering impurities and dried at 50 °C in the drying oven. Then, these fibers were used to interact with nZVI. First, 80 mL of 5% w/v of $FeCl_3.6H_2O$ solution was added onto 10 g of TDWp. Thus, Fe^{3+} ions were introduced into the porous support through sorption at the respective functional groups. After that, the porous support material was treated with 0.5 M $NaBH_4$ solution (80 mL). In this way, the adsorbed ferrous ions (Fe^{3+} ions) were reduced to zero-valent ions (Fe°). As the solution of $NaBH_4$ was added to the mixture, black droplets developed instantly. The slurry was mixed completely for 2 h at room temperature 25 ± 1.0 °C and then it was filtered to separate nZVI⊙TDWp. Then, nZVI⊙TDWp was drained, washed with deoxygenated deionize water, and was stored in ethanol solution to prevent it from any further oxidation at room temperature. The ionic equation for a ferric iron decrease to nZVI follows (Eq. 1):

$$4Fe^{3+} + 3BH_4^- + 9H_2O \longrightarrow 4Fe^{\circ}\downarrow + 3H_2BO_3^- + 12H^+ + 6H_2\uparrow \qquad (1)$$

2.3. Batch reactor experiments

The batch adsorption trials of MG and MB were directed to investigate the equilibrium at 25 °C as follows: The saturation of adsorbent by dye was examined by including 2 g/L dosages of nZVI⊙TDWp with 250 ppm MG and MB solution. The beakers were replaced into an incubator shaker (250 rpm) for various periods of interaction (5 min, 15 min, 30 min, 45 min., 1h, 1.5 h, 2 h, 3h, 4 h, and 6 h) at 25 °C. The effect of nZVI⊙TDWp amount on the removal of MG and MB was tried by mixing 250 ppm MG and MB solutions with the different quantity of the adsorbent for 1.5 h. The amount of nZVI⊙TDWp in the solution phase was 0.5, 1, 2, 3 and 4 g/L for each vessel. Initial pH impact on removal was investigated by adding 2 g/L of nZVI⊙TDWp in 250 ppm dye solution at original pHs ranging from 2 to 10. The solution's pH was regulated by adding solution NaOH and HCl. The isotherms data were modelled by mixing 2 g/L dosages of nZVI⊙TDWp with the different molarities of MG and MB (5, 10, 25, 50, 75, 100, 150, 200, 250, 300 and 350 ppm). The samples were tested two times to ascertain the accuracy, reliability and reproducibility of the data obtained from the experimental results. MG and MB concentration in the filtrate was identified with the UV-vis Spectrophotometer (λ: 617 nm for MG and λ: 664 nm for MB) using diphenyl carbazide reagent. The equilibrium adsorption capacity and percent adsorption of MG and MB was calculated using the following Eq. (2 and 3):

$$q_e = \frac{C_o - C_e}{m} \times V \qquad (2)$$

$$\%Adsorption = \frac{C_o - C_e}{C_o} \times 100 \qquad (3)$$

where q_e (mg g^{-1}) is the adsorption capacity of the nZVI⊙TDWp, C_o and C_e(mg L^{-1}) are the initial and final concentration of MG and MB respectively, V (mL) is the volume of the solution, and m (g) is the amount of the nZVI⊙TDWp.

3. RESULTS AND DISCUSSION

3.1. Characterization of nZVI⊙TDWp

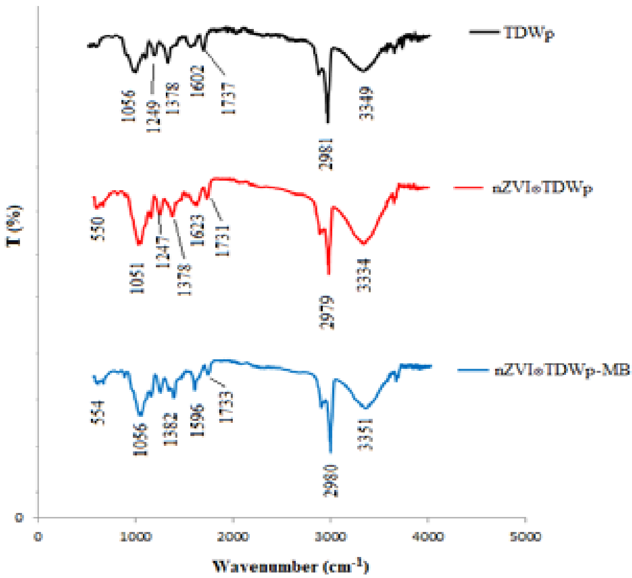

Figure 1. *The FT-IR spectral characteristics of TDWp, nZVI⊙TDWp and nZVI⊙TDWp -MB*

The FT-IR spectroscopy in the wavenumber range of 500 ~ 4000 cm^{-1} was used to examine to the chemical structures of nZVI⊙TDWp and dye loaded nZVI⊙TDWp (Figure 1). -OH stretching vibrations appeared at 3340 cm^{-1} and the wavelength at 2979 and 2906 cm^{-1} is caused by the aliphatic C-H stretching vibrations of lignocellulosic components (Yallappa et al., 2017). -COOH indicates strong peaks of strain vibrations at 1616 cm^{-1}. The peak of -C-O vibration at 1056 cm^{-1} wavelength supports the presence in the cellulose and hemicelluloses (Aljoumaa et al., 2017). The FT-IR spectral studies have shown that nZVI⊙TDWp primarily consists of lignin, hemicellulose, and cellulose, including functional groups such as alcoholic, ketonic, and carboxylic. These groups may participate with MB, MV dyes in the complexation reactions. Fe-O vibration bonds are assigned to the bands at 654 and 560 cm^{-1} in nZVI⊙TDWp, confirming the presence of Fe components (Norouzian and Lakouraj, 2015; Sun et al., 2014). After MG and MB adsorption on nZVI⊙TDWp; it was seen that some bands shifted and there were changes in the intensity of them. These changes in the FT-IR spectrum of nZVI⊙TDWp after the adsorption of MG and MB confirmed the adsorption of dyes with the functional groups in nZVI⊙TDWp.

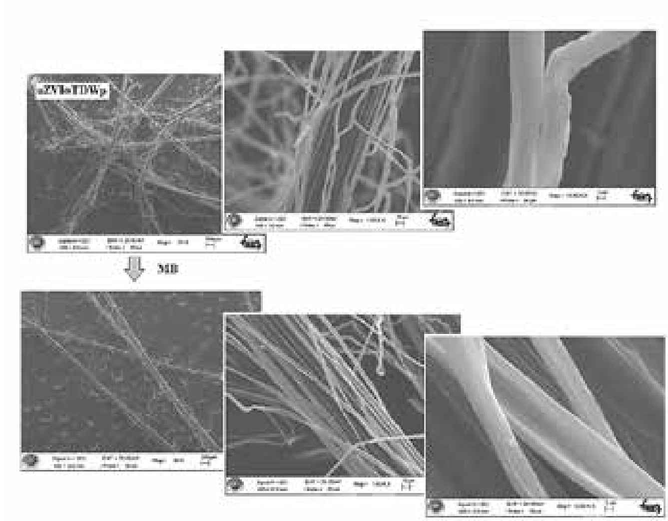

Figure 2. *The SEM images of nZVI⊙TDWp and after MB adsorption*

SEM analysis was made to explore the surface morphology of nZVI⊙TDWp. The surface morphology of SEM images before and after the adsorption of MB was given in Figure 2. This figure showed that the nZVI⊙TDWp surface was smooth. After the dye absorption, a significant change in the structure of nZVI⊙TDWp was observed. The surface of the nZVI⊙TDWp can be seen to be rough because it is coated by the dye molecules.

3.2. Effect of The MG and MB Initial Concentration

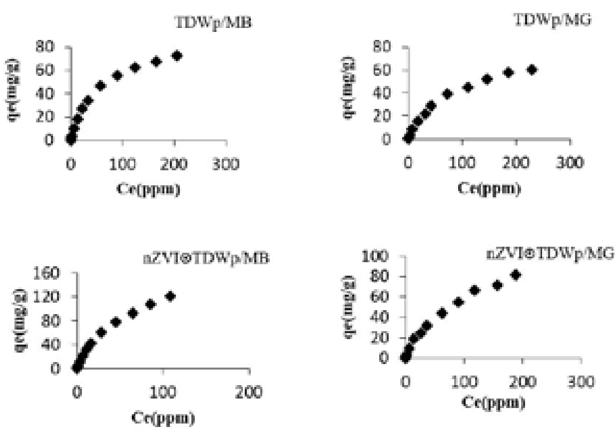

Figure 3. *Adsorption isotherms of MG and MB adsorbed by TDWp and nZVI⊙TDWp*

The adsorption of MG and MB in various concentrations were changed to determine the effect of adsorbate initial concentrations on the adsorption. Therefore, 5, 10, 25, 50, 75, 100, 150, 200, 250, 300, 350 ppm MG and MB solutions were prepared in the experiments using nZVI⊙TDWp. The adsorption experiments were carried out by treating the solutions with nZVI⊙TDWp. The amount of MG and MB remaining in the solution phase by using different concentrations after the filtration was measured with UV-Vis. spectrophotometer. As seen in Figure 3., the initial MG and MB concentration increased, the adsorption capacity increased. The increase in the capacity of adsorbent was slowed down by the fact that the bonding parts in the nZVI⊙TDWp structure were saturated.

Table 1. *Parameters of Langmuir, Freundlich, Scarthard and D-R Isotherms for Adsorption of MG and MB on TDWp and nZVI⊙TDWp*

Model	Equation	Eq.	Adsorbent	Dye	Parameters for dye				Ref.
Langmuir					A_s	K_b	R^2	R_L	
	$\frac{C_e}{q_e} = \frac{C_e}{A_s} + \frac{1}{K_b A_s}$	(4)	TDWp	MB	87.72	0.021	0.997	0.161	(Langmuir, 1918)
			nZVI⊙TDWp	MB	155.45	0.024	0.985	0.144	
			TDWp	MG	78.74	0.014	0.993	0.228	
			nZVI⊙TDWp	MG	104.5	0.014	0.968	0.217	
Freundlich					K_f	n	R^2		
	$ln\ q_e = ln\ K_f + \frac{1}{n} ln\ C_e$	(5)	TDWp	MB	2.71	1.50	0.975		(Freundlich, 1906)
			nZVI⊙TDWp	MB	4.47	1.35	0.990		
			TDWp	MG	1.64	1.41	0.974		
			nZVI⊙TDWp	MG	2.32	1.42	0.987		
D-R					X_m	K	E	R^2	
	$\ln q_e = \ln q_m - \beta \varepsilon^2$	(6)	TDWp	MB	0.002	0.005	9.53	0.993	(Dubinin and Radushkevich, 1947)
			nZVI⊙TDWp	MB	0.004	0.006	9.37	0.999	
			TDWp	MG	0.001	0.006	9.28	0.990	
			nZVI⊙TDWp	MG	0.002	0.006	9.45	0.996	
Scatchard					Q_s	K_s	R^2		
	$q_e/C_e = Q_s K_s - q_e K_s$	(7)	TDWp	MB	8.94	0.023	0.973		(Scatchard, 1949)
			nZVI⊙TDWp	MB	150.59	0.026	0.929		
			TDWp	MG	73.81	0.015	0.946		
			nZVI⊙TDWp	MG	94.66	0.018	0.895		

Langmuir, Freundlich, Scatchard and D-R model (Table 1.) were applied for the equilibrium (Eq. (4, 5, 6, 7)). The Freundlich isotherm shows physical adsorption. According to Freundlich, MG and MB filled sections on the surface of adsorbent are heterogeneous. K_f and n parameters were calculated for Freundlich isotherm. If the n values between 1 and 10 indicates that adsorption is favourable. In this study, n values were found to be 1.35 for MB, 1.42 for MG adsorption by nZVI⊙TDWp and 1.50 for MB, 1.41 for MG adsorption by TDWp. Langmuir isotherm expressed chemical and single layer adsorption. This model is defined as the simplest theoretical model for a single layer adsorption. The values of A_s calculated from the Langmuir isotherm model were 87.72 mg/g for MB-TDWp, 78.74 mg/g for MG-TDWp, 155.45 mg/g for MB-nZVI⊙TDWp, and 104.54 mg/g for MG-nZVI⊙TDWp. The results can be considered to be viable for the removal of MG and MB by nZVI⊙TDWp from aqueous solutions. The R^2 values obtained from Langmuir isotherm plots are $R^2>0.99$ for nZVI⊙TDWp and TDWp (in Table 1). Langmuir isotherm was found to be more suitable for the adsorption. If the value of R_L lies between 0 and 1, the adsorption process is favourable and if R_L is greater than 1, the process is unfavourable. The R_L values obtained in this study (Table 1.) range from 0 to 1, suggesting a strong attraction for MG and MB by nZVI⊙TDWp and TDWp. The adsorption isotherms were measured and tested using the Scatchard equation to determine and compare the saturation capacities of nZVI⊙TDWp towards the MG and MB ions. When Scatchard plot revealed a deviation from linearity, greater emphasis was placed on Freundlich model adsorption data to create MG and MB adsorption isotherms at different concentrations in the solution. In the adsorption of MG and MB, a linear plot was created by Scatchard analysis of the equilibrium binding data for MG and MB on nZVI⊙TDWp signifying that Langmuir model could be preferred.

3.3. Effect of pH

The solution phase was considered in the different pH values (2, 3, 4, 5, 6, 7, 8, 9) for the adsorption of MG and MB. The change in the pH value of the solution affects the adsorption sites on the adsorbent surface and the charge profiles of the adsorbate, thus significantly affecting the adsorption. The distinctive mechanical, chemical and electrical properties of interfaces of the solid and solution phase create great and highly varied effects on the adsorbent behavior. The surface layer of the nZVI⊙TDWp exhibits an electrical charge effect on MG and MB. The change in the adsorption capacities of MG and MB ions against pH change is plotted in Figure 4a. The sorption of cationic dyes is affected by the number of negative charges provided by adjusting the solution pH in a certain level. The solution has a net positive charge at pH=2, so there is less absorption, whereas at pH=9 there is an increase in negative charges and increases the adsorption of dyes. The adsorption capacity of MB at pH 2 was 38.04 mg/g and increased to 102.80 mg/g at pH 9 for the nZVI⊙TDWp. On the other hand, the adsorption capacity of MV by nZVI⊙TDWp at pH 2 was 67.65 mg/g and increased to 117.50 mg/g at pH 9. In the adsorption experiments, the adsorption values of MG and MB ions were found to be optimum at pH 6 for the pH range 2-9.0 of the solution phase. At low pH, most of the functional groups (such as -COOH, -OH) in the adsorbent were protonated and existed in the positively charged groups. The electrostatic repulsion between the positively charged groups and the cationic dye could prevent the potential of adsorption (Monier and Abdel-Latif, 2012). These results showed that the adsorption capability nZVI⊙TDWp is favored by the neutral or at higher pH values (pH6-pH9). The optimum pH 6 has been selected for the further adsorption applications.

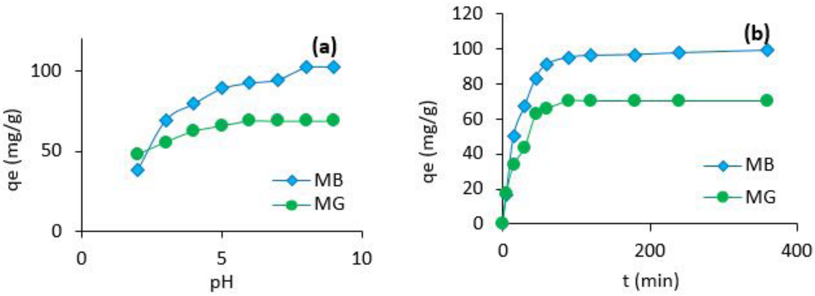

Figure 4. *The effect of pH on the adsorption of MG and MB by nZVI⊙TDWp (a) and the effect of contact time on the adsorption of MG and MB by nZVI⊙TDWp (b).*

3.4. The Effect of Contact Time

The effect of contact time on the adsorption of MG and MB in the adsorption experiments using nZVI⊙TDWp is shown in Figure 4b. In this study, 250 ppm MG and MB solution were added to 1.0 g/L of nZVI⊙TDWp, separately for the adsorption process. The mixture was stirred in the magnetic stirrer at the specified time intervals (5, 15, 30, 45, 60, 90, 120, 180, 240, 360 min) and MG and MB contents of the remaining solution after the filtration was measured with the UV-Vis spectrometer. As seen in Figure 4b., the adsorption of MG and MB by nZVI⊙TDWp increased rapidly in the first 5-15 min. and then reached the equilibrium between 15-45 min. The longer contact time was not effective on the adsorption, and the contact time was taken as 45 minutes for both of dyes. It has been observed that the adsorption is fixed to the point of reaching the equilibrium for both of them. Due to the large surface area of nZVI⊙TDWp and the existence of functional groups in the matrix, the first part (15 min.) of the adsorption is fast because MG and MB ions tend to interact with the functional groups of the adsorbent. At the end of the applied contact time, the optimum time was determined as 45 min. for MG and MB.

3.5. Kinetic models

The pseudo-first-order and pseudo-second-order equations are put to use for the kinetics of MG and MB adsorption onto nZVI⊙TDWp. All parameters related to the adsorption kinetics calculated from the related models of MG and MB are presented in Table 2. MG and MB sorption on nZVI⊙TDWp possesses higher R^2 value of the pseudo-second-order kinetic model, compared to the pseudo-first-order kinetic model and the pseudo-second-order equation showed a reliable connection of the experimental data results with linearized form ($R^2 > 0.99$). The calculated capacity value (q_e, cal) for the pseudo-second-order model deviates less than the experimental data (q_e, exp) (Table 2). Hence, the pseudo-second-order model equation is more suitable compared to others for the kinetic studies.

Table 2. *The pseudo-first-order and pseudo-second-order parameters for the adsorption of MG and MB on nZVI⊙TDWp.*

		Pseudo First-order			Pseudo Second-order		
Dye	$q_{e\ exp}$	k_1	q_e	R^2	k_2	q_e	R^2
MG	101	0.0019	61.8	0.445	0.0006	84.75	0.989
MB	110	0.0025	68.07	0.926	0.0004	114.94	0.994

3.6. Effect of nZVI⊙TDWp Dosage

An optimal adsorbent dose should be determined to maximize the interactions between the dye and adsorption sites of nZVI⊙TDWp in the solution phase. The relationship between nZVI⊙TDWp dose and the adsorption capacity, as much as the removal efficiency of MG and MB, are illustrated in Figure 5. 0.5; 1.0; 2.0; 3.0 and 4.0 g/L of the nZVI⊙TDWp dosages were separately bottled and 250 ppm of dye solutions were mixed with the adsorbent, then stirred for 45 minutes at 250 rpm in a magnetic stirrer. MG and MB contents of the remaining solution after the filtration were measured with the UV-Vis spectrometer. The results of the experiment (Figure 5.) showed that the adsorption process is depend on the amount of adsorbent. The adsorption capacity of MG and MB follows with the increase of adsorbent dose until 2.0 g/L. The adsorption capacity of nZVI⊙TDWp decreases from 107.18 to 56.60 mg/g by increasing the adsorbent dosage between 0.5 and 4.0 g/L for MB and the adsorption capacity of nZVI⊙TDWp decreases from 163.96 to 61.08 mg/g by increasing the adsorbent dosage between 0.5 and 4.0 g/L for MV. The optimum adsorbent dosage was found as 2.0 g/L for both of dyes. By applying 1–2 g/L of the composite dose, a relatively slow increase in the percent of MG and MB removal (R,%) from 58.52 to 85.28 % was obtained. Further increase in the composite amount did not change significantly the value of adsorption. These results can be interpreted as the increase of adsorbent amount provides more contact surface area and available active sites of the solid, leading to the higher adsorption percentage. The high composite amount can result in the aggregation of nZVI⊙TDWp with an attendant decrease of the surface area. This was particularly realized at the dosage of 2 g/L.

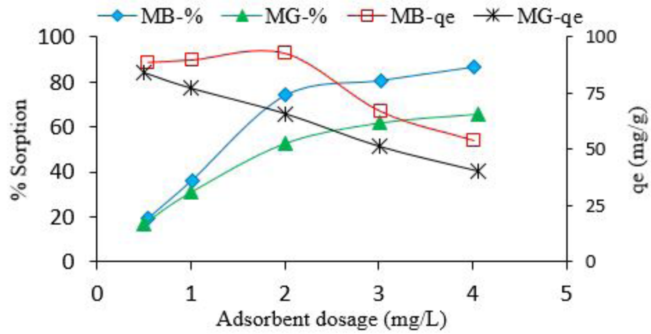

Figure 5. *The effect of adsorbent dosage on the adsorption capacity and the percentage removal of MG and MB by nZVI⊙TDWp.*

3.7. Thermodynamic Studies

Adsorption of MG and MB dyes on nZVI⊙TDWp was carried out at different temperatures (25 °C, 35 °C, 45 °C and 55 °C) for thermodynamic analysis (Figure 6). The equilibrium constant was calculated by the following equation (Shrestha et al., 2013) (Eq 8, Eq 9):

$$\Delta G^{o} = -RT \ln K_c \tag{8}$$

$$\ln K_c = \frac{\Delta S^{o}}{R} - \frac{\Delta H^{o}}{RT} \tag{9}$$

where, T, temperature (K); R, ideal gas constant; K_c, equilibrium constant. The thermodynamic parameters including ΔH°, ΔS° and ΔG° for the adsorption of dyes are calculated from equations 8-9 and the results were given in Table 3. The positive values of ΔH° show that the adsorption process is endothermic for MG and MB adsorption on nZVI⊙TDWp. The positive value of ΔS° demonstrates the presence of a disorder at the adsorbent–solution boundary during the adsorption of the dyes on the nZVI⊙TDWp. Negative values of ΔG° indicate the applicability of the method and that the adsorption is spontaneous. ΔG° is negative and that the adsorption is spontaneous.

Table 3. *Thermodynamic parameters a for MG and MB adsorption onto nZVI⊙TDWp.*

Dye	ΔS° (J $K^{-1}mol^{-1}$)	ΔH° J mol-1	ΔG° (J mol^{-1}) T=298.15K	T=308.15K	T=318.15K	T=328.15K	R^2
MG	46.55	13584.15	-296.1	-761.6	-1227.2	-1692.7	0.997
MB	33.102	7299.54	-2569.9	-2900.9	-3231.9	-3562.9	0.949

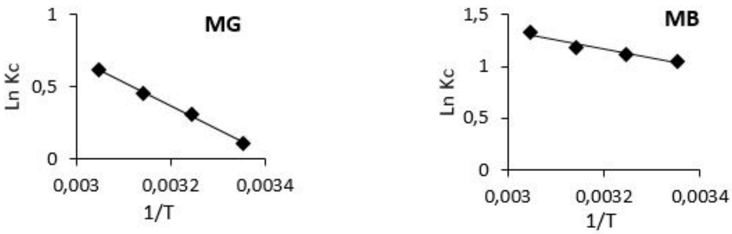

Figure 6. *Effect of temperature on the adsorption of MG and MB adsorption onto nZVI⊙TDWp*

4. CONCLUSIONS

nZVI⊙TDWp was prepared to be an active adsorbent for the adsorption of MG and MB from aqueous solutions. The adsorption behavior of MG and MB by nZVI⊙TDWp was investigated and it was found to be dependent on solution pH, initial MG and MB concentration, nZVI⊙TDWp dosage, and agitation time. Langmuir, Freundlich, Scatchard and D-R isotherms were tried and the adsorption constants were calculated. The adsorption mechanism is best described by the Langmuir isotherm model (R^2 is 0.99) and the values of the R_L factor suggesting a good binding at nZVI⊙TDWp's active sites. By applying the Langmuir model equation, the maximum dye capacities of TDWp and nZVI⊙TDWp were found to be 87.72 mg/g for MB-TDWp, 78.74 mg/g for MG-TDWp, 155.45 mg/g for MB- nZVI⊙TDWp, and 104.54 mg/g for MG-nZVI⊙TDWp. nZVI⊙TDWp has a good adsorption capacity for removal of MG and MB in the aqueous solutions, which is compared with the raw TDWp. The adsorbent dosage was taken as 2.0 g/L and contact time was selected as 45 min. for both dyes. The adsorption kinetics was well described by the pseudo-second-order model. The optimum pH 6 was determined for the adsorption of MG and MB. Thermodynamic properties were investigated and it was found that the adsorption occurred spontaneously and the process was endothermic. nZVI⊙TDWp was produced from the natural sources which claim it is an environmentally friendly adsorbent for the application of MG and MB removal from the polluted solution.

REFERENCES

A. Andrzejewska, A. Krysztafkiewicz, T. Jesionowski, "Adsorption of Organic Dyes on the Aminosilane Modified TiO_2 Surface," *Dyes and Pigments*, 62(2):121–130, 2004.

C. Z. Liang, S. P. Sun, F. Y. Li, Y. K. Ong, T. S. Chung, "Treatment of Highly Concentrated Wastewater Containing Multiple Synthetic Dyes by a Combined Process of Coagulation/Flocculation and Nanofiltration," *Journal of Membrane Science*, 469:306-315, 2014.

D. Zhang, T. Cong, L. Xia, L. Pan, "Growth of Black TiO_2 Nanowire/Carbon Fiber Composites with Dendritic Structure for Efficient Visible-Light-Driven Photocatalytic Degradation of Methylene Blue," *Journal of Materials Science*, 54(10):7576-7588, 2019.

G. Scatchard, "The Attractions of Proteins for Small Molecules and Ions," *Annals of the New York Academy of Science*, 51:660–672, 1949.

H. M. F. Freundlich, "Over the Adsorption in Solution," *The Journal of Physical Chemistry*, 57:385–470, 1906.

I. Langmuir, "The Adsorption of Gases on Plane Surfaces of Glass, Mica and Platinum," *Journal of the American Chemical Society*, 40(9):1361–1403, 1918.

J. Labanda, J. Sabaté, J. Llorens, "Experimental and Modeling Study of the Adsorption of Single and Binary Dye Solutions with an Ion-Exchange Membrane Adsorber," *Chemical Engineering Journal*, 166(2):536-543, 2011.

J. Sun, G. Yu, L. Liu, Z. Li, Q. Kan, Q. Huo, J. Guan, "Core-Shell Structured Fe_3O_4@ SiO_2 Supported Cobalt (II) or Copper (II) Acetylacetonate Complexes: Magnetically Recoverable Nanocatalysts for Aerobic Epoxidation of Styrene," *Catalysis Science & Technology*, 4(5):1246-1252, 2014.

K. Aljoumaa, H. Tabeikh, M. Abboudi, "Characterization of Apricot Kernel Shells (Prunus Armeniaca) by FTIR Spectroscopy, DSC and TGA," *Journal of the Indian Academy of Wood Science*, 14(2), 127–132, 2017.

K. C. Bedin, I. P. Souza, A. L. Cazetta, L. Spessato, A. Ronix, V. C. Almeida, "CO_2-Spherical Activated Carbon as a New Adsorbent for Methylene Blue Removal: Kinetic, Equilibrium and Thermodynamic Studies," *Journal of Molecular Liquids*, 269:132-139, 2018.

M. I. Khan, T. K. Min, K. Azizli, S. Sufian, H. Ullah, Z. Man, "Effective Removal of Methylene Blue from Water Using Phosphoric Acid Based Geopolymers: Synthesis, Characterizations and Adsorption Studies," *RSC Advances*, 5(75):61410-61420, 2015.

M. M. Dubinin, L. V. Radushkevich, "Equation of the Characteristic Curve of Activated Charcoal," *In: Dokl. Akad. Nauk. SSSR.*, 55:327–329, 1947.

M. M. El-Moselhy, S. M. Kamal, "Selective Removal and Preconcentration of Methylene Blue from Polluted Water Using Cation Exchange Polymeric Material," *Groundwater for Sustainable Development*, 6:6-13, 2018.

M. Monier, D. A. Abdel-Latif, "Preparation of Cross-Linked Magnetic Chitosan-Phenylthiourea Resin for Adsorption of Hg (II), Cd (II) and Zn (II) ions from aqueous solutions," *Journal of Hazardous Materials*, 209:240-249, 2012.

N. Mehrabi, A. Masud, M. Afolabi, J. Hwang, G. A. C. Ortiz, N. Aich, "Magnetic Graphene Oxide-Nano Zero Valent Iron (GO–nZVI) Nanohybrids Synthesized Using Biocompatible Cross-Linkers for Methylene Blue Removal," *RSC Advances*, 9(2):963-973, 2019.

N.T. Abdel-Ghani, M. Hefny, G. A. F. El-Chaghaby, "Removal of Lead from Aqueous Solution Using Low Cost Abundantly Available Adsorbents," *International Journal of Environmental Science & Technology*, 4 (1), 67–73, 2007.

P.K.M. Reddy, P. Verma, C. Subrahmanyam, "Bio-Waste Derived Adsorbent Material for Methylene Blue Adsorption," *Journal of the Taiwan Institute of Chemical Engineers*, 58:500-508, 2016.

P. Yu, H. Yu, Q. Sun, B. Ma, "Filter Paper Supported nZVI for Continuous Treatment of Simulated Dyeing Wastewater," *Scientific Reports*, 9(1):1-8, 2019.

Q. Wang, J. Ju, Y. Tan, L. Hao, Y. Ma, Y. Wu, H. Zhang, Y. Xia, K. Sui, "Controlled Synthesis of Sodium Alginate Electrospun Nanofiber Membranes for Multi-Occasion Adsorption and Separation of Methylene Blue," *Carbohydrate Polymers*, 205:125-134, 2019a.

R. S. Norouzian, M. M. Lakouraj, "Preparation and Heavy Metal Ion Adsorption Behavior of Novel Supermagnetic Nanocomposite Based on Thiacalix [4] Arene and Polyaniline: Conductivity, Isotherm and Kinetic Study," *Synthetic Metals*, 203:135-148, 2015.

S. Shrestha, G. Son, S. H. Lee, T. G. Lee, "Isotherm and Thermodynamic Studies of Zn (II) Adsorption on Lignite and Coconut Shell-Based Activated Carbon Fiber," *Chemosphere*, 92:1053-1061, 2013.

S. Srivastava, R. Sinha, D. Roy, "Toxicological Effects of Malachite Green," *Aquatic Toxicology*, 66(3):319-329, 2004.

S. Yallappa, D. R. Deepthi, S. Yashaswin, R. Hamsanandini, M. Chandraprasad, S. A. Kumar, G. Hegde, "Natural Biowaste of Groundnut Shell Derived Nano Carbons: Synthesis, Characterization and Its in Vitro Antibacterial Activity," *Nano-Structures & Nano-Objects*, 12:84–90, 2017.

X. Yang, D. Jin, M. Zhang, P. Wu, H. Jin, J. Li, X. Wang, H. Ge, Z. Wang, H. Lou, "Fabrication and Application of Magnetic Starch-Based Activated Hierarchical Porous Carbon Spheres for the Efficient Removal of Dyes from Water," *Materials Chemistry and Physics*, 174:179-186, 2016.

Y. Wang, Y. Li, H. Li, H. Zheng, Q. Du, "Equilibrium, Kinetic and Thermodynamic Studies on Methylene Blue Adsorption by Konjac Glucomannan/Activated Carbon Aerogel," *Journal of Polymers and the Environment*, 27(6):1342-1351, 2019b.

Z. Chen, D. Wei, Q. Li, X. Wang, S. Yu, L. Liu, B. Liu, S. Xie, J. Wang, D. Chen, T. Hayat, X. Wang, "Macroscopic and Microscopic Investigation of Cr(VI) Immobilization by Nanoscaled Zero-Valent Iron Supported Zeolite MCM-41 Via Batch, Visual, XPS and EXAFS Techniques," *Journal of Cleaner Production*, 181:745-752, 2018.

Z. Li, L. Wang, J. Meng, X. Liu, J. Xu, F. Wang, P. Brookes, "Zeolite-Supported Nanoscale Zero-Valent Iron: New Findings on Simultaneous Adsorption of Cd (II), Pb (II), and As (III) in Aqueous Solution and Soil," *Journal of Hazardous Materials*, 344:1–11, 2018.

CATIONIC DYES DECOLOURIZATION BY LOW-COST ALGINATE/ BENTONITE COMPOSITE CAPSULES

CHAPTER

2

Şerife PARLAYICI[1]
Erol PEHLİVAN[2]

1 Assoc. Prof. Dr. Department of Chemical Engineering, Konya Technical University, Campus, 42079, Konya, Turkey.
2 Prof. Dr. Department of Chemical Engineering, Konya Technical University, Campus, 42079, Konya, Turkey.

1. INTRODUCTION

Wastewater generated by rapid population growth and industrialization poses a threat to our underground and surface water resources. The increasing use of dyes in various industries (textiles, plastics, leather, cosmetics, etc.) leads to an increase in the colour burden of wastewaters. Discharging these wastewaters without treatment disrupts the aesthetic appearance of the receiving water environment and destroys the aquatic life. These wastewaters, which can reach the human body through receiving water environments, also have carcinogenic and toxic effects on humans. Today there are more than $1x10^5$ commercial paints and $7x10^5$ tons/year of dyestuff production is made worldwide. During the dyeing process, it was calculated that approximately 10-15% of the dye passed to the wastewater stream (Gomez et al., 2007). Colour limiting is not a parameter according to wastewater discharge standards. However, it is important to treat the environment and human health.

Considering the rapid development in the textile industry in the world, the treatment of coloured wastewater is of great importance for the environment and human health. In the textile industry, for continuous improvement, the products are produced resistant to various chemicals, detergents, light and heat. The biodegradation of dyes are very difficult in wastewater and takes a long time. Dye removal is provided by using many biological, physical and chemical methods, for examples; aerobic treatment, flocculation/coagulation, membrane filtration, adsorption, biosorption, photo catalysis, Fenton process, electrocoagulation and ion exchange (De Castro et al. 2018; Puri and Sumana, 2018; Xu et al., 2018). Adsorption is an effective and economical method for the removal of dyes, pigments and other colourants (Gonawala and Mehta, 2014). The dyes in the wastewater have functional groups and they can interact with the adsorbent surface. This interaction can be explained in terms of adsorption characteristics and physical properties of the adsorbent.

In order to remove the colour of the wastewater with cheap adsorbents; zeolite, natural clay, bentonite and montmorillonite (Marco-Brown et al. 2018; Bulut et al. 2008; Han et al. 2009; Bentahar et al. 2017), activated carbon (Chowdhury et al. 2019; Mahmoodi et al., 2018), agricultural wastes (Bashanaini et al. 2019; Mashhadi et al., 2016; Banerjee and Chattopadhyaya, 2017), coal ash (Astuti et al. 2019) is known to be used as an adsorbent. All of the materials used have important advantages such as being easy to find, renewable, locally applicable and cost-effective. Clays find a wide range of applications due to their high surface area, chemical and mechanical stability, surface and structural properties and diversity. Chemical structures and pore structures usually determine the sorption capabilities of clays. Bentonite, smectite group is a clay mineral and consists mainly of montmorillonite. The montmorillonite forming the bentonite consists of an octahedral layer between two tetrahedral layers. Bentonite is an important ion exchanger that exhibits swelling properties when exists in water or organic molecules. On the other hand, one of the most economical methods used in the removal of dyestuffs is the adsorption by biopolymers as adsorbents. In the study, bentonite natural mineral was added to the structure of biopolymers in the production of composite. Natural polymers are used frequently in chemical engineering, food and pharmaceutical industries and agriculture in recent years due to their non-toxic, low price, suitable properties and biodegradability. Many natural polymers such as polysaccharides; they have disadvantages such as low mechanical strength, uncontrolled water intake and microbial contamination. Alginate is non-toxic, biocompatible, biodegradable and biodegradable materials containing carboxyl and hydroxyl groups in their structures. For this reason, it is used in many areas such as heavy metal ion and dye removal, heat and sound insulation and controlled drug release processes.

In the literature studies, it has been observed that the use of clay as an adsorbent material has been the subject of curiosity in recent years and has been intensively investigated. The purpose of this study is; (i) investigation of raw bentonite as an alternative adsorbent for removal of cationic dyes from coloured waters, (ii) synthesis of composite microspheres for dye removal and observation of change in the adsorption capacity of alginate coated bentonite (iii) determination of adsorption kinetics, thermodynamic and isotherms of the adsorption process. In the first stage, various adsorption parameters such as adsorbent amount, temperature, the concentration of MB, MG and MV dye solutions, equilibrium time and pH were applied and morphological behaviours before and after interactions were examined. Sorption equilibrium isotherms (Langmuir, Freundlich, Scatchard, Temkin models), kinetic (pseudo-first and pseudo-second-order) and thermodynamic studies were applied in this study.

2. EXPERIMENTAL

2.1. Materials

Sodium alginate powder (CAS No: 9005-38-3), was obtained from Sigma-Aldrich. Bentonite was purchased from Sigma-Aldrich. The chemical composition of the bentonite is given in Table 1.

Table 1. *Chemical composition of bentonite (wt%)*

Compound	Bentonite*(wt %)	Compound	Bentonite*(wt %)
SiO_2	60.5	MnO	0.01
Al_2O_3	21.0	K_2O	0.32
MgO	2.76	Na_2O	2.11
CaO	1.02	P_2O_5	0.04
Fe_2O_3	3.88	SO_3	0.74
TiO_2	0.15	* (Goh et al. 2011)	

Methylene Blue hydrate (CAS No: 122965-43-9; Molecular formula: $C_{16}H_{18}ClN_3S.xH_2O$; Molecular weight ($g.mol^{-1}$): 319.85; λ_{max}(nm): 664), Malachite Green oxalate (CAS No: 2437-29-8; Molecular formula: $C_{23}H_{25}N_2$ $.1/2C_2H_2O_4.C_2HO_4$; Molecular weight ($g.mol^{-1}$): 463.51; λ_{max-}(nm): 617) and Methyl Violet 2B (CAS No: 8004-87-3; Molecular formula: $C_{24}H_{28}ClN_3$; Molecular weight ($g.mol^{-1}$): 393.96; λ_{max}(nm): 579) abbreviated as MB, MG and MV were purchased from Acros Organics. $CaCl_2$, NaOH and HCl solutions were purchased from Merck Company. All related chemicals used in the experiments were of analytical grade and pure water water was used for the preparation of the necessary solutions. The pH of solutions was adjusted by adding NaOH and HCl. The structure of the dyes studied is shown below (Figure 1):

Figure 1. *Chemical structures of Methylene Blue, Malachite Green and Methyl Violet.*

2.2. Apparatus

Thermo stated shaker of GFL 3033 model was used for mixing the bulk solutions in the experiments. The pH meter (Orion 900S2) with an internal reference electrode and a glass electrode was used for pH measurements. UV-Visible Spectrophotometer (Shimadzu UV-1700) was used to determine MB, MG and MV content in standard and treated solutions. The FT-IR spectrum for single-form and MB, MG and MV loaded forms raw and composites were recorded by a Bruker-Platinum ATR-vertex 70 (Germany) between 550-4000 cm^{-1} wavenumbers at a resolution of 4 cm^{-1} using an attenuated total reflectance (ATR) accessory.

2.3. Preparation of composite beads

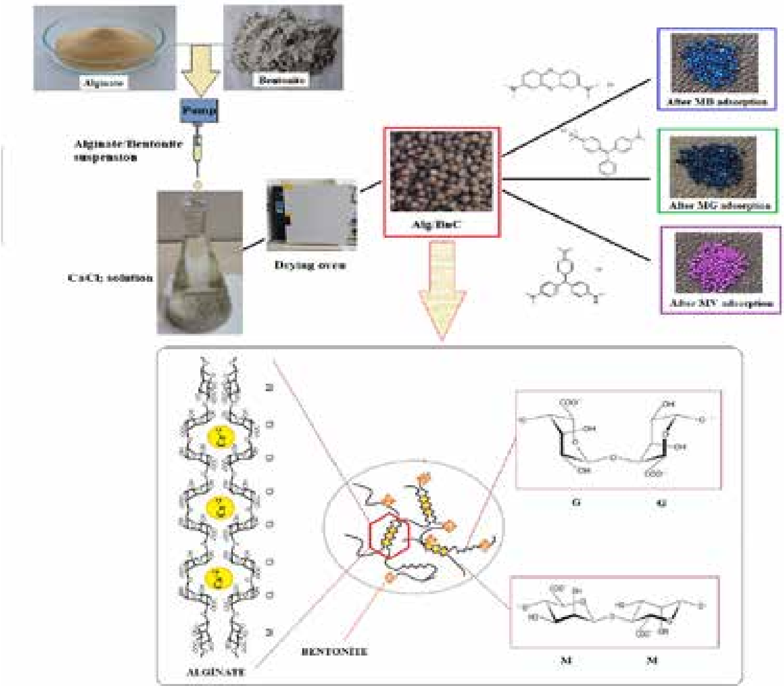

Figure 2. *Synthesis of Alg/BnC.*

Suspension of 5% (w/v) of sodium alginate was prepared by mixing sodium alginate powder with distilled water. This suspension was dissolved by stirring with a magnetic stirrer for 2 hours. The suspension of bentonite 5% (w/v) was prepared and dispersed in distilled water. The prepared bentonite suspension was added to the alginate gel in the form of 1/1 mass ratio (bentonite/alginate). The mixture was stirred with a magnetic stirrer for about 6 hours until it became homogeneous. After that, the solution was kept in a dark medium overnight. The resulting slurry was added dropwise, by using a 5 mL syringe (needle size 0.6 mm) from a 5 cm height, into 0.5 M $CaCl_2$ solution (1 ml gel/5 ml $CaCl_2$) under constant stirring 100 rpm. The beads were kept in a dark medium for overnight. The beads formed and the slurry was filtrated and washed with distilled water until neutral (Figure 2.). They were then dried at ambient temperature. Synthesized alginate coated bentonite composite capsules were abbreviated as Alg/BnC.

2.4. Batch reactor experiments

The dyes batch adsorption tests were directed to investigate the equilibrium at 25 °C as follows: the saturation of the composite by adsorbate was examined at an original pH of the solution by including 1 g/L dosages of Alg/BnC to a sequence of 200 ppm dyes solution. For different interaction periods (5-240 min), the beakers were replaced in an incubator shaker (250 rpm) kept at 25 °C. The impact of Alg/BnC quantity on the colour removal was tested by mixing 200 ppm dyes solution with the adsorbent for 4 h. In the solution phase, the amount of Alg/BnC was 0.5, 1.0, 1.5, 2.0 and 2.5 g / L for each vessel. The isotherm data were modelled by mixing Alg/BnC composite 1 g/L dosage with the different dye molarities (50, 100, 200, 300, 400, 500, 600 and 700 ppm). Initial pH impact on the removal was investigated by adding 1 g/L of Alg/BnC composite dosages to a series of 200 ppm dyes solution at original pHs ranging from 2 to 10. The solution's pH was regulated by adding solution NaOH and HCl. The mixture was blended in a shaker for 4 hours (250 rpm). The samples were tested two times to ascertain the accuracy, reliability and reproducibility of the data obtained from the experimental results. The dye concentration in the filtrate was identified with the UV-vis Spectrophotometer. The amount of dye in the Alg/BnC matrix was found by the following Eq. (1):

$$q_e = \frac{C_i - C_f}{m} \times V \tag{1}$$

where q_e (mg g^{-1}) is the adsorption capacity of the Alg/BnC, C_i and C_f (mg L^{-1}) are the initial and final concentration of dye, respectively, V (mL) is the volume of the solution, and m (g) is the amount of the Alg/BnC. The percent adsorption of dye can be demonstrated as follows Equation (2):

$$\%\ Adsorption = \frac{C_i - C_f}{C_i} \times 100 \tag{2}$$

3. RESULTS AND DISCUSSION

3.1. Characterization of the beads

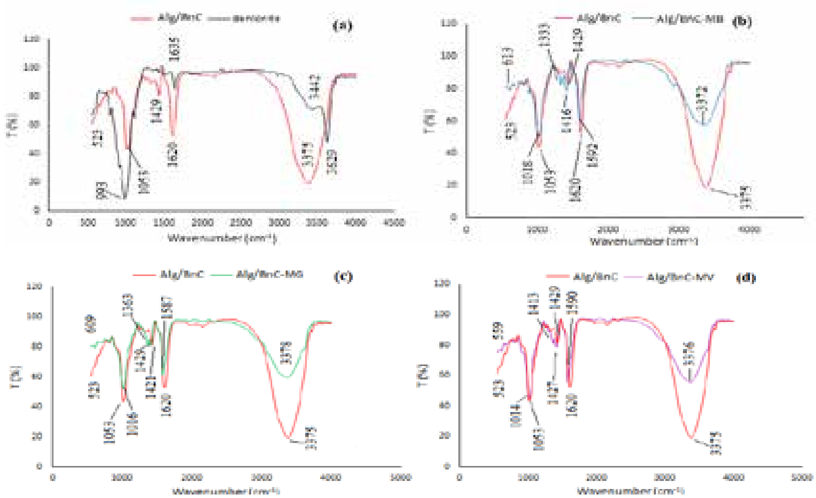

Figure 3. *The FT-IR spectral characteristics of Alg/BnC before and after dye adsorption.*

The FTIR spectra of the Alg/BnC microspheres used in the adsorption in raw form and after the adsorption of MB, MG, MV dyes were measured within the range of 500–4000 cm^{-1} and were displayed in Figure 3. Some modifications were noted in the distinctive peaks varying from 900 to 3600 cm^{-1} and some noticeable shifts of Alg/BnC peak places before and after dyestuff adsorption. The FTIR spectra showed major peaks related to raw bentonite's functional groups. H–O–H stretching vibrations were observed in one broadband around 3442 cm^{-1} and Al–O–H stretching vibrations was also appeared at around 3629 cm^{-1} (Figure 3a.). Bending vibrations of H–O–H is signified by the peak found at 1635 cm^{-1} (De Castro et al. 2018). The peaks near 1200 and 800 cm^{-1} were due to Si–O and Al–O stretching vibrations and that at 523 cm^{-1} was related to Si–O–Mg stretching vibration (Akpomie et al. 2015). Figure 3. confirmed the presence of alginate and bentonite functional groups in the capsule. The peak of 551 cm^{-1} is due to the Si-O stretching band and the stretching vibration of an octahedral layer of aluminosilicate band at 767 cm^{-1} confirmed the presence of the bentonite in the capsule (Choudhury et al., 2015). The asymmetric and symmetric stretching vibration bands of C–O–O at 1620 and 1429 cm^{-1} in FTIR spectra (Liao et al. 2015; Watthanaphanit et al. 2009) confirmed the presence of alginate in the capsule. The FTIR spectra of MB, MG and MV before and after adsorption onto Alg/BnC is depicted in Figure 3(b, c, d). For MB adsorption; the band in 3375 cm^{-1} slightly shifted to a lower frequency band at 3372 cm^{-1}, 1620 cm^{-1} to 1592 cm^{-1}, the band in 1429

cm^{-1} to 1416 cm^{-1}, the band in 1338 cm^{-1} to 1333 cm^{-1}, the band in 1053 cm^{-1} to 1018 cm^{-1}, the band in 551 cm^{-1} transferred to higher frequencies at 613 cm^{-1}. For MG adsorption; the band in 3375 cm^{-1} slightly shifted to a lower frequency band at 3378 cm^{-1}, 1620 cm^{-1} to 1587 cm^{-1}, the band in 1429 cm^{-1} to 1421 cm^{-1}, the band in 1338 cm^{-1} to 1363 cm^{-1}, the band in 1053 cm^{-1} to 1016 cm^{-1}, the band in 551 cm^{-1} transferred to higher frequencies at 609 cm^{-1}. For MV adsorption; the band in 3375 cm^{-1} slightly shifted to a lower frequency band at 3376 cm^{-1}, 1620 cm^{-1} to 1590 cm^{-1}, the band in 1429 cm^{-1} to 1427 cm^{-1}, the band in 1338 cm^{-1} to 1413 cm^{-1}, the band in 1053 cm^{-1} to 1014 cm^{-1}, the band in 551 cm^{-1} transferred to higher frequencies at 559 cm^{-1} band after adsorption and the intensity of the peak was decreased. It is seen that the band shrinks in its range around 3378.67 cm^{-1} after all three colours have been adsorbed. This reason for the sharp decrease is due to ionic interactions in the structure between the -OH groups and the dyes. Where bands intensity change happened shows the functional groups communication with the molecules of MB, MG, and MV (Xu et al. 2011). After the adsorption of dyestuffs, many functional groups shifted to different bands, disappeared or have changed severity. These changes indicate that the possible interaction of the Alg/BnC with MB, MG and MV dye molecules via these functional groups and the loading of dyes onto the Alg/BnC.

3.2. Effect of adsorbent dosage

The effect of the Alg/BnC dosage quantity (0.5, 1.0, 1.5, 2.0 and 2.5 g/L) on the dyestuff removal percentage and the adsorption capacity effect was given in Figure 4a. As shown in the figure, the adsorbent amount increases as dyes adsorption increases, and then reached a certain value. The rise in the quantity of adsorbent does not influence the adsorption considerably after this plateau value. After this stage; there was no important impact of raising the quantity of adsorbent on the removal of the dye due to the reality that the adsorption event was an equilibrium event. The rise in the percentage of adsorbent dye removal with increased adsorbent dose could be ascribed to increased adsorption sites accessibility. At equilibrium, the percent removal became constant probably because of the saturation of the available adsorption sites. Another outcome of Figure 4a. is that the adsorption capability (q_e) decreased substantially with the increasing the quantity of Alg/BnC. The percentage of removal of dyes increases as the amount of adsorbent increases, but the capacity of adsorption decreases. Possible causes of this situation can be the presence in the setting of a big amount of vacant active centers relative to the concentration of fixed dye. The adsorbed particles were decreased from the solution phase and diffuse to the adsorbent's surface (Ghaedi et al., 2014). The equilibrium was achieved at an adsorbent dose of 1 g/L for Alg/BnC.

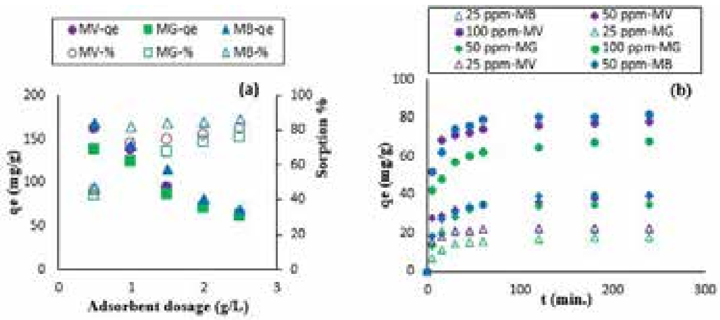

Figure 4. *The effect of adsorbent dosage on removal of MB, MG and MV by Alg/BnC (a) and the effect of contact time on the adsorption of MB, MG and MV by Alg/BnC (b)*

3.3. Effect of contact time

The adsorption was very fast for the different dye concentrations in Figure 4b. The reason was that the surface area for adsorption was large. Those locations start to fill up over time and the adsorption rate slows down as the equilibrium approaches. As can be seen from the figure, more than half of the dye amount was adsorbed in the first 15 minutes by Alg/BnC. For adsorption of MB, MG and MV; the adsorption gradually increased in the 15 minutes and reaches an equilibrium in 45 minutes. The equilibrium period for all dyes for Alg/BnC was 45 minutes.

3.4. Effect of pH

In terms of adsorption ability, the adsorption medium of the original pH is very important. The medium's starting pH was altered in the 2-10 range. As the pH for three dyestuffs is increased from 2 to 10, the adsorption ability of Alg/BnC has been increased (Figure 5a.). This is an expected result because MB, MG and MV are in cationic form.

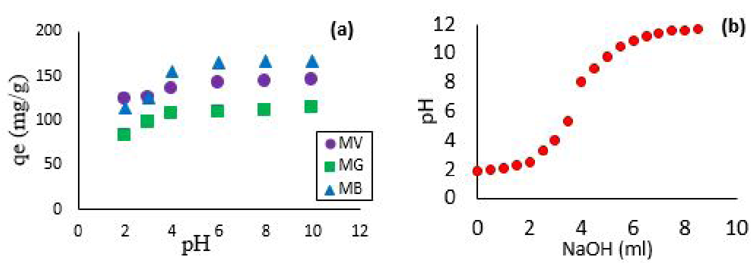

Figure 5. The effect of pH on the adsorption of MB, MG and MV by Alg/BnC (a) and the zero charge point of Alg/BnC (b)

The zero charge point (pH_{PZC}) of the Alg/BnC was discovered to be at pH 6.1. Using the pHpzc idea, Alg/BnC surface is predominantly charged negatively when solution pH>6.1, while predominantly charged positively when solution pH<6.1 is charged. The $pH>pH_{PZC}$ shows more pronounced adsorption of cationic dyes by Alg/BnC. Considering the adsorption between the negatively charged surface and the cationic dyes, excess H^+ ions at the acidic pH in the medium were placed in the appropriate adsorption centers in the adsorbent and prevented the adsorption of cationic dyes. Because of the electrostatic repulsion between the positively charged adsorbent surface and the dyes, the removing ions from the aqueous solution is therefore difficult at low pH values. As can be seen from Figure 5b., a point is reached where the surface load is zero (pH range) with increasing pH. After this point, Alg/BnC surfaces have a negative character with the increase in pH value, and the adsorption of MB, MG and MV is increased. Therefore, in high pH circumstances, adsorption becomes more and the optimum pH value was discovered in the range of 6-7. The literature contains similar outcomes (Thakur et al. 2016). The initial pH values are 6.8, 6.4, and 6.7, for MB, MG, and, MV respectively and are close to their maximum adsorption at pH:6.0.

3.5. Adsorption Isotherms

Dyestuff adsorption with various concentrations plays an important role in determining the adsorbent's adsorption capacity (Figure 6.) (Gobi et al. 2011). A series of samples were prepared at different concentrations from stock MB, MG and MV solution. These samples were treated with Alg/BnC to complete the equilibrium. The mass transfer strength between the dye solution and the adsorbent surface is easier to exceed at greater initial concentrations levels. With growing dye concentration, vacant active centers on the adsorbent surface were quickly filled. The adsorption capability increased as the dye initial concentration increased and then it remained at approximately constant values (plateau line). The results of Langmuir, Freundlich, Scatchard, and Temkin isotherms analysis for the removal of MB, MG and MV from aqueous solutions on Alg/BnC are given in Table 2. Adsorption isotherms described the equilibrium interactions between adsorbent and dyestuff. Alg/BnC and MB, MG and MV adsorption results were found to be acceptable when compared with experimental data. The suitability of the equilibrium curve for the Langmuir isotherm was investigated and K_b and A_s values were presented in Table 2.

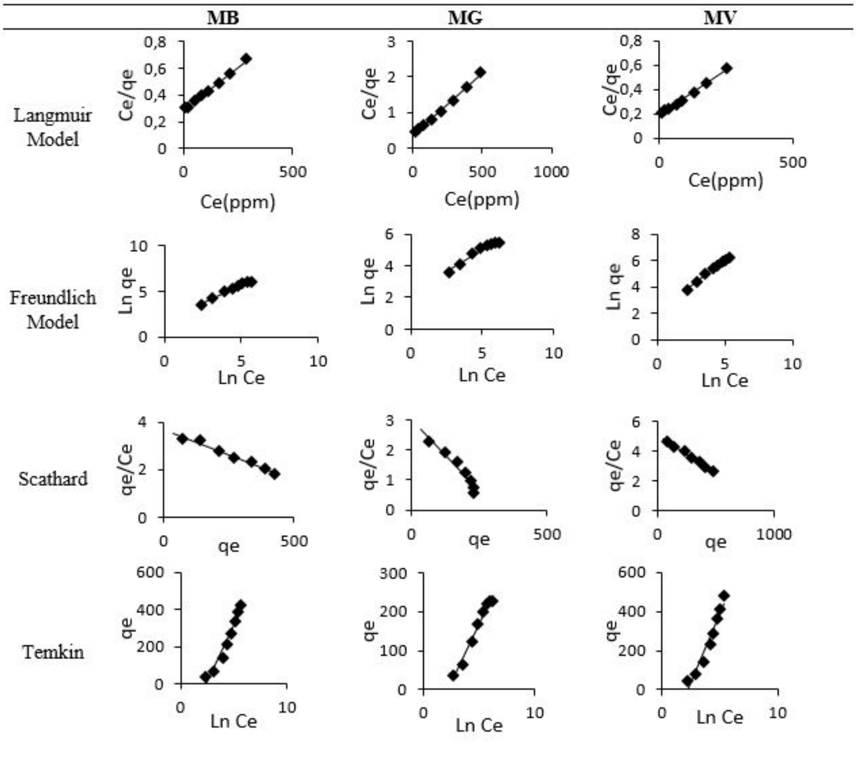

Figure 6. *Langmuir, Freundlich, Scatchard and Temkin isotherms plot for the adsorption of MB, MG and MV by Alg/BnC.*

Compared to other isotherms data, the Langmuir isotherm was more relevant for the dye adsorption. Correlation coefficient (R^2) is close to 1 for Langmuir isotherm. The A_s value for Langmuir isotherm was calculated to be 769.2 mg/g for Alg/BnC/MB; 285.7 mg/g for Alg/BnC/MG and 666.7 mg/g for Alg/BnC/MV. According to the maximum adsorption capacities values, it was observed that MB dye adsorption on Alg/BnC was higher than MG and MV. K_f and n values were calculated from Freundlich equation. If n value is between 1 and 10, the efficiency of the adsorption is high. n values were calculated as 1.0 for MB, 1.80 for MG, 1.39 for MV and R^2 values are 0.989 for MB, 0.948 for MG, and 0.978 for MV. The slope n measures the surface heterogeneity. Temkin isotherm parameters are given in Table 2. B values were 124.2, 61.8, and 127.5 kJ mol^{-1}, for MB, MG, and MV, respectively. Values higher than 8 indicated stronger cohesive forces in between Alg/BnC and dye. The R^2 value for Scatchard isotherm for MB, MG and MV adsorption were 0.978, 0.932, 0.955 and the maximum capacity were 857.8, 314.5, 811.9 mg/g, respectively. The results were supported by the Langmuir isotherm. A dimensionless separation factor, R_L, is given as in Eq. 3 (Parlayıcı et al., 2016):

$$R_L = \frac{1}{1+K_L C_o} \tag{3}$$

where C_o is the highest initial dye concentration. The value of R_L supports the isotherm shape to be favourable ($0 < R_L < 1$). The values of R_L obtained were 0.52, 0.34 and 0.39 for MB, MG and MV adsorption, respectively (Table 2). These results supported that the Langmuir isotherm was more favourable than others.

Table 2. *Parameters of Langmuir, Freundlich, Scarthard and Temkin isotherms for adsorption of MB, MG and MV by Alg/BnC.*

Model	Dye	Parameters			
Langmuir		**A_s**	**K_b**	**R_L**	**R^2**
	MB	769.2	0.005	0.52	0.994
	MG	285.7	0.010	0.34	0.995
	MV	666.7	0.008	0.39	0.993
Freundlich		**K_f**	**n**	**R^2**	
	MB	6.37	1.30	0.989	
	MG	9.16	1.80	0.948	
	MV	10.12	1.39	0.978	
Scatchard		**Q_S**	**Ks**	**R^2**	
	MB	857.8	0.004	0.978	
	MG	314.5	0.010	0.932	
	MV	811.9	0.007	0.955	
Temkin		**B**	**Kt**	**R^2**	
	MB	124.2	0.087	0.953	
	MG	61.8	0.104	0.984	
	MV	127.5	0.112	0.976	

3.6. Kinetic models

Adsorption kinetics is important for understanding the adsorption steps that affect the rate of adsorption. In this study, adsorption kinetics of MB, MG and MV on Alg/BnC were investigated and used according to the pseudo-first and pseudo-second-order models' equations given in Eq. 4 and 5 (Figure 7). Table 3 presents the kinetic parameters calculated from the kinetic models and the correlation coefficients (R^2).

$$ln(q_e - q_t) = ln\, q_e - k_1 t \tag{4}$$

$$\frac{1}{q_t} = \frac{1}{k_2\; qe^2} + \frac{1}{q_e\, t} \tag{5}$$

where k_1 is the rate constant of pseudo-first-order adsorption, k_2 is the rate constant of pseudo-second-order adsorption, q_e and q_t is the adsorption capacity (mg/g) at equilibrium and at a time (t), respectively. The correlation coefficients (R^2) obtained with the pseudo second-order kinetic model are above 0.99. This shows that MB, MG and MV adsorption on Alg/BnC adsorption is suitable for pseudo-second-order velocity model. This supports the adhesion of MB, MG and MV molecules to Alg/BnC by chemical adsorption.

Table 3. *Comparison of the pseudo-first-order, pseudo-second-order adsorption rate constants and experimental q_e values obtained at different initial dyes concentrations.*

			Pseudo First-order			Pseudo Second-order		
Dye	C_o(ppm)	$q_{e\ exp}$	k_1	q_e	R^2	k_2	q_e	R^2
MB	25	23.90	0.008	5.12	0.765	0.0133	23.09	1.000
MB	50	40.71	0.013	15.24	0.894	0.0029	41.15	1.000
MB	100	81.40	0.014	13.38	0.729	0.0035	82.64	0.999
MG	25	19.49	0.008	8.58	0.855	0.0052	18.55	1.000
MG	50	35.07	0.016	9.68	0.686	0.0032	36.23	0.999
MG	100	69.83	0.011	21.25	0.938	0.0024	69.44	1.000
MV	25	22.50	0.007	1.77	0.439	0.0439	22.12	1.000
MV	50	40.87	0.008	12.16	0.975	0.0041	39.37	0.999
MV	100	78.83	0.013	14.61	0.921	0.0041	78.74	1.000

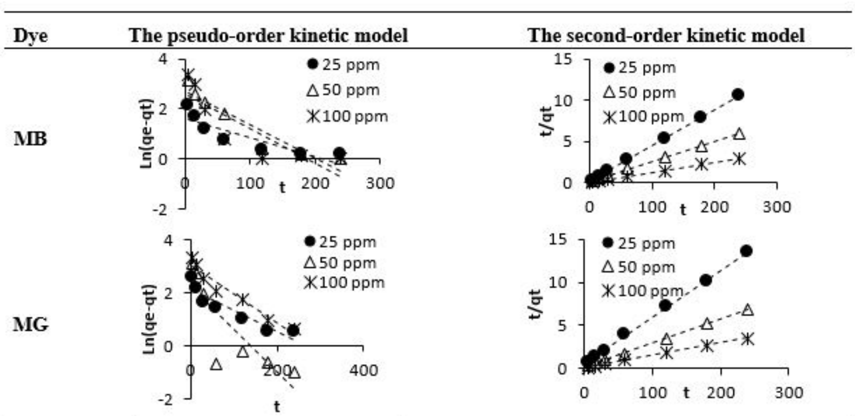

Figure 7. *Adsorption kinetics data of MB, MG and MV by Alg/BnC for different initial dye concentrations.*

3.7. Thermodynamic Studies

The thermodynamic behaviour of the adsorption process was explained by using adsorption experiments data at different temperatures (25 °C, 35 °C, 45 °C and 55 °C) (Figure 8). Using the following equations 6-7, thermodynamic parameters such as the free energy change (ΔG°), entropy change (ΔS°) and enthalpy change (ΔH°) of the adsorption were calculated (Table 4):

$$\Delta G^\circ = -\,RT\ln K_c \qquad (6)$$

$$\ln K_c = \frac{\Delta S^o}{R} - \frac{\Delta H^o}{RT} \qquad (7)$$

The ΔS° values are positive in the adsorption of MB, MG and MV by Alg/BnC. This shows that there is an increase in the randomness at the solid/solution interface during the adsorption process. Negative values of ΔG° show that the method's applicability and spontaneous adsorption. If ΔH° values are positive, it indicates that adsorption is the endothermic process. As seen from the outcomes, the ΔG° values are negative in three dyes removal by Alg/BnC and that the adsorption is spontaneous. ΔH° values are positive for the dyes. So, the adsorption of MB, MG and MV onto Alg/BnC was endothermic processes and the adsorption is spontaneous.

Table 4. *Thermodynamic parameters for the dyes adsorption by Alg/BnC.*

Dye	ΔS° (J $K^{-1}mol^{-1}$)	ΔH° J mol-1	ΔG° (J mol-1) T=298.15K	T=308.15K	T=318.15K	T=328.15K	R^2
MB	185.01	52594.18	-2567.1	-4417.2	-6267.3	-8117.4	0.993
MG	45.04	12232.08	-1195.3	-1645.6	-2095.9	-2546.3	0.993
MV	37.83	7493.97	-3784.7	-4163.0	-4541.3	-4919.6	0.989

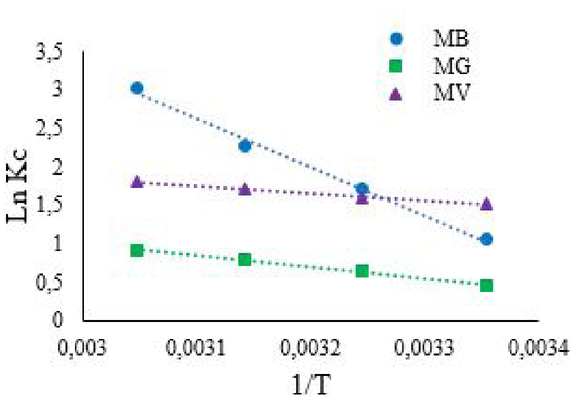

Figure 8. *Effect of temperature on the adsorption of MB, MG and MV by Alg/BnC.*

4. CONCLUSION

Adsorption of MB, MG and MV by the Alg/BnC was discussed in this research. The original pH solution has a significant impact on MB, MG and MV adsorption. Adsorption information for the equilibrium was evaluated with Langmuir, Freundlich, Scatchard and Temkin isotherm equations. Isotherm studies revealed that MB, MG and MV equilibrium data was well described with the Langmuir model. For the Langmuir isotherm model, the highest adsorption capacity was 769.2 mg/g-(Alg/BnC): MB, 285.7 mg/g-(Alg/BnC): MG and 666.7 mg/g-(Alg/BnC): MV. Changes in the FTIR spectrum that occur after adsorption resulted in the disappearance of new peaks which are involved in the adsorption. The equilibrium of adsorption were achieved in 45 min. Kinetic information showed that pseudo-second-order kinetic model could define the dynamic trend of MB, MG, and MV adsorption. Thermodynamic calculations showed a spontaneous nature of the adsorption of MB, MG and MV dyes. This research demonstrated that the Alg/BnC played an important role and a higher capacity for the removing of MB, MG, and MV from the aqueous solutions.

REFERENCES

A. Watthanaphanit, P. Supaphol, T. Furuike, S. Tokura, H. Tamura, R. Rujiravanit, "Novel Chitosan-Spotted Alginate Fibers from Wet-Spinning of Alginate Solutions Containing Emulsified Chitosan-Citrate Complex and Their Characterization," *Biomacromolecules*, 10(2):320–327, 2009.

E. Bulut, M. Özacar, İ. A. Şengil, "Adsorption of Malachite Green onto Bentonite: Equilibrium and Kinetic Studies and Process Design," *Microporous and Mesoporous Materials*, 115(3):234-246, 2008.

C. Puri, G. Sumana, "Highly Effective Adsorption of Crystal Violet Dye from Contaminated Water Using Graphene Oxide Intercalated Montmorillonite Nanocomposite," *Applied Clay Science*, 166:102-112, 2018.

J. L. Marco-Brown, L. Guz, M. S. Olivelli, B. Schampera, R. T. Sánchez, G. Curutchet, R. Candal, "New Insights on Crystal Violet Dye Adsorption on Montmorillonite: Kinetics and Surface Complexes Studies," *Chemical Engineering Journal*, *333*:495-504, 2018.

K. Gobi, M. D. Mashitah, V. M. Vadivelu, "Adsorptive Removal of Methylene Blue Using Novel Adsorbent from Palm Oil Mill Effluent Waste Activated Sludge: Equilibrium, Thermodynamics and Kinetic Studies," *Chemical Engineering Journal*, 171(3):1246-1252, 2011.

K.G. Akpomie, F.A. Dawodu, K.O. Adebowale, "Mechanism on the Sorption of Heavy Metals from Binary-Solution by a Low Cost Montmorillonite and Its Desorption Potential," *Alexandria Engineering Journal*, 54:757-767, 2015.

K. H. Gonawala, M. J. Mehta, "Removal of Color from Different Dye Wastewater by Using Ferric Oxide as an Adsorbent," *Journal of Engineering Research and Applications*, 4(5):102-109, 2014.

M. Ghaedi, A. G. Nasab, S. Khodadoust, M. Rajabi, S. Azizian, "Application of Activated Carbon as Adsorbents for Efficient Removal of Methylene Blue: Kinetics and Equilibrium Study," *Journal of Industrial and Engineering Chemistry*, 20(4), 2317-2324, 2014.

M. L. F. A. De Castro, M. L. B. Abad, D. A. G. Sumalinog, R. R. M. Abarca, P. Paoprasert, M. D. G. de Luna, "Adsorption of Methylene Blue Dye and Cu (II) Ions on EDTA-Modified Bentonite: Isotherm, Kinetic and Thermodynamic Studies," *Sustainable Environment Research*, 28(5):197-205, 2018.

M. S. Bashanaini, M. H. Al-Douh, H. S. Al-Ameri, "Removal of Malachite Green Dye from Aqueous Solution by Adsorption Using Modified and Unmodified Local Agriculture Waste," *Science*, *7*(2):42-56, 2019.

N. M. Mahmoodi, M. Taghizadeh, A. Taghizadeh, "Mesoporous Activated Carbons of Low-Cost Agricultural Bio-Wastes with High Adsorption Capacity: Preparation and Artificial Neural Network Modeling of Dye Removal from Single and Multicomponent (Binary and Ternary) Systems," *Journal of Molecular Liquids*, *269*:217-228, 2018.

P. R. Choudhury, P. Mondal, S. Majumdar, "Synthesis of Bentonite Clay Based Hydroxyapatite Nanocomposites Cross-Linked by Glutaraldehyde and

Optimization by Response Surface Methodology for Lead Removal from Aqueous Solution," *RSC Advances*, 5(122):100838-100848, 2015.

R. Goh, Y. K. Leong, B. Lehane, "Bentonite Slurries-Zeta Potential, Yield Stress, Adsorbed Additive and Time-Dependent Behavior," Rheologica Acta, 50(1):29-38, 2011.

R. Han, J. Zhang, P. Han, Y. Wang, Z. Zhao, M. Tang, "Study of Equilibrium, Kinetic and Thermodynamic Parameters About Methylene Blue Adsorption onto Natural Zeolite," *Chemical Engineering Journal*, *145*(3):496-504, 2009.

R. K. Xu, S. C. Xiao, J. H. Yuan, A. Z. Zhao, "Adsorption of Methyl Violet from Aqueous Solutions by The Biochars Derived from Crop Residues," *Bioresource Technology*, 102(22):10293-10298, 2011.

R. Xu, J. Mao, N. Peng, X. Luo, C. Chang, "Chitin/Clay Microspheres with Hierarchical Architecture for Highly Efficient Removal of Organic Dyes," *Carbohydrate Polymers*, 188:143-150, 2018.

S. Banerjee, M. C. Chattopadhyaya, "Adsorption Characteristics for the Removal of a Toxic Dye, Tartrazine from Aqueous Solutions by a Low Cost Agricultural by-Product," *Arabian Journal of Chemistry*, 10:S1629-S1638, 2017.

S. Bentahar, A. Dbik, M. El Khomri, N. El Messaoudi, A. Lacherai, "Adsorption of Methylene Blue, Crystal Violet and Congo Red from Binary and Ternary Systems with Natural Clay: Kinetic, Isotherm, and Thermodynamic," *Journal of Environmental Chemical Engineering*, *5*(6):5921-5932, 2017.

S. Chowdhury, S. Pan, R. Balasubramanian, P. Das, "Date Palm Based Activated Carbon for the Efficient Removal of Organic Dyes from Aqueous Environment," In *Sustainable Agriculture Reviews, 34*:247-263, 2019.

S. H. Liao, C. H. Liu, B. P. Bastakoti, N. Suzuki, Y. Chang, Y. Yamauchi, F. H. Lin, K. C. Wu, "Functionalized Magnetic Iron Oxide/Alginate Core-Shell Nanoparticles for Targeting Hyperthermia," *International Journal of Nanomedicine*, 10:3315, 2015.

S. Mashhadi, H. Javadian, M. Ghasemi, T. A. Saleh, V. K. Gupta, "Microwave-Induced H2SO4 Activation of Activated Carbon Derived from Rice Agricultural Wastes for Sorption of Methylene Blue from Aqueous Solution," *Desalination and Water Treatment*, *57*(44):21091-21104, 2016.

S. Parlayıcı, A. Yar, A. Avcı, E. Pehlivan, "Removal of Hexavalent Chromium Using Polyacrylonitrile/Titanium Dioxide Nanofiber Membrane," *Desalination and Water Treatment,* 57:16177-16183, 2016.

S. Thakur, S. Pandey, O. A. Arotiba, "Development of a Sodium Alginate-Based Organic/Inorganic Superabsorbent Composite Hydrogel for Adsorption of Methylene Blue," *Carbohydrate Polymers*, 153:34-46, 2016.

W. Astuti, A. Chafidz, E. T. Wahyuni, A. Prasetya, I. M. Bendiyasa, A. E. Abasaeed, "Methyl Violet Dye Removal Using Coal Fly Ash (CFA) as a Dual Sites Adsorbent," *Journal of Environmental Chemical Engineering*, *7*(5):103262, 2019.

V. Gomez, M.S. Larrenchi, M.P. Callao, "Kinetic and Adsorption Study of Acid Dye Removal Using Activated Carbon," *Chemosphere*, 69:1151-1158, 2007.

THE SIGNIFICANT HYDROCARBON SEEPAGES IN THE EASTERN MEDITERRANEAN REGION: ÇIRALI (CHIMERA) NATURAL GAS POTENTIAL, KEMER-ANTALYA, SW-TURKEY

CHAPTER

3

Fuzuli YAĞMURLU[1]
Ezher TAGLIASACCHI[2]
Murat ŞENTÜRK[3]

[1] Süleyman Demirel University, Engineering Faculty, Department of Geological Engineering, Çünür/Isparta, Turkey
[2] Pamukkale University, Engineering Faculty, Department of Geological Engineering, Kınıklı/Denizli, Turkey
[3] Süleyman Demirel University, Engineering Faculty, Department of Geological Engineering, Çünür/Isparta, Turkey

1.INTRODUCTION

The giant natural gas deposits of marine Neogene basins in the Eastern Mediterranean region have been discovered in the last decades and these Tertiary basins have become more attention year by year (Fig. 1). Natural gas is an environmental friendly, clean-burning fuel, offering important environmental utilities compared to other fossil fuels (Mokhatab and Poe, 2006).

The studies of the geological setting of the natural gas seeps and the stratigraphic features of the main Neogene basins in SW-Anatolia and their natural gas potentials effectively are coming into value. For that reason, many researchers who focused on Isparta angle and SW-Anatolia, dealt with the stratigraphic position and features of Tertiary sedimentary sequences located widespread in the northern and eastern part of the Gulf of Antalya (Korkmaz and Gedik, 1990; Flecker et al., 1995, 2005; Altunsoy, 1999; Atabey et al., 2000; Poisson et al., 2003; Yağmurlu et al., 2007; Özçelik et al., 2009). Accordingly, several studies carried out by Poisson et al. (2003), Flecker et al. (1995,2005) and Yağmurlu et al. (2007), reefal carbonates located in the southern Isparta Çay and surroundings overlie with angular disconformably on Triassic pelagic sediments belong to Antalya Nappes whereas Burdigalian turbiditic clastics conformably overlie on these reefal carbonates. On the other hand, Korkmaz and Gedik (1990), Altunsoy (1999), Atabey et al. (2000) and Özçelik et al. (2009) mentioned that Early Miocene marine carbonates which well observed in Isparta, Kaş-Kasaba and Mut basins have good features of source rock. Furthermore, the stratigraphic features and lithofacies distributions of sediments filled in Antalya, Adana and Mut basins have been investigated by Görür (1973), Gedik et al. (1979), Akay et al. (1985), Korkmaz, (1990), Atabey et al. (2000), İslamoğlu, (2002), Özdoğan (2004) ile Işler et al. (2005). Likewise, the stratigraphy and sedimentological features of Miocene sequences cropping out Kaş-Kasaba basin have been studied by Hayward (1982), İslamoğlu and Taner (2002) and Koşun et al. (2009). However, the geological features and setting within the regional tectonic structures of Cyprus and east Mediterranean basins have been focused on detail by Robertson (1998), Robertson et al. (1995, 2004), Payne and Robertson (1995), Eaton and Robertson (2004), Boulton and Robertson (2007), Aksu et al. (2005, 2009), Hall et al. (2005), Hakyemez and Toker (2010).

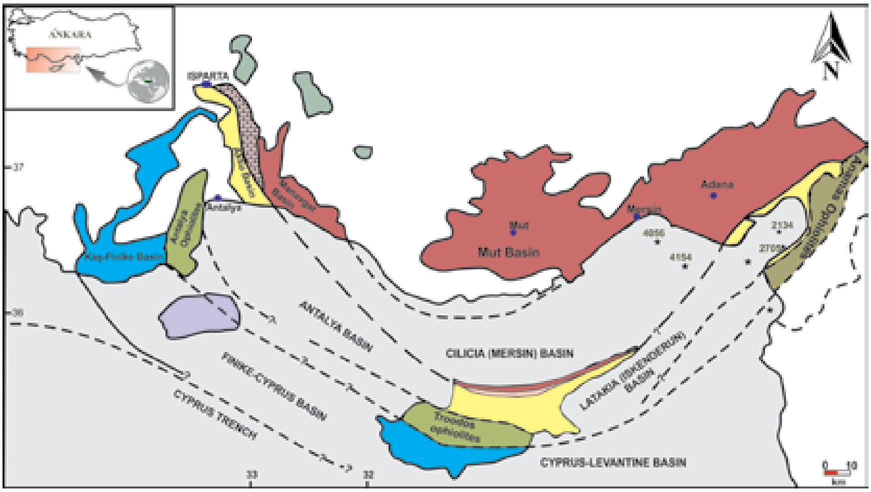

Fig. 1. *Showing generalized map of Tertiary Basins in the Eastern Mediterranean region and surrounding the Gulf of Antalya*

Some of the researchers have focused on the origin of occurrences of natural gas in Çıralı and it has been pointed out that this natural gas circumstantial evidence has abiotic origin and it could be depending on serpentinization (Hoşgörmez, 2006; Hoşgörmez et al. 2008; Etiope et al. 2011). However, the studies of the east Mediterranean basin in recent years, it shows that natural gas sources are found in Tertiary sedimentary sequences. Geophysical data indicated that eastern part of the Anaximander Seamount located in the south of Çıralı shows presence of the mud volcanoes connected with natural gas outputs. For that reason, as well as Kemer-Çıralı region, Finike-Kumluca basin which is very well observed in marine Tertiary sequences has become inevitable to investigate after the latest developments.

This present study focuses on stratigraphic, sedimentologic, tectonic and organic geochemistry features of Tertiary deposits in Finike-Kumluca and Kemer region and the main goal of this paper to evaluate the modelling of geological setting and origin of the natural gas evidences in Kemer-Çıralı. Generally considering, natural gas outputs in Çıralı region which are controlled by geological structures related with sedimentological and stratigraphical features of Kumluca-Finike basin deposits and moreover, autochthonous and allochthonous units have not been revealed in detail. For that reason, in this current study, the geological features of Finike basin and Çıralı natural gas outputs have been discussed and investigated in all aspect.

2. GEOLOGICAL SETTING

Kemer-Çıralı region is located west part of the Isparta angle and north of the Antalya Gulf in SW-Anatolia (Fig. 2). The Isparta angle is the link between the Aegean–West Anatolian extensional province bounded to the south by the actively subduction of Hellenic arc and the uplifted Anatolian plateau bounded to the south by the Cyprus arc (Glover and Robertson, 1998). The Isparta angle also reflects Miocene convergent tectonics, whereby the autochthonous Beydağları massif was over thrusted by several nappes (i.e. Antalya complex, Lycian nappe and Hoyran Beysehir nappe; (e.g. Robertson and Woodcock, 1984; Şenel, 1984; Poisson et al., 2003; Robertson et al., 2003). The reverse rotation of the east and west flanks of Isparta angle causes E-W tension forces in the apex part. Thus, this event brought about to occur of N-S trending Eğirdir-Kovada graben (Yağmurlu and Şentürk, 2005). Isparta angle has been divided by N-S trending Eğirdir-Kovada graben in two different regions such as Beydağları autochthonous and Akseki-Anamas sequences. Beydağları autochthonous as defined by (Poisson (1977), Gutnic (1977), Dumont (1976), Monod (1977), Özgül (1976), Marcoux (1977), Demirtaşlı (1979), Koçyiğit (1983), Poisson et al.,1984, Şenel 1984, Yağmurlu et al. (1995), Bozcu and Yağmurlu (2001), Poisson et al., (2003) encompasses a large region consisted of mainly carbonate rocks bounded by Eğirdir-Kovada graben in the west and in addition, the other region is Akseki-Anamas sequences chiefly composed of autochthon carbonates in the east (Fig. 2).

Marine Tertiary sediments have been deposited in Finike, Aksu and Manavgat basins located in Isparta angle and surroundings, from west to east respectively. These sediments mainly compose of reefal limestone (Aquitanian) between turbiditic sediments (Eocene and Burdigalian) unconformably overlie on Mesozoic carbonates and tectonically overlain by ophiolithic rock units belonged to Lycian and Antalya nappes.

The thickness of the Aqutanian reefal limestones in Tertiary sequences reaches to the 500 meter from north to south. Turbiditic sediments in this sequence contain rich organic matter in intercalated with carbonaceous mudstone in some part.

3. LITHOSTRATIGRAPHIC TYPE SUCCESSIONS

Following the first stratigraphic studies of the Kemer-Çıralı region (Poisson, 1977, 1984) are focused on autochthonous and allochthonous units by the previous researchers. This region has been characterized by marine turbidites (Garipçe and Karakuştepe Formations) and neritic limestones (Beydağları and Karabayır Formations) (Fig. 3). All these formations are given in below, respectively.

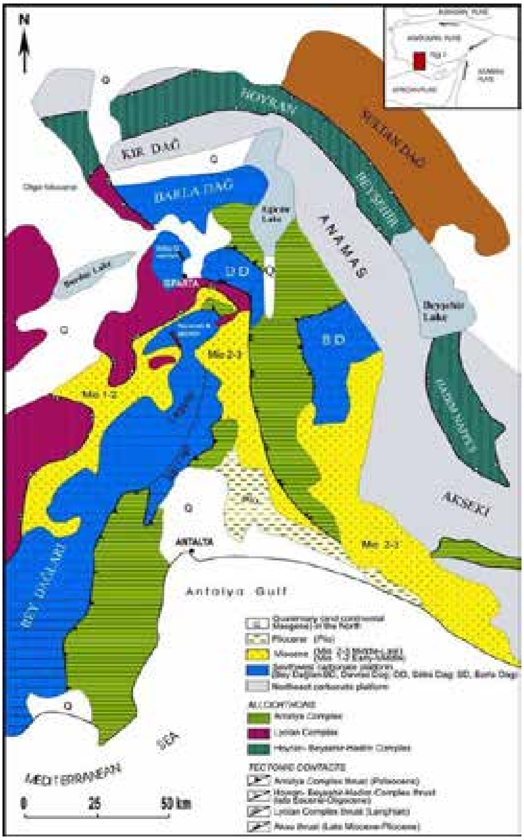

Fig. 2. *Main geological units of the Isparta Angle and Antalya Gulf region and surrounding areas (after, Poisson et al., 2007).*

3.1. Autochthonous Rock Units

3.1.1. Beydağları Formation (Jura- Cretaceous Neritic limestones)

The Beydağları Formation comprises thick neritic limestones at the top and thin hemipelagic limestones at the base which is located widespread in Antalya- Beydağları and west flake of Isparta Angle in SW- Anatolia. Approximately, 1000m thick, Jura-Cretaceous neritic part consists of shallow water limestones and hemipelagic limestones which gradually overlie the neritic limestones (Figs. 3 and 4). The upper part of the Beydağları sequences mostly composes of thick bedded Rudist limestones and they overlaid on pelagic limestone with Globotruncana accompanied with shale and mudstones intercalated (Poisson, 1984; Şenel, 1984). Beydağları Formation overlies the Kuyubaşı dolomites and Paleozoic sedimentary rock units in the western Antalya. The neritic limestones belong to Beydağları Formation are unconformable overlaid by Aquitanian limestone in Salurdağ region located the western part of Kumluca.

3.1.2. Garipçe Formation (Eocene turbiditic sediments)

The Garipçe Formation widely located in the northern part of Finike, Kaş-Kasaba basin and the north of the Finike basin named and defined by Poisson (1984) and Şenel (1984) unconformably overlies the Cretaceous carbonate rock units. Eocene turbiditic sediments tectonically overlying on early Miocene sediments observed in Ispartaçay region and the south of the Sav town are named as a “Yavuz nappe” by Poisson et al. (2003). This formation is named as “Kayıköy Formation” by Karaman (1990) and Yağmurlu (1991) having similar stratigraphical position and mainly composed of turbiditic sediments. The presence of benthic foraminifera contents in carbonate levels such as *Alveolina* sp., *Assilina* sp., *Discocylina* sp., show that formation age could be Lutetian (middle Eocene). The thickness is up to 500m in some part. Unit mostly composes of greenish grey sandstones derived from ophiolithic rock fragments and shale intercalated. Shales are main component of the Garipçe formation and chiefly greyish light green coloured, intercalated with sandstones. The carbonized plant remains and organic matter rich mudstones are found in this shale unit.

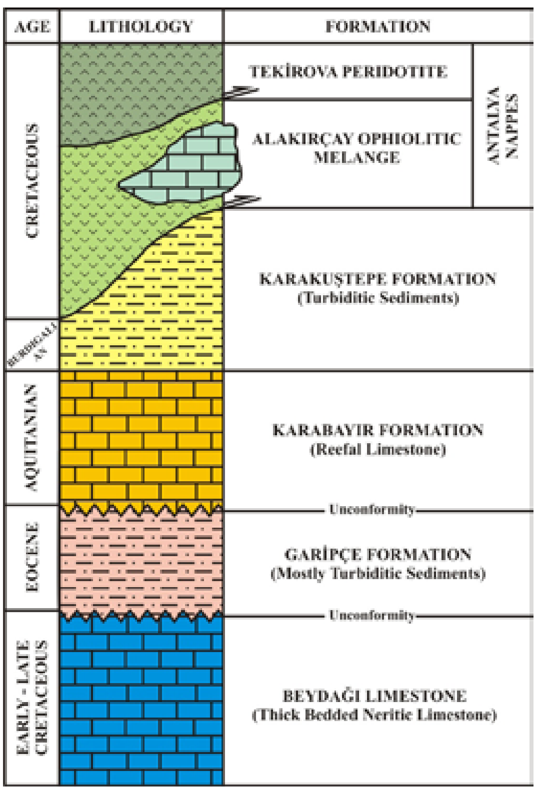

Fig. 3. *Generalized stratigraphic columnar section and main rock units of Çıralı and surroundings (after modified from, Poisson et al.,1984; Şenel 1984; Koşun et al., 2009; and Özçelik et al., 2009).*

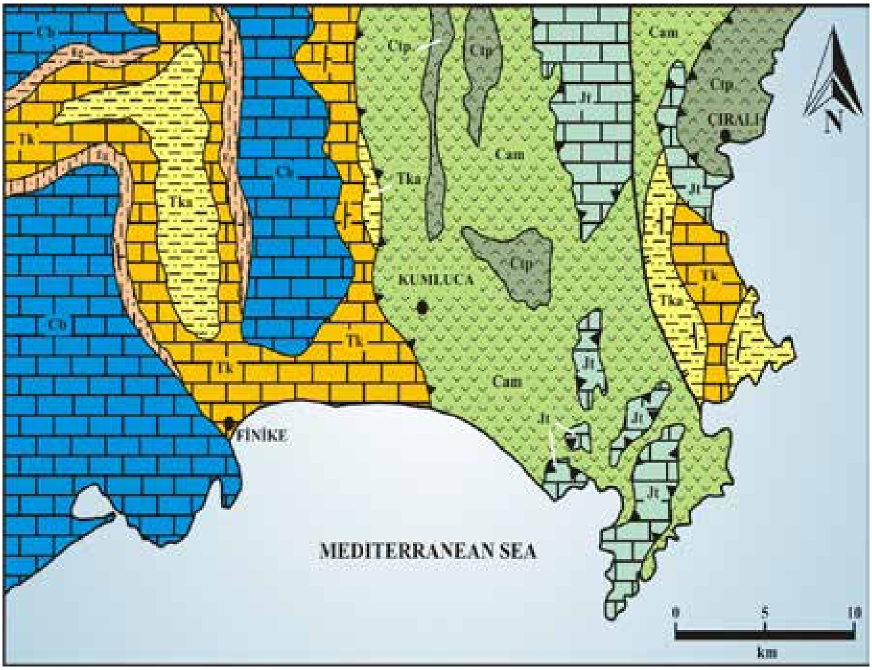

Fig. 4. *Simplified geological map and main rock units of the Çıralı region and surroundings (Modified from geological map of Turkey, 1/500 000 in scale). Cb: Beydağları Formation, Eg: Garipçe Formation (Eocene turbidites), Tk: Karabayır Formation (Aquitanian reefal limestones, Tka: Karakuştepe Formation (Burdigalian turbiditic sediments, Cam: Alakırçay ophiolithic mélange, Ctp: Tekirova peridotite, Jt: Tahtalıdağ nappe.*

3.1.3. Karabayır Formation (Aquitanian reefal limestones)

Karabayır Formation is located in Kaş-Kasaba and surroundings and mainly composed of Aquitanian reefal limestone. Formation name is given by Poisson (1984) and Şenel (1984). Moreover, this reefal limestone bearing bituminous shale also called as "Yazır limestone" by Karaman (1990) and Yağmurlu (1994) is mainly composed of boundstone and packstone components (Fig.5). Abubakar and Yağmurlu (2017) indicate that the Aquitanian reefal limestones, which are distributed to the south of Isparta, show a porous texture and that most of the pores are filled with hydrocarbons (natural gas). In addition, the authors emphasize that the Aquitanian reefal limestones, which unconformably overlie the Mesozoic carbonate rock units in the region, could be correlated to the Karabayır Formation located in the Finike basin.

Fig. 5. *The panaromic overview of thick bedded Aquitanian Karabayır limestone in Finike Tertiary basin.*

3.1.4. Karakuştepe Formation (Burdigalian turbiditic sediments)

Karakuştepe formation is situated in Kaş-Kasaba Basin and is mainly composed of turbiditic sediments mostly occurred by sandstone, shale and calcareous shale (Fig. 6). This formation name is given by Poisson (1984) and Şenel (1984). Shale-flysch facies included shale, calcareous shale, mudstone, fine grained sandstone are characteristic lithofacies of this formation and shale which is main component of the facies dominantly composes of dark greyish black coloured, carbonized plant remains. The depositional environment of the Karakuştepe Formation indicates deep marine conditions, as suggested by bioturbation traces (*Helminthoides* sp.) represented in Nereithes ichnofacies. In addition, sedimentary structures (flute, groove and tool marks) are clearly observed particularly under side of sandstone layers (Fig. 6C and D). These sole marks are generally associated with turbidity currents and quite useful for paleocurrent direction. The thickness is up to 200m and the age of deposition the most probably Burdigalian because of the stratigraphic position.

Fig. 6. *(A) and (B) The field view of Burdigalian aged Karakuştepe Formation composed of sandstone-shale couplets; (C) The closer view of medium-thick bedded sandstone and thin-bedded shale alternations with scour marks; (D) Groove and flute sole marks observing under turbiditic sandstone bed.*

3.2. Allochthonous Rock Units

3.2.1. Lycian Nappes

Lycian Nappes are an allochthonous rock assemblage of ophiolite complex overlying the Menderes metamorphic massif at north and Beydağları carbonate platform at south. In the previous years, most of the researchers focused on SW-Anatolia stated that the Lycian nappes, which form the northern branch of the Tethys ocean, were emplaced in the Middle-Late Miocene period and preserved their present position. (Poisson, 1977; Poisson et al., 2003).

3.2.2. Antalya Nappes

The ophiolitic rock assemblages forming the Antalya Nappes are mostly spread in the southern part of the Isparta Angle. According to previous researchers, the Antalya nappes overlies on the Akseki-Anamas and Beydağları platforms with thrust faults emplaced between the Late Cretaceous and Early Paleocene (Poisson, 1977; Gutnic et al., 1979; Robertson, 2000; Robertson et al., 2003; Poisson et. al., 2003). These researchers concurred that rock units belonging to Antalya nappes have represented to the southern branch of the Tethys Ocean even if strongly debated.

4. TECTONIC STRUCTURES

The tectonic structures of Çıralı and Kumluca mainly are represented by trust fault, normal fault and folding systems. Major faults of this region are Kumluca, Adrasan, Tahtalıdağ and Çıralı faults, respectively (Fig.7). Kumluca trust is a significant fault shows NNW trending which is located between autochthonous units of the Beydağları and Alakırçay mélange belongs to Antalya nappes. Adrasan fault is a normal fault occurred between Alakırçay mélange and Tertiary sediments which spreading in this region. The main N-S trending fault, starting from bay of Adrasan to the north constitutes the boundary between Tahtalıdağ carbonate unit and Tekirova peridodites. Karstic springs and some breccias are observed in particularly Tertiary sediments and ophiolitic rocks along the Adrasan fault. Çıralı trust has been described as Tekirova peridodite by Yılmaz (1984) developed between serpentinized allochthonous ultramafic rocks and Alakırçay mélange. The natural gas marks called Chimeira have been exposed on the north of this trust (Fig. 8)

Fig.7. *The position of the Tekirova peridodite nappe and Çıralı natural gas seeps on the Google-Earth satellite image. Ctp: Tekirova peridodite nappe, Jt: Tahtalıdağ limestone nappe, Tk: Aquitanian reefal limestone (Karabayır Formation).*

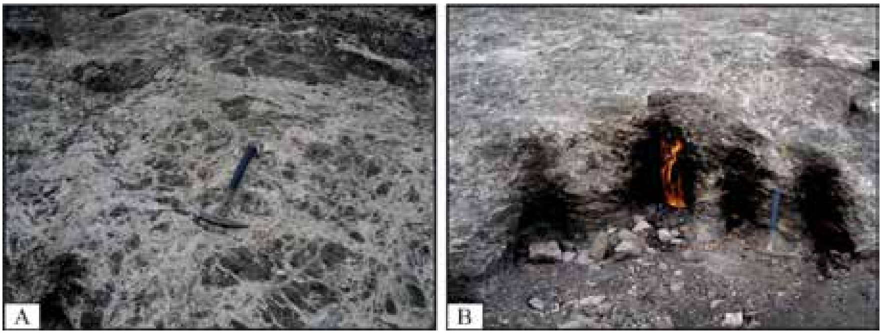

Fig. 8. *(A) The view of breccia serpentinites and (B)* **"***Chimera" natural gas seeps and located in Yanartaş settlement (see location in Fig.7).*

5. PETROLEUM CONTENTS

It can be focused on three group rock units which are the host rocks that are richest by organic materials in **Çıralı**, Finike and Kaş regions. These are from bottom to top, respectively 1) Eocene turbiditic sediments (Garipçe Fm), 2) Aquitanian reefal limestone (Karabayır Fm) and 3) Early Miocene (Burdigalian) turbiditic deposits (Karakuş Fm) (Fig. 9). Moreover, Aquitanian reefal limestone which is up to 500meter thick has both host and reservoir rocks features according to its rich fauna contents, porosity and included heavy bituminous smell. The bituminous shale which is rich organic materials has been exposed a pressure by limestones.

Eocene turbiditic sediments (Garipçe Fm) mainly represent as distal part of turbidites consisted of bituminous shale in the investigated area. The Aquitanian reefal limestones located in Finike Basin have 3.47% total organic matter (TOC) while another turbiditic deposits (Karakuştepe Fm) have 0.2-0.51% organic matter (TOC) in Kaş-Kasaba Basin (**Özçelik** et al., 2009). According to these values, Early Miocene units are more suitable for hydrocarbon reservoir depending on properties of source rocks.

Fig. 9. *The view of organic rich shales exposed in the Burdigalian turbiditic sediments (Karakuştepe Fm) within the Finike Tertiary basin.*

6. DISCUSSION

6. 1. The origin of the Natural Gas Seeps

The origins of the natural gas occurrences in the serpentinized peridotites in the Çıralı region have been investigated by many researchers (Hoşgörmez (2006), Etiope et al. (2011) and Hoşgörmez et al. (2008). Hoşgörmez (2006) implies that the main rocks causing the formation of natural gas in the region could be rich in organic matter in the Upper Palaeozoic and Lower Mesozoic sedimentary rocks. Moreover, Hoşgörmez (2006), Etiope et al. (2011) and Hoşgörmez et al. (2008) pointed out that, based on the carbon isotope data, it is abiotic in origin with most of the natural gas indications particularly in Chimera, and that the intercalation of carbonate rocks with serpentinites may result in interactions. (CH4) in the range of 65 - 93% and nitrogen (N) in the range of 5 - 34% of the natural gas exposed in Çıralı region based on gas chromatographic analyses.

All of the natural gas deposits discovered in the Eastern Mediterranean Region in recent years are found in sedimentary deposits that fill Tertiary aged basins. For this reason, the source and reservoir rock characteristics of the Tertiary sediments in the region for the origin of natural gas occurrences in the **Çıralı** region must be taken into account. As a matter of fact, detailed geological studies in the **Çıralı** region revealed that the Tekirova peridotites belonging to the Antalya nappe containing the natural gas exposures and the accompanying Tahtalıdağ limestones were overlain by the Tertiary aged units (Aqitanian reef limestones and Burdigalian turbiditic sediments).

The schematic geologic cross-section showing the geological location and origin of the natural gas accents in the **Çıralı** region is presented in Figure 10. As seen on this cross section, the Tekirova peridotite nappe tectonically overlying the Tertiary sediments in the **Çıralı** region is probably a unit with an allochthonous cover in the investigated area. For this reason, it is more appropriate to predict Tertiary autochthonous sediments which underlying serpentinites for explanation of the origin of natural gas in serpentinized peridotites. On the other hand, TOC analysis results of the Tertiary sediments in the region (**Özçelik** et al., 2009) are quite important because they show that a very large proportion of the natural gas indications in this region could be biotic origin.

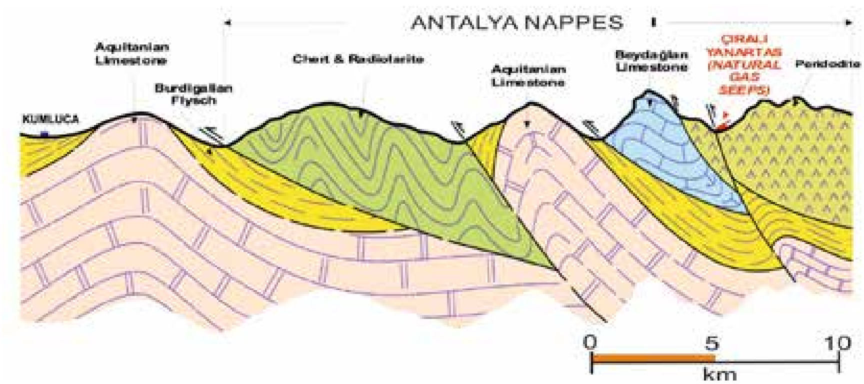

Fig. 10. *Simplified geological cross section passing through* **Çıralı-Kumluca** *line and locations of* **Çıralı** *natural gas seeps on this section.*

6.2. Comparison of Regional Natural Gas Occurrences

Since 2009, new natural gas deposits in the eastern Mediterranean region, especially in the Levant basin and on the Nile River delta region, have been increasingly important for hydrocarbons in this region. After the discovery of new natural gas, many countries in the region have joined the group of countries exporting natural gas. Ratner (2016) concluded that after 2009, after the discovery of new giant natural gas deposits in the Eastern Mediterranean region, the dynamics of the region's energy policies have completely changed. On the other hand, Duo Fu Chen et al., (2005), summarized that the thick marine sediments rich with organic matter on the northern continental slope basins of the South Chine sea and are a large potential source of natural gas like as East Mediterranean region.

As can be seen from the map of the regional geology of the Eastern Mediterranean region given in Figure 1, it is possible to correlate the Kas-Finike basin with the Cyprus-Levantine basin. In recent years, in the offshore drilling in the Cyprus- Levantine basin, very large natural gas deposits have been discovered in Miocene sedimentary deposits. Considering the geological position and origin of the natural gas seeps in the Çıralı region, it is revealed that the areas under the sea in the Kaş-Finike basin and in the south of this basin should be examined in detail in terms of natural gas potential.

7. CONCLUSION

The natural gas seeps located in **Çıralı** region is one of the most important hydrocarbon reservoirs in the southern region of Turkey. The natural gas marks in the serpentinized peridotites belonging to Tekirova nappes are mainly methane compounds. Many of the previous researchers

(Hoşgörmez (2006), Etiope et al. (2011) and Hoşgörmez et al. (2008) have suggested that most of the natural gas occurrences in this region are of abiotic origin and they are the resultant interactions of serpentinites and surrounding carbonate rocks. However, in the various regions of SW-Anatolia, there are many serpentinitized peridotite nappes in the Antalya and Lycia nappes, which could be in contact with the limestones. Moreover, none of these nappe systems have been found natural gas evidences. For this reason, it would be more sensible to look for a source of biotic origin, instead of abiotic origin, for the natural gas indications in the **Çıralı** region. On the other hand, when the geological structure of the **Çıralı** region is studied in detail, Tekirova peridodite nappe, which contains natural gas in this region, is observed to be tectonically over Tertiary units which can be considered as rich organic matter at the bottom. For this reason, it would be more appropriate to take into account the Tertiary (Eocene-Early Miocene) organic rich matter which underlying serpentinized peridodite as a source of natural gas indications in the **Çıralı** region, possibly of biotic origin.

In addition, a significant part of the Tertiary sediments deposited in marine facies in SW-Anatolia were overlain by nappe system of Lycian and Antalya. The autochthonous Tertiary sediments, underlying this allochthonous cover, can be observed as a tectonic window in some part. Therefore, it would be useful to investigate in detail the Early Miocene turbiditic and carbonate units (Burdigalian turbiditic sediments and Aquitanian reefal limestones), which are below the allochthonous cover of the region, in terms of natural gas potential.

Considering the locations of the geological units forming the island of Cyprus, it turns out that the Levantine basin located to the south of the Troodos ophiolites and the Finike basin located to the west of the Antalya ophiolitic nappes may be Tertiary basins linked to each other.

As a conclusion, the NNW-extended multi-level overlapped contacts which separating the autochthonous units in the Beydağları region and the Antalya Nappes and the related tectonic constructions continue through to the sea in the southern part of **Çıralı** and it must be expected that accompanying gas signs could be found at the bottom of the sea.

Acknowledgements

This present study has been financially supported by a part of the Project Research Foundation of the Süleyman Demirel University (Project No: 4247-YL1-15). The authors also thank to reviewers for their insight and detailed comments which improved the manuscript considerably.

REFERENCES

Abubakar, İ. İ. and Yağmurlu, F. (2017), 'Investigation of Hydrocarbon Possibilities of the Tertiary Rock Units in South of Isparta (SW-Turkey)', *Süleyman Demirel University Journal of Natural and Applied Sciences,* Vol. 21/1, pp.38-50.

Altunsoy, M. (1999). 'Organic Geochemical Characteristics of the Miocene Yazır Limestones in the Southern Isparta', *Geology Bulletin of Turkey*, Vol. 42, No.2, pp.51-62.

Akay, E., Uysal, Ş., Poisson, A., Cravatte, J. and Müller, C. (1985), 'Stratigraphy of the Antalya Neogene Basin', Bulletin *of the Geological Society of Turkey*, Vol. 28, pp.105-119.

Aksu, A. E., Hall, J. and Yaltırak, C. (2009), 'Miocene-Recent evolution of Anaximander Mountains and Finike Basin at the junction of Hellenic and Cyprus Arcs, eastern Mediterranean', *Marine Geology*, Vol. 258, pp. 24-47.

Aksu, A.E., Calon, T.J. and Hall, J. (2005), 'The Cilicia-Adana basin complex, Eastern Mediterranean: Neogene evolution of an active fore-arc basin in an obliquely convergent margin', *Marine Geology*, Vol. 221, pp. 121-159.

Atabey, E., Atabey, N., Hakyemez, A., Islamoğlu, Y., Sözeri, Ş., Özçelik, N., Saraç, G., Ünay, E., and Babayiğit, S. (2000), 'Mut – Karaman arası Miyosen Havzasının litostratigrafisi ve sedimantolojisi (Orta Toroslar)', MTA, Vol.122, pp. 53-72.

Boulton, S.J. and Robertson, A.H.F. (2007), 'The Miocene of the Hatay area, S Turkey: Transition from the Arabian passive margin to an under filled foreland basin related to closure of the Southern Neotethys Ocean', *Sedimentary Geology*, Vol. 198, pp. 93-124.

Eatons, S. and Robertson, A. (1993), 'The miocene Pakhna Formation,southern Cyprus and its relationship to the Neogene tectonic evolution of the Eastern Mediterranean', *Sedimentary Geology*, Vol. 86, pp. 273-296.

Etiope, G., Schoell, M., and Hoşgörmez, H. (2011), 'Abiotic methane flux from the Chimaera seep and Tekirova ophiolites (Turkey): Understanding gas exhalations from low serpantinization and implications for Mars', *Earth and Planetary Science Letters*, Vol.310, pp.96-104.

Flecker, R.,Poisson, A. and Robertson, A.H.F. (2005), 'Facies and palaeogeographic evidence for the Miocene evolution of the Isparta Angle in its regional Eastern Mediterranean context', *Sedimentary Geology,* Vol. 173, pp.277-314.

Hall,J., Aksu, A.E. and Calon ,T.J. (2005), 'Varying tectonic control on basin development at an active microplate margin: Latakia Basin, Eastern Mediterranean', *Marine Geology*, Vol. 221, pp.15-60.

Hall, J., Calon, T.J. and Aksu, A.E. (2005), 'Structural evolution of the Latakia Ridge and Cyprus Basin at the front of the Cyprus Arc, Eastem Mediterranean Sea', *Marine Geology*, Vol. 221, pp. 261-297.

Hakyemez , A. and Toker , V. (2010), 'Planktonic foraminiferal biostratigraphy from the sedimentary cover of Troodos Massif, Northern Cyprus: Remarks on Aquitanian-Langhian biozonation', *Stratigraph*y, Vol. 7, pp.33-59.

Hayward, A. (1982), 'Stratigraphy of the Miocene clastic sediments, the Bey Dağları and Susuz Dağ Massifs, Southwestern Turkey', Bulletin of the Geological Society of Turkey, Vol. 25, pp.81 – 09.

Hoşgörmez, H. (2007), 'Origin of the natural gas seep of Çıralı (Chimaera), Turkey: Site of the first Olympic fire', *Journal of Asian Earth Sciences*, Vol. 30, pp.131-141.

Hoşgörmez, H., Etiope, G., and Yalçın, N. (2008), 'New evidence for a mixed inorganic and organic origin the Olympic Chimaera fire (Turkey): a large onshore seepage of abiogenic gas' *Geofluids*, Vol.8, pp.263-273.

Gedik, A., Birgili, Ş., Yılmaz, H. and Yoldaş, R. (1979), 'Geology of the Mut- Ermenek- Silifke (Konya, Mersin) area and petroleum possibilities', *Bulletin of the Geological Society of Turkey,* Vol. 22, pp.7-26.

Görür, N. (1973), 'Sedimentology of the Karaisalı Limestone', *Bulletin of the Geological Society of Turkey*, Vol. 22, pp.227-232.

İslamoğlu, Y. and Taner, G. (2002), 'Kasaba Miyosen havzasında Uçarsu ve Kasaba formasyonlarının mollusk faunası ve stratigrafisi (Batı Toroslar,GB Türkiye)': *The Journal of MTA* ,Vol.125, pp.31-57.

İslamoğlu, Y. (2002), 'Antalya Miyosen havzasının mollusk faunası ile stratigrafisi (Batı- Orta Toroslar, GB Türkiye)' MTA Dergisi Vol. 123-124, pp. 27-58.

İsler, F. I., Aksu, A. E., Hall, J., Calon, T. J. and Yaşar, D. (2005), 'Neogene development of the Antalya Basin, Eastern Mediterranean: An active forearc basin adjacent to an arc junction' *Marine Geology*, Vol. 221, pp.299-330.

Korkmaz, S. and Gedik, A. (1990), 'Study of source rock fades and petroleum occurrence in Mut-Ermenek-Silifke (Konya-Mersin) basin, through organic geochemical methods', *Geological Bulletin of Turkey*, Vol. 33, pp.29-38.

Koşun, E., Poisson, A., Ciner, A., Wernli, R. and Monod,O. (2009), 'Syn-tectonic sedimentary evolution of the Miocene Çatallar Basin, southwestern Turkey', *Journal of Asian Earth Sciences*, Vol. 34 , pp.466-479.

Özdogan, M, (2004), 'An example of cyclic sequences: Miocene stratigraphy of the Mut basin, its correlation with Adana basin and paleogeographic evolution', *Bulletin of Earth Sciences Application and Research Centre of Hacettepe University*, Vol.29, pp.77-95.

Özçelik, O., Altunsoy, M., and Acar, F. (2009), 'Organic geochemical characteristics of the Miocene Lycian Basin, western Taurides, Turkey', *International Geological Review*, Vol.51/1, pp.77-93.

Payne, A.S. and Robertson, A.H.F. (1995), 'Neogene supra-subduction zone extension in the Polis Graben system, West Cyprus', *Journal of the Geological Society*, Vol. 152, pp.613-628.

Poisson, A., Yağmurlu, F., Bozcu, M., and Şentürk, M. (2003), 'New insights on the tectonic setting and evolution around the apex of the Isparta Angle (SW-Turkey)', *Geological Journal*, Vol.38, pp. 257-282.

Robertson, A.H.F. (1998), 'Tectonic evolution of Cyprus in its eastern most Mediterranean setting',Third International Conference On The Geology Of the Eastern Mediterranean, Proceedings, pp.11-44.

Robertson, A.H.F., Eatons, S. and Follows, E.J. (1995), Depositional processes and basin analysis of Messinian evaporates in Cyprus', *Terra Nova*, Vol. 7, pp.233-253.

Robertson, A., Unlugenc, O.C. and Inan, N. (2004), 'The Misis-Andirin complex: a Mid-Tertiary melange related to late-stage subduction of the southern Neotethys in S Turkey', *Journal of Asian Earth Sciences*, Vol. 22, pp. 413-453.

Veen, J.H., Woodside, J.M. and Zitter, T.A.C. (2004), 'Neotectonic evolution of the Anaximander Mountains at the junction of the Hellenic and Cyprus arc', *Tectonophysics*, Vol. 391, pp.35-65.

Yağmurlu, F., Poisson, Bozcu, A. and Şentürk, M. (2007), 'Isparta Açısının tektonostratigrafik özellikleri ve petrol jeolojisi açısından irdelenmesi: The Bulletin of TPJD , 19, 23-34.

A SPATIAL AND DESCRIPTIVE EVALUATION OF LOGISTICS CENTRES IN TURKEY: KONYA SAMPLE

CHAPTER

4

Hesham ALRAGHEBA[1]
H. Canan GUNGORB[2]

[1] Necmettin Erbakan University, Faculty of Engineering, Department of Civil Engineering Konya, Turkey
[2] Necmettin Erbakan University, Seydisehir Vocational School, Department of Civil Defense and Firefighting, Konya, Turkey

INTRO

Logistics is a planning system works for the flow of goods, energy, information and other resources such as: products and services and even though the people, from the production area to market. It's totally hard or impossible to accomplish any global trade or the movement of export and import process . Or the transportation of raw materials or products and manufacturers without the support of the professional logistics. (Bay, Erol, 2016).

Logistics sector is advancing rapidly all over the world in general. In order to achieve this progress; (increase in global trade, decrease in population growth rate, rapid delivery gaining importance in all areas, spreading environmental sensitivity to all sectors, changes in organizational methods, new legal arrangements in communication, transportation and public sectors, increase in outsourcing and application of new communication technologies) has been effective in this field.

One of the things that needs to be done in order to stand out from the competition between countries is to target maximum success in all areas where business is done. As in all sectors, success in the logistics sector is achieved through the correct planning and efficient use of logistics infrastructures.

This study focused on the concept and development of logistics centers, on the basic functions of logistics centers and logistics centers focused on the main factors affecting the establishment of logistics centers in Turkey. Then, the geographical location, administrative, socio-economic status of konya, some basic indicators of konya, agriculture and industry, export-import figures made by konya, transportation infrastructure of konya were presented. In the last section, the study is concluded with a general evaluation and recommendations.

MATERIALS AND METHODS

The concept of logistics village:

The expression of logistic villages has been made to describe founded with the purpose of achieving all the activities related to logistics in a dynamic and productive technique. Although there are some common features in different definitions of logistic villages, there is no single standard definition in this field.

European Logistics Community Platform which is also called Europlatform made the first definition at the logistic village. logistic villages are the fields which are active on which specialist projects operate in different levels on domestic and international scale with regard to transport, logistics and physical distribution. (Europlatforms, 2004).

The latest comprehensive definition of logistic villages is made by (Bay, Erol, 2016) which is the area created with special purposes in certain regions where the moving units are installed and these areas can be operated by independent entities or the government, and can operate in the field of transport and services.

The importance of logistics villages:

Logistics villages located near the city which is the most important feature. Because intermodal freight transport, warehousing, maintenance and a lot of other services are performed together as the nearest places to the consumption centers. (Aydın and Öğüt, 2008).There are many advantages of logistic villages to the both of community and business. These can be listed as follows.

(Özgen, 2011):

- Improve effective and environmentally friend useful distribution patterns for consumption centers.
- improve the economic competition and investment opportunities.
- Reduces traffic congestion and improves the traffic flow.
- Reducing the load leads to improve alternative transportation methods and Improve combined transport.
- Improve regional employment.
- Bring aesthetic arrangements in the fields.
- Improve containers in fields of loading and unloading activities.
- Faster respond to the consumer requests because of logistic bases.
- Less production costs.
- They serve as a center for regional development.
- Expand networks of sea, land, air and railway.
- Improve distribution channels and supply chains to be more flexibil.
- Expand the companies’ growth capability.

The properties and factores of logistics villages:

In order to provide effective and efficient logistics services, there are some fundamental features logistics villages need to have. The features of logistic villages can be listed as follows:

(Akandere, 2013):

- Existence of intermodal station.
- Technical services in logistics villages.
- Physical quality in logistics villages.
- Management features in logistics villages.
- Basic characteristics of logistics villages.

The elements that enable the establishment of efficient and productive logistic villages include multi-modal transport facilities, and the use of effective infrastructure and logistic services.

These elements are listed below:

(Akandere, 2013).

- Intermodal Transportation Facilities
- Efficient Use of Sub-Structure and Regional Planning
- Logistic Service Quality and Diversity

The logistic village structures in Turkey:

Turkey distinguishes by the geographical advantages such as : being surrounded by seas and the combination of the continents. Also, in China and the development of the East Asian market, today increases the strategic importance of Turkey as a transit country.

The logistics village started work in 2006, Also 21 logistics village projects have been included in the agenda eight of them (Eskişehir, Balıkesir, İzmit, Uşak, Denizli, İstanbul/Halkalı, Samsun, Türkoğluu/Kahramanmaraş) started working and 6 other logistic villages are expected to be operational (Bilecik, Erzurum, Mardin, Kahramanmaraş, Mersin, İzmir/Kemalpaşa).

Moreover, The process of expropriation is carried out in 7 centers (Konya, İstanbul/Yeşilbayır, Kars, Kayseri, Sivas, Bitlis/Tatvan, Habur)

In addition, The aim of the centres is for Turkey to become a regional logistic base as it's coordinating with many institutions and organizations. With the introduction of planned logistics villages, it planned to provide 40 billion dolar in contribution to the logistics sector, 27 million tons of additional transportation and 9 million square metres of container holdings. Logistics centers spread across Turkey and also provide more jobs for more than 10,000 people.

Finally, the logistic villages were added that Turkey according to the vision of 2023 aims to export 500 billion dolar in order to become the largest logistic force in Asia, Europe and Africa.

The village of Izmir (Kemalpaşa) is the largest logistic village under construction, while the smallest logistic village is Denizli (Kaklık).

See Appendix, the (Thematic map) for logistics villages in Turkey and the covered areas.

(TCDD, 2010, URL4, Tutar, 2009)

Figure 1. *Logistic Villages in Turkey, Source: (URL4)*

Choosing the location of logistics village:

The location of logistics village can be quite critical which it has a big role to achieve goals of village. Therefore the site selection process must be take a number of criteria and elements These include: production areas, climate, residential areas, vacant areas, public transport networks and topography .We can get this information and analyze it by giving each criteria a special weights as its importance.

When we study these criterias and apply them to existing data. we can get the best location to create the logistics village. There are many applications which help us to make the correct decisions such as ArcGIS.

The table 1. down showes the main factors affecting the establishment locations of logistic centers:

Land	Costs
The size Expansion possibilities Infrastructure Physical conditions	Land Facility Cost to users
Proximity (Distance)	**Socio-Economic Factors**
Production centers Consumption centers Airport, port Railway, highways	Environmental effects Impact on urban traffic Impact on economic life Impact on disaster logistics

Table 1. *Main Factors Affecting the Establishment Locations of Logistic Centers Source: (Filik, 2011)*

Konya economy and logistics center potential

Konya's general geography and earth shapes:

The city of Konya is located in the southern part of the Central Anatolia Region, which is in the middle of the Anatolian Peninsula, in the part of the city called Konya. Its surface area is 41,001 km2. This area is the province with the largest area of Turkey. The average elevation is 1,016 m. It is surrounded by Ankara from the north, Isparta from the west, Afyonkarahisar, Eskişehir, south, İçel, Karaman, Antalya, east, Niğde and Aksaray provinces.

In Konya province, the plain with the most area is the plain and plateaus. Closed basins were formed in the pits at the bottom of the plains. The elevations are small and generally collected in the south of the province. The plains are separated from each other by plateaus. The plateaus are not deeply fragmented by the rivers. There are also open basin sections.

In Konya, winters are hard, cold and snowy, summers are hot and dry. The average annual temperature is 11.5° C. The highest temperature is 40° C and the lowest temperature is -28.2° C. On average 10 days of the year the temperature is less than -10° C. The number of days seen frost event is 100. Frost can be seen from 14 September to 15 May. The average relative humidity is 60'. Konya is foggy for about 23 days. (URL5)

KONYA	Jan	Feb	Mar	Apr	May	Jun	Jul	Aug	Sep	Oct	Nov	Dec
Maximum Temp.	17.6	23.8	28.9	31.5	34.4	37.2	40.6	39.0	36.1	31.6	25.4	21.8
Minimum Temp.	-28.2	-26.5	-16.4	-8.6	-1.2	1.8	6.0	5.3	-3.0	-8.4	-20.0	-26.0
Average Temp. (1981-2018)	-0.2	0.8	5.5	11.0	15.7	20.4	23.6	23.4	18.9	12.7	5.8	1.6
Average Max. Temp. (1981-2018)	4.8	6.5	12.0	17.6	22.4	27.1	30.4	30.4	26.5	20.0	12.3	6.3
Average Min. Temp. (1981-2018)	-4.2	-3.8	-0.3	4.5	8.7	13.1	16.5	16.3	11.6	6.4	0.7	-2.4

Table 2. Extreme Maximum, Minimum and Average Temperatures Measured in Long Period (°C)

Source: Ministry of Agriculture And Forestry: (URL7)

Economic activities of Konya

The economy of Konya is based on agriculture and especially wheat agriculture. Turkey's wheat warehouse counted. 40% of its annual income is obtained from agriculture. There are 600 thousand hectares of forest and 200 thousand hectares of shrubland. 140,000 m3 of industrial wood and 104,000 sterling firewood are obtained annually. (URL3)

Konya is also considered rich in materials. for example bauxite, salt, mercury, magnesite, lignite and barite are also important minerals.

Konya becomes a city of industry with expanding workplaces. Industry is developing based on agriculture. Industrialization accelerated after 1960. However, until 1960, in Konya, apart from flour mills in 1937, the Sümerbank Cotton Industry and Sugar Factory was established in 1954. After 1960, manufacturing industry rapidly increased. Konya is a province that has become an industrial center in the future. (URL5)

Criteria	Year	Konya	Turkey
Total population (Person)	2018	2,205,609	82,003,882
County Number	2018	31	919
Number of Municipalities	2018	32	1397
Population density (person / km2)	2018	57	107
Annual population growth rate (per thousand)	2018	11.6	14.7
Unemployment rate (percent)	2018	4.7	8.8
Employment rate (percent)	2018	46.2	46.2

Table 3. *KONYA Province Basic Indicators*

Source: Turkish Statistical Institute (URL6)

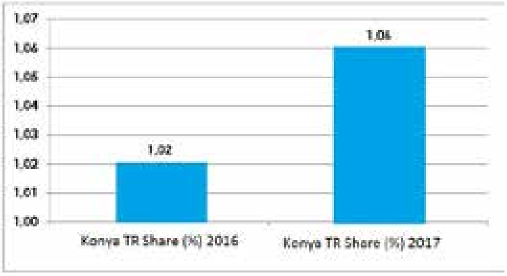

Figure 2. Exports of Konya

As a result of the development of the economy in Konya, Konya's contribution to foreign trade in Turkey is reflected.

Figure 2. Exports of Konya, Turkey Share of Exports (%) Source: Turkish Statistical Institute: (URL6)

The transportation in Konya:

Konya is rich in land, air and rail transportation. It is connected to all corners and districts of Anatolia by highways extending in 7 directions, especially in terms of highway. Konya has the longest road network in Turkey. The state roads are 1652 km, the provincial roads are 1500 km and total 3152 km. 970 villages and suburbs were built. 152 of them are on provincial and state roads. A dirt road was built covering 652 villages and straightening to 191 villages.

Figure 3.: *Konya Province Highway Infrastructure*

Source: Ministry of Transport (URL2)

The railway passes through Konya and the district center. There's a rail line from Istanbul to Konya across to Adana. there are train lines between Konya and Kerman.The journeys by a high speed rail available for (Konya - Istanbul, Konya - Ankara and Konya - Eskişehir) . It also provides a line linked with Konya to Afyoun , and another line connected between Konya and Tasucu and the last one between Konya to Mersin.

Figure 4.: *Konya Province Railway Infrastructure*
Source: Ministry of Transport and Infrastructure: (URL2)

Geographic Information Systems and make decisions:

Geographic Information Systems (GIS); is a computer system used for collecting, storing, processing, managing, spatially querying and analyzing the data associated with the location on the world surface in order to better analyze, understand and see the relationships, textures, spatial distributions and densities. There are many applications in engineering, planning, logistics/transfer, telecommunications and disaster. (Esri Turkey, 2018, URL8)

GIS has increased its use in the fields of science, institutions, business and industry, sustainable development, natural resources, regional and community planning, transport and logistics, with continuous improvements in hardware and software components and lower costs. In spatial decision problems, processing of data with traditional methods is difficult and time consuming. (Kurt, M., & Erener, A. 2018).

GIS is one of the indispensable elements of spatial decision support systems due to the variety of functions and data structure in spatial analysis. Multi-Criteria Decision Making Analysis can be performed through

GIS to improve the decision-maker's performance in spatial decision problems that are not well defined (Kurt, M., & Erener, A. 2018).

In the decision-making process, the creation of multiple alternatives to solve problems arising from spatial data, evaluation of different criteria and independent criteria in the same environment, the possibility of sorting and selecting alternatives is provided by the use of GIS and MCDA method together. (Kurt, M., & Erener, A. 2018).

There are various studies in the literature such as landfill area detection, defense industry applications, flood risk analysis, landslide susceptibility analysis and economic performance assessment by MCDA analysis. (Kurt, M., & Erener, A. 2018).

MCDA techniques and GIS technologies have started to be used in order to increase efficiency in logistics activities and transportation sectors. One of these studies, Birkin (1996), discusses how geographical modeling and spatial information are used to improve planning in their studies with examples from real situations.

Forster (2000) summarized the use of GIS in the planning of logistics services and conducted studies on the role of logistics service providers in decision-making and involvement in high-level decision-making.

Around the world, Geographic Information System solutions are helping analyze, transportation organizations better manage and leverage their spatial data. These organizations are improving expanding their business, enhancing customer service and network planning by making more strategic decisions. Implementing GIS as our logistics solution will benefit us in the same way. (Esri Turkey, 2018, URL8)

GIS technology allows a more rational, analyzing customer trends, integrated approach planning network expansions, and developing green initiatives.

Creating the best location of logistics facilities relative to your allocation networks and customers is critical. GIS technology gives you the ability to analyze business reports, street and demographic data, and retail store locations to supply first-class service to current clients while developing future customer opportunities. Information can be shared throughout departments, which brings down superfluity in marketing and sales efforts and growths employee capability.

(Esri Turkey, 2018, URL8)

GIS Intgrates Information Throughout All Departments:

Market Analysis	Network Planning	Sales and Service	Customer Care
• Sales Forecasting • Business Intelligence • Revenue Analysis	• Capital Efficiency • Capacity Analysis • Demand Forecasting	• New Client Acquisition • Work Force anagement • Routing Optimization	• Delivery Reports • Green Solutions • On-Time elivery

The logistics village in Konya (Kayacik):

TCDD has taken into consideration two important criteria in determining the logistic villages. The first of these is the connection of the logistic village to the organized industrial zones, and the second is that the load carrying potential is intense.

These criteria were also effective in determining Kayacık (Konya) as a logistic village. Apart from these criteria of TCDD, some other criteria also played a role in establishing a logistics village in Konya. These criteria are classified as follows in a scientific study. (Elgün, A. G. D. M. N., & Elitaş, C. 2011).

Transportation Connection; land, sea, rail and airway facilities and connections,

Location and Related Business Activities; connections and relations between national and international location and business consumption centers, Land Properties; the location of the land and its suitability for logistics activities and developments, Location Suitability; suitability of the site in terms of infrastructure, technical facilities and environment, social structure and security.

Figure 5.: *Google.Maps, 2018.*

The (Konya-Mersin) railway project is working to eliminate the disadvantage of konya's lack of sea which increases its logistics value also konya's transports characterized by connecting it to east-west cities, major cities and other logistics villages.

Konya has a rare advantage in Turkey which is the topographic extends over large areas with near-zero slopes and the land permits that help investors to construction and production.

In addition to the criteria for mission in Konya which is the existence of the industrial zone, which contains dedicated sites for the production of the various industrial synthetic materials and the prosperous (coal, cement, marble, sugar, fertilizer,..) consumption of these products is domestically consumed and exported by large amounts of them.

Also,The figure 5. shows the location of the village that is near of the industrial zone, the airport and the intersection of roads which is leading to neighboring cities on an area of million square meters.

Then, All of the construction tenders have been completed and the village is still under construction.

The services to be provided upon the commissioning of Konya Logistics Village can be summarized as follows:

Switch between transport modes.

Intermodal transfers and operations will be provided.

Loading, unloading, handling and weighing services will be provided.

Storage and warehousing services will be provided.

Customs services will be provided.

Parking services will be provided.

Konya logistics village (KAYACIK)

Figure 6.: *Youtube. Konyamız Channel, 2018. (URL1)*

RESULTS AND DISCUSSION

The study concluded that the choice of the logistics village site in Konya was successful as it largely achieved many important criteria, including the connection to the transportation network and the appropriate far distance from populated areas and easy access to the areas of consumption, production and topography..etc.

However, the cold climate will be an obstacle during the winter days for the continuity of the village's work . Then, as well as its far distance from the sea formed as a noticeable defect that can be overcome according to the plan of the construction of the Railway (Konya-Mersin).

Finally, the operating of the logistical villages and the establishment of the logistics villages are also important. then, it'll contribute to the proper management of logistics services in the national economy and the logistics services sector.

The high potential for the return of the logistics and logistics sector in Turkey and expansion of the logistical villages will be beneficial for both the logistics and economy sectors.

In recent years, Konya has became one of the most important industrial centres in Turkey. The movement of exports to 189 countries have become in many different sectors.

Moreover, The number of factories was 105 in two years, and the number of companies in the industrial area in conjunction was 600. So, with other investments in the city, Konya will get a new production step. In addition, now we've subsidiary structure of industry preferred by international investors. Then we expect the volume of international investment in the city, which contains more than 300 euro million of international investment in the last three years, to 700 million euro.

APPENDIX

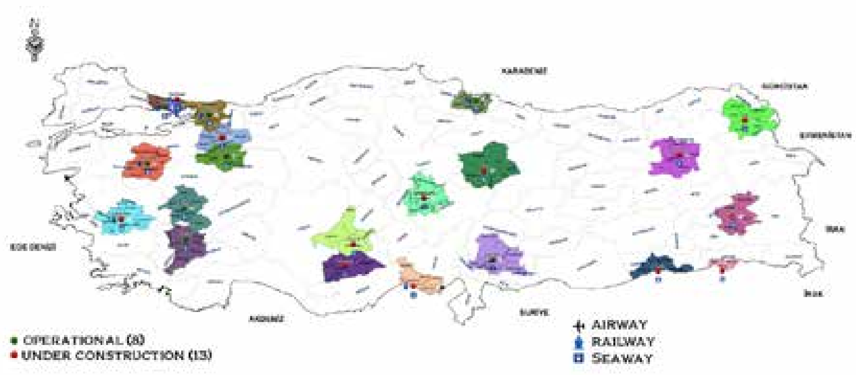

App 1. *Logistic Villages in Turkey By GIS* (Self-source).

REFERENCES

Akandere, G. (2013). Lojistik Köylerin Etkin Yönetimi: Konya İline Yönelik Bir Model Önerisi (Doctoral Dissertation, Selçuk Üniversitesi Sosyal Bilimler Enstitüsü).

Akandere, G. 2013. Effective Management Of Logistics Villages: A Model Proposal For Konya. Selcuk University, Institute Of Social Sciences, Department Of Business Administration, Department Of Management And Organization, Master Thesis, Konya, Turkey.

Aydin, G., Öğüt, K.S. (2008) "What Is Logistics Village", 2nd International Railway Symposium, Tcdd, Istanbul, 15-17.10, Volume: 2.

Bay, M., 2016. Importance Of Logistic Villages And Supporting Intermodal Transportation Activities: An Application In Karaman Province., Karamanoğlu Mehmetbey Uni. Faculty Of Economics And Administrative Sciences., Karaman., Turkey.

ELGÜN, A. G. D. M. N., & ELİTAŞ, C. (2011). Yerel, Ulusal Ve Uluslararası Taşıma Ve Ticaret Açısından Lojistik Köy Merkezlerinin Seçiminde Bir Model Önerisi. Celal Bayar Üniversitesi Sosyal Bilimler Dergisi, 9(2), 630-645.

Europlatforms (2004) "Intermodal Transport Between Europe And Asia: Opportunities &Hallenges",http://Www.Internationaltransportforum.Org/Intorg/Ecmt/Intermodal/Pdf/K Ievgalloni.Pdf, 01/05/2014.

Filik, F. (2011). Lojistik Merkezlerin Rolü ve Önemi. Tanyaş, M. ve Hazır K.(Ed.), Lojistik Temel Kavramlar (Lojistiğe Giriş), 1. Baskı içinde (199-250), Tarsus, Mersin: Arzu Ofset Matbaacılık.

Kurt, M., & Erener, A. Lojistik Merkezlerin Planlanmasında Coğrafi Bilgi Teknolojileri Kullanımı-Kocaeli Örneği. Journal Of Transportation And Logistics, 3(1), 1-12.

Malczewski, J. (1999). GIS and multicriteria decision analysis. John Wiley & Sons.

Özgen, H. (2011). Samsun Modern Lojistik Köyünün 21. YY Ekonomisine Entegrasyonu: Gelişen ve Değişen Şartlara Uyumu: Stratejik Yaklaşımlar. Samsun Sempozyumu.

Tutar, E., Tutar, F., & Yetişen, H. (2009). Türkiye'de Lojistik Sektörünün Gelişmişlik Düzeyinin Seçilmiş Ab Ülkeleri (Romanya Ve Macaristan) İle Karşılaştırmalı Bir Analizi. Karamanoğlu Mehmetbey Üniversitesi Sosyal Ve Ekonomik Araştırmalar Dergisi, 2009(2), 190-216.

[URL1] Konyamız Channel, 2018, Konya Büyükşehir Belediyesi, Erişim Tarihi 21 Haziran 2018, <https://www.youtube.Com>.

[URL2] Ministry Of Transport And Infrastructure, 2019, Erişim Tarihi 21 Haziran 2019, <https://www.uab.Gov.Tr>.

[URL3] Investment In Konya, 2019, Erişim Tarihi 21 Haziran 2019, <http://www.Konyadayatirim.Gov.Tr>.

[URL4]: Republic Of Turkey Ministry Of Transportation And Infrastructure, 2019, Erişim Tarihi 21 Haziran 2019, <http://www.Tcdd.Gov.Tr>.

[URL5] The World Of Geography, 2019, Erişim Tarihi 21 Haziran 2019, <http://www.Cografya.Gen.Tr>.

[URL6] Turkish Statistical Institute, 2019, Türkiye Cumhuriyeti, Erişim Tarihi 17 Ağustos 2019, <http://www.Tuik.Gov.Tr>.

[URL7] Turkish State Meteorological Service, 2019, Erişim Tarihi 14 Haziran 2019, <https://www.Mgm.Gov.Tr>.

[URL8] Esri Tükriye, 2018, 2019, Erişim Tarihi 10 Haziran 2019, < https://www.esriturkey.com.tr>.

RAPID EXPLORİNG RANDOM TREES (RRT) ALGORITHM

CHAPTER

5

Elaf Jirjees DHULKEFL DHULKEFL[1]
Akif DURDU[2]
Hakan TERZİOĞLU[3]

1 Konya Technical University, e-mail: elif.cercis94@gmail.com
2 Konya Technical University, e-mail: hterzioglu@ktun.edu.tr
3 Konya Technical University, e-mail: adurdu@ktun.edu.tr

INTRODUCTION

Unmanned Aerial Vehicles (UAV) studies have begun to develop with faster acceleration after a gradual 100-year growth, particularly after 1990. It can be said that the development processes pursued by the automotive industry followed 100 years ago, taking into account efforts to begin mass production, efforts to meet the need for model standardization and high accident statistics [1]. Today, military activities consume most of the budgets and investments made for UAVs. Such military activities are mainly in the form of tasks of surveillance, control and intelligence. Furthermore, chemical, biological, nuclear and radiological operations are another area of use in the military field. Land, navy and air forces all benefit from UAV technology in various activities[2]. Battery problem is one of the biggest problems in UAVs. In order to overcome this problem, renewable energy sources are connected to the drones to ensure that their batteries are charged during flight or during standby. In drones, it may be considered to use wind turbines to benefit from the wind generated by drone motor blades from renewable energy sources for charging their batteries, to use solar panels during flight or during standby, and to use thermoelectric generator modules to utilize the heat generated by drone blade motors[3,4]. This makes scientific studies on renewable energy sources gain additional importance[5]. The number of UAV-based studies has significantly increased over the past 20 years compared to previous years[6]. With this rise, UAVs have been used both in military aviation and in civil-commercial applications, making it easy to adapt to everyday life and becoming a current issue for academic studies [7,8]. Discussing the legitimate use of civilian UAV. First of all, the topic of UAV use will be addressed by discussing what UAV device is for this reason. The scope of international and national legal frameworks will then be investigated and finally a new regulatory framework for the use of civilian UAVs will be proposed on a limited scale [9,10]. UAV use is increasingly common. Due to its ease of use of UAVs in long-term, very time-consuming areas (e.g. 40-50 hours) and inefficient human use, it is favored particularly in dangerous and risky applications. For practices such as nuclear activities, which can be deemed dangerous and where human use is at risk, it can also be favored. UAV technology also benefits Internet services (especially Google) and social media applications that we use in all aspects of our lives [11,12].

Today, most of the budgets or investments made for UAVs are covered by military activities. These military activities are mainly in the form of supervision, surveillance and intelligence activities.

- Screening,

- Instant / general goal setting,
- General oversight in peacetime,
- Oversight of enemy activities during the war,
- Instant weather forecast,
- Determining the route in closed weather,
- Finding directions,
- Tracking the enemy,
- Transmission of radio signals,
- Safety of aircraft runways,
- Damage determination studies,
- If necessary, it can be used as a radar / jammer and in many other areas UAVs are used [2].

Studies in literature, Mariusz and Patrick (2006) suggested an autonomous system for planning the path for UAV. It was achieved by reviewing the development process and removing the upper limits and, at the moment, by contacting a PRM (probabilistic road maps) or RRT (rapid exploring random trees) planner to create fresh plans that could be missed [13]. Mert Turanlı et al. This paper deals with the design of a test environment to be used for universal control and trajectory planning of autonomous mobile ground vehicles. The path planning algorithm runs offline and the approach used is an adaptive variant of the RRT algorithm for the robot model, a sampling based incremental search process [41]. Jayesh Amin et al. (2006) The RRT algorithm created paths showed the path through the Dijkstra algorithm, which adds the shortest path between the points on the path without any obstacle. While the RRT method is expected to find an appropriate path from specific impaired areas that are likely to approach exploration as the number of iterations increases, the resulting paths may not be the only criteria included in RRT study. The paths generated by the RRT algorithm therefore showed that they passed the Dijkstra algorithm, which found the shortest unhindered path between the points on the path [15]. Yoshiaki Kuwata et al. The aim of this paper is to provide numerous extensions to the standard RRT algorithm enabling RRT to be used online in robotic vehicles with complex, unstable dynamics and substantial drift, while retaining uncertainty protection and restricted detection. The proposed method tends to yield better results [16]. Kwangjin Yang and Salah Sukkarieh (2008) In this review, an algorithm for 3D path planning for unmanned aerial vehicles (UAVs) operating in mixed natural environments is presented. The Random Trees (RRT) algorithm that has been quickly discovered is used to produce collision-free waypoints. The proposed method works better according to the results [17]. Bo Wang et al. (2018) The next location-based step scenario was predicted by using radar to provide real-time target position feedback, and mixed feedback and scenario forecast data for dynamic path planning. Kalman filtering was used to obtain status positions and planned target locations, and the ant colony's algorithm used to plan routes for different moving targets. This proposed plan indicates that the time needed to reach the target has been shortened and the route is rising [18]. Jung Leng et al. (2006) PSO have a distinctive approach to formulating and solving problems with 3D route planning. They aim to reduce fuel consumption and minimize the risk of threats to the enemy [19]. Aleksandar et al. (2010) Suggested number if path optimization techniques are based on intelligence for unmanned aerial vehicles (UAVs). We showed that the Ant System algorithm could be used to optimize the UAV system in the map coverage situation. By comparing another form, the NNS (nearest neighbor search) implies that the algorithm is more efficient than the nearest neighbor search [20]. Xiao et al. (2005) Suggested a UAV route planning technique in complex genetic algorithm-based environments. The results showed that the suggested algorithm was able to find a non-optimal, unimpeded path in a rapidly changing setting [21]. Mohammad Mozaffari et al. (2016) Flying base stations provide an ideal aerial vehicle deployment environment for unmanned use. Compared to the standard Voronoi cell assembly approach with fixed UAV places, the proposed deployment strategy has been shown to increase the system's energy efficiency by 20 times [22]. Victor vladareanu et al. (2016) The techniques and algorithms described in this article are widely studied and simulated and suggested for the application of UAV motion strategies in non-manned aerospace projects as well as high-level decision algorithms and flight optimization processes as well as in low-level applications. Smart techniques used in this study to refine a UAV task plan using sensory input [23]. Han Tong et al. (2012) A solution approach to ensure cooperative timing between vehicle teams is given in this article. A prevailing control method was established based on the voronoi diagram and DPSO. The results show that the suggested genetic algorithm can be used for complex group assignments with time limitations [24].

PATH PLANNING

Path planning is an important foundation for autonomous mobile robots, enabling robots to look for the shortest – or best – path between two points. Conversely, optimal paths can be paths that eliminate turning, accelerating, or whatever a particular application needs. Algorithms are important to find a shortest path in robotics as well as network routing, UAV, video games and gene sequencing. Figure 1 shows path planning example.

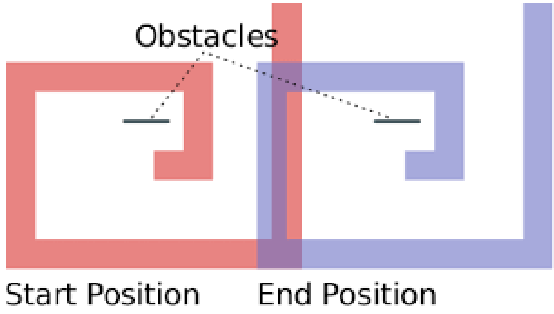

Figure 1. *path planning example*

A RAPIDLY-EXPLORING RANDOM TREE (RRT)

The RRT algorithm has become popular in recent years as mobile robots offer probabilistic solutions in the path planning process where classical and heuristic methods require more processing load and media information is not available. Especially in cases where the movement area is wide, other methods are forced, and this method enables to reach the target with the most suitable route progression point on a tree structure mapping by scanning the whole area quickly. This method was first developed in 1998 by S. LaValle and J. Kuffner.

In this method, the aim is to make branches by selecting random points from the first moment and to create the most suitable route to the destination according to these branches. For this purpose, it selects random points in many fields, but it selects the new point to be selected outside of the selected ones and converges to the target, providing ease of operation. In addition to the classical one-way implementation, the RRT method presents two-way, multi-tree structure, differential constraints.

It is an algorithm designed to efficiently search for non-convex, high-dimensional areas by randomly generating a field-filled tree. The tree is built incrementally from randomly drawn samples from the search area and is naturally biased to grow into large unexplored areas of the problem. They easily handle problems with barriers and differential constraints (non-holonomic and kinodynamic) and are widely used in autonomous robotic motion planning. Figure 1 displays the flow diagram for the RRT Algorithm.

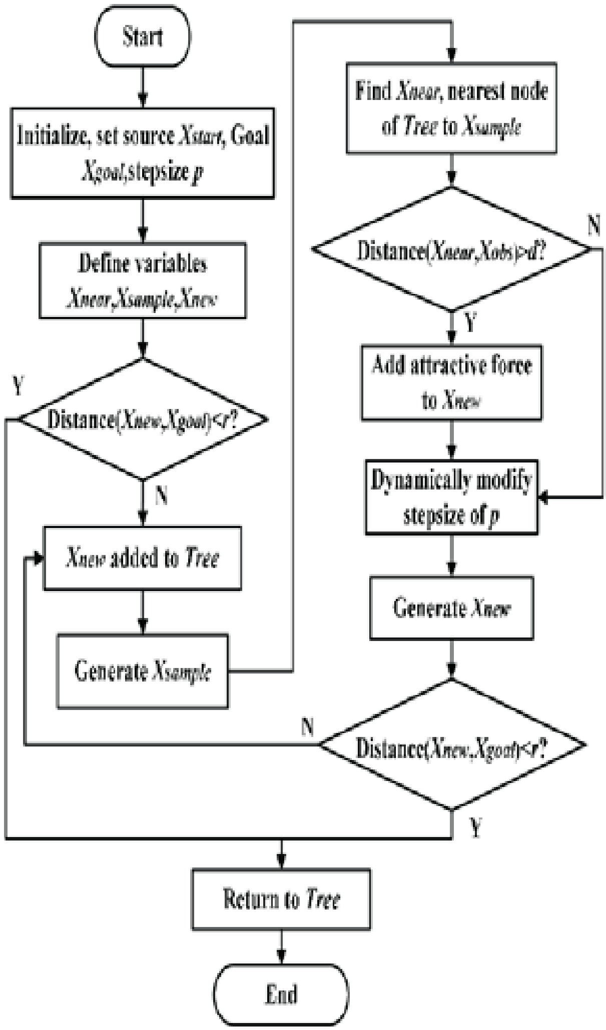

Figure 2. *Flow chart for RRT algorithm*

Rapidly Random Exploring Tree (RRT) is a data structure and algorithm designed to efficiently search for non-concave high dimensional gaps. RRTs are constructed incrementally to quickly reduce the distance from a randomly selected point to the expected tree. RRTs are particularly suitable for road planning problems involving barriers and differential constraints (non-holonomic or kinodynamic). RRTs can be considered a technique for creating open loop trajectories for nonlinear systems with state constraints. The RRT can be intuitively conceived as a Monte-Carlo bias way to search the largest Voronoi regions. Some variations may be considered stochastic fractals. Generally, a stand-alone RRT is insufficient to solve a planning problem. Therefore, it can be considered as a component that can be included in the development of various different planning algorithms.

The RRT expands in several directions to quickly explore the four corners of the frame. While the construction method is simple, finding a method that provides this desired behavior is not an easy task. For example, consider a pure random tree that is incrementally generated by selecting a random vertex, a random entry, and then applying the entry to create a new vertex. Although he intuitively expects a “random area of the tree to be discovered, there is indeed a very strong bias towards the discovered places (simulation experiments provide a very high peak density with very few other discoveries near qinit). A random walk also suffers from biases towards previously visited places. An RRT works in the opposite direction to places not yet visited. This can be seen by considering the Voronoi diagram of the RRT corners. The major Voronoi regions appear at the “border “of the tree. Since corner selection is based on the nearest neighbors, this means that corner areas with large Voronoi regions are more likely to be selected for expansion. On average, the RRT is formed by iteratively breaking the large Voronoi regions into smaller ones.

RRT is one of the only query algorithms in probabilistic roadmaps. It is probably a complete and really simple algorithm. The construction of the general tree begins with two separate graphs. One starts with the target and randomly adds it to the new node, the q-target. The other starts with the initial configuration, finds the nearest q-new node in the graph, and moves to the q-target until a collision check fails at the newly added node. Here is the graphic representation. The purpose of this algorithm is to quickly detect obstacles in dynamic unknown environments and reduce unnecessary maneuver points.

Steps of the RRT algorithm:

- One tree grown using random target

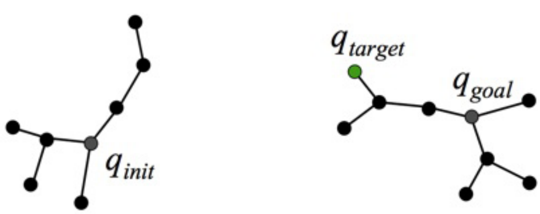

- New node becomes target for other tree

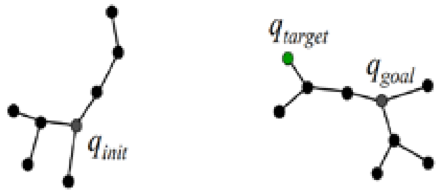

- Calculate node "nearest "to target

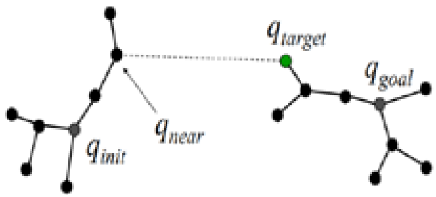

- Try to add new collision-free branch

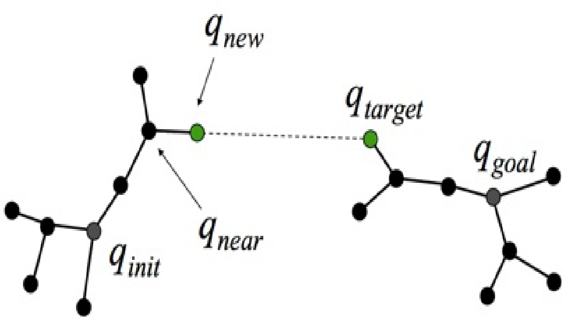

- If successful, keep extending branch

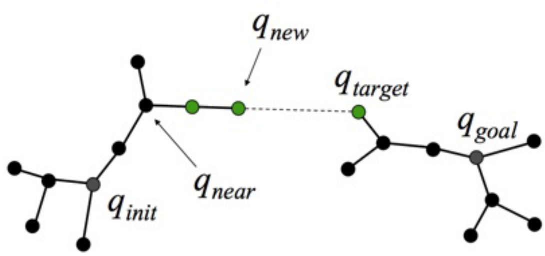

- Path found if branch reaches target

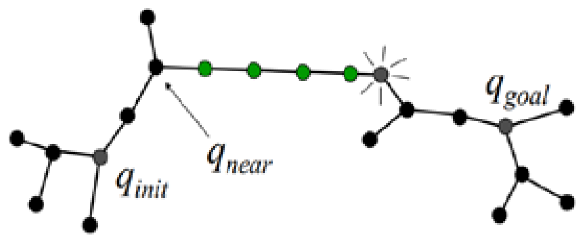

- Return path connecting start and goal

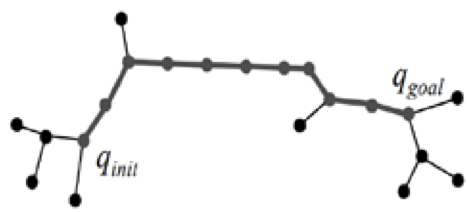

An RRT grows a tree rooted in its initial configuration using random samples from the search field. As each sample is drawn, a connection between the tree and the nearest state is attempted. If the connection is possible (passing through the completely free space and meeting any restrictions), this results in the addition of the new status to the tree. The probability of expanding an existing situation by properly sampling the search area is proportional to the size of the Voronoi region. Since the largest Voronoi regions belong to the states on the border of the search, this means that the tree preferably expands into large, non-searchable areas.

The length of the connection between the tree and a new state is usually limited by a growth factor. If the random sample is more than this limit permits, the new sample at the maximum distance from the tree is used instead of the random sample along the line. Random samples can then be viewed as controlling the direction of tree growth when determining the growth factor ratio. This retains the gap-filling bias of the RRT while limiting the size of incremental growth.

RRT growth can be biased by increasing the likelihood of sampling situations from a particular region. Most practical applications of RRTs use this to guide research towards planning problem objectives. This is achieved by introducing a small sampling probability of targeting into the sampling procedure of the situation. The higher the probability, the more the tree greedily grows towards the target.

RESULT

Advantage of this algorithm RRT, a tree quickly searches the entire area instead of "staying near the starting node, programming the RRT algorithm is very simple; so this leads to a quick analysis to find a way to quality, many extra options can be added to the basic algorithm, the RRT algorithm can be incorporated into many planning systems, single parameter, the balance between greedy search and exploration, approaches sampling distribution at the limit, simple and easy to apply. There are disadvantages to a basic RRT algorithm, the algorithm is not deterministic, the path found is not the same when next time a path must exist on the same starting node, because of this feature, it is possible that some of the roads found are not the paths that a human chooses, if there are too many obstacles in the state area, there is little chance of finding a point that can be connected to a tree that is not in the obstacle, a narrow passage is also difficult to pass, the road found is sharp and cannot be driven easily, metric precision, nearest neighbor efficiency, unknown convergence rate and long queue in the calculation time distribution.

REFERENCE

Hobbs A. (Ph.D.), "Unmanned Aircraft Systems", (2010), San Jose State University Human Systems Integration Division NASA Ames Research Center, Chapter 16.

Gupta S.G., Ghonge M.M., Jawandhiya Dr. P. M., (2013), "Review of Unmanned Aircraft System (UAS)", International Journal of Advanced Research in Computer Engineering & Technology (IJARCET) Volume 2, Issue 4.

Ağaçayak, A.C., Terzioğlu, H., Neşeli, S., Yalçın G., (2018). "Small Power Wind Turbine Design," Acad. Studies in Eng., Gece Publishing, pp. 121-130.

Neşeli, S., Terzioğlu, H., Ağaçayak, A.C., Yalçın, G., (2017). "Electrical Power Generation by Thermoelectric Generator Using Geothermal energy and The Low-Power Dc-Dc Buck_Boost Converter Application", In Grad. Sch. of Natur. and App. Scien., Selçuk University.

Ağaçayak, A.C., Terzioğlu, H., Neşeli, S., Yalçın G., (2018). "Mathematical Modelling of Thermoelectric Generator by Regression Analysis ," International Conference on Engineering Technologies (ICENTE'18). Selçuk University, Vol:3, pp.523-527.

Neşeli, S., Terzioğlu, H., Ağaçayak, A.C., Yalçın, G., (2018). "Düşük Hızlı Hava Araçları için Ön Kanatçık Tasarımı ve Akış Analizi", International Science and Academic Congress'18 (INSAC'18). Selçuk University, Vol:3, pp.709-721

Finn R.L., Wright D., (2012), "Unmanned Aircraft Systems: Surveillance, ethics and privacy in civil applications", Computer Law & Security Review 28,184-194.

Neşeli, S., Terzioğlu, H., Ağaçayak, A.C., Yalçın, G., (2018). "İnsansız Hava Taşıtları için Rüzgar Tüneli Tasarımı ve Hava Akış Analizi", International Science and Academic Congress'18 (INSAC'18). Selçuk University, Vol:3, pp.689-708

Mustafa DİKMEN, (2015), "İnsansız Hava Aracı (İHA) Sistemlerinin Hava Hukuku Bakımından İncelenmesi", The Journal of Defense Sciences, Volume 14, Issue 1, 145-176.

Yalçın, G., Neşeli, S., (2019). "Drone'lara Genel Bir Bakış", Mühendislik Alanında Yeni Ufuklar, Gece Kitaplığı,vol. 29377, pp. 165-191.

Emrah YİĞİT, Işıl YAZAR, T. Hikmet KARAKOÇ, (2018), '' İNSANSIZ HAVA ARAÇLARI (İHA) 'NIN KAPSAMLI SINIFLANDIRMASI VE GELECEK PERSPEKTİFİ", Sürdürülebilir Havacılık Araştırmaları Dergisi, C3-S1, 10-19.

Ağaçayak, A.C., Sungur, C., (2019). "Drone Ağları için Topoloji İncelemesi", Mühendislik Alanında Yeni Ufuklar, Gece Kitaplığı,vol. 29377, pp. 5-32.

Mariusz Wzorek and Patrick Doherty. (2006). Reconfigurable Path Planning for an Autonomous Unmanned Aerial Vehicle. AAAI Conference on American Association for Artificial Intelligence, 438-441.

Mert Turanlı Emre Koyuncu and Gökhan İnalhan. OTONOM MOBİL ROBOTLAR İÇİN ÇOK AMAÇLI BİR DENEME ORTAMININ TASARIMI: ITUKAL ROBOT TEST ORTAMI.

Jayesh Amin, Jovan Boškovic and Raman Mehra, (2006), "A fast and efficient approach to path planning for unmanned vehicles", AIAA Guidance, Navigation, and Control Conference and Exhibit, 6103.

Yoshiaki Kuwata, Gaston A. Fiore, Justin Teo, Emilio Frazzoli, and Jonathan P. How. Motion Planning for Urban Driving using RRT.

Kwangjin Yang and Salah Sukkarieh, (2008), "3D smooth path planning for a UAV in cluttered natural environments", 2008 IEEE/RSJ International Conference on Intelligent Robots and Systems, 794-800.

BO Wang, Jianwei Bao, Li Zhang and Qinghong Sheng. (2018). UAV autonomous path optimization simulation based on radar tracking prediction. EURASIP Journal on Wireless Communications and network.

Jung Leng Foo, Jared S. Knutzon, James H. Oliver and Eliot H. Winer. (2006). Three-Dimensional Path Planning of Unmanned Aerial Vehicles Using Particle Swarm Optimization. Mechanical Engineering Conference Presentations, Papers, and proceedings.

Aleksandar Jevtic, Diego Andina and Aldo Jaimes, Jose Gomez, Mo Jamshidi. Unmanned Aerial Vehicle Route Optimization Using Ant System Algorithm. International Conference on system of system Engineering.

Xiao-Guang GAO, Xiao-Wei Fu and Da-Qing Chen. (2005). A Genetic-Algorithm-Based Approach to UAV Path Planning Problem. Conf. On SIMULATION, MODELING AND OPTIMIZATION, 503-507.

Mohammad Mozaffari, Walid Saad, Mehdi Bennis and Merouane Debbah. (2016). Optimal Transport Theory for Power-Efficient Deployment of Unmanned Aerial Vehicles. IEEE International Conference on Communications (ICC).

Victor VLADAREANU, Elena-Corina BOSCOIANU, Ovidiu-Ilie SANDRU and Mircea BOSCOIANU. (2016). Development of Intellıgent Algorıthms for Uav Plannıng and Control. SCIENTIFIC RESEARCH AND EDUCATION IN THE AIR FORCE-AFASES, 221-226.

Han Tong, Wu Wen chao, Huang Chang qiang and Xuan Yong bo. (2012). Path Planning of UAV Based on Voronoi Diagram and DPSO. IWIEE, International Workshop on Information and Electronics Engineering, 4198-4203.

Elaf Jirjees DHULKEFL and Akif DURDU (2019). Path Planning Algorithms for Unmanned Aerial Vehicles. International Journal of Trend in Scientific Research and Development (ijtsrd), 359-362.

CHAPTER

6

A* AND DIJKSTRA ALGORITHM

Elaf Jirjees DHULKEFL DHULKEFL[1]
Akif DURDU[2]
Hakan TERZİOĞLU[3]

[1] Konya Technical University, e-mail: elif.cercis94@gmail.com
[2] Konya Technical University, e-mail: hterzioglu@ktun.edu.tr
[3] Konya Technical University, e-mail: adurdu@ktun.edu.tr

INTRODUCTION

Unmanned aerial vehicles (UAV), commonly known as drone, The development of unmanned aerial vehicles began in 1916 with Archibald Low. In the simplest terms, UAVs are non-human vehicles that can be steered by remote control or autonomously directing themselves, or both can work together, the useful loads can be loaded into and removed from the main body and can return and land at the end of the mission [1]. In parallel with advancing technological developments, the field of use of UAV systems is increasing day by day. Although it had a long historical development and individual practices, the demand for UAVs was always in the military field until the end of the two thousand years. However, with the rapid development of technology, the use of UAVs not only in the military field but also in the civilian field is increasing day by day. In addition to activities such as border control, anti-smuggling, photographing and meteorological determinations, its use as a hobby is becoming widespread [2-4].

The basic components of UAV are; The main body is called the skeleton, propeller, wing, motor driver, motor, battery, control board. In addition to these basic components, electronic sensors, communication electronics, various sensors and cameras can also be found on the UAV. The term “for UAV Systems” has been used in these unmanned vehicles, which have recently been known as “really in the UAV process”. This is because the expression UAV means only the platform of the plane and does not cover the entire system that passes it. However, it is believed that both states and institutions use different terms for these aircraft.

Today, the use of unmanned aerial vehicles (UAV) is increasing. Especially in rotary wing UAVs, the battery problem is one of the biggest problems. Efforts are underway to improve drone batteries and prolong airborne times. Renewable energy sources are connected to the drones to ensure that their batteries are charged during flight or on the ground. Thermoelectric generator modules can be considered in drones to benefit from the renewable energy sources of wind, solar energy and the heat generated by the drone motors[5,6]. This makes the studies on renewable energy sources gain more importance[7]. Furthermore, in autonomous mobile and flying robots, three-dimensional (3D) path planning is an important issue due to the battery problem. Non-human, remote control or self-management can operate the UAVs independently, or both can work together. The Design and performance of drones for both civil and military purposes has been given great attention in the last years. Use UAVs that can operate independently in vibrant and complicated environmental settings has become increasingly common. UAVs need to be rady for emergencies during the process. Under certain constraints, determining an optimal or time-based path between the appropriate locations is the normal path planning issue.

Nowadays, UAVs are used to fulfill many civilian tasks such as weather forecasts, environmental surveys and traffic control. UAVs are also frequently used in military applications such as border control, surveillance, mine detection, or in civil applications such as environmental protection, forest fire control, cargo handling, filming [8-10]. The reasons for such widespread use are as follows:

- Production and purchasing costs are low.
- There is no risk of loss of life during the mission.
- Able to follow up and report dangerous situations through imaging techniques.
- They are less affected by the weather conditions and the duration of the stay can be increased depending on the battery.
- They can work day and night.
- Sensor networks can fly in a team-based and coordinated flight and scan more areas in a short time.

Studies in literature, Akshay Kumar Guruji et al. (2016) The human function is replaced by robots to achieve good precision, high efficiency, speed and multiplicity. Some robots are used to carry heavy objects at work in industries. The proposed A* algorithm determines the value of the heuristic function immediately before the collision and shows a good decrease in processing time with higher speed [11]. Halil Cicibaş et al. (2015) Defined a multi-criteria model of path planning for unmanned mid-altitude and long-air vehicles. Taking into account the complexity of the environment, the A* algorithm was proposed for optimal paths for unmanned aerial vehicles in terms of range, time and fuel consumption [12]. Weiwei Zhan et. al (2014) This article explores the implementation of a real-time track planning algorithm for Unmanned Aerial Vehicles in a 3D large battlefield environment to solve the problem that UAVs require high survival and low fuel consumption. The algorithm will find the optimal path in the target space between two waypoints, taking into account factors such as altitude, detection probability, and path width. The improved A* algorithm is therefore stable, convergent and efficient [13]. František Duchoň et al. (2014) They explain in this article road planning based on a mobile map grid. We add a variety of modifications and enhancements to the A* algorithm (Basic Theta*, Phi*). The results show that the A* algorithm's calculation time is lower than other algorithms [14]. Dong et al. (2010) Studied the

UAV path planning method based on the FVF. For UAV path planning, the FVF (Fuzzy Virtual Force) method is convenient and quick. When comparing the FVF method with the A* search algorithm, the FVF method is superior to the online UAV path planning in the complex environment [15]. Felipe and Jose (2010) Suggested field-based Dijkstra algorithm for UAV fixed wing trajectory preparation The MDA (Modified Dijkstra Algorithm) approach is used to prove that the EDA (Elevation Based Dijkstra Algorithm) decreases the calculation time significantly [16]. Lyle Parungao et al. (2018) A smart path planning is suggested which uses a shortest path algorithm specifically the Dijkstra's algorithm and can provide wireless communication to improve this proposed idea with the use of wireless ad hoc network. The results obtained show that our intelligent path planning algorithm works in three different approaches as expected and that the principle of this algorithm, which can avoid blocked parts on a path, is successfully implemented and an alternate route is found, which is the shortest [17]. S. Julius Fusic et al. (2018) The development of the mobile robot was created using the V-REP open source simulation software and the Dijkstra algorithm was applied to determine the sub-optimal and collision-free path. The simulated results showed that the reduction approach was effective in terms of time and speed in the developed robot path planning environments [18]. Ter-Feng et al. (2017) Using the algorithm used by modified Dijkstra, an obstacle-avoiding path connecting the starting point, the turning point of the obstacle and the end point was found. The algorithm used by modified Dijkstra has been used to find an obstacle-avoiding path that connects the starting point, the turning point of the obstacle and the end point. The results show that the proposed method is not only feasible in path planning, it is also possible to obtain good results [19]. Julius Sekaran Hariharan Kaluvan (2018) Different environments have been developed and updated parameters have been implemented in the Dijkstra algorithm in a robot to find a suitable path to reach the destination. The simulated results showed that the reduction approach was effective in terms of time and speed in the generated robot path planning environments [20]. Rosli Omar and Dawei (2010) They proposed algorithms focused on 2D frames for 3D path planning. they also suggested the method of the Visibility Line (VL), which could produce the shortest path from a starting point to a target point in a polygonal obstacle zone. This shows that it is efficient in measuring and suitable for applications in real time [21]. Wang Honglun et al. (2015) In difficult terrain conditions, they have 3D path planning for low-flying unmanned aerial vehicles (UAVs). This suggested an interfered adaptive fluid system (IFDS) to achieve the optimal 3D direction for path length and flight height. The form suggested showed better results [22]. Jinbae et al. (2017) Suggested an autonomous approach to enhancing training in the UAV flight plan. They also introduced Q-learning, a sort of reinforcement learning algorithm, to eliminate obstacles until the UAV hits the destination point. The approach suggested suggests a shorter time of arrival [23]. Jayesh et al. (2006) The fresh combination of data structures and algorithms was implemented as a fast and effective operational technique for UAV path planning. The RRT algorithm's paths show that the path through the Dijkstra algorithm provides the shortest path without any obstacles between the points on the road [24]. Argel and Reagan (2014) Quadrotor-type unmanned aerial vehicles (UAVs) also provide path planning to reduce vehicle power consumption, which is important over time in order to prevent waste of energy. It uses the Genetic Algorithm (GA) to determine the shortest path to fly without an obstacle to save time and energy [25].

Path-planning:

Path-planning it is a significant basic for autonomous mobile robots, enabling robots to seek the shortest – or best – path between two points. Alternatively, optimal paths may be paths that minimize the amount of turning, the amount of braking, or whatever a specific application requires. In robotics as well as network routing, UAV, video games and gene sequencing, algorithms are important for finding a shortest path. Figure 1 shows path planning example.

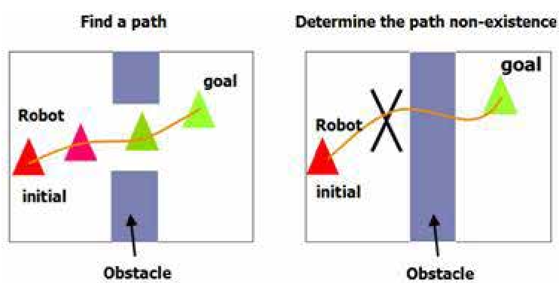

Figure 1. path planning exapmle

1. A* Algorithm

It is one of the algorithms used in computer science to find the shortest path. It can be used, for example, to solve a problem like (traveling salesman issue, TSP). Likewise, it is often used in game programming to find the shortest path to go to the target for players in the game. An intuitive solution algorithm is the A* algorithm. In short, finding the shortest nodes from the starting point to a destination node is the "best fit" algorithm. A* The search algorithm is one of the best and most popular navigation and charting techniques used. By adding an intuitive cost to the cost of the road, the total cost is calculated. The algorithm effectively draws a walkable path between the chart's multiple nodes or points. It is preferred to use the lowest total cost route. It is a computer algorithm widely used in finding and graphing paths, and it draws a path that can be effectively moved between the points called nodes. Figure 2 shows A* Example algorithm nodes. Algorithms in which computer science applies a heuristic approach to problem solving.

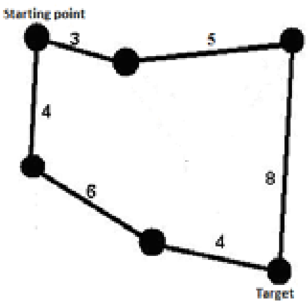

Figure 2. Example nodes for the A* Algorithm

There is no need to prove the accuracy of the applied method, the only desirable is that it makes a complex problem simpler or that the algorithm can find a satisfactory result. In general, one of the two aims in computer science is the solution of a problem. Either the solution of the problem should be fast and this solution should always be available. For this reason, the worst case analysis is frequently performed. In heuristic algorithms, one of these two possibilities is ignored. So either a quick solution to the problem is produced, but it cannot be guaranteed that it will always solve the problem, or it will solve the problem in a reasonable time, but it is not always guaranteed that it will be solved at the same speed. Heuristic algorithms are the approaches we use every day in real life. For example, moving from one place to another, based on our sense of direction and without knowing where the road will lead us, is such an approach to make intuitive choices at the crossings.

Purpose: To find the least cost solution from one node to the other

Type: Search Algorithm, Heuristic Algorithm (Artificial Intelligence)

Usage places:

- Finding the way
- Determining the paths to be followed by the actor in the games
- Solution of traveling salesman problem
- Finding the shortest exit from the maze

A* was first introduced in 1963 and has since become a common path planning and graphics switching system for the robot. For simple path planning, the A* algorithm is an elegant function-based algorithm. To find the lowest cost path from a first node to a destination node, it uses the best initial search. This path planning's 2D implementation algorithm was developed quite mature and extensively. Nevertheless, there are still technical difficulties in the 3D framework. Then, without considering many disturbances, the experimental application of this algorithm to unmanned aerial vehicles was examined without any evidence of feasibility, efficiency or convergence. To construct a linked network graph, some researchers use the two-dimensional Voronoi map to divide the target area into multiple sections. A* algorithm for real-time road planning of unmanned aerial vehicles on a 3D large-scale battlefield is introduced to achieve high survival rates and low fuel consumption of unmanned aerial vehicles.

A* algorithm can be categorized as an appropriate heuristic algorithm, as the algorithm uses the distance calculation function:

$$f(n)=g(n)+h(n) \qquad (1)$$

As it appears in the equation,

f (n): heuristic function,

g (n): The cost of moving from the starting node to the current node,

h (n): Estimated distance from the current node to the destination node.

It should be noted that the reason f(n) is intuitive is the heuristic h(n), which is predictive dependent. Figure 3 displays the flow diagram for the A* algorithm.

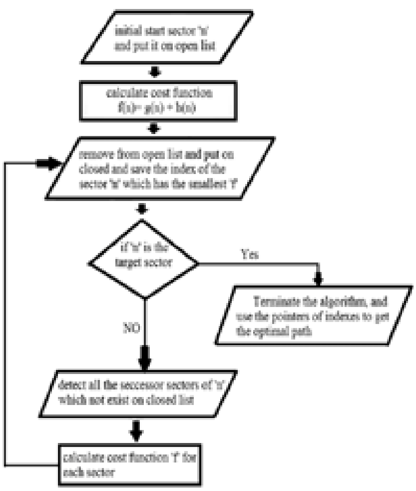

Figure 3. *Flow chart for the A* algorithm*

Algorithm operation:

The algorithm has a very simple structure that uses the above addition. In the algorithm that uses a priority queue as the data structure, the node with the highest priority is the node with the lowest f (n) value. A* uses the best initial search feature and finds the lowest cost path from a particular first node to a destination node. As the A* graph passes, it follows the lowest known heuristic cost path, maintaining a sequential priority order of alternate path segments along the path. Greedy is similar to the best initial search, but is more accurate because A* considers nodes that have already been passed. As an intuitive function, it takes the distance of a node's flight to the target.

The algorithm has a very simple structure using the addition process in the above equation. In the algorithm that uses a priority queue as the data structure, the node with the highest priority is the node with the lowest f(n) value.

- The algorithm takes the lowest value (and therefore the most important) node at each step (goes to this node) and subtracts the node from the queue.
- According to this node, the values of all neighboring nodes are updated (there is a cost to come to this node, and if you pay attention, this value is included in the function f (n).
- The algorithm repeats the above steps until the destination reaches the target node (priority queue in the priority queue) or until there is no node in the queue.

The operation of the algorithm is as follows:

- In the graph below, let's go from the node in the upper left corner to the node in the lower right corner. In this case, the distance value constituting the function f (n) can be calculated as the road costs on the graph. As an intuitive function, it takes the distance of a node's bird's flight to the target. The algorithm takes the lowest value for a node at each step and removes the node from the queue.

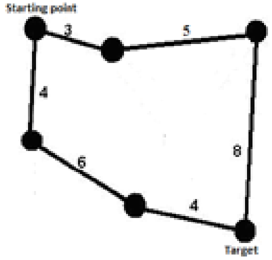

Figure 4. *Example nodes for the A* Algorithm*

- The values shown in red in this graph below show the bird's flight distance from that node to the node in the lower right corner of the target node. We can briefly accept these values as h(n).

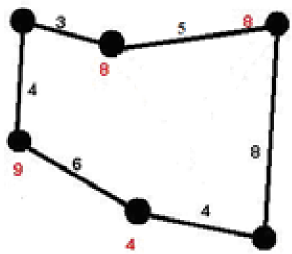

Figure 5. *Bird flight distance for A* Algorithm*

Let's calculate the value of the two nodes starting from the node in the upper left corner, which is our starting node. For the node under the start, h (n) = 9 and g (n) = 4.

For the node to the right of the start, h (n) = 8 and g (n) = 3. According to this:

f (down) = 9 + 4 = 13

f (right) = 8 +3 = 11

as. Our algorithm prefers to go to the right, which is small (and high priority) among these selections.

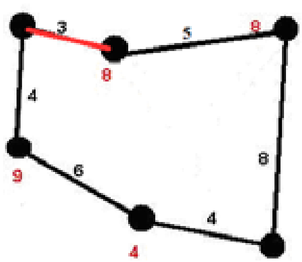

Figure 6. *Algorithm is updated on each node*

After this selection, the values are recalculated. According to the selection made above, the values of the nodes are again calculated as f (n) = g (n) + h (n).

- As shown in this graph below, there are two nodes in the queue and the values of the two nodes are 13 and 11, respectively.

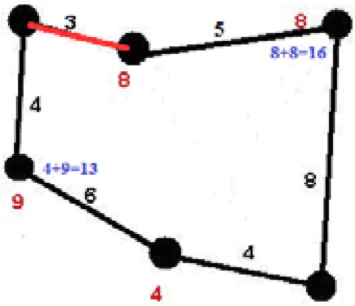

Figure 7. *The algorithm takes the lowest node*

According to this node, the values of all neighboring nodes are updated (now there is a cost to access this node and this value is included in the function f (n).

- When selecting between two nodes with values 13 and 16 in the last case below, because the short value is 13, our A* search algorithm gives up the alternative path at this stage and thinks that the shortest path may be this new node.

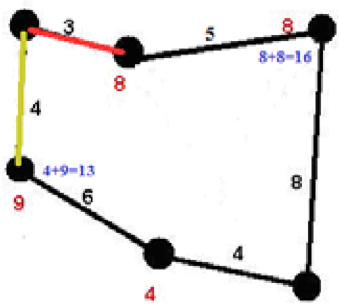

Figure 8. *The algorithm selects the lowest between the two nodes*

- In the figure below, this new selection is shown in green. The neighboring nodes reached after the new selection have values 16 and 14. In this case, the more priority node with a value of 14 will be moved.

When the new values are calculated, it is possible to go to the result node and the transport value is lower than the above navigation.

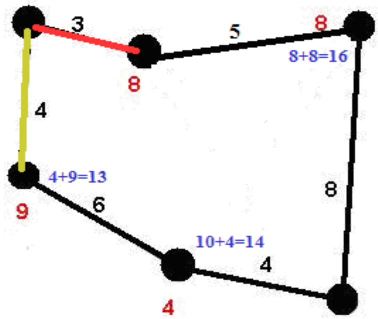

Figure 9. *Finding the shortest path between the starting point and the destination*

- The algorithm repeats the above steps until the target reaches the target node or there is no queue.

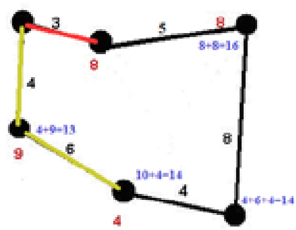

Figure 10. Deciding between two ways

- In the last case the target was reached and the following path was used. As a result, when the distance spent for transportation is added, the distance of 4 + 6 + 4 = 14 is shorter than the other alternative, 3 + 5 + 8 = 16. The shortest path is as shown in figure 8.

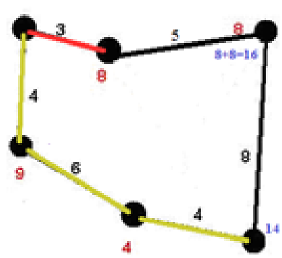

Figure 11. *The green road is the shortest path*

2. Dijkstra Algorithm

In a series showing the distance between two nodes, the problem is to find the route with the minimum length of the edge from the starting node (source node) to a given ending node (destination node).

Starting point: Initial node

End node: terminal node

Shortest path: path of minimum length

A weighted graph is an algorithm offering the shortest distance with values on a weighted graph between any two nodes. This algorithm was invented by Edsger Wybe Dijkstra, a Dutch mathematician and computer scientist. In many places, algorithm is used, especially routing. Dijkstra's Greedy algorithm is a greedy algorithm. That is, when moving from one node to another, the dijkstra algorithm selects the best solution of the current state. The Dijkstra algorithm used in computer science, which bears the name of the person who introduced the algorithm to the literature, is used in the following graph to find the shortest path. Figure 12 shows Dijkstra Example algorithm nodes.

- Assuming that all edge lengths are nonnegative,
- Finds the shortest routes from one node (for example, the first node) to all other nodes.
- While determining the shortest route from start to finish, it also gives the shortest route of each node relative to the beginning, thus finding the shortest routes from start to all nodes.

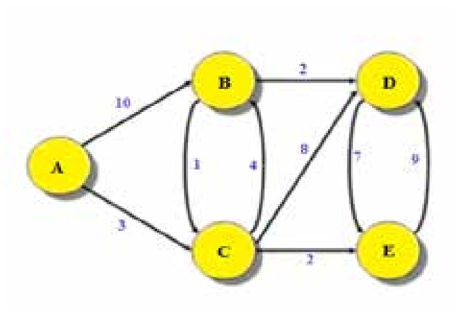

Figure 12. *Example nodes for the Dijkstra algorithm*

Edsger W. Dijkstra developed this algorithm in 1956. This algorithm's main purpose is to develop a coveted implementation method, such as shortest path planning. Strong adjustment reduced the algorithm's complexity. The basis for this algorithm is the theory of relaxation. More precise values change the correct approach to distance slowly until the optimum solution is finally reached. Dijkstra's algorithm takes its name from its developer. The main purpose of the algorithm is to find the shortest path of Graf. Graphs are widely favored to display each other's node relationships. Dijkstra algorithm flow diagram is shown in Figure 13.

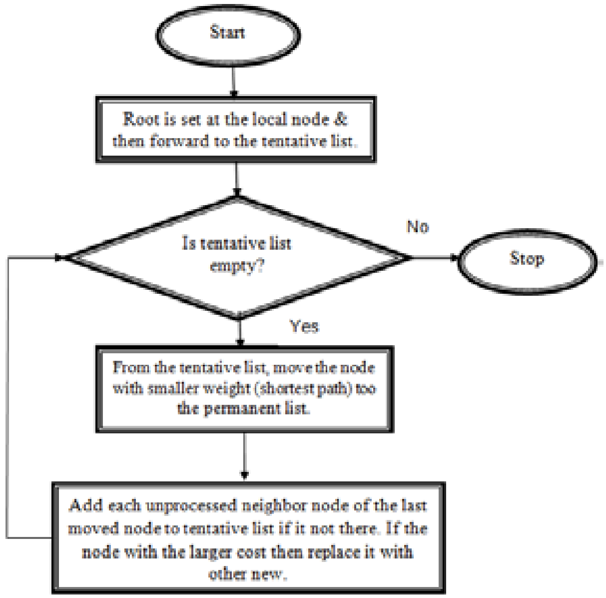

Figure 13. *Flow chart for the Dijkstra algorithm*

The calculation function used in this algorithm is:

$$f(n) = g(n) \tag{2}$$

As it appears in the equation,

f (n): heuristic function,

g (n): The cost of moving from the starting node to the current node.

To use the Dijkstra algorithm:

- Developed for weighted and directional graphs,
- The weight value of the edges must be zero or greater than zero, if the edge values are less than zero, the Bellman-Ford algorithm can be used,
- Does not work for negative weights.

Algorithm operation:

A starting point is selected in the Dijkstra algorithm. It should be known that all the remaining nodes are indefinitely far away. As we reach nodes, we change distances. The neighbors coming out of a node are examined at each step in Dijkstra, and the distances are updated when a shorter path is found. And again to the nearest node. This will rotate all the nodes on the graph and find the shortest path. The algorithm of Dijkstra works by visiting the corners of the graph from the starting point of the object. It then adds the corners to the array of corners to be investigated, checking repeatedly the nearest corner that has not been examined yet. From the starting point, it extends outward until it hits the target. Dijkstra's Algorithm is guaranteed to find the shortest route to the destination from the starting point. The algorithm from Dijkstra calculates the shortest paths to all other nodes from one node. The weight value of the edges should be zero or greater than zero, established for weighted and directional graphs.

If the edge values are less than zero, it is possible to use Bellman-Ford in more general algorithms. Because the edge still generates a better result than the current situation at the negative value, and the algorithm never becomes stable. The shortest path from the initially selected node to all other nodes is measured in the Dijkstra algorithm. There is no target node in the Dijkstra algorithm. If a target node is identified as a problem, the Dijkstra algorithm will find the shortest path to all nodes, then choose one of them. So the shortest distance to all nodes is determined if you use the Dijkstra algorithm, whether you have a goal or not. If you have a destination, you are already determining the shortest path to that destination. At Dijkstra, each move is considered on a node's neighbors, and when a shorter path is found, distances are changed.

The operation of the algorithm is as follows:

- As shown in Figure 11, node A is first selected by the Dijkstra algorithm as the starting point.
- First step A is given zero distance value after starting point A is given infinite distance value to all other nodes. The following figure 14 shows the node A starting point.

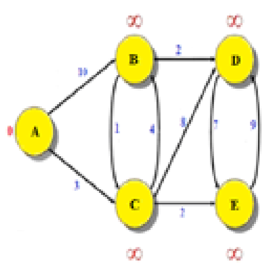

Figure 14. *A node is starting point*

- The second step is to calculate the distances from node A to other paths. It then passes all the other nodes to the starting node and updates its access. Figure 15 below shows the distance from node A to other roads.

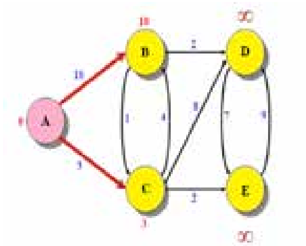

Figure 15. *Distance from node A to other roads*

After this update operation, it updates the neighbors of the updated nodes and continues until all nodes are updated and no new updates are available on the figure.

- The third step selects the smallest distance from node A and B and C which are adjacent nodes. After this update, it updates the updated nodes and continues until all nodes are updated and no new updates are available in the graph. (See Figure 16).

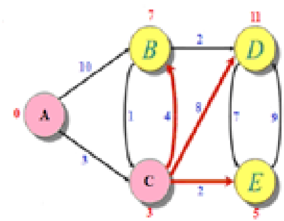

Figure 16. *Minimum distance from node A to other roads*

- The fourth step only visits node E, as shown in Figure 17 below.

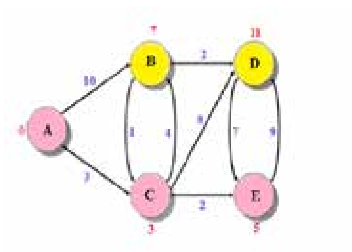

Figure 17. Visiting node E

As a result of all the steps summarized as shown in table 1.

Table 1. Visited nodes

A	B	C	D	E
0	∞	∞	∞	∞
	10	3	∞	∞
	7		11	5
	7		11	
			9	

The purpose of this algorithm is:

The main purpose of this algorithm is to calculate the minimum distance to the nearest costs to all other roads from the point where it is located. Starting from a node, it guarantees that the node reaches the shortest distance to all nodes on the graph. He also claims that there will be no shorter path than that. Can be equal distance. Google map is used in transactions. It can be used to determine the shortest path from one node in a graph to all other nodes within the same graph data structure.

Weakness of Dijkstra algorithm

Unfortunately, the algorithm does not work successfully if there is an edge with a negative (-) value. This is because the edge of the negative (-) value consistently produces a better result than the current situation and the algorithm can never be stable.

RESULT

A* algorithm and Dijkstra algorithm show that A* is faster and Dijkstra spends more time than the comparison result. The A* algorithm only scans the area towards the target, while the Dijkstra algorithm shows a much larger area. As a result, the A* algorithm performs better in terms of time. In the test environments seen, as you can see, the time A* Algorithm spends to solve the problem is almost half the time spent by Dijkstra's Algorithm to solve the same problem.

The advantages and disadvantages of these two algorithms are listed in the literature, A* is faster than Dijkstra's algorithm because it uses Best First Search, Dijkstra's Greedy uses Best First Search, Dijkstra's are simple compared to A*, the main disadvantage of Dijkstra's algorithm is that it does a blind research by wasting a lot of time on the necessary resources, another disadvantage is the inability to remove negative edges, which leads to acyclicity, the major drawback of the algorithm is that it does a blind research by spending a lot of time on the necessary resources. Dijkstra is essentially the same as A* because it is not intuitive (H is always 0). Because it is non-intuitive, it searches equally in all directions, but A* scans the area only in the direction of arrival. As you can imagine, the reason for this Dijkstra often results in exploring a much larger area before the target is found. This usually makes it slower than A*. But both have their own importance.

REFERENCE

Pakkan, B. ve Ermiş, M. (2010). İnsansız hava araçlarının genetik algoritma yöntemiyle çoklu hedeflere planlanması. Havacılık ve uzay teknolojileri dergisi, 4. (3), 77-84

Mustafa DİKMEN, (2015), "İnsansız Hava Aracı (İHA) Sistemlerinin Hava Hukuku Bakımından İncelenmesi", The Journal of Defense Sciences, Volume 14, Issue 1, 145-176.

Neşeli, S., Terzioğlu, H., Ağaçayak, A.C., Yalçın, G., (2018). "Düşük Hızlı Hava Araçları için Ön Kanatçık Tasarımı ve Akış Analizi", International Science and Academic Congress'18 (INSAC'18). Selçuk University, Vol:3, pp.709-721

Neşeli, S., Terzioğlu, H., Ağaçayak, A.C., Yalçın, G., (2018). "İnsansız Hava Taşıtları için Rüzgar Tüneli Tasarımı ve Hava Akış Analizi", International Science and Academic Congress'18 (INSAC'18). Selçuk University, Vol:3, pp.689-708

Ağaçayak, A.C., Terzioğlu, H., Neşeli, S., Yalçın G., (2017). "The Impact of Different Electric Connection Types in Thermoelectric Generator Modules on Power", International Journal of Engineering Research & Science (IJOER), Vol.3, pp.2395-6992.

Ağaçayak, A.C., Terzioğlu, H., Neşeli, S., Yalçın G., (2018). "Small Power Wind Turbine Design," Acad. Studies in Eng., Gece Publishing, pp. 121-130.

Ağaçayak, A.C., Terzioğlu, H., (2018). "Analysis of Thermoelectric Cooler Used to Produce Electrical Energy in terms of Efficiency," Acad. Studies in Eng., Gece Publishing, pp. 111-120.

Gupta S.G., Ghonge M.M., Jawandhiya Dr. P. M., (2013), "Review of Unmanned Aircraft System (UAS)", International Journal of Advanced Research in Computer Engineering & Technology (IJARCET) Volume 2, Issue 4

Ağaçayak, A.C., Sungur, C., (2019). "Drone Ağları için Topoloji İncelemesi", Mühendislik Alanında Yeni Ufuklar, Gece Kitaplığı,vol. 29377, pp. 5-32.

Yalçın, G., Neşeli, S., (2019). "Drone'lara Genel Bir Bakış", Mühendislik Alanında Yeni Ufuklar, Gece Kitaplığı,vol. 29377, pp. 165-191.

Akshay Kumar Guruji, HimanshAgarwal and D.K.Parsediya. (2016). Time-efficient A* Algorithm for Robot Path Planning. 3rdInternational Conference on Innovations in Automation and Mechatronics Engineering, ICIAME 2016, 144 – 149.

Halil Cicibaş, Nafiz Arica and Kadir Alpaslan Demir. (2015). İnsansız Hava Araçları için Çok Kriterli Güzergah Planlama Modeli. Savunma Bilimleri Dergisi.

Weiwei Zhan, Wei Wang, Nengcheng Chen and Chao Wang, 2014, Efficient UAV path planning with multiconstraints in a 3D large battlefield environment, Mathematical Problems in Engineering, 2014.

František Duchoň, Andrej Babinec, Martin Kajan, Peter Beňo, Martin Florek, FicoTomáš ve Ladislav Jurišica, 2014, Path planning with modified a star algorithm for a mobile robot, Procedia Engineering, 96, 59-69.

Dong Zhuoning, Zhang Rulin, Chen Zongji ve Zhou Rui, 2010, Study on UAV path planning approach based on fuzzy virtual force, Chinese Journal of Aeronautics, 23 (3), 341-350.

Felipe Leonardo Lobo Medeiros and Jose Demisio Simoes da Silva. (2010). A Dijkstra Algorithm for Fixed-Wing UAV Motion Planning Based on Terrain Elevation. Springer-Verlag Berlin Heidelberg, 213-222.

Lyle Parungao, Fabian Hein and Wansu Lim. (2018). Dijkstra Algorithm Based Intelligent Path Planning with Topological Map and Wireless Communication, ARPN Journal of Engineering and Applied Sciences, 2753-2763.

S. Julius Fusic , P. Ramkumar and K. Hariharan. (2018). Path Planning of Robot Using Modified Dijkstra Algorithm, 2018 National Power Engineering Conference (NPEC).

Ter-Feng Wu, Pu-Sheng, Nien-Tsu Hu and Jen-Yeng Chen. (2017). Combining turning point detection and Dijkstra's algorithm to search the shortest path, journal.

Julius Sekaran and Julius Sekaran. (2018). Path planning of robot using modified dijkstra Algorithm. 2018 National Power Engineering Conference (NPEC).

Rosli Omar ve Dawei Gu, 2010, 3D Path Planning for Unmanned Aerial Vehicles using Visibility Line based Method, ICINCO (1), 80-85.

Honglun Wang, Wentao Lyu, Peng Yao, Xiao Liang ve Chang Liu, 2015, Three-dimensional path planning for unmanned aerial vehicle based on interfered fluid dynamical system, Chinese Journal of Aeronautics, 28 (1), 229-239.

Jinbae Kim, Saebyuk Shin, Juan Wu, Shin-Dug Kim and Cheong-Ghil Kim. (2017). Obstacle Avoidance Path Planning for Uav Using Reinforcement Learning Under Simulated Environment. IASER 3rd International Conference.

Jayesh N. Aminy, Jovan D. Boskovic, and Raman K. Mehra. (2006). A Fast and Efficient Approach to Path Planning for Unmanned Vehicles. AIAA Guidance, Navigation and Control Conference, keystone.

Galvez, RL, Dadios, EP ve Bandala, AA (2014, November). Genetik algoritmayı kullanarak dörtlü İHA için yol planlama. In Humanoid, Nanoteknoloji, Bilgi Teknolojileri, İletişim ve Kontrol, Çevre ve Yönetimi (HNICEM) hakkında 2014 Uluslararası Konferansı (s. 1-6). IEEE.

KINETIC EVALUATION OF HEAVY METALS AND ORGANIC POLLUTIONS ADSORPTION ON CLAYS

CHAPTER

7

Mesut YILMAZOĞLU[1]
Jülide HIZAL[2]

1 Department of Chemical and Process Engineering, Faculty of Engineering, Yalova University, 77100, Yalova, Turkey
2 Department of Chemical and Process Engineering, Faculty of Engineering, Yalova University, 77100, Yalova, Turkey

1.INTRODUCTION

When heavy metal cations or organic matters (i.e. dyes, pharmaceuticals etc.) are discharged into environment, they cause serious problems. Many processes as ion exchange, membrane technologies, and adsorption are used in order to remove these contaminants from wastewater. Adsorption process has many advantages with respect to their low-cost, having environment-friendly nature, abundance on earth, high specific surface area, small particle size, high cation exchange capacity (CEC), applicability in a wide pH range and high chemical stability [1, 2]. All type of pollutants can be remove by the aid of adsorption process [3].

Primary natural adsorbents are clays and clay minerals such as bentonite, kaolinite, clinoptilolite, zeolite. They are abundant and relatively cost effective sorbents [4]. Clays are differentiated from other soils as regards of their mineralogy and size. They are economically and technically convenient to be an adsorbent. Additionally, they are good and effective sorbents for radionuclides. The clay minerals occur as a result of chemical weathering of rocks. They consist of octahedral and tetrahedral structures which are formed by oxygen or hydroxyl groups, symmetrically disposed in planar layers. Two types of clay mineral exist in nature with respect to their tetrahedral/octahedral ratio: 1:1 structures and 2:1 structures. The tetrahedral sheet of kaolinite has permanently negative charge due to isomorphic substitution of Si(IV) by Al(III), and a single negative charge leaves at the end of each substitution on the surface.

This substitution allows electrostatic interaction with positively-charged ions. 2:1 structured clays have excellent adsorber property which is sourced from negative charge existence on two silanol surfaces. Both the octahedral sheet and the cystal edges have a pH-dependent variable charge caused by protonation and deprotonation of surface hydroxyl groups. Cation adsorption mainly occurs on proton bearing surface functional groups such as silanols and aluminols. In addition, the donor atom included in organic components may exist inside the gaps of lattice, and may be responsible for heavy metal retention [5]. Variety of active sites with different character allows strong physical and chemical interactions which result in sorption and/or specific cation exchange of adsorbate/solute [6].

Adsorption is one of the most important technique which is fundamentally based on mass transfer of a solute from bulk solution to solid surface. The mass transfer of adsorbate in adsorption process takes place through several steps;

i. bulk diffusion; when a solid puts into a liquid, electrical double layer occurs beyond solid-liquid interface. Triple Layer Model (TLM) is generally used for explaining the clay-water interface [7]. Because there is an adsorbate concentration gradient between bulk solution and Outer Helmholtz Plane (OHP), adsorbate ions or molecules migrate from bulk solution to adsorbent surface. This migration is the fastest step of adsorption process [8,9]. Then, the adsorbate molecules achieved OHP may be transfered to IHP (Inner Helmholtz Plane) where the adsorbate ions or molecules are specifically adsorbed (inner-sphere complexation) (Figure 1).

ii. film diffusion (boundary layer diffusion); when the molecules or ions involved in flowing solution encounter a solid surface, their velocity decreases due to frictional forces between solid and liquid phases, and the effects of viscosity becomes significant. The mass transfer occurred at that time results in adsorption of ion or molecule. The adsorbate served by boundary layer diffusion onto solid surface can pass through OHP, then achieve IHP in which the specific adsorption occurred. These two stages are defined as exterior surface adsorption [9].

iii. pore diffusion or intraparticle diffusion; when the adsorption of the exterior surface reaches saturation, adsorbate ions or molecules may diffuse from the surface to interior of the particle and encounter fresh adsorption sites [10].

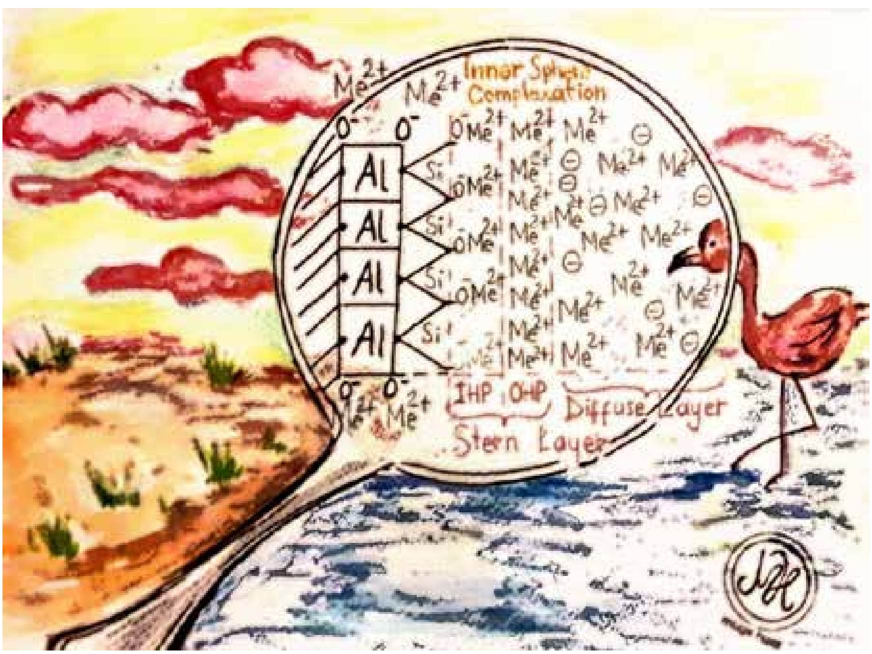

Figure 1. *The schematic diagram of the mass transfer of heavy metal (Me^{2+}) from bulk solution onto solid surface through Electrical Triple Layer.*

Considering that heavy metal and ligand adsorptions onto clays occur as a result of ion exchange, surface complexation, hydrophobic interaction, and electrostatic interaction, possible reactions can be written as below [11, 12]:

proton adsorption and surface acidity:

$$\equiv SOH_2^+ \rightleftharpoons \equiv SOH + H^+ \qquad K_{a1}$$

$$\equiv SOH \rightleftharpoons \equiv SO^- + H^+ \qquad K_{a2}$$

monodentate binary metal (Me^{2+}) – surface ($\equiv SOH$) complexation:

$$\equiv SOH + Me^{2+} \rightleftharpoons \equiv SOMe^+ + H^+ \qquad K_1$$

bidentate binary metal (Me^{2+}) – surface ($\equiv SOH$) complexation:

$$2 \equiv SOH + Me^{2+} \rightleftharpoons (\equiv SO)_2Me + 2H^+ \qquad K_2$$

surface complexation with hydrolized metal species:

$$\equiv SOH + MeOH^+ \rightleftharpoons \equiv SOMeOH + H^+ \qquad K_3$$

monodentate and bidentate anion adsorption via ligand exhange:

$$\equiv SOH + L^- \rightleftharpoons \equiv SL + OH^- \qquad K_4$$

$$2 \equiv SOH + L^- \rightleftharpoons \equiv S_2L^+ + 2OH^- \qquad K_5$$

ternary surface complexation (ligand bridged and metal bridged, respectively):

$$\equiv SOH + L^- + Me^{2+} \rightleftharpoons \equiv S\text{-}L\text{-}Me^{2+} + OH^- \qquad K_6$$

$$\equiv SOH + L^- + Me^{2+} \rightleftharpoons \equiv SOMe\text{-}L + H^+ \qquad K_7$$

attachment of inert electrolyte ions onto diffuse layer:

$$\equiv SOH_2^+ + Cl^- \rightleftharpoons \equiv SOH_2^+ \ldots\ldots\ldots\ Cl^- \qquad K_8$$

$$\equiv SO^- + Na^+ \rightleftharpoons \equiv SO^- \ldots\ldots\ Na^+ \qquad K_9$$

electrostatic interaction between permanently negative charged surface (X^-) and metal cation

$$2\,NaX + Me^{2+} \rightleftharpoons MeX_2 + 2\,Na^+ \qquad K_{10}$$

2. Importance of Kinetic Properties in Environment

Determination of the kinetic properties of a process is the most important searching methods due to showing the scheme of adsorption process, estimating of adsorbate concentration at any step of process, and enabling to choose optimum operating conditions to design and model the adsorption [13]. However, kinetic analysis of adsorption process clears up to control of solubility and mobilization of heavy metals and/or organic pollutants in environmental medium such as surface water, clay and/or soil layers [14]. Defination of interaction between adsorbate and adsorbent, and determination of controlling mechanism of adsorption are performed by applying pseudo first- and second order kinetic models, intraparticle diffusion model, Elovich model and Bangham's model [4]. Pseudo first order (Lagergren Model) and second order (Ho and McKay Model) models define the bulk diffusion rate [15-18]. A pseudo second order model is based on the assumption that the adsorption is chemically achieved [17]. The pseudo- first and second order models are given in equations 1 and 2, respectively:

$$\text{Log}\,(Q_E - Q_t) = \text{Log}\,Q_E - (k_1/2.303)\,t \quad (1)$$

$$t/Q_t = 1 / k_2 Q_{E2} + (1/Q_E)\,t \quad (2)$$

where k_1 is the first order rate constant (min^{-1}), and k_2 is the second order rate constant, t is the contact time (min), Q_E is the adsorbed amount of solute at equilibrium ($mg\ g^{-1}$), and Q_t is the adsorbed amount of solute at any time. The rate constants can be calculated from the slope of the linear plots. In order to explain the boundary layer and pore diffusion rate, Intraparticle Diffusion (Eg.3) and Bangham's Model (Eq. 4) are used [15, 16, 18]:

$$Q_t = k_i\,t^{1/2} + C \quad (3)$$

where k_i is the intraparticle diffusion rate constant and C is the intercept. $t^{1/2}$ vs. Q_t curve represents more than one linear region having different slope and intercept. It means intraparticle diffusion is involved in the adsorption process. If the extrapolation of the first straight line passes through origin, the rate controlling step of whole adsorption process is of intraparticle diffusion step. Otherwise, intraparticle diffusion may not be sole rate-limiting step for whole adsorption process. Bangham's Model (Eq. 4) defines the adsorption as an activated process, and assumes that the activation energy varies logarithmically with the adsorbed amount of solute [19];

$$\text{Log}\,[C_0/(C_0 - Q_t\,m)] = \text{Log}\,[(k_0\,m)/(2.303\,V)] + \alpha\,\text{Log}\,t \quad (4)$$

C_0 is the initial concentration of adsorbate ($mol\ L^{-1}$) V is the volume of solution (mL), m is the solid/liquid ratio ($g\ L^{-1}$), k_0 and α are constants. High determination coefficient obtained from application of Bangham's Model makes think that pore diffusion could be the slowest mass transfer step. Consequently, the evaluation of Bangham and Intraparticle Diffusion Models reflects multiple steps in whole adsorption process.

Other model, which is generally used for kinetic evaluation of adsorption process, is Elovich (Roginsky–Zeldovich) model. It explains chemical adsorption mechanism considering initial adsorption rate constant and desorption rate constant, and is simply expressed as follows;

$$Q_t = (1/\beta)\ln(\alpha\,\beta) + (1/\beta)\ln t \qquad (5)$$

where Q_t is the amount of adsorbate at any time, α is the initial adsorption rate (mg g^{-1} min^{-1}) and β is the desorption rate constant (g mg^{-1}) which is related with the surface activation energy. Low activation energy (E_a) means diffusion controlled process (physisorption), whereas high values indicate chemical process (chemisorption) [20]. The elementary step in chemisorption is to achieve E_a, unlike in physosorption.

In some cases, natural clay may not be efficient for the purpose due to their textural and structural properties. Thus, modification of natural clays with agents having reactive functional groups or surfactants. Modification may enable increase in surface area and porosity [3, 4]. Because thiol groups are capable of forming chelate complex with metal cations, the external surface silanol groups of a natural clay can be functionalized by using organic ligand including thiol groups, or these type of organic ligands may be intercalated into layers of a clay. Thus, the adsorption affinity of clays to high toxic heavy metal such as Pb(II) and Hg(II) is enhanced [21]. Modification may change kinetic properties. For example, dye adsorption on bis imidazolium coated bentonite fits the pseudo first order model, while adsorption on hexadecyltrimethyl ammonium modified bentonite shows the pseudo second order kinetic behavior. Type of adsorbate also changes kinetic properties. For instance, when bentonite was modified with hexadecyltrimethyl ammonium, kinetic behavior of acid red varied from pseudo second order to pseudo first order [4].

All kinetic evaluations should be considered together with thermodynamic evaluations because the activation energy for chemisorption is of the same magnitude as the heat of chemical reactions [22]. The activation energy of physisorption is utmost 4.2 kJ mol^{-1} due to having weak interactions. Contrary, since chemisorption has much stronger interactions, the activation energy of this type of adsorption is quite high. The activation energy of adsorption increases with increasing concentration of covered surface sites. When E_a is between 8.4 and 83.7 kJ mol^{-1}, it means the adsorption rate is time dependent. Activated chemisorption means that the rate varies with temperature according to finite activation energy (between) in the Arrhenius equation (high Ea). However, in some systems the chemisorption occurs very rapidly, suggesting the activation energy is near zero. This is termed as a nonactivated chemisorption.

2.1. Kinetic Properties of Heavy Metal Adsorption on Various Natural Adsorbents

Heavy metals are serious environmental pollutants, and they cause ecological, genetical, nutritional and environmental threatens. They are essential for organism to maintain various biochemical and physiological functions in trace amounts, but become toxic and hazardous when they exceed certain threshold concentrations [23]. When discharged as a waste of many industrial processes, heavy metals accumulate in soil and/or water basin. They may join into food chain via plant and animal organisms. The most commonly found heavy metals in waste water are arsenic, cadmium, chromium, copper, lead, nickel, and zinc, etc. [23]. The EU Restriction of Hazardous Substances Directive and The EU End of Life Vehicles Directive restrict the use of many highly toxic heavy metal ions such as As (III, V), Sb(III, V), Pb(II), Cd(II), Hg(I, II) and Cr(VI) [24, 25]. Various water treatment methods have been applying to remove heavy metals from waste water effluents. But, the adsorption process has more advantage as regard of its cost-effectiveness and easy applicability. There are too much study about removal of heavy metals based on the adsorption of them onto natural or modified adsorbents in literature.

Pb(II) is a widely distributed accumulative pollutant, and releases to environment via battery manufacturing, acid metal plating, ceramic and glass industries etc. It is the third most common toxic element in the heavy metal toxicity. In a study, illite and smectite (having 2:1 type layered structure) mixture in nanosized used as adsorbent to remove Pb(II) ions from aqueous solution. As a result of experiments, it was observed that Pb(II) adsorption on nanosized clay mixture fits both pseudo first- and second-order models with the R^2 0.999. But theoretical Q_E, calculated by using k_2 rate constant obtained from the application of pseudo second order model, better matched with the experimental Q_E value. Thus, it was assumed that adsorption kinetic fits pseudo second order model [2]. In another study, Al-Degs et al. studied Pb(II) adsorption onto four different natural clays, and they observed strong correlation adsorption and cation exchange capacity. It was mentioned by the authors that external diffusion to the exterior surface was the major mechanism. Adsorption was a fast process that 80 % of equilibrium was attained in the first few minutes [26]. Khalfa et al. were investigated the efficiency of natural and acid activated clay minerals collected from south Tunisia in order to removal of Zn(II) and Pb(II) from synthetic waste water solutions. The equilibrium was achieved after 90 min for both metal ions. The faster step of adsorption was completed in 30 min, and the reaction got slower until 90 min. This variation in rate can be explain by occupation of empty active sites due to concentration gradient between surface sites and the bulk solution. When most of the active sites are occupied, the gradient decreases, thus the adsorption gets slower. The results showed the pseudo second order kinetic model described the adsorption, and the intraparticle diffusion was the limiting step [27]. In another study, Pb(II) adsorption on Iranian Sepiolite and Zeolite was investigated [28]. Sepiolite is a fibrous hydrated magnesium silicate which has a 2:1 structured, and because of isomorphic substitution it has permanently negative charge on both silica sites. The equilibrium was attained in 6 h (fast reaction occurred in first 1 h, and attained the equilibrium in next 5 h), and experimental data fitted Pseudo-Second Order Model with the 10^{-3} order of magnitude of k_2 [28]. In order to remove Pb(II) and Cd(II) ions from waste water, Meneguin et al. (2017) tried to adsorb them onto natural and calcium calcined bentonite. They applied pseudo- first order, pseudo second order and intraparticle kinetic models to determine adsorption kinetic, and they expressed that metal ions diffusion from bulk solution to the surface fitted pseuso-second order model, and intraparticle diffusion was not preferable adsorption mechanism. The maximum adsorption was achieved in 30 min [29].

The kinetic study of Zn(II) removal by the aid of Na-enriched Brazilian Gray Clay showed that fast adsorption process occurred in 2 minutes, and the equilibrium was reached in 40 min [30]. The authors implied that Pseudo Second Order Model could be successfully explained the interactions between Zn(II) and clay surface during adsorption. The removal of Cu(II) and Zn(II) is investigated using Cankırı bentonite by Veli and Alyüz [31].

They determined that the maximum removal efficiencies were achieved within 10 min for both metals. The adsorption from aqueous solutions was well described with the second order reaction kinetic. The calculated and experimental Q_E values are quite close to each other. In another study, kinetic of Cu(II) adsorption on bentonite was investigated by the aid of pseudo first order model, pseudo second order model and intraparticle diffusion model. In another study, it was determined that 4 hours of contacting is sufficient for achieving equilibrium for Cu(II) adsorption onto montmorillonite. The regression coefficient (R^2) of pseudo second order model is much higher than gained for pseudo first order model. The calculated Q_E values from the pseudo first order model are in good agreement with the experimental values [10].

Cd(II) adsorption on feldspar showed pseudo first order kinetics, as is apparent from the much higher correlation coefficient (R^2) close to 1 with the 0.011 k_1 value which conforms the theoretical Q_E with the experimental Q_E. The permanent negative-charged sites are responsible for Cd(II) adsorption only at acidic pHs. Adsorption seems to result from the interaction between the unhydrolyzed Cd^{2+} ion and the neutral surface sites plus negatively charged surface sites. This interaction takes place via formation of binary surface-metal inner-sphere complexes and of outer-sphere complexes between ion exchangeable X_2^- surface sites and Cd(II) ions [32]. Ball clay can be used as an effective adsorbent for the removal and recovery of Cd(II) from aqueous solution. This adsorption is pH dependent and the maximum adsorption occurred at pH 6. Adsorption followed pseudo- first order and second order kinetics at lower initial concentrations of Cd(II). The adsorption percent of Cd(II) increased with increase in adsorbent amount [33]. As seen from the studies, heavy metal adsorption on natural clays is a fast process. The other study, which was performed by using natural clay obtained from the Middle Atlas Mountains region, Morocco, showed that about 90% of Cd(II) and Cu(II) adsorption on this clay occurred within first 30 min of contact time. Adsorption rate increased with the increasing initial metal ions concentrations and the sorption rate conformed the pseudo second order model. The data according to mass transfer and intraparticle diffusion models confirmed diffusion of adsorbate is the rate-controlling step [34].

On the other hand, aluminum is the most abundant metal in the earth's crust. When consumed via drinking water it causes health problem as Alzheimer and dialysis encephalopathy. The maximum allowable aluminum amount in drinking water is limited with 0.2 mg L^{-1} by the Environmental Protection Agency (EPA) [35]. As a bauxite processing waste water, Al(III) ions discharges into environment after suit water treatment. Al(III) adsorption on kaolinite and bentonite were searched as regard of kinetic and isotherm by Chai et al. (2017). It was shown that the pseudo-second order model decribed the adsorption process, and the intraparticle diffusion was not the rate controlling step [36].

In another study, the adsorption of Sr^{2+} and Cs^{+} on a purified Na-MX80 bentonite was investigated as a function of pH and initial concentration of Sr^{2+} and Cs^{+}, and kinetic of adsorption was searched for Sr^{2+} adsorption. As a result of this study, those were mentioned by the author that Sr^{2+} and Cs^{+} were readily adsorbed especially by clay minerals as illite and kaolinite, Na-conditioned montmorillonite (obtained by washing with 1 M NaCl solution) played an important role in the adsorption of these cations because of its high cation exchange capacity (CEC). The reported CEC for the MX80 varied from 0.71 to 1.03 mmol g^{-1}. The curve of R_D variation as a function of contact time showed that the system reaches to equilibrium in a few minutes. The R_D value is constant all through the experiments with an average value of $R_D \sim 192$ L kg^{-1} [37]. The partition coefficient R_D (L/kg) were calculated using;

$$R_D = ((C_o/C_E)-1)\ V/m \qquad (6)$$

Abdel Karim et al. investigated the adsorptions of Sr^{2+} and Cs^{+} on a particular local clay in terms of isotherm and kinetic models. For this purpose, pseudo first- and second- order models were used, and found that both adsorptions fitted Pseudo-Second Order Model with the R^2 of 0.999. The kinetic investigation of Sr^{2+} and Cs^{+} on a clay at pH 7 was searched by measuring the varied amount of cations depending the contact time at different temperatures. It was shown that the equilibrium was achieved in 20-30 min, and the temperature of environment did not effect the time required for achieving the equilibrium, but caused decrease in adsorbed amount of cations by increasing temperature which showed exothermic character of Sr^{2+} and Cs^{+} adsorption of this clay. Additionaly, it was mentioned that the adsorbed amount of Cs^{+} on clay was higher than that of Sr^{2+} because of the selectivity of clay for Cs^{+}. Good regression coefficients were yielded from the application of pseudo- second order model, and it was proved by the conformity between experimental and theoretical Q_E values [6].

Adsorption process has important role and effect in the mobility and bioavailability of potassium in soils. KCl is the major potash fertilizer used in agriculture. It is not toxic for organism, has not negative effect on quality of surface and drinking water. Potassium ions can be leached into deeper soil layers, followed by reaching the aquifers. Thus, understanding the K^{+} adsorption mechanism onto soil is important due to soils may contain widely variable pools of K which are potentially mobilized by chemical weathering of soil minerals. [38, 39]. A kinetic study for K^{+} ion exchange mechanism on Ca(II)-saturated clays was performed by Ogwada et al. in 1986. They compared the rate constants (k) considering the contact style of liquid and solid phases. Higher rate constants obtained for wriggling based methods in the order of batch>stirred>vortex batch. They declared that the ion exchange/adsorption of K^{+} conformed pseudo first order model [20]. While potassium ions do not induce eutrophication in surface waters, other inorganic nutrition factor ammonium, which is used as fertilizer in agricultural practice, ammonium causes eutrophication in rivers, estuaries, lakes, and other water reservoirs. It mixes into environment by domestic and industrial wastewater discharge [40]. NH_4^{+} ions onto six natural clay minerals (NCM) was searched by Alshameri et al. in 2018 [40]. The kinetic of ammonium adsorptions on those clay minerals fitted pseudo-second order kinetic model. Kinetic experiments were performed by conducting particular volume of 10 ppm NH_4^{+} with clay minerals for time interval of 5-120 minutes. As a result of experiments these were observed that i) all systems achieved to equilibrium in 30 min, ii) vermiculite showed high removal efficiency at the same conditions, iii) rapid achieving to equilibrium was explained by fast diffusion of NH_4^{+} ions to available adsorption sites of NCMs. In kinetic evaluation both pseudo first- and second order models were applied [40].

The short term clay-lime interactions results in adsorption of free Ca^{2+} ions onto clay minerals by cation exchange mechanism. On the other hand, free Ca^{2+} ions can interact with dissolved mineral components (i.e. silica or alümina) by long term pozzolonic reactions. As a result of these type of reactions cementilious compounds occur [41]. Thus, Ca adsorption onto clay is an important process due to it controls the fortune of stabilization of soil in environment. It is known that the exchange of Ca^{2+} ions with other cations held on the negatively charged surface of clay is the primary process in the acidic media. Additionally, $Ca(OH)^+$ cation, which is formed as a result of hydrolysis of Ca^{2+} ions, determines Ca^{2+} retention on clays at high pHs [41].

In an adsorption system, although many equilibria are valid, the primary reactions especially effecting onto divalent heavy metal adsorption are;

- solubility of metal ion, and the formation of metal hydroxo complexes

$$Me(OH)_2 \rightleftarrows Me^{2+} + 2\,OH^- \qquad K_{sp}$$

$$Me(OH)_x^{(x-2)} \rightleftarrows Me^{2+} + (x-2)\,OH^- \qquad K_{in}$$

the attachment onto surface

$$\equiv SOH + Me^{2+} \rightleftarrows \equiv SOMe^+ + H^+ \qquad K$$

The formation of surface-metal inner sphere complex with stability constant (K) extracts metal ions from aqueous solution. Thus the first reaction (K_{sp}) proceed to in support of solubility while the second reaction (K_{in}) proceed to degradation of metal-hydroxo complexes. In this situation limiting solubility pH of metal ion in particular concentration enhances [42]. Consequently, rate of bulk diffusion of metal ion increases.

1.1. Kinetic Properties of Organic Pollutions Adsorption on Clays and Clay Minerals

Many organic pollutions, which are highly harmfull for organism and environment, are discharged into environment through different ways. Organic dyes, pharmaceutics and pesticids can be listed in these type of organic pollutants. On the other hand, even if organic compounds, which are considered under Natural Organic Matter (NOM: primarily fulvic acid and humic acid), have not toxic effect, their adsorption on clays or soil must be taken into account due to the importance in nature as regards of their solubility, mobilization, and complexation with heavy metals.

Dyes are widely used in textile and food industries. They have chromophoric (as $-NR_2$, -NHR, -COOH and -OH) and auxochromic (as -NO and $-NO_2$) groups that make them colored. They are also used in cosmetics, paper, ink-jet printing, leather dyeing, plastics, and pharmaceutics industries. Thus, large amount of dye waste is discharged to environment every day. Although many water treatment (chemical, physico-chemical or biological) method have been used for removal of dyes from waste water, there are still quite difficulties to remove them by using single process. Adsorption appears as pretreatment process for removing dyes, many studies have been dealt with dye adsorption [43, 44]. Natural, synthetic and/or modified adsorbents have been used for this purpose [4]. Organic dye adsorption on montmorillonite mostly shows pseudo second order kinetic properties which points out high affinity of clays to organic dye, hence chemisorption.

The adsorptions of methylene blue (MB), Crystal Violet (CV), and Congo Red (CR) on a natural clay were investigated by Bentahar et al. in terms of contact time, initial dye concentration, temperature, and pH of solutions. As a result of experiments, it was revealed that organic dyes adsorption on clay fits pseudo-second order model. The equilibrium was achieved in 20 min for all systems (both individual dye and dye mixture). The increasing curve in graphs was explained by gradually occupiatence of available surface sites. When the surface was saturated, the equilibrium was attained. The pseudo first- and second- order models were used to explain adsorption kinetic. The adsorption in all conditions fitted to pseudo second order model with the k in magnitude of 10^{-1}-10^{-3} [1]. Erçağ et al. were investigated the individual and competitive adsorption of three types of azo organic dyes which are commercially named as Red 46, Blue 41 and Basic Yellow 28 onto montmorillonite. The kinetic parameters indicated that basic dye adsorption fitted pseudo second order kinetic model, as apparent from the much higher correlation coefficient (R^2) and lower SSE% value. The adsorption reactions achieve to equilibrium in a short time by electrostatic interaction between positive charges on nitrogen atoms of five membered siclic rings and permanently negative charge on silica sites of montmorillonite which is pH-independent sites and occured as a result of isomorphic substitution [8]. In another study, individual and competitive methylene blue and other organic dyes adsorption were investigated. Mesoporous synthetic hectorite (MSH) beads which was priorily coated with Na-alginate was contacted with MB and/or MB-other dye binary solution for different time interval from 2h to 15 h. The kinetic evaluation was performed by applying pseudo first- and second- order models, intraparticle diffusion, and Elovich models. MB and dye mixture adsorption fit pseudo-second order kinetic model. The rate of diffusion from external sites into internal sites was searched by using Weber and Morris's kinetic model which determines rate controlling step. As a result, it was mentioned that intraparticle diffusion was note sole rate limiting step for MB and other dye adsorption on MSH [3]. The adsorption of Acid Red G (ARG) onto octadecyl trimethylammonium montmorillonite was inspected by Tong et al. in 2010. They expressed that the fast reaction of ARG occurred in few minutes at all worked temperature. Kinetic investigation of pH dependent adsorption of ARG was performed by using pseudo- first and –second order models, and it was determined that the pseudo-second-order model represented the experimental data better than the pseudo-first-order model [45].

As known, pharmaceutical products are important organic compounds which treated human and animal health. When pharmaceuticals and/or their degradation by products discharged into environment via urine and/or feces they become treat risk [13]. Naproxen is a pharmaceutically active compounds (PhACs) classified as non-steroidal anti-inflammatory drug (NSAID) which shows analgesic, antipruritic and anti inflammatory effect. Degradation of naproxen is quite slow under extreme conditions (pH, high temperature, etc.) [46]. As all non-steroidal anti-inflammatory drugs, naproxen cannot be metabolized and causes serious environmental problems by passing through human body [47]. Recently, naproxen has been detected in engineered and natural aquatic environments, mentioned that it exists in the range of 0.1–2.6 μg/L in wastewater treatment plant effluents [48-50] and 0.01–0.1 μg/L in surface waters [48, 51, 52]. Boyd et al. (2003) explained that coagulation and sedimentation were not effective naproxen removal by drinking water treatment processes, but disinfection and adsorption processes could remove naproxen efficiently. Rafati et al. studied kinetic investigation of naproxen adsorption on β-Cyclodextrine functionalized polymer-clay composite. They explained that the naproxen diffusion from bulk solution towards the surface of composite fits pseudo second order kinetic model, and according to results of Elovich model adsorption occurs on energetic sites of surface [13].

The removal of a Pharmaceutically Active Compound (PhAC) pool using a well referenced clay mineral from Wyoming (SWy-2) as a geosorbent was studied for a better understanding of the environmental fate. Tramadol (a cationic PhAC) and the ibuprofen as well as the gemfibrozil (anionic PhACs), which are representative to those of the studied organic compounds of each family. Cationic PhACs, for which the driving force for their adsorption results from electrostatic interaction via the exchange with the inorganic cations of the clay mineral, are almost completely removed for all studied experimental conditions where it appears that the S/L ratio plays a minor role and the only one limitation for their removal is the cation exchange capacity of the adsorbent. Adsorption fits pseudo second order model, and attained to equilibrium in 15 min. For both neutral and anionic species, where the removal was completed after 15 minutes, a steady state was obtained between 90 and 150 minutes [17]. Diclofenac is a pharmaceutical product used for anti-inflammatory purpose. It uses as potassium salt. The removal of Diclofenac potassium, from aqueous solution was investigated by Mabrouki and Akretche. adsorption kinetics and the mechanism of adsorption of diclofenac potassium onto Na–bentonite and iron-pillared bentonite. The adsorption of diclofenac potassium occurred very quickly from the beginning of the experiments. This situation explained that it might be indicative of chemical adsorption [53]. In another study, adsorptive removal of diclofenac was performed by using micelle (otadecyltrimethylammonium, ODTMA)–clay (monmorillonite) composites having positive charge. It was observed that the fast reaction occured within several minutes which points out high affinity of surface for diclofenac [54].

Phenol and its derivatives are hazardous chemicals which have adverse effect on humans and all organisms. They released into environment as a waste of many industries such as pharmaceutical, petroleum and petrochemical, pesticides, plastic, paper and other manufactures. The existence of phenolic compounds cause unpleasant odours and tastes in drinking water. They are listed as priority pollutants by the United States Environmental Protection Agency (EPA). Park et al. (2013) were inspected p-chlorophenol (PCP) and p-nitrophenol (PNP) adsorption onto adsorbents, obtained by intercalation of montmorillonite with dodecyltrimethylammonium bromide ((DDTMA) and didodecyldimethylammonium bromide (DDDMA). The kinetic study of PCP and PNP adsorption on related intercalated adsorbents showed pseudo-second order kinetic properties. When used DDDMA intercalating adsorbent, the fast reactions of PCP and PNP occur in a shorter time [55]. Nafees and Waseem implied that several kinetic models had been used for the adsorption process but pseudo-first-order and second-order kinetic models were most extensively employed to study the rate kinetics for phenols sorption [56].

As being another type of organic pollutant, denatonium cation is a benzoate salt which is added into poisonous household good to prevent the child or animal to consume. It enters to environment by accidental discharge. Crosson and Sandmann investigated the adsorption kinetic of denatonium on different montmorillonite samples obtained from different regions. pseudo-first order and second order model were applied to search kinetic, and found that the adsorption conformed pseudo-second order model. The equilibrium was achieved in 30 min [57].

Humic acids contain carboxylic and phenolic groups, which give hydrophilic character, and also aliphatic and aromatic groups which give hydrophobic character. Due to these functional groups, humic acids specify physical and chemical properties of soils such as aggregate stability, sorption/desorption transport of organic compounds, complexation, mobilization and bioavailability of heavy metal cations [58]. Because of having higher solubility than humic acids, fulvic acids induce metal mobilization to deeper zones. Despite its lower solubility, humic acid gives stable complexes with metal cations. Thus, it provides controlled mobilization of metal ions and keeps them in shallow zones. Beside all these properties, humic substance helps the uptake of micronutritients by plant [59]. Avena and Koopal studied the kinetics of HA adsorption and desorption on an iron oxide surface. They declared that most of the equilibrium was achieved in first 100 s, then slower processes followed. Completion to equilibrium occured in many hours. The authors mentioned that the first slow step could be attributed to electrostatic repulsion and/or rearrangements in the adsorbed layer by conformation changes or by exchange of adsorbed HA molecules [60]. In follow-up study, they searched the initial adsorption kinetics of humic acids on solid surfaces depending the salt concentration. They explained that the rate of transport and attachment on the surface is decisive for the initial rate of adsorption. As a result of this investigation they are reported that carboxylic and phenolic groups of humic acid have capable of to interact the surface hydroxyl groups, and that the attachment with the surface hydroxyl groups of Fe and Al oxide surfaces is a quick process. If sur face has hydrophobic character the attachment onto surface is relatively slow due to hydrophobic groups of HA cannot interact in aqueous solution [61].

Geothite–humic acid (GHA)-modified kaolinite adsorbent was used for the adsorption of Pb^{2+}, Cd^{2+}, Zn^{2+}, Ni^{2+}, and Cu^{2+} from Single and quinary metal ion systems. When the kaolinite surface was coated with geothite-humic acid mixture, the CEC of adsorbent enhanced five times comparing the raw kaolinite. Brouers– Weron–Sotolongo (BWS) kinetic model gave better fit to kinetic data, which indicated that adsorption of metal ions onto GHA-modified adsorbent has diffusion-controlled mechanism [62].

Bovine Serum Albumine (BSA) adsorption on montmorillonite was performed under environmentally relevant condition by Schmidt and Martinez. Adsorption of proteins onto layered clay is influenced by pH, surface and protein species, ionic strength and species of interlayer cations. In their study, kinetic evaluation was performed by considering surface coverage of BSA. pseudo- first order, pseudo- second order, intraparticle diffusion, and Elovich model were used to investigate kinetic of adsorption, and it was determined that the adsorption kinetic fitted Elovich model which expressed that decisive mechanism on adsorption rate is surface related heterogeneous energetics limitations and lateral adsorbate interactions. Montmorillonite has two distinc surface in the edge and planar siloxane, which may be responsible for the energetic heterogeneity of BSA adsorption. On the other hand, lateral interactions and continuous rearragment between adsorbed protein molecules, and electrostatic forces have been attributed to energetic heterogeneity, Consequently, it can be said that the reaction rate is controlled by heterogeneous energetic barriers [63].

Many samples for mostly used kinetics models valid for heavy metal and organic matter adsorption onto clays were summarized in Table 1.

Table 1. *The mostly used kinetic models for the adsorption of different types of pollutant onto modified or non-modified clays and clay minerals*

Adsorbent	Adsorbate	Kinetic Model	k * (rate constant)	Ref.
Bentonite	Cd(II)	p-second order model	2.01	[64]
Modified Kaolinite	Bromophenol blue	p-first order model	0.230	[65]
Illitic Clay	Cd(II)	p-second order model	0.045	[66]
Hectorite Clay	Ni(II)	p-second order model	0.0137	[67]
Palygorskite Clay	Ni(II)	p-first order model	0.11	[68]
Bentonite	Ni(II)	p-second order model	1.414	[60]
Humic Acid Immobilized Bentonite	Malachite G. Methylene B. Crystal V.	p-second order model	483 483 -433	[70]
TBA-Kaolinite TBA-Montmorillonite	Ni(II)	p-second order model	0.013 0.025	[71]
Smectite Clay	Co(II)	p-second order model	7.07	[72]
Bentonite/Zeolite Mixture	Co(II)	p-second order model	0.0124	[73]
Organo- Bentonite	Cu(II)	p-second order model	1.29	[74]
Ca-Bentonite	Congo Red	p-second order model	0.003	[75]
Pottery Glaze	Cu(II)	p-second order model	70.67	[76]

Functionalised Bentonite	Cu(II)	p-second order model	0.012 (mmol^{-1}min^{-1})	[77]
Alginate/Mauritanian Clay Composite	Cu(II)	p-second order model	0.116	[78]
Montmorillonite	Cu(II)	p-second order model	0.077	[79]
Cr(III)-İntercalated Montmorillonite	Supranol Yellow 4 GL	p-second order model	0.032	[80]
Chitosan-G-Polyacrylic Acid/ Montmorillonite Nanocomposite	Methylene Blue	p-second order model	3.9×10^{-4}	[81]
Beidellite	Pb(II)	p-second order model	0.105	[82]
Clinoptilolite	Pb(II)	p-first order model	0.005	[83]
Clay–PMEA Composite	Pb(II)	p-second order model	0.029	[84]
Perlite	Hg(II)	p-second order model	0.458	[85]
Amine Functionalised Bentonite	Hg(II)	p-second order model	0.010	[77]
Carboxylate Func. Bentonite	Hg(II)	p-second order model	0.011	[77]
Gray Clay	Zn(II)	p-second order model	1.13	[30]
Natural Bofe Clay	Zn(II)	p-second order model	0.15	[86]
Calcined Bofe Clay	Zn(II)	p-second order model	0.21	[86]
Diatomite-Perlite Composite	Mn(II)	p-second order model	0.023	[87]
Bikougou Clay	Mn(II)	p-second order model	6.02	[88]
Metakaolin Based Geopolymer	Mn(II)	p-second order model	0.033	[89]
Nigerian Kaolinite Clay	Mn(II)	elovich model	0.647	[90]
Spent Activated Clay	Cr(VI)	p-first order model	0.178	[91]
Cellulose-Montmorillonite	Cr(VI)	second order model	0.28	[92]
Fe^{2+} - Modified Vermiculite	Cr(VI)	p-second order model	0.11	[93]

Clay Mineral	Naphthalene	p-second order model	$7x10^{-4}$	[94]
Acid Activated Bentonite Unactivated Bentonite	Naphthalene	p-second order model	0.13 1.30	[95]
Rutile	Eu(III)	p-second order model	5342 ($gmmol^{-1}h^{-1}$) 73341 ($gmmol^{-1}h^{-1}$)	[96]

***: The unit of rate constants are min^{-1} and g $mg^{-1}min^{-1}$ for p-first order model and p-second order models, respectively.**

CONCLUSION

Consequently, as being an environmentally friend method, adsorption process is preferred, furthermore, it readily occurs in nature. Especially, natural clays and clay minerals have high affinity to pollutants both heavy metals and organic matters. This type of adsorption is fast process, and the equilibrium is attained in few minutes. This kinetic property is decisive for the fortune (solubility or mobilization in surface water, ground water or soil) of pollutant in environment.

Conflict of interest The authors declare that they have no conflict of interest.

REFERENCES

Bentahar S, Dbik A, El Khomri M, El Messaoudi N, Lacherai A. Journal of Environmental Chemical Engineering, 2017, 5: 5921–5932.

Yin J, Deng C, Yu Z, Wang X, Xu G. Water,2018, 10:210-222.

Pawar RR, Lalhmunsiama GPL, Sawant SY, Shahmoradi B, Lee SM. Int J Biol Macromol., 2018, 14:1315-1324.

Kausar A, Iqbal M, Javed A, Aftab K, Nazli ZH, Bhatti HN, Nouren S. Journal of Molecular Liquids, 2018, 256: 395-407.

Hızal J, Apak R. J. Colloid and Interface Science, 2006, 295: 1-13.

Abdel Karim AM, Zaki AA, Elwan W, El-Naggar MR, Gouda MM. Applied Clay Sci., 2016, 133: 391-401.

Leroy P, Revil A. Journal of Colloid and Interface Science, 2004, 270: 371–380.

Erçağ A, Demirçivi P, Hizal J. Desalination and Water Treatment, 2015, 56 (9): 2447-2456.

Eren E. J. Hazardous Materials, 2009, 166: 88-93.

Hızal J, Demirçivi P, Karadirek Ş, Apak R. Desalination and Water Treatment, 2016, 57: 22441-22453.

Hizal J. Modeling of Heavy Metal Adsorption onto Clay Minerals [dissertation]. Reşat Apak: Istanbul University; 2001.

Hızal J, Apak R. Applied Clay Science, 2006, 32: 232-244.

Rafati L, Ehrampoush MH, Rafati AA, Mokhtari M, Mahvi AH. Journal of Molecular Liquids, 2016, 224: 832-841.

Walker WJ, Kronan CS, Patterson HH. Geochimica et Cosmochimica Acta, 1988, 52: 55-62.

Sivakumar P, Palanisamy N. Advances in Applied Science Research, 2010, 1: 58-65.

Gouamid M, Ouahrani MR, Bensaci MB. Energy Procedia, 2013, 36: 898-907.

Thiebault T, Boussafir M, Le Forestier L, Le Milbeau C, Monnin L, Guegan R. RSC Adv., 2016, 6: 65257- 65265.

Kuo CY, Wu CH, Wu JY. J. Colloid and Interface Sci., 2008, 327: 308-315.

Aharoni C, Sideman S, Hoffer E. J. Chem. Tech. Biotechnol., 1979, 29: 404-412.

Ogwada RA, Spark DL. Soil Sci. Soc. Am. J., 1986, 50: 1158-1162.

Celis R, Hermosian MC, Cornejo J. 2000, Environ. Sci. Technol., 2010, 34: 4593-4599.

Saha P, Chowdhury S., Insight Into Adsorption Thermodynamics, 2011, Mizutani Tadashi (Ed.), ISBN: 978-953-307-544-0, InTech, pp. 349-364.

Jaishankar M, Tseten T, Anbalagan N, Mathew BB, Beeregowda KN. Interdiscip Toxicol., 2014, 7(2): 60–72.

The European Union (EU) End of Life Vehicles (ELV), Directive 2000/53/EC.

The European Union (EU) Restriction of the use of certain Hazardous Substances(RoHS), Directive 2002/95/EC.

Al-Degs YS, Tutunji MF, Baker HM. ClayMinerals, 2003, 38: 501–509.

Khalfa I, Bagane M, Cervera ML, Najjar S. World Academy of Sci. and Technol. Int. J. Chem and Molecular Engineering, 2016, 10: 586-589.

Sharifipour F, Hojati S, Landi A, Faz Cano A. Int. J. Environ. Res., 2015, 9: 1001-1010.

Meneguin JG, Moises MP, Karchiyappan T, Faria SHB, Gimenes ML, de Barros MASD, Venkatachalam S. Process Safety and Environmental Protection, 2017, 111: 244-252.

Vasconcelos P.N.M., Lima W.S., Silva M.L.P., Brito A.L.F., Laborde H.M., Rodrigues M.G. F., American Journal of Analytical Chemistry, 2013, 4:510-519.

Veli S., Alyüz B. J Hazardous Materials, 2007, 149: 226–233.

Hızal J., Apak R. Fresenius Environmental Bulletin, 2013, 22: 764-769.

Rao R.A.K., Kashifuddin M. Arabian Journal of Chemistry, 2016, 9: 1233-1241.

El Ass K. Global NEST Journal, 2018, 20(2): 198-207.

Pour PG, Takassi MA, Hamoule T. Oriental J. Chem., 2014, 30: 1365-1369.

Chai W, Huang Y, Han G, Liu J, Yang S, Cao Y. Mineral Processing and Extractive Metallurgy Review, 2017, 38: 106-115.

Siroux B, Beaucaire C, Tabarant M, Benedetti MF, Reiller PE. Applied Geochemistry, 2017, 87: 167–175.

Kafkafi U., Xu G., Imas P., Magen H., Tarchitzky J., Potassium and chloride in crops and soils: the role of potassium chloride fertilizer in crop nutrition, IPI Research Topics No. 22 , 2001.

Amouzadeh A., Landi A., Hojati S., Majallah-i āb va Khāk, 2017, 30:782-795.

Alshameri A, Hongping H, Jianxi Z, Yunfei X, Runliang Z, Lingya M, Qi T. Applied Clay Sci., 2018, 159: 83-93.

Cherian C, Kollanur NJ, Bandipally S, Arnepalli DN. Applied Clay Science, 2018, 160: 282-289.

Apak R, Hızal J, Ustaer C. J. Colloid and Interface Science, 1999, 211: 185-192.

Kyzas GZ, Lazaridis NK. J. Colloid and Interface Sci., 2009, 331: 32-39.

Shakir K, Elkafrawy AF, Ghoneimy HF, Beheir SGE, Refaat M. Water Research, 2010, 44: 1449-1461.

Tong DS, Zhou CH, Lu Y, Yu HY, Zhang GF, Yu WH. Appl. Clay Sci., 2010, 50: 427–443.

Quintana JB1, Weiss S, Reemtsma T., Water Res., 2005, 39(12):2654-64.

Li X.. He Q., Li H., Gao X., Hu M., Li S., Zhai Q., Jiang Y., Wang X., Biochemical Engineering Journal, 2017: 120:7-16.

Stumpf, M., Ternes, T.A., Wilken, R.-D., Rodrigues, S.V., Baumann, W., Brazil. Sci. Total Environ., 1999, 225:135–141.

Tixier, C., Singer, H.P., Oellers, S., Muller, S.R., Environ. Sci. Technol., 2003, 37:1061–1068.

Metcalfe, C.D., Koenig, B.G., Bennie, D.T., Servos, M., Ternes, T.A., Hirsch, R., Environ. Toxicol. Chem., 2003, 22 (12):2872–2880.

Boyd G. R., Zhang S., Grimm A., Water Research, 2005, 39:668–676.

Boyd, G.R., Palmeri, J.M., Zhang, S., Grimm, D.A., Sci. Total Environ. 2004, 333:137–148.

Mabrouki H, Akretche DE. Desalination and Water Treatment, 2016, 57: 6033-6043.

Karaman R, Khamis M, Quried M, Halabieh R, Makharzeh I, Manassra A, Abbadi J, Qtait A, Bufo SA, Nasser A, Nir S. Environmental Technology, 2012, 33: 1279-1287.

Park Y, Ayoko GA, Kurdi R, Horváth E, Kristóf J, Frost RL. J. Colloid & Interface Sci., 2013, 406: 196–208.

Nafees M, Waseem A. CLEAN-Soil, Air, Water, 2014, 42: 1500-1508.

Crosson GS, Sandmann E. Environ. Eng. Sci., 2013, 30: 311-316.

Demirçivi P, Karadirek Ş, Anilanmert B, Tutar A, Hızal J, Apak R. Fresenius Environmental Bulletin, 2015, 24: 4743-4750.

Dhanapal S, Sekar DS, Manasa P. International Journal of Agriculture Innovations and Research, 2014, 2: 429-435.

Avena MJ, Koopal LK. Environ. Sci. Technol., 1998, 32: 2572-2577.

Avena MJ, Koopal LK. Environ. Sci. Technol., 1999, 33: 2739-2744.

Unuabonah EI, Olu-Owolabi BI, Adebowale KO. Int. J. Environ. Sci. Technol., 2016, 13: 1043–1054.

Schmidt MP, Martinez CE. Langmuir, 2016, 32: 7719–7729.

Dal Bosco SM, Jimenez RS, Vignado C, Fontana J, Geraldo B, Figueiredo FCA, Mandelli D, Carvalho WA. Adsorption, 2006, 12:133–146.

El-Zahhar AA, Awwad NS, El-Katori EE. Journal of Molecular Liquids, 2014, 199: 454-461.

Ozdes D, Duran C, Senturk HB. Journal of Environmental Management, 2011, 92: 3082-3090.

Ramamurthi V, Priya PG, Saranya S, Basha CA. Modern Applied Science, 2009, 3(9): 37-51.

Potgieter JH, Potgieter-Vermaak SS, Kalibantonga PD. Minerals Engineering, 2006, 19: 463–470.

Sathyanarayana B, Seshaiah K. E-Journal of Chemistry, 2011, 8(1): 373-385.

Anirudhan TS, Suchithra PS, Radhakrishnan PG. Applied Clay Science, 2009, 43: 336–342.

Bhattacharyya KG, Gupta SS. Applied Clay Science, 2009, 46: 216–221.

Guerra DL, Airoldi C. Journal of Solid State Chemistry, 2008, 181: 2507– 2515.

Al Dwairi RA, Al-Rawajfeh AE. Journal of the University of Chemical Technology and Metallurgy, 2012, 47(1): 69-76.

Maramis V, Kurniawan A, Ayucitra A, Sunarso J, Ismadji S. Front. Chem. Sci. Eng., 2012, 6(1): 58–66.

Lian L, Guo L, Guo C. Journal of Hazardous Materials, 2009, 161: 126–131.

Rao RAK, Kashifuddin M. Chin. J. Geochem., 2012, 31:136–146.

Anirudhan TS, Jalajamon S, Sreekumari SS. Applied Clay Science, 2012, 65–66: 67–71.

Elya A, Baudu M, Kankou M, Basly JP. Chemical Engineering Journal, 2011, 178: 168– 174.

Sdiri A, Higashi T, Hatta T, Jamoussi F, Tase N. Chemical Engineering Journal, 2011, 172: 37– 46.

Bouberka Z, Khenifi A, Benderdouche N, Derriche Z. Journal of Hazardous Materials, 2006, B133: 154–161.

Wanga L, Zhang J, Wang A. Colloids and Surfaces A: Physicochem. Eng. Aspects, 2008, 322: 47–53.

Etci O, Bektas N¸ Oncel MS. Environ. Earth Sci., ,2010, 61:231–240.

Sprynskyy M, Buszewski B, Terzyk AP, Namiesnik J. Journal of Colloid and Interface Science, 2006, 304: 21–28.

Sölener M, Tunali S, Özcan AS, Özcan A, Gedikbey T. Desalination, 2008, 223: 308–322.

Ghassabzadeh H, Mohadespour A, Mostaedi MT, Zaheri P, Maragheh MG, Taheri H. Journal of Hazardous Materials, 2010, 177: 950–955.

de Araujo ALP, Gimenes ML, de Barros MASD, da Silva MGC. Materials Research, 2013, 16(1): 128-136.

Shabani KS, Ardejani FD, Badii K, Olya ME. Arabian Journal of Chemistry, 2013.

Eba F, Gueu S, Mvongbote AEA, Ondo JA, Yao BK, Nlo JN, Biboutou RK. International Journal of Engineering Science and Technology, 2010, 2(10): 5001-5016.

Kara I, Tunc D, Sayin F, Akar ST. Applied Clay Science, 2018, 161: 184–193.

Dawodu FA, Akpomie KG. Journal of Materials Reserach and Tech., 2014, 3(2):129–141.

Weng CH, Sharma YC, Chu SH. Journal of Hazardous Materials, 2008, 155: 65–75.

Kumar ASK, Kalidhasan S, Rajesh V, Rajesh N. Ind. Eng. Chem. Res., 2012, 51: 58–69.

Liu Y, Li H, Tan GQ, Zhu X. Separation Science and Technology, 2011, 46: 290–299.

Osagie E.I., Owabor C.N., Advances in Chemical Engineering and Science, 2015, 5:345-351.

Obi C, Okoye IP, J., Appl. Sci. Environ. Manage. 2014, 18 (1): 143-149.

Xue Feng W., Ke Liang SHI, Zhi Jun GUO, Wang Suo WU. Sci. China Chem., 2010, 53: 2628–2636.

DISPLAY EFFECT ON FLAME ZONE AND CONTOURS OF TEMPERATURE, CO_2, CO AND SO_2 EMISSIONS IN DIFFERENT BIOGAS CONTENT

CHAPTER

8

Murat ŞAHİN[1]
Emre AYTAV[2]
Burak ÇANAKÇI[3]

1 National Defence University, Military Academy, Department of Mechanical Engineering, Ankara-Turkey. msahin@kho.edu.tr
2 National Defence University, Military Academy, Department of Mechanical Engineering, Ankara-Turkey. eaytav@kho.edu.tr
3 National Defence University, Military Academy, Department of Mechanical Engineering, Ankara-Turkey
bcanakci@kho.edu.tr

1. INTRODUCTION

The studies in the field of renewable energy and environmental technologies are increasing day by day and gaining importance. Biogas plants, despite the sharp rise in the world, it has not yet reached the importance and the number that had to accompany it in Turkey. When Turkey began to be used until the potential of biogas systems, it is expected to have an effect in reducing the gas imports. Research on the use of biogas as a fuel in systems such as cogeneration, trigeneration and micro gas turbines [Somehsaraei et al., 2019]. Therefore, scientists, industrialists and NGO representatives have begun to work on the use of biogas as an alterative to natural gas. Turkey, especially in the alternative energy source made in the field of engineering research and development (R & D) of the number and quality of work is important to increase [Aytaç et al., 2019]. Examining research on the potential of renewable energy sources in Turkey, have been studied for technological roadmap. It can be said that reducing energy imports by using renewable energy sources will increase the Gross National Product [Aytaç et al., 2019]. The full factorial experimental design method developed for the use of wind energy in renewable energy sources can be used in biogas systems. [Çanakçı et al., 2019]. This study is displayed contours of characteristics of the combustion. The main properties of the biogas are showed in the Table 1.

Table 1. *The main properties of the biogas.*

	Biogas (Volume %)
CH_4	55
CO_2	43,1
N_2	1,53
H_2S	200 ppm
O_2	0,3

2. MODELLING

3D CFD modelling has been performed by using contours on combustion characteristics of the different biogas content in the present study. Hydraulic diameters of fuel and air inlets are 6 mm and 32 mm. Also, hydraulic diameter of the combustor outlet is 110 mm. Fuel and air inlet temperatures, combustion gauge pressures are also fixed at 283 K and 21 mbar, respectively. The combustor outlet is open to atmosphere[Mustafa et al., 2018].

3. RESULTS AND DISCUSSION

In this study, It was observed that the changes in the content of biogas fuel caused changes in the distribution of the emission values and temperatures obtained in the combustion chamber. Distributed combustion studies show it has made on the effect on the pollutant emissions of NO_X and CO is reduced to almost zero emissions, the CO_2 emission levels in the distributed combustion conditions, it was concluded that increased a little at the burner exit[Serhat, 2018]. Countours of temperature, CO_2, CO and SO_2 emissions are demonstrated in the Figure 1, Figure 2, Figure 3 and Figure 4. In this study, the distribution of temperature and emissions occuring in the combustion champer in different biogas content is shown. Flame zone temperature obtained as a result of combustion according to changing biogas contents was investigated. The length and width of the flame zone decreases as the H_2O content increases. The homogeneous or heterogeneous distributions within the combustion chamber of the emissions and temperature caused by combustion are visually expressed. Investigations have been performed by using a CFD code. PDF/Mixture Fraction combustion and k-Ɛ standard turbulence models were used during predictions. Findings show that changes in biogas content highly affect the temperature and emission counters of the combustor. In addition to these findings, it can be said that the CO_2 distribution is more homogeneous as the amount of H_2O content in the biogas fuel in the combustion chamber decreases.

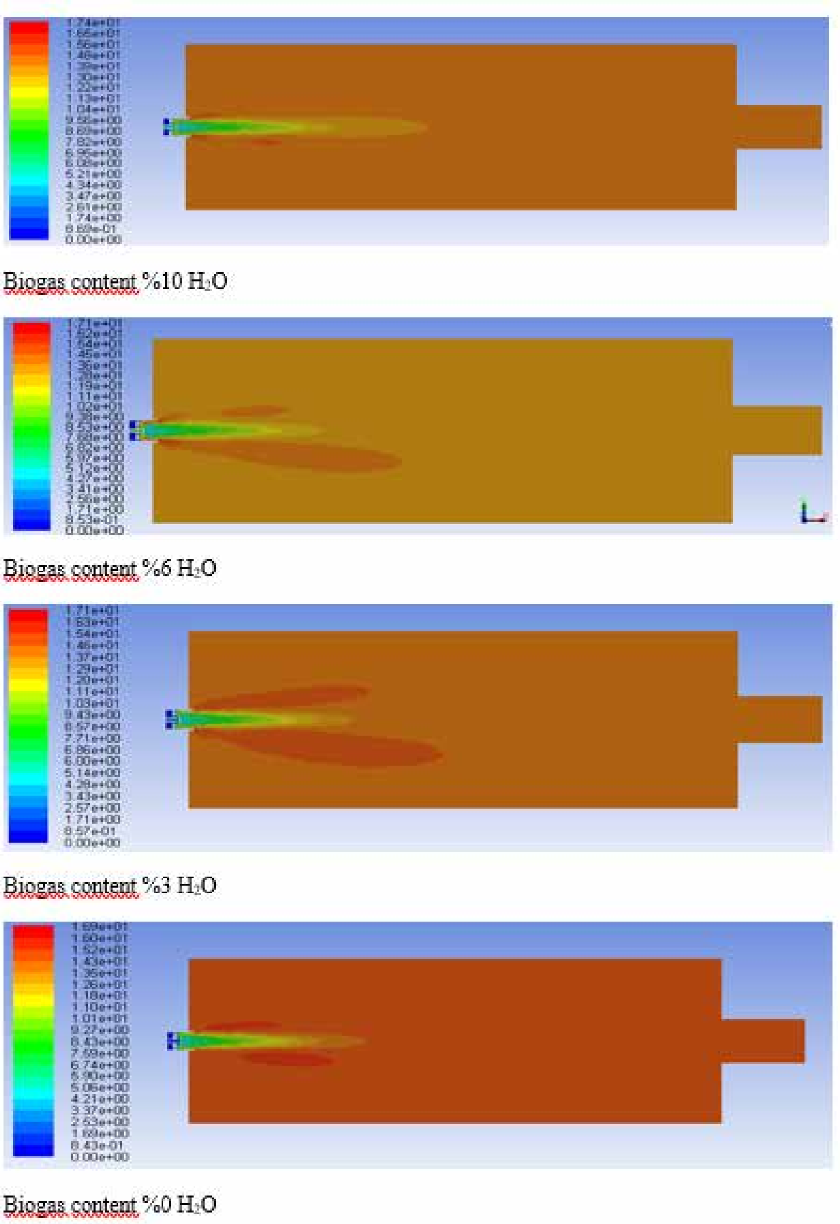

Figure 1. *Display contours of the temperature distributions of different biogas content H_2O*

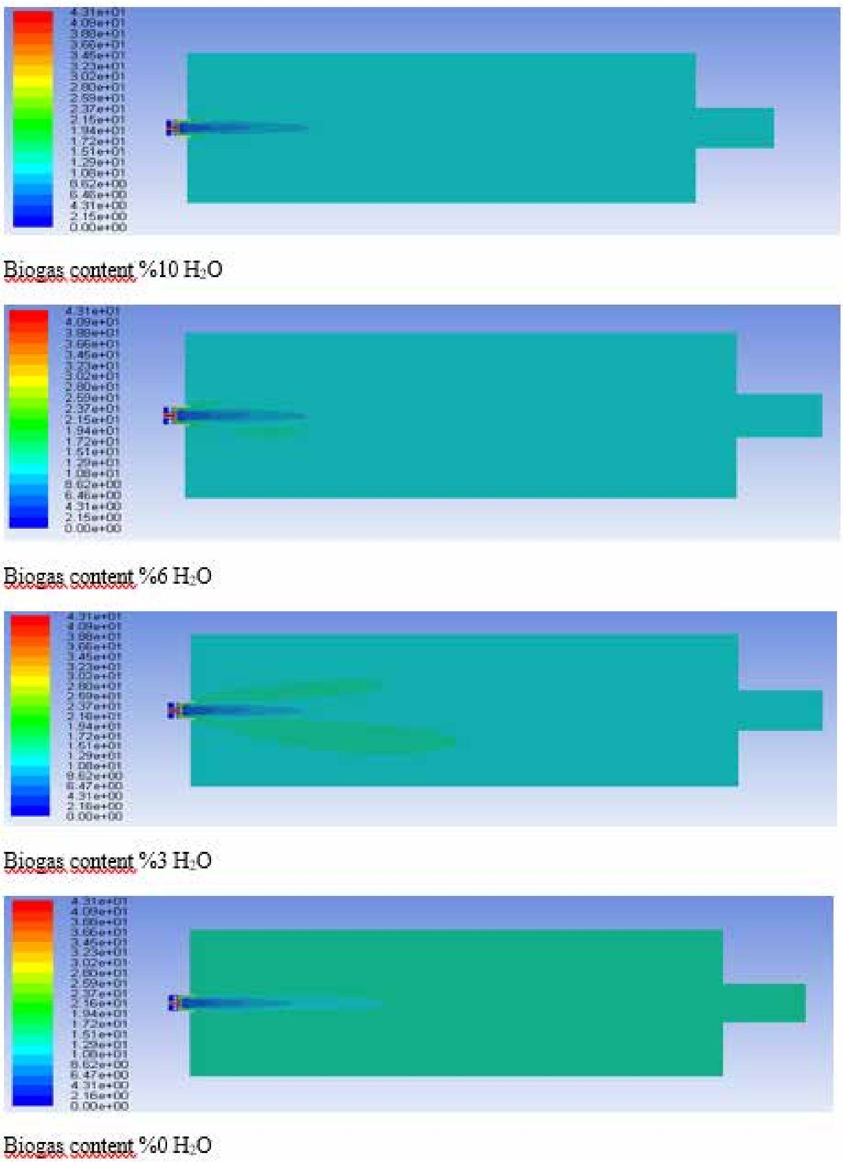

Figure 2. *Display contours of the CO_2 distributions of different biogas content H_2O*

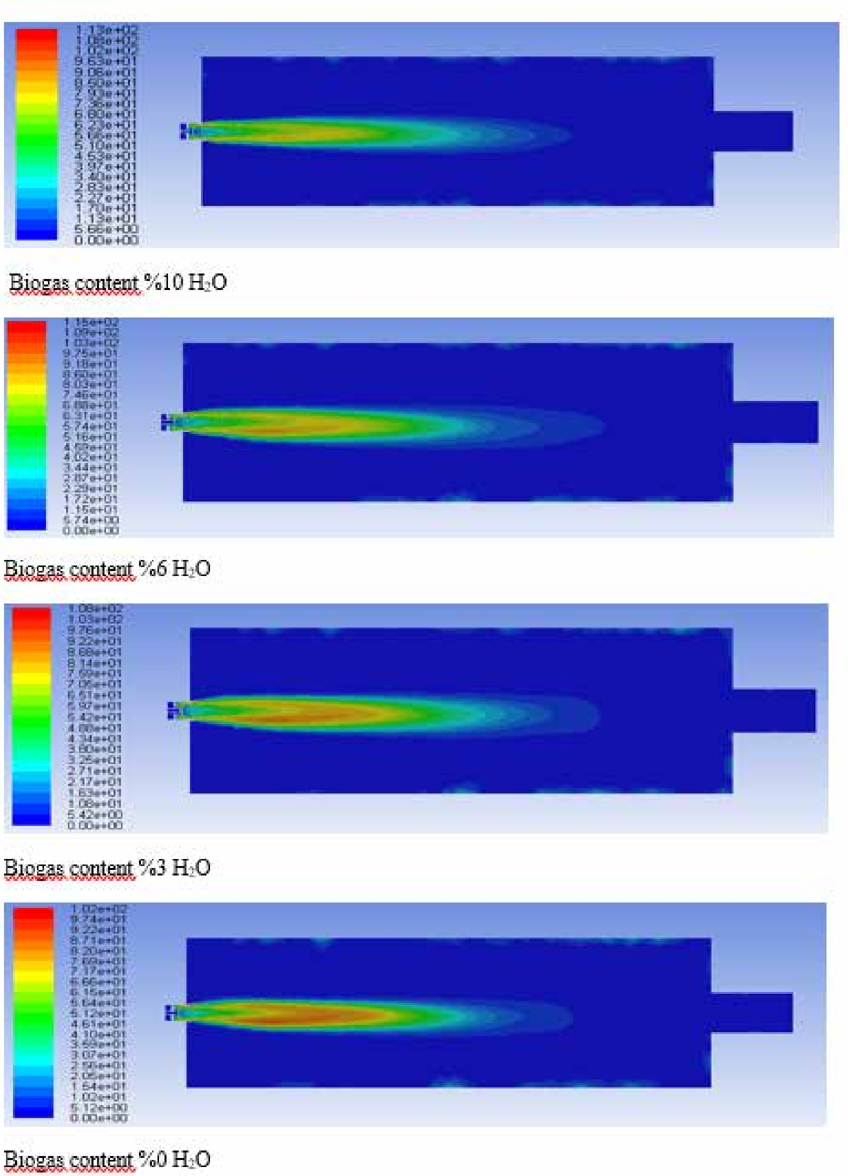

Figure 3. Display contours of the SO_2 (ppm) distributions of different biogas content H_2O

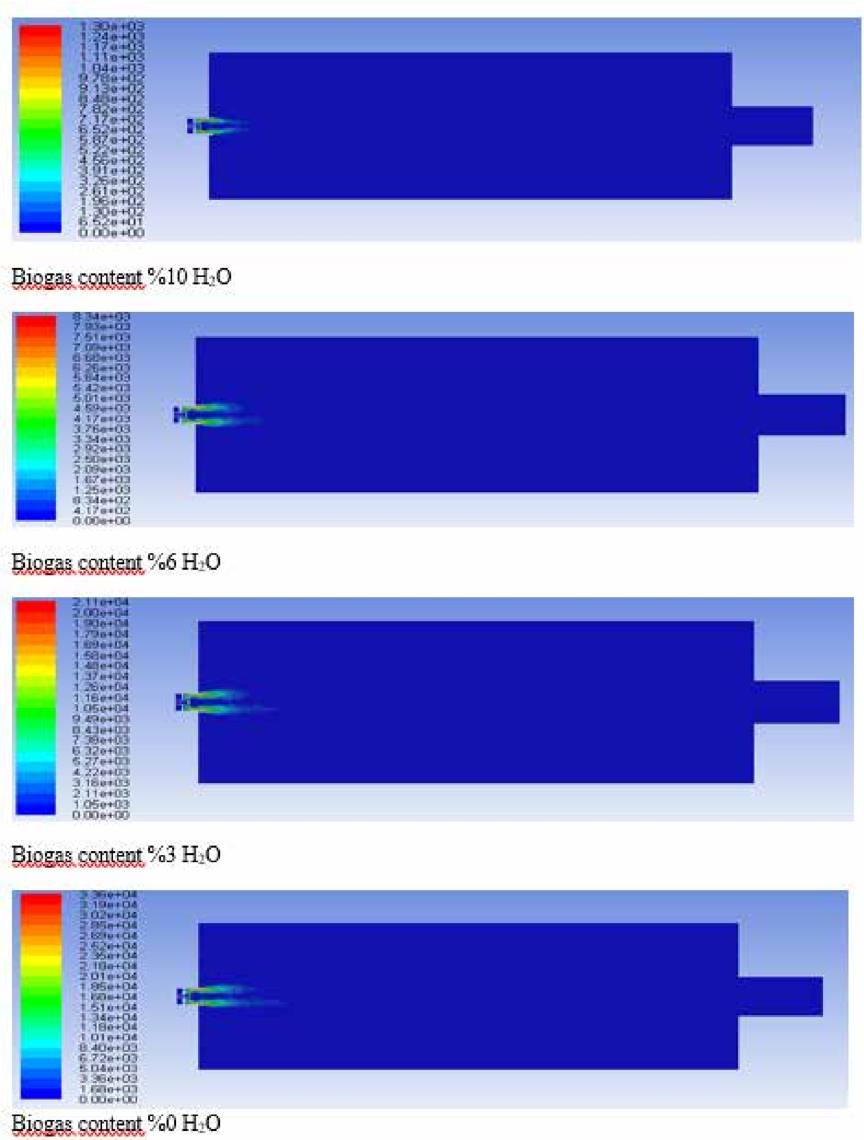

Figure 4. *Display contours of the CO (ppm) distributions of different biogas content H_2O*

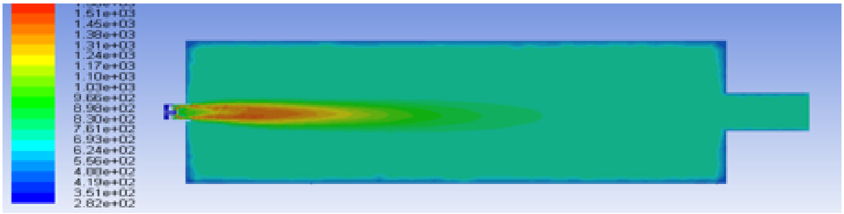

Temperature distributions of %79 N and %21 O_2 in air

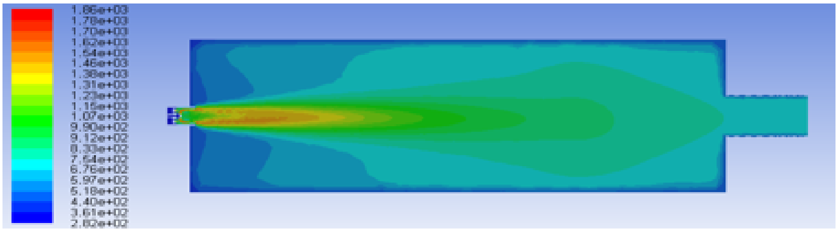

Temperature distributions of %50 N and %50 O_2 in air

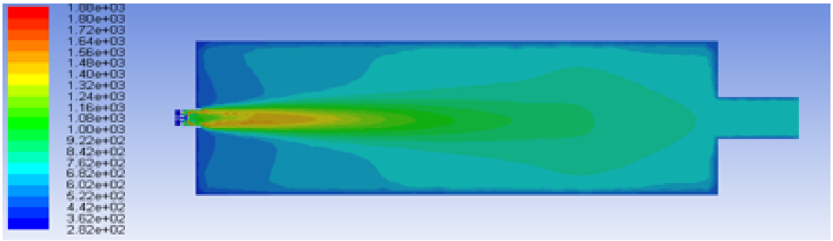

Temperature distributions of %21 N and %79 O_2 in air

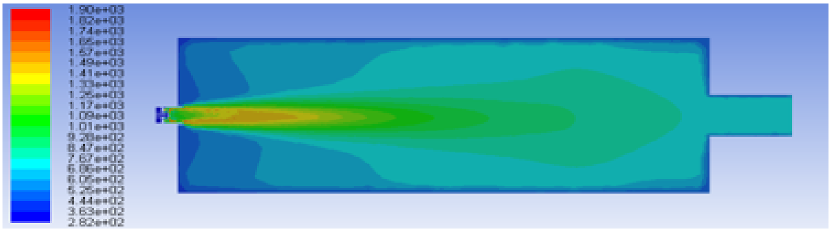

Temperature distributions of %21 N and %79 O_2 in air

Figure 5. *Display contours of the vary N and O_2 in air*

4. CONCLUSIONS

A numerical study has been performed in order to demonstrate contours behaviours of the biogas. The author has obtained the following conclusions from the predictions:

- The length and width of the flame zone decreases as the H_2O content increases.
- CO_2 distribution is more homogeneous in the combustor as the amount of H_2O content in the biogas fuel in the combustion chamber decreases.
- As the H_2O content decreases, both higher and more homogeneous distribution is obtained in the combustion chamber content of flame temperature zone.
- It can be said that as the amount of N content in the air increases, the flame zone distribution in the combustion chamber provides more homogeneous distribution.

Acknowledgements

Thanks to National Defense University and Gazi University for the support in this study.

REFERENCES

Somehsaraei H.N, Majoumerda M.M., Breuhausb P., Assadia M., “Performance analysis of a biogas-fueled micro gas turbine using a validated thermodynamic model”, Applied Thermal Engineering, 66, 181-190, 2014.

Aytaç A., Ilivan M. İ, Scientific Studies in the Area of Mechanical Engineering: A Descriptive Analysis Related to Researches in Turkey. American Journal of Engineering Research, 7(12), 87-96, (2018).

Aytaç A., Aksu S.B., Aytav E., Aztekin K. (2019). Turkey’s Renewable Energy Sources and Policies, International Symposium on Multidisciplinary Academic Studies. (78-80) (IMASES 2019).

Çanakçi, B., Çakir, U., Aytaç, A., Özdemir, T., Aztekin, K., Işik, M. S. (2018). Determination of Parameters Affecting Aerodynamic Performance in S833 Airfoil. Presented at the International Congress on New Trends in Science, Engineering and Technology (ICONTRENDS 2018), (29–41), 2018, Rome, Italy.

Ilbas M., Sahin M., Karyeyen S., 3D Numerical Modelling of Turbulent Biogas Combustion in a Newly Generated 10 KW burner, J. Energy Institute, (91-1), (87-99) February 2018.

Karyeyen S., Combustion Characteristics of a Non-Premixed Methane Flame in a Generated Burner Under Distributed Combustion Conditions: A numerical study, Fuel, (230) (163-171) 15 October 2018.

INVESTIGATION OF FLEXIBLE ARMOR PRODUCTION MATERIALS USED FOR BALLISTIC PROTECTION AND EVALUATION OF MATERIALS IN TERMS OF BALLISTIC PROTECTION TEST AND STANDARDS

CHAPTER

9

Ayhan AYTAÇ[1]
Şükrü Burak KAHRAMAN[2]
Muhammed İLİVAN[3]
Murat ŞAHİN[4]

1 Ayhan Aytaç, National Defence University, Military Academy, Department of Mechanical Engineering, Ankara-Turkey. aytac@kho.edu.tr , aaytac2001@gmail.com

2 Şükrü Burak Kahraman, National Defense University, Alparslan Defence Sciences Instutute, Ankara-Turkey. burak3024@gmail.com

3 Muhammed İlivan, Dumlupınar University, Pazarlar Vocational School, Kutahya, Turkey milivan@dpu.edu.tr

4 Murat Şahin, National Defence University, Military Academy, Department of Mechanical Engineering, Ankara-Turkey. msahin@kho.edu.tr

I1. INTRODUCTION

Throughout the world war history, as weapons diversified, armor materials improved itself and became a defense weapon among the war materials. The materials and types of armor has been shaped according to the effect of the weapons used in each historical period. In today's technology both weapons and armor are still developing.

The armor, used for defensive purposes, has been used according to the weapon used by the enemy, throughout the history. Depending on the advancement of technology and geographic location, new materials or material compositions have emerged in each histrocial period (Aytaç, Yavuz, et al., 2018). The material to be used in vehicles, equipment and especially armor should be selected appropriately and have the necessary mechanical properties (Işık et al., 2018).

The fabric, which is made of coconut fiber string and used by the people of Gilbert, was able to break the impact of the slingshot, the most important offensive weapon on the entire island, while not stopping a steel pike tip. The elder Celts brought a new sense of armor by intertwining the ring and chains. This armor, which was more flexible than most armor, significantly prevented attacks with the sword and dagger. However, it could not protect the warrior against a very sharp-edged sword. Bronze was used by the ancient Greeks because, it could be easily melted and broken into large pieces. Arabs, Persians, Hindus added metal plates to armor. Thus, armors were weighted to strengthen, with the strengthening of weapons. In the First World War, the Germans equipped their soldiers, with a special armor and a helmet that is made of steel armor and protects the entire head except for the eyes, for the use of machine gunners and some snipers (Ford and Grant, 2016; Weir, 2005). Armor steels are actively used in armored vehicles because of their good mechanical properties such as hardness and protection against explosives, as well as ease of joining by welding (Aytaç, Işık, et al., 2018; Özdemir et al., 2018). In 1916, French General Adrian provided a lightweight and easy to wear armor protecting abdomen for the French army. This armor was formed by twisting a metal plate so that it was bent to fit the abdomen. Hip and groin shieldings were fitted with armor (Dean, 1920). In the Korean War, a nylon-armored vest was provided, which could stop the bullet from a 45-caliber pistol. This armor was also used in the Vietnam War (Çifci, 2011). The combat soldier of the Iraq War used a Kevlar® helmet and armored vest, made of a synthetic material that was lighter and more durable than steel. Kevlar® vests, called "soft armor", consisted of fragments called "hard armor", made of metal, ceramic or plastic plates. This vest was preventing the rifle bullet from penetrating. The most widely used type of new armor stopped the 7.62x39 caliber AK-47 bullet (Ford and Grant, 2016; Weir, 2005).

To be successful in a war, maneuverability of vehicles is just as important as its power. Therefore, one of the important details is how much armor restricts its mobility (Aytaç et al., 2019). The level of protection required for survivability is limited by the need for power, speed and maneuverability in harsh terrain. In order to provide the most effective protection level, newly developed impact resistance ballistic fabrics such as high strength Zylon®, Kevlar®, Spectra® are used. These materials have high strength, fracture toughness, fatigue strength and ballistic properties (Işık et al., 2013; Yavuz et al., 2018).

2. ARMOR PRODUCTION MATERIALS USED FOR BALLISTIC PROTECTION

2.1. Plates

In the design of armor used for ballistic protection, heavy metals are used, such as ceramic armor plates, alumina ballistic armor plates, silicon carbide armor plates, boron carbide armor plates. In this study, fibers and polymers with high resistance properties were examined, not metal plates.

2.2. Fibers and Fabrics

Aramid polyamides such as Kevlar®, Twaron® and high density polyethylene fibers such as Spectra® and Dyneema® are the main materials used in ballistic protection. However, the usability of Vectran fibers, PBO fibers, carbon nanotubes and spider silk fibers in ballistic protection is among the current research topics. In composite panels; carbon, glass and ceramic fibers are used and polyamide, polyester and polypropylene fibers are used as components of composite panels (Çerkez and Ulcay, 2007).

Great improvement has been achieved in high strength fabric armor systems with the production of high strength fibers. As materials capable of absorbing impact energy, fabrics and flexible fiber reinforced composites are widely used in bulletproof vests and other body armors (Çay et al., 2007).

It is possible to divide the fabrics used in ballistic field into knitted and woven fabrics. Although knitted fabrics have superior properties than woven fabrics, woven fabrics are generally preferred in military areas due to their complex production methods and costs.

The most common types of woven fabrics are plain and basket weaving. Basket weaving provides 10% more energy absorption than plain weaving due to its woven characteristics. Fabrics produced with different types of knitting and weaving are shown in Figure 1 (Sozen et al., 2016).

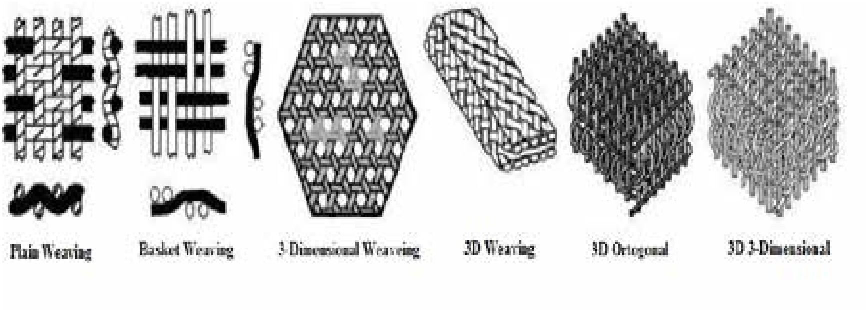

Figure 1: *Woven types used in fabrics exhibiting high resistance properties*

2.2.1. Aramid Fibers

The US Federal Trade Commission defines aramid fibers, an abbreviation of aromatic polyamide, as fibers in which at least 85% of the amide (–CO – NH–) bonds in the chain are directly connected to two aromatic rings. The chemical structures of aramides appear as rigid bars. Due to this structure, the glazing temperatures are very high and their solubility is very low. Therefore, it is necessary to form liquid crystalline polymer solutions other than conventional methods for the processing of polymers.

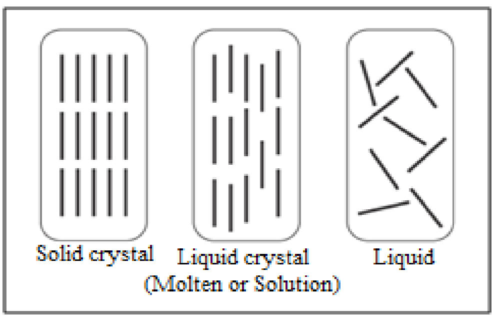

Figure 2: *Structures of Solid crystal, liquid crystal and liquid*

Polymers are generally obtained by methods such as interface polymerization and low temperature polycondensation. Aromatic polymers are generally classified as homopolymer para-aramides, meta-aramid and copolymer aramides.

- <u>Homopolymer para-aramides</u>: poly (1,4-benzamide) (PBA), poly-p-phenylene-terephthalamide (PPTA) and poly p-phenylene benzimidazole terafitalamide (PBIA)
- <u>Meta-aramid:</u> poly-m-phenylene isophthalamide (MPIA)
- <u>Copolymers aramides:</u> co-poly-p-phenylene / 3,4’-oxyphenylene terephthalamide (3,4--POP-T)

In para-aramides, the aromatic group is attached to the chain via carbon atoms 1 and 4. The simplest form is called p poly p-phenyleneterephthalamide ve and is commercially available as Kevlar® and Twaron® fibers. In meta-aramides, the aromatic group is attached to the chain via carbon atoms 1 and 3. These fibers, commercialized under the name Nomex®, are poly-m-phenylenisophthalamide. Kevlar® is used extensively in the production of personal dress and boots in the field of ballistics and is known for its high mechanical properties (Mathur and Netravali, 1996).

Figure 3 presents the chemical structure of para and meta-aramides. Meta-aramid fibers are not preferred in ballistic protection products due to their low modulus due to their low degree of orientation (Çay and Süpüren, 2007). Therefore, para-aramid fibers will be discussed in this section.

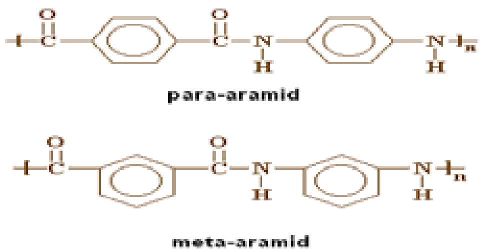

Figure 3: *Para-aramid (Kevlar®) ve metaaramid*

Commercially known PPTA aramides; Kevlar® (DuPont, USA), Twaron® (Teijin Aramid, Japan), MPIA Nomex® (DuPont, USA), Teijinconex® (Teijin Aramid, Japan) and Technora® (Teijin Aramid, Japan) 3,4'-POP-T copolymer fibers.

Aramid fibers were originally produced to reinforce plastics with poor mechanical properties. High strength properties of these fabrics has contributed to find a place in space technologies, automotive, defense industry and aviation (Karahan, 2008). The general properties of para-aramid fabrics are shown in Table 1.

Table 1: *Para-aramid Kevlar 29 (Afshari et al., 2011)*

Physical properties of Kevlar 29 fabric	Value
Density(g/cm^3)	1.45
Young Modulus (GPa)	130
Tensile Modulus (g/denye)	1100
Tensile strength (GPa)	3.6
Electrical resistance (ohm-meter)	1015
Thermal conductivity (W/mK)	0.04-0.08
Erime noktası (°C)	460 °C
Compressive strength (MPa)	393

They show excellent durability properties over a wide range of temperatures over long periods of time. Aramides do not melt at high temperatures and do not support combustion (oxidation). They start to carbonize at 427 °C. They do not lose their durability even at temperatures as low as -196 °C. They also have excellent dimensional stability. The density of aramid fibers is 1.44 g/cm^3. The square meter weight of aramid fabric is 210 g/m^2 (Yavaş, 2009).

Aramid fibers have low moisture holding and compressive strength. In the aerospace industry, especially in aircraft manufacturing, the low compressive strength properties of aramid fibers are improved by using carbon fibers as hybrid composites. In Table 2, mechanical properties of some commonly used kevlars are given (Öztürk, 2015).

Table 2: *Mechanical Properties of Kevlar®*

	Tensile Strength [N/mm^2]	**Elastic Modulus [GPa]**	**Elongation [%]**	**Density [g/cm^3]**
Kevlar 29	2920	70	3,6	1,44
Kevlar 49	3000	112	2,4	1,44
Kevlar 149	3450	179	2	1,47

In addition to the impact depth and impact diameter, the energy absorbed by the fabric, the energy parameters transmitted to the back surface, the number of fabric fold and stitch pattern were found to be effective on ballistic properties (Karahan, 2008).

2.2.2. High Performance Polythene (HPPE)

High performance polyethylene (HPPE) fibers exhibit superior performance with low density and high mechanical properties as well as high strength and elasticity modulus. Generally, HPPE fibers which are produced by using gel spinning method are low in densities, high in friction and fatigue strength and are resistant to most chemicals (Kalayci et al., 2015). Ultra-pullout is required to obtain ultra high modulus PE fiber. Ultra-pullout is that the crystals in the curled state are tear off and then come into a long chain microfibril structure (Çelikkanat, 2003).

These fibers, which can float on water with low densities below 1 g/cm^3, have become a preferred material in many areas of maritime thanks to their combination of high mechanical properties and resistance to water and moisture.

In addition, the high energy absorption of these fibers makes it suitable for use in ballistic products. Although the low melting temperature limits its use, it is possible to find usage in almost all technical textiles, especially medical, protective, transportation or sports technical textiles (Kalayci et al., 2016). As a result of the studies, it has been shown that polyethylene has a very high energy absorption capacity as well as low density property. Therefore, polyethylene fiber composite materials as the support layer of the armor will be a suitable choice in terms of superior energy absorption behavior (Özşahin and Tolun, 2009).

The most important factors for the commercial success of high performance polyethylene (HPPE) fibers are as follows:

- High specific strength and high tensile energy with specific module
- Low specific gravity
- Very good abrasion resistance
- Excellent electrical and chemical resistance
- Good UV resistance
- Low dehumidification

High performance polyethylene (HPPE) fibers have high strength and low elongation. Its burst performance factor under pressure is about 45% higher than aramides. HPPE fiber is also used to protect against cutting, sewing and ballistic impacts. High modulus HPPE fibers have a much better strength than aramid and glass fibers. A bulletproof vest made of HPPE is 60% lighter and much more comfortable than a steel vest with the same protection value. Products such as protective gloves, fencing garments are made with HPPE (Çelikkanat, 2003).

2.2.3. PBO (Polybenzobisoxazole) Fabrics

Among the fibers produced with high technology, fibers which have superior features to conventional textile fibers such as strength, modulus, thermal resistance, chemical resistance and weather resistance are referred to as “high performance fibers”. High performance fibers can be classified into three categories as heat resistant fibers, high strength fibers and chemical resistant fibers according to their properties and application areas (Kalayci et al., 2015).

PBO (Polybenzobisoxazole) is one of the species of polybenzazoles containing various cyclic aromatic structures. It emerged in the 1980s as a result of the efforts of the American Air Force to produce more durable materials than aramid fibers (Sozen et al., 2016). PBO Fibers are obtained by polycondensation of PBO (poly-p-phenylenebenzobisoxazole), 4,6-diamino-1,3-benzenedioldihydrochloride (DABDO) and terephthalic acid (TA) in polyphosphoric acid (PPA). Poly-p-phenylenebenzobisoxazole (PBO) fibers have been developed as high temperature resistant polymers and are insoluble with the exception of several solvent systems. For the production of PBO fibers, therefore, conventional fiber or solution fiber spinning methods cannot be applied. PBO fibers have excellent mechanical properties compared to other high performance fibers. It has a very high fire resistance and high thermal stability (Peru, 2019).

General properties of PBO fibers;

- High distortion temperature
- High creep resistance
- High abrasion resistance
- Low ultraviolet resistance
- Low moisture resistance (Seely et al., 2004).

PBO fibers which are produced in a color close to golden color are extremely lightweight, flexible and have a soft handle despite their extremely high mechanical properties (Kalayci et al., 2015). Its resistance to temperature is quite good (Peru, 2019). The ballistic strength of PBO fibers is much higher than the fibers available so far and the vests made of these fibers fall into the lightest category of the existing vests. However, its use is not common due to its high cost (Eruğur, n.d.). In addition, PBO fibers have almost twice the strength of para-aramid fibers. Although it has one of the highest modulus of elasticity among organic fibers, their shear modulus has been observed to be lower compared to other high strength fibers.

2.2.4. High Performance Glass Fibers

Glass fibers are one of the most widely used reinforcing materials in the production of glass fiber composites. In addition to its superior properties, it is an economical type of reinforcement, making it widely used in composite production. Although it is used with various matrix materials, the main application area is glass reinforced plastic (GRP) industry (Yavaş, 2009).

The commercial history of glass fiber as a high-performance fiber begins with the joint investment of Owens Illinois and Corning Glass.

With this start, glass fiber production increased by an average of 15-25% every year until the 1970s. In the following years, the glass fiber market was left to aramid carbon fibers and reinforced composites. However, glass is currently one of the most important reinforcing materials. Glass fiber consumption has increased by around 8-10% in the last decade. The major producers of high-performance glass fibers are Owens Corning, Wentrotex, Ashltrom and Pilkinton (Çelikkanat, 2003).

Glass is an amorphous material. Glass fibers are composed of oxides of elements such as aluminum, boron, iron, calcium and sodium in certain proportions according to glass fiber types, although more than 50% by weight silicon dioxide (SiO2).

E-glass, C-glass and S-glass are among the most widely used glass fiber types. The weight of E-glass fiber fabric is 225 ± 7 g/m^2 (Öztürk, 2015).

Four different types of glass fibers are available:

Glass A (Alkali): Glass A is a highly alkaline glass. Therefore, the electrical insulating property is poor. It is the most common type of glass with high chemical resistance.

C (Corrosion) Glass: Very high resistance to chemical solutions.

E (Electrical) Glass: Due to its low alkali ratio, its electrical insulation is very good compared to other glass types. It has high strength. Water resistance is also quite good. Composite developed for humid environments generally uses E glass.

S (Strength) Glass: It is a high strength glass. Tensile strength is 33% higher than E glass. It also has a very good fatigue resistance at high temperatures. Due to these properties, it is preferred in aerospace industry. Glass fibers are usually used with plastic or epoxy resins (Yavaş, 2009).

Some properties of glass fibers are as follows:

- High tensile strength.
- Low thermal resistance. They do not burn but soften at high temperatures.
- They are resistant to chemical materials. No moisture absorbing properties.
- They do not conduct electricity.

2.2.5. PPID Fibers

PPID (Polypyridobisimidazole) fiber group with high ballistic performance was developed by Akzo Nobel. PPID fibers which are widely used for a very short period of time just like PBO fibers, are a group of fibers with high tensile stress, high elasticity modulus and high electrical conductivity. Increasing the durability of PPID fibers with production technologies and spreading their usage areas is still a research subject (Yumak et al., 2013).

3. BALLISTIC PROTECTION AND TEST STANDARTS

3.1. Ballistic Protection Standarts

There are many standards in the world for testing ballistic protection. Commonly accepted standards are those adopted by NIJ (The US National Institute of Justice) and HOSDB (UK Home Office Scientific Development Branch). In addition, various military standards have been developed by NATO and the Turkish Standards Institute. The standards TS 11164 and TS 13349 of the Turkish Standards Institute include test methods for ballistic protection of personal body armor against firearms. The values stated in the widely used NIJ (National Institute of Justice) standard are taken as reference in measuring the ballistic performance of products developed for protective armor against light weapons in today's technology (Bozdoğan et al., 2015). Protection level; caliber, type, weight and speed of bullet ammunition used in ballistic applications is a criterion determined by taking into account (Yavaş, 2009). The protection levels are listed in table 3 and table 4 below.

Table 3: *NIJ-STD-0101.04 standard, protection levels for ballistic protectors (Candan, 2007).*

Protection Level	Calibre Bullet Type	Bullet weight (g)	Bullet speed (m/s)	Depth of Trauma (max)
I (5 m, range)	22 LR Long-rifle lead round nose bullets (LR, LRN) 380 ACP Full metal jacket round nose bullets(FMJ RN)	2,6 6,2	320 312	44 mm
IIA(5 m, range)	9 mm Full metal jacket round nose bullets (FMJ RN) 40 S&W Full metal jacket bullets (FMJ)	8,0 11,7	332 312	44 mm
II(5 m, range)	9 mm Full metal jacket round nose bullets (FMJ RN) 357 Magnum jacketed soft point (JSP)	8,0 10,2	358 427	44 mm
IIIA (5 m, range)	9 mm Full metal jacket round nose bullets (FMJ RN) 44 Jacketed hollow point (JHP)	8,0 15,6	427 427	44 mm

III (15 m, range)	7,62 mm Full metal jacket bullets (FMJ)	9,6	838	44 mm
IV (15 m, range)	30 mm Armor piercing (AP) bullets	10,8	869	44 mm

Table 4: *Home Office Body Armour Standart (Payne et al., 2017)*

Protection level	Classification and calibre	Test round designation	Bullet mass	Range min.	Single shot BFS limit (mm)	Velocity ($m.s^{-1}$)
HO1	9 mm FMJ	MEN 9 mm FMJ DM11A1B2	8.0 g (124 grain)	5 m	44.0	365±10
	9 mm JHP	Federal Premium 9 mm JHP P9HST1	8.0 g (124 grain)	5 m	44.0	365±10
HO2	9mm FMJ	MEN 9 mm FMJ DM11A1B2	8.0 g (124 grain)	5 m	44.0	430±10
	9 mm JHP	Federal Premium 9 mm JHP P9HST1	8.0 g (124 grain)	5 m	44.0	4 ±10
HO3	Rifle 7.62 calibre	Radway Green 7.62 mm NATO Ball L44A1 or L2A2	9.3 g (144 grain)	10 m	30.0	83±15
	Rifle 7.62 calibre	7.62 × 39 mm surrogate19	7.9 g (122 grain)	10 m	30.0	70±15
HO4^20	Rifle 7.62 calibre	SAKO .308 Win 480A Powerhead or Barnes .308 TSX BT	10.7 g (165 grain)	10 m	30.0	820±15
SG1	Shotgun 12 gauge True Cylinder	Winchester 1 oz. Rifled 12RSE	28.4 g	10 m	30.0	435±25

The basis of these standards is to establish a common success criterion for armor work. Certain parameters such as test conditions, equipment to be used and evaluation of the results constitute the content of these standards (Şen, 2013). Table 5 lists some of the national and international ballistic standards.

Table 5: *Some of international ballistic protection standarts (Yavaş, 2009).*

STANDART NO	STANDART
MIL-STD-662 F	Balistic Test For Armor
NIJ-STD-0101.04	Balistic Resistance of Personel Body Armor
STANAG 2920	Balistic Test Method For Personel Armor
TS 11164	Balistik Koruyucu Yelek
PPAA STD-1989-05	Personel Protective Armor Assosiation Testing Standards For
MIL-P-46199	Balistic Resistance of Personel Body Armors Aluminium Oxide Ceramic (For Use In Armor Composite)
PR EN ISO 14876-2	Protective Clothing-Body Armor-Part-2:Bullet Resistance- Requirements and Methods

3.2. Ballistic Protection Tests

3.2.1. V50 Ballistic Limit Test

One of the problems encountered in the investigation of the impact event is the determination of the bullet velocity that an object can withstand without being damaged. This speed is called "ballistic impact velocity" or "ballistic limit" (Cerit, 2004). V50 is the speed at which the particle that hits the target perpendicular to the target is stopped with a 50% probability. In order to calculate the actual V50 value, the highest three velocities in which the particles are stopped by the armor and the lowest three velocities of the shots passing through the armor are taken (Soykan et al., 2013). Furthermore, the difference between the impact velocity of the projectile that pierces the plate at the highest speed and the impact velocity of the projectile at the lowest speed that does not penetrate the plate does not exceed 18,29 m/s velocity is required.

Velocities lower than V50 produce partial perforation in the material, whereas velocities higher than this value produce full perforation in the material. Full penetration is defined as the complete perforation of the plate used by the projectile or particles broken from the plate. Partial penetration (partial penetration) is valid only if no puncture occurs along the plate (Bozdoğan et al., 2015).

3.2.2. STANAG 2920

The Stanag 2920 standard describes ballistic testing methods for personnel armor developed under the NATO Standardization Agreement. It is also possible to compare the preservatives with each other, since one type of bullet is used during the test. One of the series Fragment Simulating Projectiles described in US-MIL-P-46593 is used. Bullets of 5,385 caliber and 1,102 grams are generally preferred (Bozdoğan et al., 2015).

The Standardization Agreement is a declaration setting the standards of NATO member states in the military field. All military equipment produced by NATO member countries must also comply with these standards. Other countries help countries that need to modernize their army to achieve standards. This is done by transferring technology/information rather than directly delivering the material (‘EUROLAB’, 2019)

The sample to be tested must be conditioned prior to testing in an environment containing 20 ± 2 °C and 65 ± 5% relative humidity. During the test, at least 6 shells are fired at the ballistic protective material and their velocities are measured. Each shot must be at least 30 mm away from the point where the shot or deformation occurs. Bullets passing through the target completely or causing rupture behind the target are considered to have completely penetrated the ballistic protective structure (Bozdoğan et al., 2015).

In this standard, projectile firing rates are adjusted by using the up and down method. The first bullet is accelerated to the armor’s V50 ballistic speed limit. If the first projectile creates a puncture on the armor surface, the second projectile is fired at a speed of 30 m/s less than the first projectile. If the first projectile creates partial puncture on the armor surface, the second projectile is fired at a rate of 30 m/s faster than the first projectile. After the first firing of the ballistic armor is completed, the firing is carried out at a projectile velocity of 15 m/s up or down. The V50 continues to fire according to the standard procedure to obtain a ballistic limit rate. After a certain number of shots, a total of six speeds are calculated, 3 of which are the highest speeds at which partial puncturing occurs, and the other 3 at the lowest speeds at which the total drill occurs. The difference between the highest and the lowest speed values detected in the groups where partial drilling and full drilling takes place should be at most 40 m/s. V50 ballistic boundary velocity is calculated by calculating the average value from the regular impacts received (Bozdoğan et al., 2015).

4. EVALUATION OF BALLISTIC PROTECTION EFFECTIVENESS

The most widely used synthetic fibers in ballistic-resistant textiles and their properties are given in table 6 below.

Table 6: *Fibers for ballistic protection*

Fiber Type	Tensile Strength (g/d)	Elongation at break (%)	Modulus (g/d)	Specific Weight (g/cm^3)
Polyamide (nylon)	5,9-9,8	15-28	21-58	1,14
Para-aramids	23-28	2,5-3,5	500-900	1,44
High Modulus Polyethylene	30-40	2,5-3,6	1400-2400	0,97
PBO	40,3	2,5-3,5	1254-1875	1,54

The fibers listed in Table 6 exhibit different behaviors under the influence of ballistic impact. For example, para-aramid fibers are fibrilized or split in the longitudinal direction under impact. Aramid fibers have very high heat resistance. Therefore, they do not melt due to the fiber-to-fiber or fiber-to-friction heat. On the contrary, in HHPE fibers, the heat generated by the ballistic impact increases the temperature of the fiber surface, whereby softening and permanent deformation occurs. On the other hand, it is stated that this energy absorption mechanism can increase the ballistic resistance of HMPE fibers. Thickness and surface density of existing ballistic protective textiles impose some limitations on suitability for use and breathability. While fiber properties continue to be improved, it is beneficial to develop alternative fabric structures to maximize energy absorption (Çay et al., 2007).

PBO (Polybenzobisoxazole) fibers have excellent mechanical properties compared to other high performance fibers. It has very high fire resistance and high thermal stability. Their ballistic strength is much higher than the existing fibers, and those made from these fibers fall into the lightest category. However, its use is not common due to its high cost.

Nowadays, cost effective aramid fibers and high density polyethylenes are preferred in flexible armor production considering low cost and superior strength values.

5. CONCLUSIONS

Due to the geographical location of our country in a strategic region, keeping security measures at the highest level is vital for survivability. Today, warfare, called as symmetrical and anti-terrorism or asymmetric warfare, can be gained with superior firepower and maneuverability. It is only possible for the units to form a center of weight at the required time and place with high mobility. In this context, the development of armor, which constitutes an important weight item, with a lighter and more powerful alternative, has an effect that can form a force multiplier.

For this purpose, metals and their derivatives, which are heavy in armor production, have been replaced by lighter fabrics consisting of fibers with high physical and mechanical properties. Academic studies and R & D studies on this subject are continuing rapidly and thus new products are obtained. The national achievements that can be obtained by directing the economic resources and qualified manpower to this field by showing the necessary sensitivity to this new technology field will enable our country to make a great leap in the field of defense as well as provide economic income.

REFERENCES

Afshari, M., Kotek, R., Chen, P. (2011). High Performance Fibers. High Performance Polymers and Engineering Plastics, 269–340.

Aytaç, A., Çanakçı, B., Aslan, B., Aytav, E. (2019). An Analysis of The Reasons That Create Helicopter Vibrations and Vibration Reduction Techniques. In Multidisciplinary Studies in the World of Science (pp. 203–223). Berikan Publishing.

Aytaç, A., Işık, M. S., Çanakçı, B., Özdemir, T., Aztekin, K., İpek, H. (2018). Investigation of Microstructure and Mechanical Properties of Heat Treatment, Carbon Ratio and Alloying Elements in AISI 1008, 1040 and 4140 Steels. The Journal of Defense Sciences, 17, 139–165. https://doi.org/10.17134/khosbd.477252

Aytaç, A., Yavuz, H. İ., Aztekin, K., Özdemir, T., Işık, M. S., Çanakçı, B., Kaya, M. T. (2018, July). Determination of the Effective Parameters in Welding Process of MIL-A 46100 Armor (pp. 417–427). Presented at the International Science and Technology Conference-ISTEC 2018, Paris, France.

Bozdoğan, F., Üngün, S., Temel, E., Mengüç, G. S. (2015). Balistik Koruma Amaçlı Kullanılan Tekstil Materyalleri, Özellikleri ve Balistik Performans Testleri. 2015 (Cilt:22), 98. Retrieved from http://www.tekstilvemuhendis.org.tr/tr/2015_-cilt-22-/98/balistik_koruma_amacli_kullanilan_tekstil_materyalleri-_ozellikleri_ve_balistik_performans_testleri--doi-_10-7216-130075992015229808

Candan, C. (2007). Investigation of Terminal Ballistic Properties of High Density Polyethylene (UHMW-PE) Armor Plates Produced by Pressing and Without Pressing Against Light Weapons. Presented at the 8. Uluslar Arası Kırılma Konferansı Bildiriler Kitabı.

Çay, A., Süpüren, G., Kanat, Z. E., Gülümser, T., Tarakçioğlu, I. (2007). BALLISTIC FIBERS (Part 1). Tekstil ve Konfeksiyon, 17(4), 232–236.

Çelikkanat, A. B. (2003). Teknik Tekstiller. İstanbul Teknik Üniversitesi.

Cerit, A. A. (2004). Investigation of Ballistic Performance of Particle and Fiber Reinforced Aluminum Matrix Composite. Erciyes Üniversitesi.

Çerkez, İ., Ulcay, Y. (2007). The Effect Of Colloidal Silica Dispersion On Energy Absorbtion Of Polyethylene Non-Woven Surface. 14.

Çifci, E. (2011, October 21). Dünya Harp Tarihi: SAVAŞLARI DEĞİŞTİREN 50 SİLAH (4) / ZIRH. Retrieved 29 December 2018, from Dünya Harp Tarihi website: http://dunyaharptarihi.blogspot.com/2011/10/savaslari-degistiren-50-silah-4-zirh.html

Dean, B. (1920). Helmets and body armor in modern warfare. Retrieved from http://archive.org/details/helmetsbodyarmor00deanuoft

Eruğur, A. (n.d.). Balistik Çalışmalarda Kullanılan Hammadde ve Kompozitler. Retrieved 3 January 2019, from http://www.acarerugur.com/FileUpload/

op325540/File/balistik__calismalarda__kullanilan__hammadde__ve__kompositler.pdf

EUROLAB. (n.d.). Retrieved 3 January 2019, from https://www.eurolab.com.tr/sektorel-test-ve-analizler/spesifik-testler/stanag-test-laboratuvari

Ford, R., Grant, R. G. (2016). Weapon: A Visual History of Arms and Armor. New York, New York: DK.

Işik, H., Değirmenci, E., Evci, C. (2013). Analysis of Energy Dissipation Mechanisms of Woven Fabrics Subjected to Ballistic Impact. The Journal of Defense Sciences, 18.

Işık, M. S., Aytaç, A., Aztekin, K., Özdemir, T., Çakır, U., Çanakçı, B. (2018, July). The Effect of Cooling Environment and Tempering Temperature on Wear Resistance of AISI 4140 Steel (pp. 550–560). Presented at the International Science and Technology Conference-ISTEC 2018, Paris, France.

Kalayci, E., Avinc, O., Yavaş, A. (2015). High Performance PBO (poly-p-phenylene benzobisoxazole) Fibers. Tekstil ve Mühendis, 22, 63–83. https://doi.org/10.7216/130075992015229807

Kalayci, E., Avinc, O., Yavaş, A. (2016). High Performance Polyethylene (HPPE) Fibers. Marmara Fen Bilimleri Dergisi, 28, 13–34. https://doi.org/10.7240/mufbed.51868

Karahan, M. (2008). Comparison of Ballistic Performance and Energy Absorption Capabilities of Woven and Unidirectional Aramid Fabrics. Textile Research Journal, 78(8), 718–730.

Mathur, A., & Netravali, A. N. (1996). Modification of mechanical properties of Kevlar fibre by polymer infiltration. Journal of Materials Science, 31(5), 1265–1274. https://doi.org/10.1007/BF00353106

Özdemir, T., Yavuz, H. İ., Çanakçı, B., Çakır, U., Aytaç, A., Işık, M. S., Aztekin, K. (2018, September). Micro-Structural Impact Energy Changes Emerging from Different Welding Processes of MIL-A 46100 Armor Steel (pp. 93–101). Presented at the Internatıonal Congress on New Trends in Scıence, Engineering and Technology-ICONTRENDS 2018, Rome, Italy.

Özşahin, E., and Tolun, S. (2009). Influence of layer sequencing on ballistic resistance of polyethylene supported AA 7075 T651 plates. J Istanbul Tech Univ/d, 8, 72–80.

Öztürk, Ö. (2015). Investigation Of Mechanical Behavior Of Composite Materials Used By Using Polyured Matrix Material And Glass, Aramide, Carbon Fiber Fabric Reinforcements. Namık Kemal Üniversitesi.

Payne, T., O'Rourke, S., Malbon, C. (2017). Body Armour Standard (2017). (012), 92.

Peru, Y. (2019). Diffusion of Localized Heat in Bullet Proof Fabrics (Sütçü İmam Üniversitesi). Retrieved from http://www.tekniktekstiller.com/articles/kursungecirmez-kumaslarda-lokalize-olmus-isinin-yayilmasi/

Seely, L., Zimmerman, M., Mclaughlin, J. (2004). The Use of Zylon Fibers in Uldb Tendons, Advances in Space Research. Advances in Space Research, 33(10), 1736–1740.

Şen, H. (2013). Investigation of Ballistic Properties of AlMg3 / SiCp Composite Materials.

Soykan, H., Aslanoğlu, Z., Karakaş, Y. (2013). METALLURGY OF ARMOR STEELS.

Sozen, E., Gunduz, G., Imren, E. (2016). Composite Materials and Fibers Used in Ballistic Panel and Protective Armor Production. Journal of Bartın Faculty of Forestry, 18(2), 194–204. https://doi.org/10.24011/barofd.267304

Weir, W. (2005). 50 Weapons That Changed Warfare. Franklin Lakes, NJ: New Page Books.

Yavaş, M. O. (2009). Composite material design and ballistic resistance for individual defense against light weaponsComposite material design and ballistic resistance for individual defense against light weapons (Selçuk Üniversitesi). Retrieved from https://www.ulusaltezmerkezi.net/hafif-silahlara-karsi-bireysel-savunma-amacli-kompozit-malzeme-tasarimi-ve-balistik-dayanimi/166/

Yavuz, H. İ., Aytaç, A., Özdemir, T., Aztekin, K., Özçelik, B. (2018). Materials modified highly absorber thermal camouflage functional nanostructures and sensors for CBRN defence and envioremental safety and security. Presented at the FNS-CBRN Defence.

Yumak, N., Pekbey, Y., Aslantaş, K. (2013). Investigation of Deformation Characteristics of CompositeMaterials Used in Armor Design. Electronic Journal of MachineTechnologies, 10(4), 1–21.

ARTIFICIAL NEURAL NETWORKS CONTROL OF 7000 SERIES ALUMINUM ALLOYS OPTIMIZATION BY RESPONSE SURFACE METHOD

CHAPTER

10

Tayyar Salih ADIGÜZEL[1]
Abdullah Mahir IŞIK[2]
Mehmet Arif SALTAN[3]
Muhammed İLİVAN[4]

1 National Defence University, Military Academy, Department of Mechanical Engineering, Ankara-Turkey. tsadiguzel@kho.edu.tr

2 National Defence University, Military Academy, Department of Mechanical Engineering, Ankara-Turkey. aisik@kho.edu.tr

3 National Defence University, Military Academy, Department of Mechanical Engineering, Ankara-Turkey. masaltan@kho.edu.tr

4 National Defence University, Military Academy, Department of Mechanical Engineering, Ankara-Turkey. muhammed.ilivan@dpu.edu.tr

1. INTRODUCTION

With the development of machining applications and technology, the use of CNC lathe and CNC vertical machining center as a bench is becoming increasingly common in the manufacturing sector (Çakır et al., 2018). Although there are many methods of machining; milling process is one of the methods needed in automotive, aerospace, defense industry products and other industries (Uğur, 2019).

Factors affecting the surface roughness in cutting operations, cutting speed, cutting depth and so on. identifying these factors as a result of the full analysis of the factors will be appropriate in terms of controlling costs (Inasaki, 2002; Olynk, 2009). One of the main objectives of machining is to maximize the level of surface roughness (Aytaç and İlivan, 2019). In order to compare machinability to a predetermined material, the 7000 series aluminum material was processed under similar cutting conditions with AISI 1050 samples (Aztekin and Ateş, 2015).

Along with its good mechanical properties, it is light, durable and easy to process, making aluminum materials widely used in the manufacturing sector. Areas of use in the sector can be cited mainly as defense industry, weapon systems and aerospace vehicles. However, aluminum materials can be used in ballistic applications, especially in missile and rocket construction (Zhao and Jiang, 2008). The use of aluminum alloys to reduce vibration in helicopter designs is also being investigated (Aytaç et al., 2019a). Efforts are continuing to expand the use of aluminum materials in thermal battery manufacturing (Aytaç et al., 2019b).

While conducting scientific research, two different paths are followed: one is the analysis obtained by defining the material properties and working conditions in the computer environment, the other is the appropriate test method and laboratory studies where the actual working conditions are tested with samples. In addition, the weldability and the use of 7000 series aluminum materials in armor applications is a current research topic (Özdemir et al., 2018).

Due to the increasing use of aluminum and its alloys in the industry, machinability levels have been a current research topic (Uğur, 2019).

Accurate cutting tools and cutting parameters are of paramount importance in terms of proper process, smooth surface quality, economy and determination of optimum machine power (Aytaç et al., 2018a). In addition, the abrasion resistance of the material is one of the important parameters that should be known at the design stage (Işık et al., 2018). The amount of alloying elements also causes changes in the microstructure and has an effect on mechanical properties (Aytaç et al., 2018b).

Inaccurate determination of cutting parameters, deterioration of material to be processed, low surface quality and damage to cutting tools.

RSM is the most common mathematical modeling and statistical evaluation method used in the optimization of input parameters (independent variables) of a system. In addition, RSM can be used easily in the determination and interpretation of the relationship of input parameters combinations with responses (dependent variables).

Artificial neural networks (ANN) are a relatively new computational tool that has found a wide range of applications to solve many complex problems.

ANN is a technology produced by influencing the design of the information processing center of the brain.

Activation functions in ANN are used to settle the amplitude of the neurons at the output in the range [0,1] or [-1,1].

In this study; the effects of machining parameters on surface roughness of Al 7075 material, which is frequently used in machining sector, are optimized by using RSM and ANN is created and compared in matlab program.

2. MATERIALS AND METHODS

2.1 Experimentel Design

In this study, it has been tried to reach the optimum surface roughness value by optimization of the parameters affecting the surface roughness value resulting from milling of Al 7075 material. The most critical criterion of surface quality during the machining stage is the average surface roughness (Ra) value (Aytaç and İlivan, 2018). In order to investigate the effect on surface roughness, the most effective parameters such as feedrate, cutting speed and chip removal were determined and a new experimental model was established and optimized with RSM. Information about the levels of the selected factors is given in Table 1. Experimental design matrix given in Table 2 was prepared by using Minitab statistical software program before coding.

Table 1: *Factors and levels*

Factors	Explanation	Low Level	Medium Level (Center Point)	High Level
A	Rate of feed	0.325 mm/rev	0.69 mm/rev	1.05 mm/rev
B	Revolutions per minute (Cutting Speed)	550 rpm	1100 rpm	1460 rpm
C	Cutting depth	0.2 mm	0.6 mm	1 mm

RSM was carried out in three stages. In order to obtain the response values in the first step, physical experiments were performed by forming an experimental parameter combination. In this way, it is aimed to reduce costs by performing fewer and more efficient tests than the number of experiments to be performed by traditional methods. Thus, with the mathematical model formed as a result of the analysis, the determination of unknown intermediate response values can be realized in a very short time. In the second stage, the relations of the responses with the input parameters were defined as a second order polynomial or exponential function and in the third stage the optimum points were determined by analysis of surface graphs and ANOVA.

Table 2: *Full Factorial Experimental Design Matrix*

Number of Tests	Factors and Levels		
	A	B	C
1	-1	-1	-1
2	+1	-1	-1
3	-1	+1	-1
4	+1	+1	-1
5	-1	-1	+1
6	+1	-1	+1
7	-1	+1	+1
8	+1	+1	+1
9	0	0	0
10	0	0	0
11	0	0	0

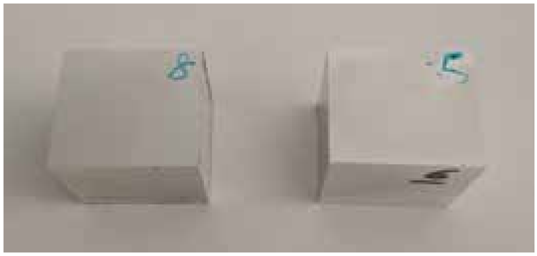

Figure 1: *Al 7075 Test Specimens*

Figure 2: *Spinner U-620 Vertical Machining Center*

In Figure 1, Al 7075 test specimens are processed and surface roughness is measured and in Figure 2, Spinner U-620 model 5 axis CNC vertical machining machine is shown.

2.2 Materials and Properties

Table 3: *AI 7075 Chemical Compound*

Specimen	Fe	Si	Cu	Mn	Mg	Zn	Cr	Zi+Ti	Diğer	Al
AI 7075	0,5	0,5	1,2-2,0	0,3	2,1-2,9	5,1-6,1	0,18-0,28	0,25	0,15	Rest

Table 4: *AI 7075 – Mechanical Properties*

Temper - -	Yield Strength (MPa) min-max	Tensile Strength (MPa) min-max	Extension (%50) min-max	Toughness (brinel) min-max
0	105	225	17	60
T6	460-505	530-570	10	140-160
T7	435	505	12	140

2.3 ANN Structure and Levenberg-Marquardt Algorithm

Although there are many different definitions for Artificial Neural Networks, it can be defined as basically giving the computer systems the ability to learn, acquire information, link and recall information and recall information by mimicking the working principles of the human brain or central nervous system in general (Kohonen, 1990). The basic point of Artificial Neural Networks, the human brain and nerve cell forming biological parts are based on the modeling and use of neurons in computer systems (Leave et al., 1992). Artificial Neural Network models are essential to the human nerve cell if we simply recognize the signals from the cells transmitting signals to the nucleus (dendrite) comes, it is called soma to the structure that connects the incoming signals and this information is transmitted to the other cells by axon, the information from the axons is pre-treated with synapses and transmitted to the dentrides of other cells. Neuron in artificial neural network models; dendrite; to the coupling function, the cell body; transfer function, axons; artificial neuron output and synapses; corresponds to weights.

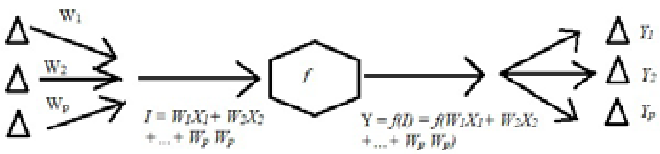

Figure 3: *Working of neural network*

The Levenberg-Marquardt learning algorithm was used in this study to generate ANN with fast learning and good convergence.

This algorithm is basically a method of calculating the least squares based on the idea of maximum neighborhood.

For ANN modeling, sigmoid activation function was used in the calculations.

All inputs and outputs are normalized in the [0 1] range.

Created model, multilayer feed forward (feed forward Multilayer Sensor, FF-MLP) ANN network structure; Includes 3 input data (chip depth, speed, optional speed), 1 hidden layer, 1 output data (surface roughness).

Table 5: *Experimental design matrix*

Std Order	Run Order	CenterPt	Blocks	Rate of Feed	RPM	Cutting Depth	Measurement 1	Measurement 2	Measurement 3	Measurement avg
1	1	1	1	3	500	0,2	0,125	0,134	0,126	0,128
2	2	1	1	7	500	0,2	0,155	0,147	0,153	0,152
3	3	1	1	3	1500	0,2	0,083	0,085	0,09	0,086
4	4	1	1	7	1500	0,2	0,159	0,163	0,153	0,158
5	5	1	1	3	500	1	0,123	0,128	0,126	0,126
6	6	1	1	7	500	1	0,19	0,188	0,189	0,189
7	7	1	1	3	1500	1	0,11	0,103	0,102	0,105
8	8	1	1	7	1500	1	0,251	0,203	0,21	0,221
9	9	0	1	5	1000	0,6	0,208	0,201	0,176	0,195
10	10	0	1	5	1000	0,6	0,186	0,152	0,184	0,174
11	11	0	1	5	1000	0,6	0,227	0,153	0,166	0,182

Table 6: *Surface roughness values in zone 1*

First Zone Revolutuion Per Minute (B) 1460 (Constant)					
Rate of Feed (A) mm/dev.	Cutting Depth (C) mm.	Measurement -1	Measurement - 2	Measurement - 3	Measurement – avg- Ra
0,125	0,15	0,105	0,124	0,097	0,109
0,205	0,15	0,114	0,116	0,116	0,115
0,125	0,25	0,104	0,12	0,12	0,115
0,205	0,25	0,133	0,11	0,111	0,118
0,068	0,2	0,076	0,074	0,083	0,078
0,262	0,2	0,107	0,116	0,13	0,118
0,165	0,08	0,133	0,149	0,125	0,136
0,165	0,32	0,159	0,144	0,149	0,151
0,165	0,2	0,14	0,124	0,121	0,128
0,165	0,2	0,109	0,101	0,092	0,101
0,165	0,2	0,116	0,101	0,113	0,110
0,165	0,2	0,118	0,104	0,099	0,107
0,165	0,2	0,11	0,136	0,104	0,117

Table 7:*Surface roughness values in zone 2*

Second Zone Revolutuion Per Minute (B) 1460 (Constant)					
Rate of Feed (A) mm/ dev.	Cutting Depth (C) mm.	Measurement -1	Measurement - 2	Measurement - 3	Measurement – avg- Ra
0,125	0,8	0,135	0,108	0,119	0,121
0,205	0,8	0,143	0,152	0,139	0,145
0,125	1,2	0,151	0,151	0,154	0,152
0,205	1,2	0,124	0,135	0,148	0,136
0,068	1	0,13	0,117	0,118	0,122
0,262	1	0,14	0,146	0,135	0,140
0,165	0,5	0,118	0,113	0,105	0,112
0,165	1,48	0,135	0,133	0,146	0,138
0,165	1	0,122	0,103	0,132	0,119
0,165	1	0,116	0,124	0,103	0,114
0,165	1	0,126	0,123	0,117	0,122
0,165	1	0,114	0,109	0,126	0,116
0,165	1	0,122	0,104	0,119	0,115

From 80 data obtained from experimental design, sigmoid was selected for the input layer and linear activation functions were used for the output layer. In the ANN model, which has the most applicable network structure, a single hidden layer of 32 neurons is used. The internal structure diagram of the ANN used is given in Figure 4.

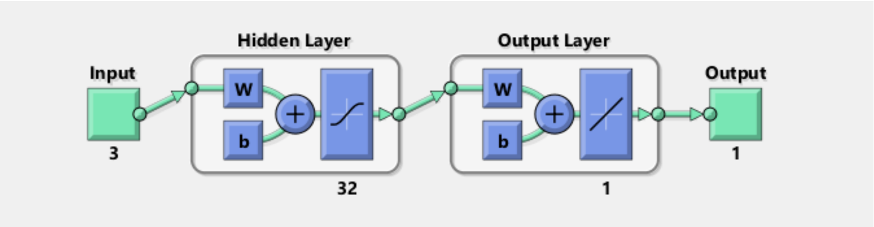

Figure 4: *Diagram of the internal structure of the ANN designed*

The ANN model performance was calculated by means of mean square error (MSE) and regression coefficient (R). MSE (Eq.1) is used to determine the error rate between the estimated value and the actual value. The MSE value should be close to zero for the model to have high predictive capabilities.

$$\mathrm{MSE} = \frac{1}{n}\sum_{i=1}^{n}(y_i - y_{di})^2 \qquad \text{Eq. (1)}$$

In the equation, n is the number of data, y_{di} is the actual value and y_i is the estimated value obtained from the neural network model.

The fact that the values obtained from the model are close to the actual values depends on the fact that R value is close to 1 value.

$$R = \sqrt{1 - \frac{\sum_{i=1}^{n}(y_i - y_{di})^2}{\sum_{i=1}^{n}(y_{di} - y_m)^2}} \qquad \text{Eq. (2)}$$

3. RESULTS AND DISCUSSION

3.1. Neural Network Optimization

In this study, Levenberg - Marquardt learning algorithm, which can learn fast and has good convergence feature, was used to train ANN. Basically, this algorithm is the method of calculating least squares based on the idea of maximum neighborhood.

Normalization process, which normalizes the data between "0" and "1", which is necessary to increase the education and learning performance of

ANN, was performed with sigmoid activation function. Showing the performance of the ANN model created; mean square error (MSE) and regression coefficient (R) graphs are reflected.

The mean square error (MSE) is used to determine the error ratio between the estimated value and the actual value, and the fact that the MSE value is close to zero means that the model's ability to estimate is increased.

The R value indicates the degree of conformity of the established artificial neural network model. The fact that the R value is close to 1 indicates that the values obtained from the established model are close to the actual values. (R=0, 92037)

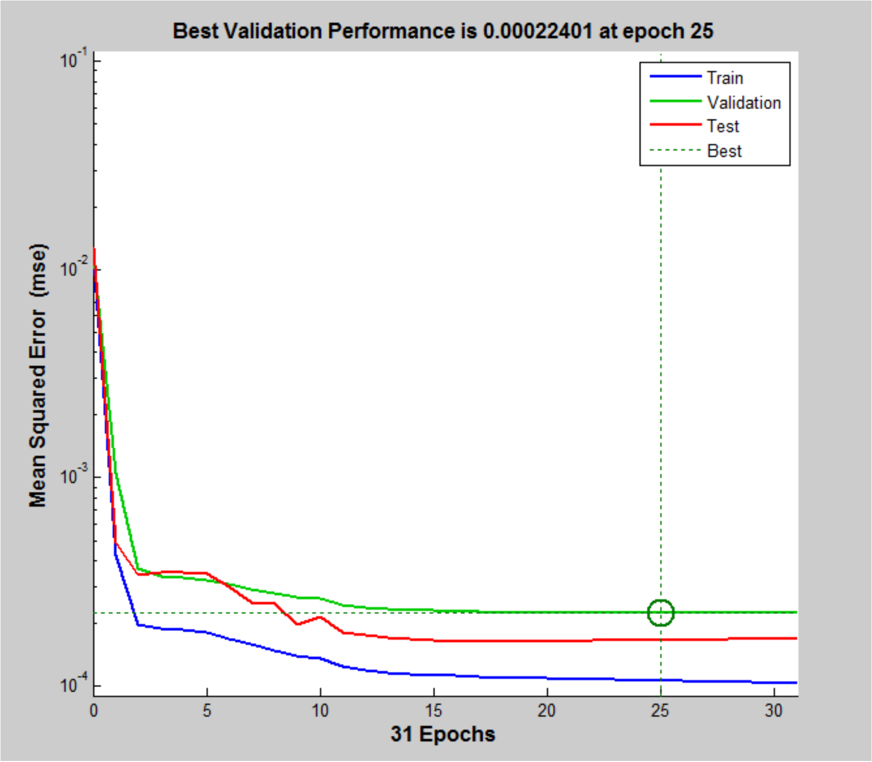

Figure 5: *Mean Square Error Value of Model*

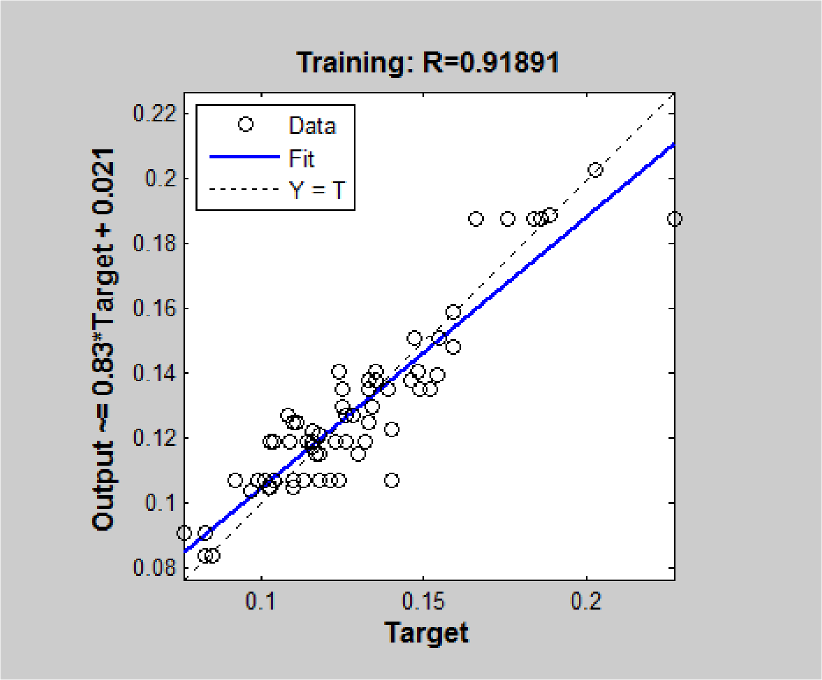

Figure 6: *Regression coefficient for training data*

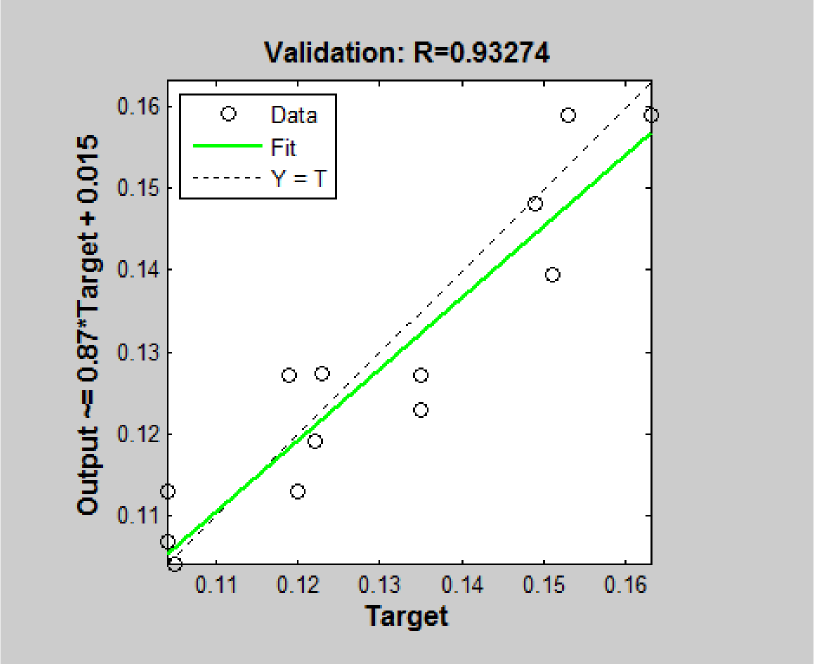

Figure 7: *Regression coefficient for validation data*

Figure 8: *Regression coefficient for test data*

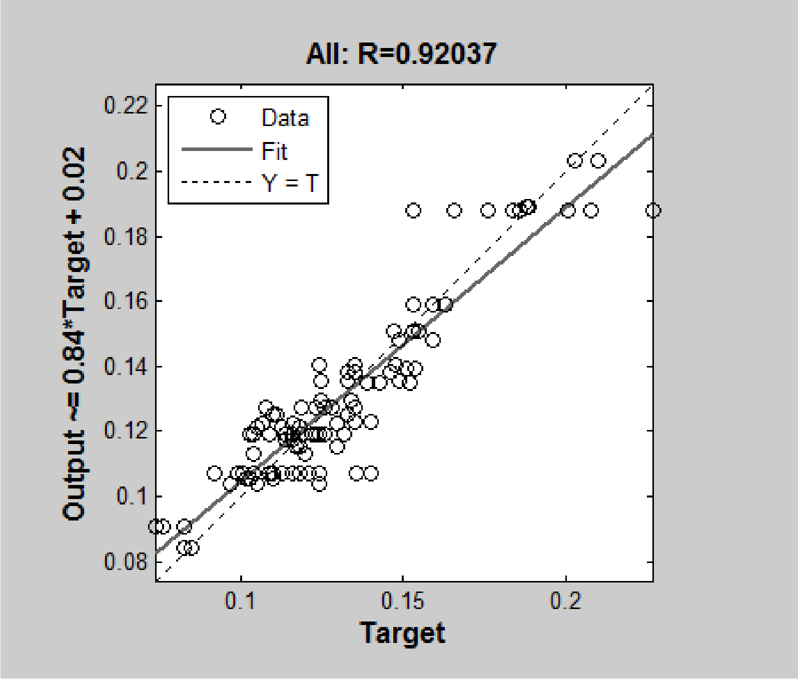

Figure 9: *Regression coefficient for all model*

3.2 Verification of ANN Model

Matlab based Simulink module was used to investigate the appropriateness of the ANN model. Afterwards, validation tests were performed with these input data and experimental results were obtained. Comparison of validation test data and Simulink estimation results are shown below.

Table 8: *Simulink Verification Data*

3	500	0,2	0,126	0,129	0
3	1500	0,2	0,09	0,08	1
7	500	1	0,19	0,189	2
7	1500	1	0,251	0,2	3
5	1000	0,6	0,152	0,1878	4
0,205	1460	0,15	0,116	0,1175	5
0,165	1460	0,32	0,144	0,148	6
0,125	1460	1,2	0,151	0,1175	7
0,262	1460	1	0,146	0,1228	8
0,165	1460	1	0,117	0,12	9

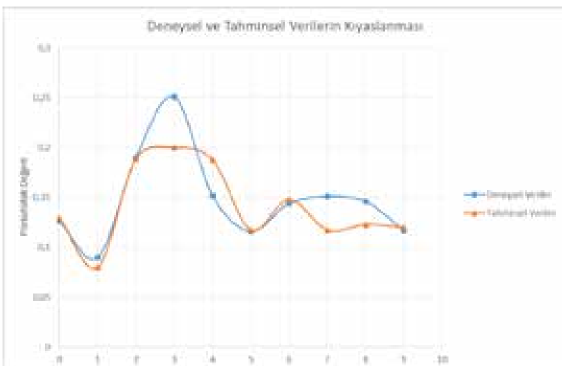

Figure 10: *Comparison of Ra*

4. CONCLUSIONS

- Neural network model was established in Matlab program using 80 experimental data.
- The performance parameters of ANN model were obtained as R = 0,99058, MSE = 0.00022401.
- Estimates were made to the model for verification with 10 different data not used in ANN training.
- The established model gave very close results to the reality.
- Verification by ANN can be practically performed instead of long-term tests with complex test setups.

REFERENCES

Aytaç, A., Çanakçı, B., Aslan, B., Aytav, E. (2019). An Analysis of The Reasons That Create Helicopter Vibrations and Vibration Reduction Techniques. In Multidisciplinary Studies in the World of Science (pp. 203–223). Berikan Publishing.

Aytaç A. and Ilivan M. (2018). Analysis of Paramaters Affected on Machinability of Dual-Phase SAE 1035 Steel by Full Factorial Experiment Design. American Journal of Engineering Research, 7(12), 43-50.

Aytaç A. and Ilivan M. (2019). Experimental Investigation Of Machinability Properties Of 5035 Steel. The Online Journal of Science and Technology (TOJSAT), 9(2), 171-178.

Aytaç, A., Ilivan, M., Aztekin, K., and Ipek, H. (2018). Determination of Optimum Cutting Parameters in Milling of AZ31 Series Magnesium Alloys by Response Surface Method. Current Academic Studies in Engineering Sciences, Vol.; Mechanical and Manufacturing Engineering, ISBN:978-9940-540-51-7

Aytaç, A., Işık, M. S., Çanakçı, B., Özdemir, T., Aztekin, K., İpek, H. (2018). Investigation of Microstructure and Mechanical Properties of Heat Treatment, Carbon Ratio and Alloying Elements in AISI 1008, 1040 and 4140 Steels. The Journal of Defense Sciences, 17(2), 139–167.

Aytaç, A., Kuşcu, R., Aytav, E., and Çanakçı, B. (2019). Thermal Batteries: Investigation of Current Technology and Its Future Directions. In Multidisciplinary Studies in the World of Science (pp. 181–203). Berikan Publishing.

Aztekin, K. and Ateş, E. (2015). Machinability Of Unsaturated Polyester Composite And AISI 1050 In Turning. Journal of Multidisciplinary Engineering Science and Technology, vol. 2, no. 11, pp. 3048–3053.

Çakır, U., Çanakçı, B., Aytaç, A., Aztekin, K. (2018). Optimization of Machining Parameters of 7000 Series Aluminum Alloys by Response Surface Method Optimization of Machining Parameters of 7000 Series Aluminum Alloys by Response Surface Method (pp. 482–489). Presented at the International Multidisciplinary Congress of Eurasia-IMCOFE 2018, Barcelona, Spain.

Inasaki, I. (2002). NII-Electronic Library Service. Chemical Pharmaceutical Bulletin, (43), 2091.

Işık, M. S., Aytaç, A., Aztekin, K., Özdemir, T., Çakır, U., Çanakçı, B. (2018). The Effect of Cooling Environment and Tempering Temperature on Wear Resistance of AISI 4140 Steel (pp. 550–560). Presented at the International Science and Technology Conference-ISTEC 2018, Paris, France.

Kohonen, T. (1990). The Self-Organizing Map (Kohonen).pdf. Proceedings of the IEEE, Vol. 78, pp. 1464–1480.

Leave, C., Freeman, J. A., and Skapura, D. M. (1992). Neural Networks: Algorithms, Applications and Programming Techniques. In The Journal of the Operational Research Society (Vol. 43). https://doi.org/10.2307/2584109

Olynk, N. J. (2009). Agricultural Producer Responses To Changes in Consumer Demand for Production Process Attributes. Michigan State University, 2(5), 128.

Özdemir, T., Yavuz, H. İ., Çanakçı, B., Çakır, U., Aytaç, A., Işık, M. S., Aztekin, K. (2018). Micro-Structural & Impact Energy Changes Emerging from Different Welding Processes of MIL-A 46100 Armor Steel (pp. 93–101). Presented at the Internatıonal Congress on New Trends in Scıence, Engineering and Technology-ICONTRENDS 2018, Rome, Italy.

Uğur, L. (2019). Optimization of Surface Roughness by Response Surface Method in Milling 7075 Aluminum Material. Erzincan Üniversitesi Fen Bilimleri Enstitüsü Dergisi, 12(1), 326–335.

Zhao, T., and Jiang, Y. (2008). Fatigue of 7075-T651 aluminum alloy. International Journal of Fatigue, 30(5), 834–849. https://doi.org/10.1016/j.ijfatigue.2007.07.005

DETERMINATION OF THE EFFECT OF SURFACE ROUGHNESS ON FATIGUE STRENGTH OF AISI 4140 STEEL BY USING ARTIFICIAL NEURAL NETWORKS METHOD

CHAPTER

11

Mehmet Arif SALTAN[1]
Abdullah Mahir IŞIK[2]
Tayyar Salih ADIGÜZEL[3]
Murat BAKLACI[4]

[1] National Defence University, Military Academy, Department of Mechanical Engineering, Ankara-Turkey. masaltan@kho.edu.tr

[2] National Defence University, Military Academy, Department of Mechanical Engineering, Ankara-Turkeya. aisik@kho.edu.tr

[3] National Defence University, Military Academy, Department of Mechanical Engineering, Ankara-Turkey. tsadiguzel@kho.edu.tr

[4] National Defence University, Military Academy, Department of Mechanical Engineering, Ankara-Turkey. mbaklaci@kho.edu.tr

1. INTRODUCTION

In cases where durability is desired in machine elements, high carbon content and alloy steels are used. Alloy steels are more preferred than other iron-based materials because of their better mechanical properties (Tayanç et al., 2007). In general, mechanical properties are improved by heat treatments applied to medium and high carbon steels (Aytaç et al., 2018).

The high toughness properties of 4140 reclaimed steels used in chromium and molybdenum alloy steels after quenching and tempering are widely used in applications where fatigue strength is demanded (Işık et al., 2018). This metal alloy has high fatigue strength and good toughness at low temperature (Aytaç and Ilivan, 2019a). In general, AISI 4140 steels are widely used in automotive, aerospace, defense etc. fields where strength and durability are required. In addition, the use of helicopters in pal design is being investigated. (Aytaç et al., 2019).

At the same time in the defense industry of various diameter gun barrels and tracked vehicles; crankshafts and track pins. For these reasons, reclamation steels are the most commonly used and produced steel types after other metals and alloys. In metal alloy materials; fatigue, brittle fracture, overloading, corrosion, high temperature corrosion, creep, abrasion etc. damage is caused. (Feng and Wang, 2002) The most important of these damages and the hardest to detect are errors caused by fatigue. Fatigue can be expressed as a decrease in the mechanical properties of the material or machine parts under dynamic loading. According to the researches, 90% of the damages caused by fatigue were determined (Savaşkan, 2015). Fatigue cracks generally start from the surface of the material. Fatigue damages occur on the surface of the material perpendicular to the maximum tensile strength, but in ductile materials the crack initiation is seen in the plane with maximum shear stress. Fatigue cracks progress in the area of maximum stress. The materials with high fatigue resistance, starting from the center, have high toughness and ductility as well as high yield stress and high strength properties. In the fatigue test, axial bending, torsional stress and combined tensile tests are performed to determine the strength of the materials.(Yalçınkaya, 2019)

The durability of AISI 4140 steels can be achieved by improving the surface properties rather than depending on the unit thickness (Li et al., 2018) The surface properties also determine the safe service life of the part (Davim et al., 2008). Fatigue cracks are generally known to start from the surface surface quality is important. Rough surface material is also likely to be damaged as it may create a notch effect when the load is repeatedly formed. In order to make the materials more useful in their lifetime, processes such as sanding, grinding and sanding are applied to their surfaces (Bilge, 2015)

Two methods are generally used in researches. Some of these studies are to enter the computer program working conditions and material properties to obtain analysis. The other method is laboratory studies in which samples are tested with appropriate test methods under real working conditions. The common point in these studies is to determine the number of tests to be performed. As the number of samples is too high, it will cause a loss of time, especially in the cost, the number of experiments to be performed is as small as possible and the results to be achieved should be as close to the truth. At the same time, the insufficient number of samples will be unsafe. For this purpose, full factorial design is an approach that aims to minimize the amount of error by taking into account all parameters. Thus, full factorial test method, Taguchi and so on. It gives faster and more accurate results than fractional factorial experiments (Aytaç and Ilivan, 2018; Aytaç and Ilivan, 2019b) Factorial design is useful for researching interactions and interactions in engineering studies (Lı et al., 2018) The most important factor in factorial designs is the equal examination of the effects of all parameters on other parameters (Erzurumlu and Oktem, 2007).

Artificial neural networks (ANNs) are intuitive algorithms that can generate new data from the data obtained by remembering, learning, generalizing by imitating the learning techniques of the human brain. ANNs are computer-based programs that simulate biological neural networks with their own memory of all components developed by the human brain inspired by programming logic (Haykin, 2009). ANN makes generalizations with the information obtained from the data entered and makes decisions by using the information learned from the examples that it has never seen before. With the ability to learn and generalize ANN, today, it successfully solves complex problems in many disciplines.

In this study, the effects of process conditions and surface roughness on fatigue strength of AISI 4140 steel were compared with the artificial neural network method of tempering temperature, cooling conditions and surface roughness data obtained by 2^k factorial experimental design method.

2. MATERIALS AND METHODS

2.1 Experimental Design

Full factorial design is defined as the observation of the effect of the result variable according to the input variables. In an experimental study, if there are many factors, factorial experiment design method is used (Aztekin et al, 2018). Factorial experimental design method is obtained by testing all combinations. In this study, 2^k factorial experimental design method, which has 2 levels (low-high), is used. The factors constituting the 2^k factorial experimental design are shown in Table 1.

Table 1: *Levels of three factors investigated on fatigue strength (Aztekin et al., 2018)*

Factors	Statement	Low Level	High Level
A	Surface Roughness	Smooth	Rough
B	Cooling Medium	Water	Salt Water
C	Tempering Temperature	200 ^{0}C	500 ^{0}C

Experimental design was carried out using Minitab-18 statistical software. According to the 2^k factorial experiment design, the number of experiments of 3 factors was calculated as 8. The experiments performed are presented in Table 2.

Table 2: *Experiments to be carried out according to the full factorial test design (Aztekin et al., 2018)*

Number of Experiments	Factors and Levels		
	A	**B**	**C**
1	Rough	Water	200 ^{0}C
2	Rough	Water	500 ^{0}C
3	Rough	Salt Water	200 ^{0}C
4	Rough	Salt Water	500^{0}C
5	Smooth	Water	200 ^{0}C
6	Smooth	Water	500 ^{0}C
7	Smooth	Salt Water	200 ^{0}C
8	Smooth	Salt Water	500 ^{0}C

2.2 Materials and Properties

In the study, AISI 4140 Reclamation Steel, prepared by Aztekin et al., was used as a joint to conduct experimental studies. AISI 4140 ıslah çeliğine ait kimyasal yapı içeriği Tablo 3'de gösterilmektedir. The chemical structure content of AISI 4140 treatment steel is shown in Table 3 .

Table 3: *AISI 4140 Chemical structure of treatment steel*

AISI 4140 Chemical structure of treatment steel			
C	0.41	**Cr**	1.02
Mn	0.12	**Mo**	0.26
Si	0.22	**P**	0.32
S	0.037		

Test specimens were obtained by processing 20 mm shafts prepared according to ASTM E 8M 4 standard on Spinner TC 400 CNC machine. Sample sizes prepared according to standards are shown in Figure 1. Samples prepared in 3D design program are shown in Figure 2.

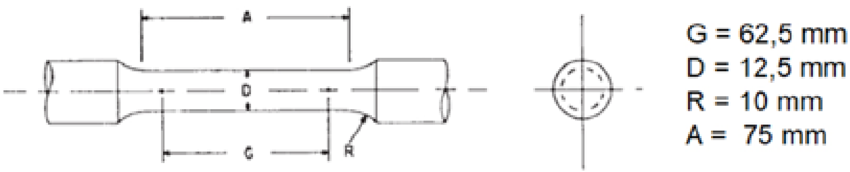

Figure 1: *Sample sizes prepared*

Figure 2: *Samples prepared in 3D design program*

2.3 Preparation of Fatigue Test Sample

Samples to be used in the experiment Figure 3 Nabertherm HT 40/17 annealing furnace was kept for 2 hours until it reached 820 ° C. After waiting 1 hour at 820 ° C, it was hardened by cooling in mains water and brine (10% NaCl). After the samples were hardened, they were divided into groups in an annealing furnace at 500 ° C and 200 ° C and then the samples were kept under this temperature conditions for 1 hour. After this, all samples were allowed to cool to room temperature. All annealing steps were carried out under pure argon gas, an inert gas, to avoid the interaction of materials with the ambient environment.

Figure 3: *Nabertherm HT Heat treatment furnace*

2.4 Surface Roughness

Samples The surface polishing process was carried out using 600, 800 and 1200 sanders on the universal lathe shown in Figure 4 and the average surface roughness value (Ra) was measured. Values obtained from at least 3 points were averaged to ensure measurement reliability. The surface roughness measuring device used in Figure 5 was measured and Ra value was found to be 2.262 µm in rough samples and Ra value was 0.556 µm in roughness reduced samples.

Figure 4: *Sanding process in lathe*

Figure 5:*Surface roughness measuring instrument*

2.5 Fatigue Tests

Fatigue tests were performed on the INSTRON 8803 Servo Hydraulic 500 kN tester at 20 Hz frequency and R = -1 tensile ratio. Before starting the experiment, the diameter of the test specimens were measured and used to calculate the tensile value at break. The tensile average of 3 samples which were not broken after 10 million cycles was accepted as fatigue strength. Figure 6 shows the fatigue tester and test setup. The technical data of the device is also given in Table 4.

Figure 6: *INSTRON 8803 Servo Hydraulic*

Table 4: *INSTRON 8803 Servohidrolik 500 kN*

INSTRON 8803 Servohidrolik 500 kN		
Daylight Opening (Maximum Between Load Cell and Actuator at Mid-stroke, with Largest Capacity Actuator)	mm	1240
	İn	48.8
Dynamic Load Capacity	kN	Up to 250
	Kip	Up to 56
Actuator Stroke (Total)	Mm	Standard offering 150
	İn	5.9
Actuator Force Rating	kN	Standard offering 50/100/250*
Configuration		Twin-Column High Stiffness Load Frame with Actuator in Lower Table or Upper Crosshead
Lift and Locks		Hydraulically-Powered Lifts and Locks
Load Cell		Patented1 Dynacell™ Fatigue-Rated Load Cell with Capacity to Suit Actuator

Load Weighing Accuracy		±0.002% of Load Cell Capacity or 0.5% of Indicated Load, Whichever is Greater - Down to 1/250th of Full Scale
Manifold Options		Single Valve or Dual Valve
Servo-Valve Options	l/ min	5, 10, 20, 40, 65 or 130
		1.3, 2.5, 5, 10, 17 or 34
Hydraulic Pressure Supply (Required)	Bar	207
	psi	3000
Frame Stiffness	kN/ mm	585
Maximum Frame Weight (Dependant on Final Configuration)	Kg	1330
	lb	2929

2.6 ANN Structure and Levenberg-Marquardt Algorithm

Artificial nerve cells are expressed as algorithms created by using the basic features of biological nerve cells. Biological nerve cells collect the signals received from other nerve cells and work as the signal value they collect to transmit to other nerve cells as soon as they exceed the threshold value. At the same time, Artificial Neural Networks are data-based systems obtained by combining artificial neural cells into layers. These systems aim to solve complex problems using simplified models of human brain responses such as learning and sudden decision making under different conditions (Koç, et al., 2004). Cells in artificial neural networks used in engineering; It consists of 5 basic elements: inputs, weights, addition function, activation function and outputs (Öztemel, 2008). Neurons in artificial neural networks are simply classified into layers. All neural networks have a similar structure as shown in figure 7. In this structure, some neurons are connected to the outer space to receive inputs and others to transmit the outputs. All the remaining neurons are hidden and only have connections within the network. (Ataseven, 2013).

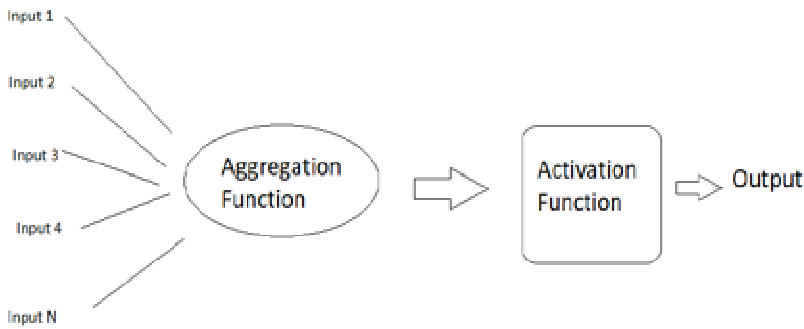

Figure 7: *Neural Network structure*

In artificial neural networks, transitions between layers are defined as the output ranges from threshold functions as [0,1] or [-1,1]. Obtained data should be drawn to these intervals in order to be trained in Artificial Neural Networks. Obtained data should be drawn to these intervals in order to be trained in Artificial Neural Networks. In general, this algorithm uses the least squares calculation method based on maximum neighborhood efficiency. This method is not affected by the slow convergence problem due to its functionality (Saranya and Manikandan, 2013). Equation 1 sigmoid activation function is used in the calculations of Artificial Neural Networks.

$$f(x) = \frac{1}{1 + e^{-x}} \qquad Eq. (1)$$

For ANN education, the data were converted to matrix form and processed. The data translated into the matrix form were trained in the neural network. The Levess-Marquart algorithm for education calculates the value of the Hessian matrix approximately as given in Equation 2.

$$H(t) = J(t)^T J(t) + \mu I \qquad Eq. (2)$$

In the equation, μ is the Marquardt parameter and I is the unit matrix. The matrix J is defined as the Jacobian matrix. The first derivatives consist of derivatives of errors.

$$J(t) = \frac{\partial E(t)}{\partial W(t-1)} \qquad Eq. (3)$$

The network errors vector is shown as Equation 3 in the matrix equation. Jacobian matrix is preferred because it is simpler in structure than Hessian matrix. The weights and gradient of the web are shown in Equations 4 and 5.

$$g(t) = J(t)^T E(t) \qquad Eq.(4)$$

$$w(t+1) = w(t) - [H(T)]^{-1} g(t) \qquad Eq.(5)$$

Tempering temperature, cooling medium and surface roughness were considered as input data for the network trained in Matlab program. Fatigue strength was determined as the output data. At the same time, a hidden layer was created using 15 neurons in the ANN model. 1 input data was obtained by using 3 input data for the training of the network. The generated ANN structure is shown in Figure 8.

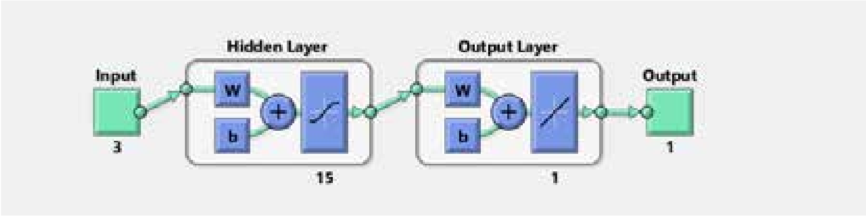

Figure 8: *Structure of Artificial Neural Network*

The mean square error (MSE) is used to determine the error rate between the estimated value and the actual value. Equation 6 shows the equation for the mean square error value.

$$MSE = \frac{1}{n}\sum_{i=1}^{n}(y_i - y_{di})^2 \qquad Eq.(6)$$

Here, the number of data shows the estimated value obtained from the artificial neural network model and the actual value y.

The R value in Eq. 7 shows the degree of conformity of the established artificial neural network model. The fact that the R value is close to 1 indicates that the values obtained from the established model are close to the real value.

$$R = \sqrt{1 - \frac{\sum_{i=1}^{n}(y_i - y_{di})^2}{\sum_{i=1}^{n}(y_{di} - y_m)^2}} \qquad Eq.(7)$$

3. RESULTS AND DISCUSSION

Obtained as a result of network training using Artificial Neural Networks in Matlab program; Mean square error, training regression, validation resection, test regression and graphs of the regression values for the overall network are presented in Figure 9, Figure 10 and Figure 11.

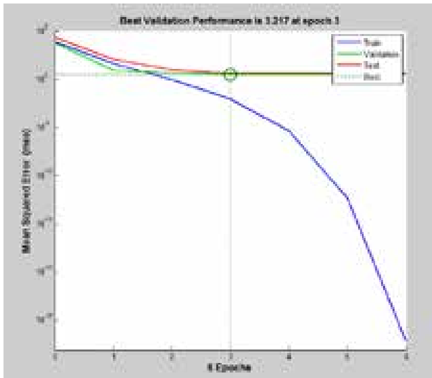

Figure 9: *Mean Square Error Value of Model*

Figure 9 shows the amount of error between the experimental data and the estimated data of the Artificial Neural Network. According to the graph, it is seen that the network makes 6 iterations in total and it reaches the best value with 3,217 in iterations 3. It was determined that the heuristic algorithms that can predict the acceptable error rate are needed because of the loss of time and cost expenses of the experimental studies.

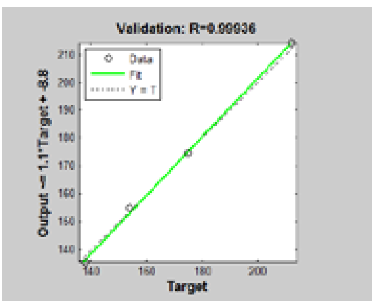

Regression coefficient for verification data

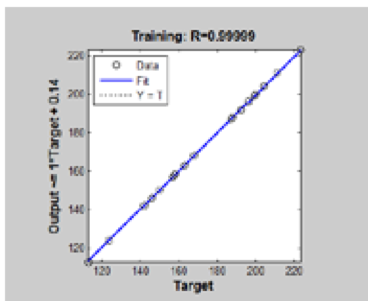

Regression coefficient for training data

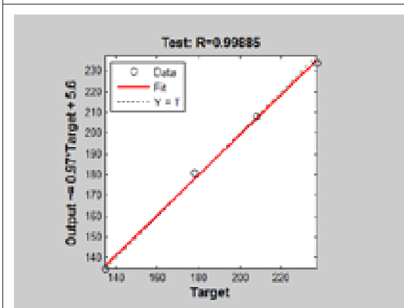

c. Regression coefficient for test data

Figure 10: *ANN Model performance data*

In this study, fatigue strength corresponding to input parameters such as surface roughness, tempering temperature and cooling medium are taken as output. The regression coefficients showing the convergence of the model to the real values gave values very close to 1 for education, estimation and test values (Figure 10). In the graphs, the horizontal axis shows the expected output values and the vertical axis shows the values given by the neural network. R = 0,99943 value was obtained for the overall model. In this case, it shows that the model can be obtained very close to the actual values with the established model (Figure 11). A total of 6 iterations were performed, and the mean square error (MSE) 3,217 for training, validation and test data was achieved at the 3rd iteration, which was the best validation performance (Figure 9). This value indicates that the established model has a high validation capability. As a result, it is expected that the results of the roughness value, cooling medium and cooling temperature values that will be given to the ANN model which has successfully completed the learning process, will be quite realistic from the model.

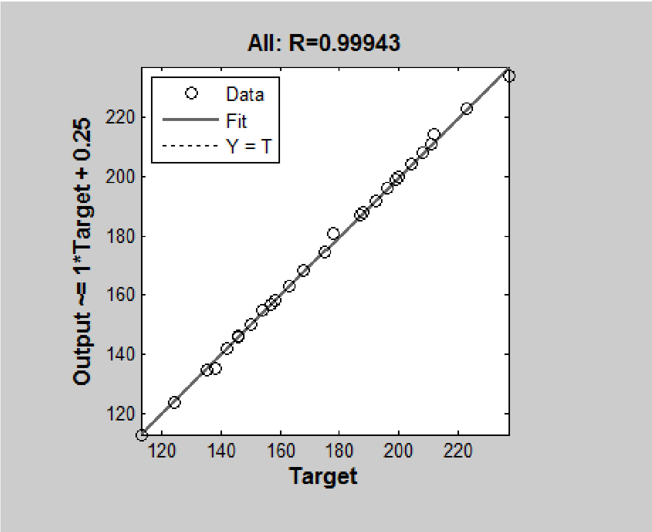

Figure 11: *Regression coefficient for all model*

The graph below compares the predictive and experimental data obtained from ANN. The appropriateness of the ANN model established at this stage of the study was questioned. Matlab based Simulink module was used for this process. Firstly, surface roughness values between 0 and 1 versus air cooling temperature and environment varying in the same value range, different input values were selected from the data entered for teaching ANN model. With this input data, fatigue values were estimated for ANN model by using simulink module. Experimental results were obtained with these input data. Comparison of validation test data and Simulink estimation results is shown in Figure 12.

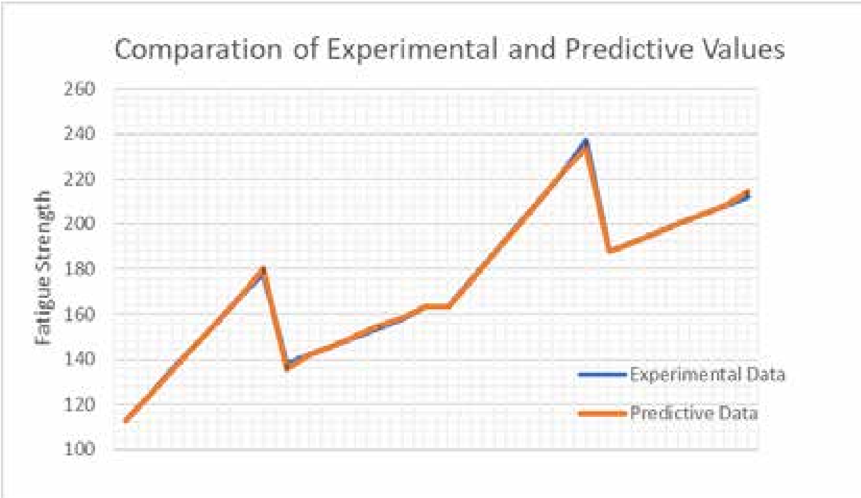

Figure 12: *ANN Verification Result*

4. CONCLUSIONS

In this study, the effect of surface roughness values on fatigue strength was investigated with the model trained with artificial neural networks. It is predicted that the effect of surface roughness on fatigue strength of AISI 4140 steels on fatigue strength by using Artificial Neural Networks method among acceptable error values obtained from ANN model will save time and cost. n this way, the effect of the surface roughness values of the materials used in various systems on fatigue strength is estimated with the network model working between certain fault tolerances. This fatigue strength, which is estimated by an heuristic algorithm, is determined between certain error values without requiring experimental setups with very serious material load.

REFERENCES

Ataseven, B. (2013). Prediction Modeling with Artificial Neural Networks. Öneri Magazine, 10(39), 101-115–115. https://doi.org/10.14783/od.v10i39.1012000311

Aytaç, A., Çanakçı, B., Aslan, B., Aytav, E. (2019). An Analysis of The Reasons That Create Helicopter Vibrations and Vibration Reduction Techniques. In Multidisciplinary Studies in the World of Science (pp. 203–223). Berikan Publishing.

Aytaç, A., and Ilivan, M. (2018). Impact Evaluation of Some Parameters Affecting Surface Qualities by Taguchi Experimental Design Method: An Experimental Study On Heat Treated Low Carbon Wheel Rim. International Journal of Engineering Science Invention (IJESI), 7(10), 76–83.

Aytaç A., and Ilivan M., (2019). Experimental Investigation Of Machinability Properties Of 5035 Steel. The Online Journal of Science and Technology (TOJSAT), 9(2), 171-178.

Aytaç, A., and Ilivan, M. (2019). Investigation Of Factors Affecting Surface Roughness Of Heat Treated 5040 Steel By Experimental Design Method. The Online Journal of Science and Technology (TOJSAT), 9(3), 215–222.

Aytaç, A., Işık, M. S., Çanakçı, B., Özdemir, T., Aztekin, K., İpek, H. (2018). Investigation of Microstructure and Mechanical Properties of Heat Treatment, Carbon Ratio and Alloying Elements in AISI 1008, 1040 and 4140 Steels. The Journal of Defense Sciences, 17(2), 139–165. https://doi.org/10.17134/khosbd.477252

Aztekin, K., Işık, M. S., Aytaç, A., Özdemir, T., Çakır, U., Çanakçı, B. (2018). Effects of Heat Treatment Conditions and Surface Roughness on Fatigue Strength of AISI 4140 Steel (pp. 298–311). Presented at the International Multidisciplinary Congress of Eurasia-IMCOFE 2018, Barcelona, Spain.

Bilge, H. (2015). Effect Of Fatigue Crack Propagation On Natural Frequencies Of System In Aisi 4140 Steel. Abant Izzet Baysal University.

Davim, J. P., Gaitonde, V. N., Karnik, S. R. (2008). Investigations into the effect of cutting conditions on surface roughness in turning of free machining steel by ANN models. Journal of Materials Processing Technology, 205(1–3), 16–23. https://doi.org/10.1016/j.jmatprotec.2007.11.082

Erzurumlu, T., and Oktem, H. (2007). Comparison of response surface model with neural network in determining the surface quality of moulded parts. Materials and Design, 28(2), 459–465. https://doi.org/10.1016/j.matdes.2005.09.004

Feng, C. X., and Wang, X. (2002). Development of empirical models for surface roughness prediction in finish turning. International Journal of Advanced Manufacturing Technology, 20(5), 348–356. https://doi.org/10.1007/s001700200162

Haykin, S. (2009). Neural Networks and Learning Machines (3rd ed.).

Işık, M. S., Aytaç, A., Aztekin, K., Özdemir, T., Çakır, U., Çanakçı, B. (2018, July). The Effect of Cooling Environment and Tempering Temperature on Wear Resistance of AISI 4140 Steel. (pp. 550–560). Presented at the International Science and Technology Conference-ISTEC 2018, Paris, France.

Koç, M. L., BALAS, C. E., and Arslan, A. (2004). Preliminary Design of Ruble Mound Breakwaters by Using Artificial Neural Networks.Teknik Magazine, 15(74). https://doi.org/10.18400/td.91438

Lı, X., Guan, C., and Zhao, P. (2018). Influences of milling and grinding on machined surface roughness and fatigue behavior of GH4169 superalloy workpieces. Chinese Journal of Aeronautics, 31(6), 1399–1405. https://doi.org/10.1016/j.cja.2017.07.013

Öztemel, E. (2008). Yapay Sinir Ağlari.

Saranya, C., and Manikandan, G. (2013). A study on normalization techniques for privacy preserving data mining. International Journal of Engineering and Technology, 5(3), 2701–2704.

Savaşkan, T. (2015). Malzeme Bilimi ve Malzeme Muayenesi.

Tayanç, M., Aztekin, K., and Bayram, A. (2007). The effect of matrix structure on the fatigue behavior of austempered ductile iron. Materials and Design, 28(3), 797–803. https://doi.org/10.1016/j.matdes.2005.11.010

Yalçınkaya, A. (2019). Fatigue Analysis of Shot Peened Tank Track Pins. National Defence University.

CHAPTER

12

INVESTIGATION OF LOW SPEED IMPACT BEHAVIOUR DEPENDING ON THE BONDING AGENT OF GRAPHENE IMPREGNATED FABRIC REINFORCED COMPOSITE PLATES

Ayhan AYTAÇ[1]
Emre AYTAV[2]
Kadir AZTEKİN[3]
Burak ÇANAKÇI[4]

1 National Defence University, Military Academy, Department of Mechanical Engineering, Ankara-Turkey. aytac@kho.edu.tr
2 National Defence University, Military Academy, Department of Mechanical Engineering, Ankara-Turkey. eaytav@kho.edu.tr
3 National Defence University, Military Academy, Department of Mechanical Engineering, Ankara-Turkey. kaztekin@kho.edu.tr
4 National Defence University, Military Academy, Department of Mechanical Engineering, Ankara-Turkey. bcanakci@kho.edu.tr

1. INTRODUCTION

Composite materials with high strength, high stiffness and lightness properties come to the fore in defense field as well as in all industrial areas. Due to the importance of ballistic vests, the works have been going on since the 16th century. With its ease of molding, weaving products are found in a wide range of application areas and also due to their superior energy damping properties, intensive R & D activities are carried out on them. Polyethylene fiber (Dyneema), which is currently widely used for commercial ballistics, is expensive, and product development activities with low density / protection levels have accelerated. Graphene reinforcement applications are examples of composite products. Graphene, where the carbon atoms are connected to each other in a hexagonal form, takes the form of a tube when folded. More robust materials can be obtained by using nanotubes that are lighter and more robust than steel, in the manufacture of different parts of clothing and vehicles used by security forces. The carbon nanotubes forming webs in the material in which they are used are thus more resistant to the weight and force acting on them. Carbon nanotubes can retain their original shape even after being compressed and released thousands of times, just like a soft tissue. Damage analysis and measured resistance with low speed impact tests are an alternative method for ballistic performance of materials.

Thermoset resin matrix composites are increasingly being used as weight-critical structural components in both commercial and military aircraft. In fact, they exhibit higher strength and hardness properties than metallic materials. Moreover, due to the high crosslink densities, thermoset (TS) resins are inherently brittle and therefore have low toughness. Due to their low damage tolerances, their use in structural applications is being improved. Therefore, the development and adaptation of TS composite properties for resistance to impact damage has become an important research topic. (Aytaç & İlivan, 2018; Nash, Young, McGrail, & Stanley, 2015; Sonnenfeld, Mendil-Jakani, Agogué, Nunez, & Beauchêne, 2017; Thakur, Thakur, & Kessler, 2017). Machine elements that are subject to wear or are in contact with impact loads are a matter that needs to be addressed with care from an economic point of view (Gül & İlivan, 2016). There are many types of matrix and reinforcing elements for use in composite applications, and therefore it is possible to produce composites for a wide variety of applications using numerous different combinations.

It was determined that the mechanical properties of the composite were increased by adding graphene to the aluminum matrix. In general, when 0.5% graphene is added to pure aluminum, the maximum tensile strength of the composite increases from 155 MPa to 315 MPa and the micro Vickers hardness value increases from 76 HV to 85 HV. Therefore, it is anticipated that the new generation of these composites may be used in many industrial fields such as automotive, defense industry, aerospace in the near future due to their superior properties (lightness, high strength, etc.). (Şenel, Gürbüz, & Koç, 2017). In addition, graphene can be easily flexed and easily coated on the surface of a variety of materials. In the light of the developments, graphene is expected to be effective on new generation materials in the coming years ("Global Research Report, Materials Science and Technology," 2019; Savage, 2012; Singh et al., 2011).

Celen et al. pre-treated polyester fabrics coated with nano-graphene powders at different concentration rates (50, 100 and 200 g/kg) with knife-over-roll technique. According to the test results, graphene coating generally has a positive effect on the performance properties of polyester fabrics (Manasoglu, Celen, Kanik, & Ulcay, 2019).

Hebert et al. investigated the response of FRP (fiber-glass reinforced polyester) composites to Shock Loading and Drop Weight Impact. They evaluated the impact performance using the energy absorbed by the samples, the depth of penetration, and the extent of internal damage. They produced the samples by infusion of three types of vinylester and one type of urethane resin with different types of glass fibers. They observed that urethane performs better than similar vinyl ester resins. Vinylester resins showed similar impact resistance. Samples with the same resin type but finer textured glass structure showed more consistent performance across all evaluation criteria (Hebert, Rousseau, & Shukla, 2008). It is important to examine the effect of impact tip, impact energy, tip geometry and resin composition on damage resistance, damage tolerance and impact behavior of layered composites.

In this study, drop weight tests of composite plates obtained by molding graphene impregnated denim fabrics in layers with three different resins were performed according to ASTM 7136 standard. The impact behavior of each test group was examined by force-time, force-displacement and energy-time curves. The impact behavior of different resins was investigated using 50, 60 and 70 J energy levels.

2. MATERIALS AND METHODS

Graphene (purity ratio 98%) was added to sprayed Ç3 denim fabric in D 3/1 Z mesh structure produced under controlled conditions selected for the study. The fabric was dried at 35 ° C before production. The structural parameters of the fabric are summarized in Table 1. 3 different resins were applied to the fabrics obtained in SUPERLIT plants. The effects of impact energy on resin after the precision cutting of composite plates were investigated experimentally.

Table 1. *Fabric material properties*

Code	Warp Frequency (1/cm)	Woof Frequency (1/cm)	Weight (gr/m2)	Warp Raw Material	Woof Raw Material	Plate Fabric Weight	Resin Applied Fabric Weight
G1	22	15	329	50% Cotton 50% Polyamide	%95,13 Cotton %4,87 elastane	250*250mm 8 layer 134 gr	BRE310W: 301 gr BRE311W: 291 gr DION9160: 263 gr

2.1. Resins Used in Experiments

Two types of polyester and one type of vinyl ester resin (BOYTEK BRE 310W (orthophthalic resin), BOYTEK BRE 311W (isophthalic resin) and REICHHOLD DION IMPACT 9160 (vinyl ester resin) were used in the study. Unsaturated polyester resins can be grouped as "orthophthalic" and "isophthalic. Vinyl ester resins are similar to the polyester resin. Their most important advantage is that they have an improved bond strength between the fiber and the matrix. These polymers are used in chemical plants, pipes and storage tanks that require chemical resistance. The properties of the resin types used are shown in Table-2.

Table-2. *Resin Properties ("DION® Corrosion Guide—Reichhold—PDF Catalogs | Technical Documentation | Brochure," n.d.; Kaya, 2011)*

Property	Unit	BRE310W	BRE 311W	REICHHOLD DION IMPACT 9160	Test Method/ Application Condition
	-	Polyester (Orthophthalic)	Polyester (İzophthalic)	Vinyl Ester	-
Curing Time	min.	20-30	20-30	20-30	30
Curing Temperature	**°C**	170-190	170-190	170-190	180
Tensile Strength	MPa	65	70	85	ISO 527
Elongation at Break	%	3	3	5	ISO 527
Tensile Modulus	MPa	3500	3600	3250	ISO 527
Flexural Strength	MPa	110	120	155	ISO 178
Flexural Modulus	MPa	3600	3700	3500	ISO 178
HDT	**°C**	80	90	115	ISO 75-A
Hardness	Barcol/ 934-1	45	40	35	ASTM D 2583

2.2. Preparation of Test Plates

Denim fabric layers (total thickness of 8 layers of fabric 6,6 mm) were converted into sandwich structure plates by adding resin by Hand lay-up technique. Precise cutting was made in the form of 57 mm square plates in accordance with ASTM 7136 standards (Figure-1). It has been ensured that notching and delamination does not occur during the sample cutting process. The structure of the plates and the resin reinforcement by Hand lay-up technique are shown schematically in Figure 1. The application of the resins is shown in Figure 2.

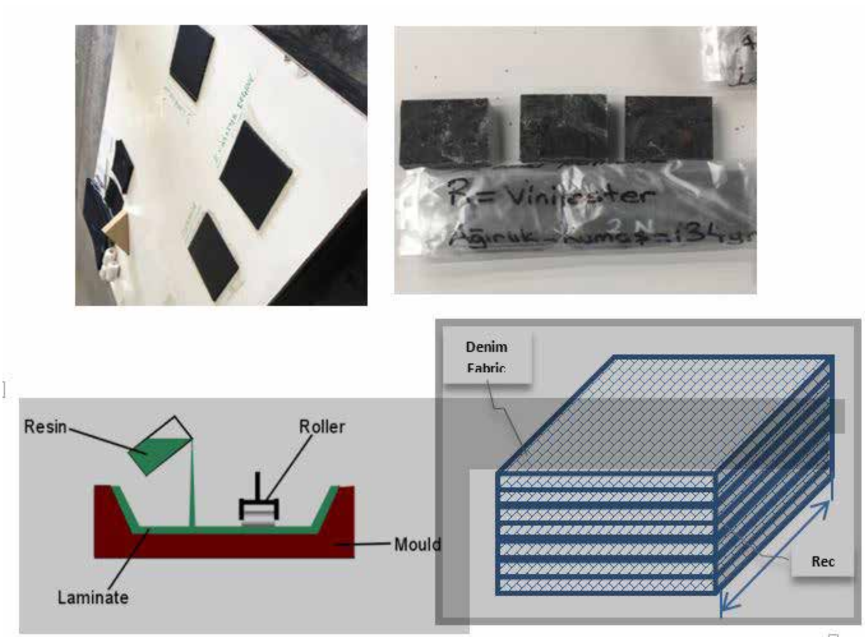

Figure 1 *Hand lay-up process and plate preparatio*

The design and production of the samples were made according to the criteria specified in ASTM standards. The layers are semi-isotropic (equal number of layers oriented at + 45 ° and -45 ° angles), balanced and symmetrical. Thicknesses are intended to be 6.5 mm. The total number of layers is 8.

2.3. Experimental Design

Drop weight impact tests were performed on three samples as 50, 60 and 70 J using 10 mm hemispherical end geometry. Experimental design matrix is presented in Table-3.

Table-3 *Experimental Design Matrix*

Experiment No	Resin	Impact Energy (J)	Tup Diameter (mm)
1	BRE310W	50	10
2	BRE311W	60	10
3	DION9160	70	10
4	BRE310W	60	10
5	BRE311W	70	10
6	DION9160	50	10
7	BRE310W	70	10
8	BRE311W	50	10
9	DION9160	60	10

2.4. Low Speed Impact Tests

Low speed impact tests were performed in MSÜ (National Defense University) material testing laboratory using Instron CEAST 9350 Droptower Impact System tester. Samples were made with 50, 60 and 70 J energy adjustment using a 10 mm diameter hemispherical tip. The features of the device are given in Table-4.

Table-4 *Operational Spesifications of CEAST 9350*

Operatıonal Range	without additional Energy System	with additional Energy System
Mass [kg] *	**2 to 5 (LH) 5 to 30 (SH) 5 to 70 (SHA)**	
Drop height [m]	0.03 to 1.1	**0.03 to 29.4 (equivalent, depending on the mass)**
Speed [m/s]	0.77 to 4.65	**0.77 to 24 (depending on the mass)**
Energy [J] *	0.59 to 54 (LH) 1.5 to 324 (SH) 1.5 to 757 (SHA)	**0.59 to 830 (LH)** **1.5 to 1250 (SH)** **1.5 to 1800 (SHA)**
Temperature [°C]	-70 to 150 (for Thermostatic Chamber, depending on the accessories)	

(*) LH: Light Falling Mass; SH: Standard Falling Mass; SHA: SH with Additional Falling Mass

The drop weight impact test is based on the principle of obtaining data on the mechanical behavior of the sample when a mass equipped with sensors is released from a certain height and strikes the sample. The working diagram of the test device is given in Figure 2.

Once the device has been set up and the data acquisition program has been run, the mass is allowed to fall free and hit the plate. The velocity (V_i) of the striking mass is measured by the sensor just before hitting the sample. The graphs are obtained by using the equations given below by CEASTVIEW 6.33 software.

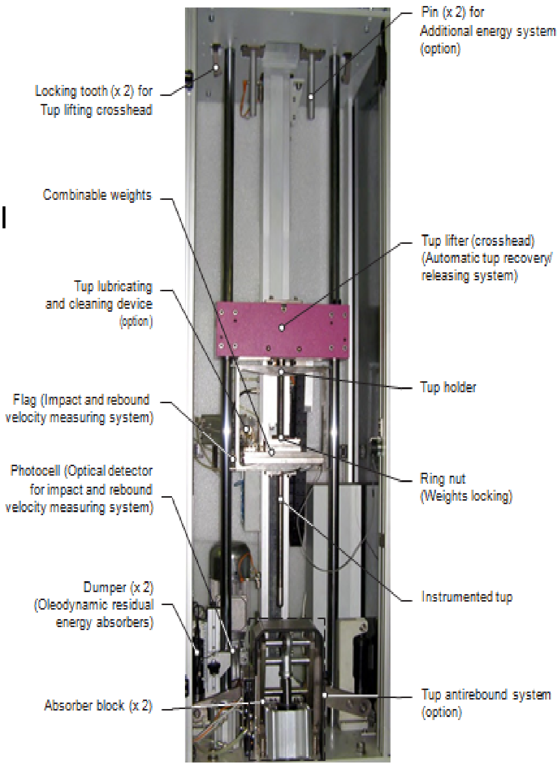

Figure 2 *Instron CEAST 9350 drop weight testing machine*

The velocity at the moment of impact (V_0) is expressed as Equ.3.1.

$$V_0=\sqrt{2gH} \tag{3.1}$$

The impact energy (E_0), the kinetic energy of the head, is expressed in Eq.3.2.

$$E_0 = \frac{1}{2}MVo^2 \quad = E_{Elastik}+E_a \tag{3.2}$$

Elastic energy ($E_{elastic}$) is the energy released by the sample and is calculated according to the acceleration, force and displacement at the moment of rebound. The absorbed energy (E_a) is the difference between the impact energy (E_0) and the elastic energy ($E_{elastic}$) and is the energy that causes damage to the sample such as matrix cracking and fiber breakage. It is also the energy absorbed by the sample in the form of vibration and heat and by the impact tester by the inelastic behavior of the striking mass and its connections.

2.5. Penetration Depth and Hardness Measurement

The depth of penetration is defined as the distance between the surface plane of the sample and the deepest collapse point in the normal direction of the surface of the sample. When evaluating the damage structure, first of all, the macroscopic damage caused by impact load was examined visually. Measurements were made with at least three point measurements based on edge points.

The Shore A Hardness Tester measures the hardness of flexible mold tires ranging from very soft and flexible, medium and slightly flexible, hard and almost non-flexible. Hardness measurements were measured using Shore A Durometer. Measurement process and hardness measuring device are shown in Figure 3.

Figure 3 *Comparator and hardness measurement device*

3. RESULTS

3.1. Effect of Energy Increase on Impact Behavior of Material

After the impacts in 50, 60 and 70 J energy intervals in the weight reduction tests, the damage structure of the sample was examined from the obtained data and cross-sectional images taken from the sample. The point at which the first sudden force drop is detected is defined as the Hertzian damage threshold. This point indicates the formation of matrix cracking or delamination in the composite material. The starting point, where the pulse energy is stationary or flat, gives the critical energy level. Penetration, rebound and perforation formation at 70J energy level where damage is most evident is shown in Figure-4. Figure 5 shows the critical displacement data at 50 and 70J energy level.

BRE310W

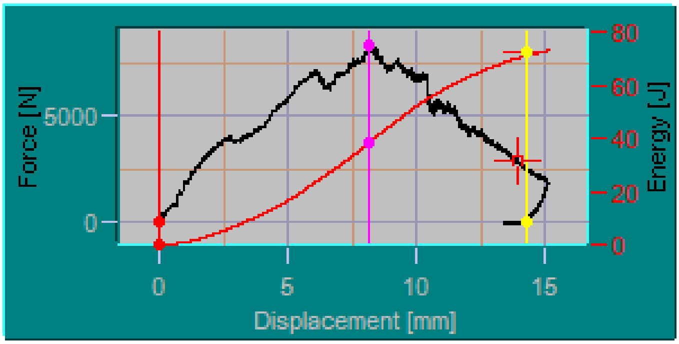

BRE311W

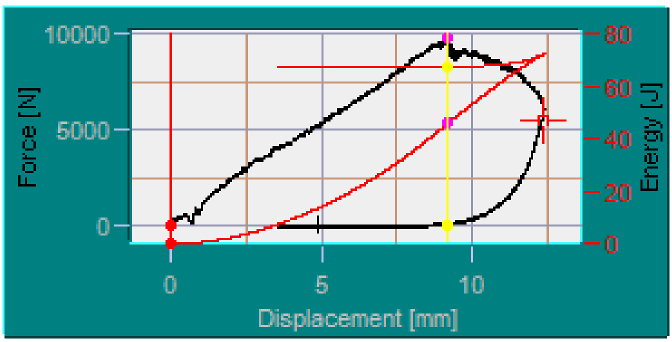

DION9160

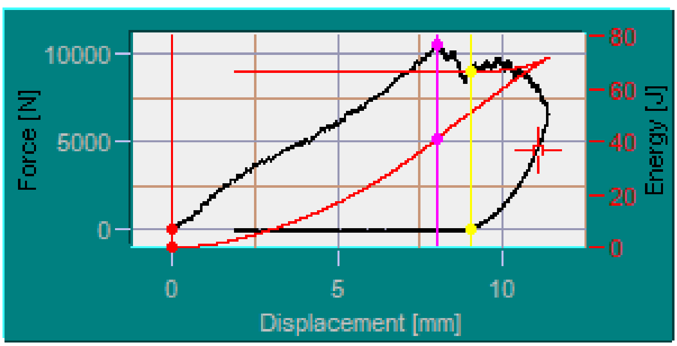

Figure-4 *Force-Absorbed Energy-Displacement graph (70J)*

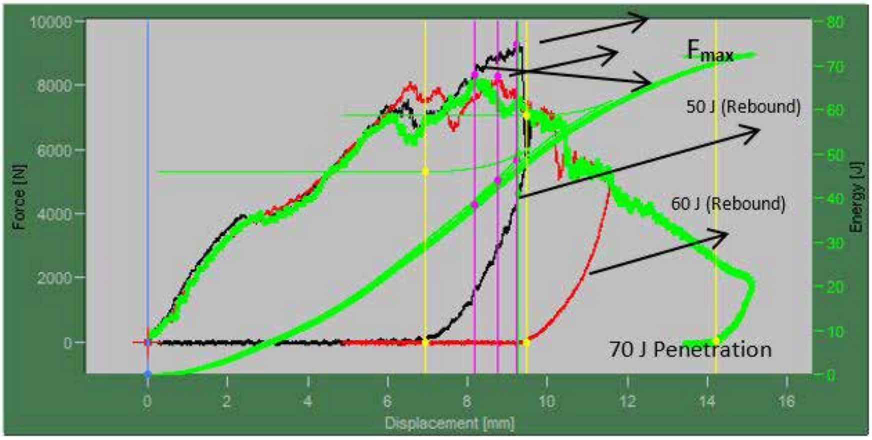

Figure-5. *Force-Displacement graph of BRE310W resins at 50,60 and 70 J energy level*

When the energy-time curve is examined, the energy levels of 50-60J and 70J BRE311W / DION9160 resins exhibit rebound behavior decrease after the energy reaches the maximum level. When penetration occurs, it remains constant. Full perforation does not occur from the increase in energy level can be determined.

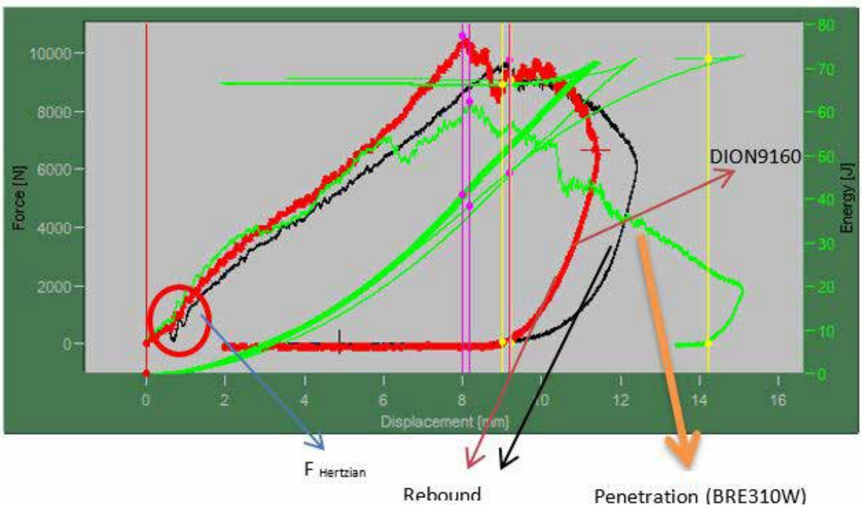

Figure 5. *Resin types at 70 J energy level Force-Displacement graph*

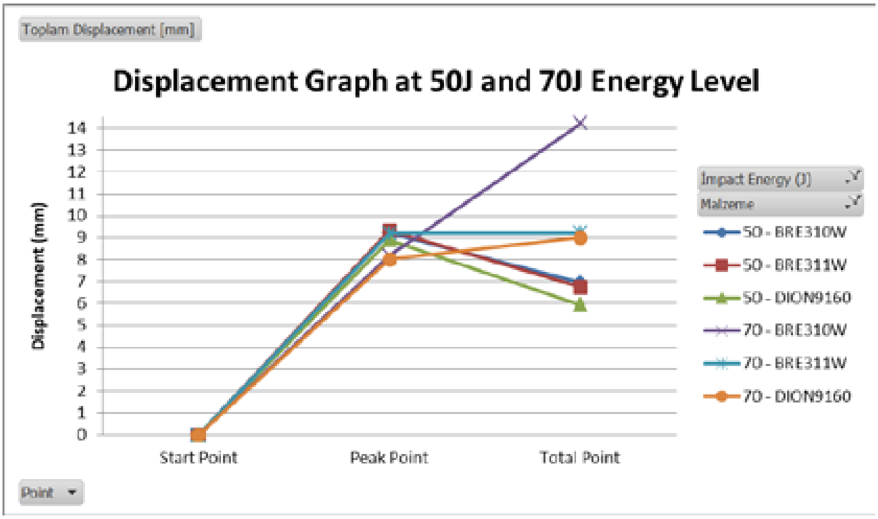

Figure 6 *Displacement graph at critical energy levels (50 and 70 J)*

When the displacement graph is examined, the damage of the BRE311W and DION9160 resins is similar, while the BRE310W resin has a significant damage rate.

3.2. Damage Analysis

Resin	İmpact Energy (J)	Impact Front Surface	Impact Back Surface	Top View
BRE310W (Orthophaltic)	50			
	60			
	70			

BRE310W (İzophaltic)	50		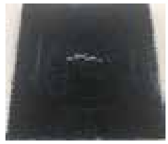	
	60			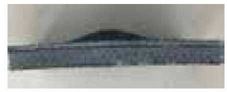
	70			
DION9160 (Vinil Ester)	50			
	60		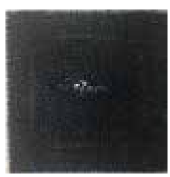	
	70			

Figure 7 *Front-back side images of samples after impact at all energy levels*

The cross-sectional images taken perpendicular to the tear (damage) line are shown in Figure 7 in order to understand the impact effect more clearly.

When the Figures 7 and 8 are examined, it is observed that the amount of damage increases due to the increase in energy. BRE 310W (orthophthalic) resins have less impact on the contact area due to their low impact energy due to their glassy structure, but they cause deflection on the wider area of the rear surface. In addition, the tear of the vinyl ester resin type did not occur in comparison to other resins in accordance with the elongation at break. BRE 311W (Izophthalic) resin shows similar damage behavior as vinyl ester resins.

Impact Energy (J) (50 J)	BRE310W BRE311W DION9160	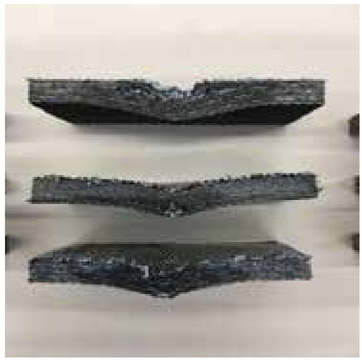
Impact Energy (J) (60 J)	BRE310W BRE311W DION9160	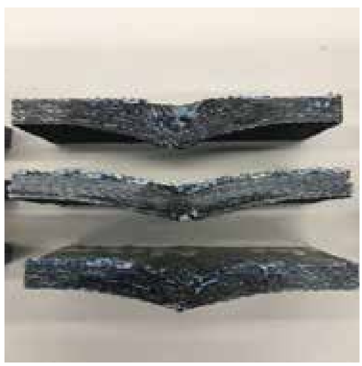
Impact Energy (J) (70 J)	BRE310W BRE311W DION9160	

Figure 8 *Cross-sectional views after impact test*

Due to the low amount of % elongation, the tensile stress of the fibers occurred as a result of the spread of the damaged area over a large area and fiber breakage occurred. The cross-sectional images overlap with the energy-damage depth data obtained in Figure-8. When examined in Figure-9, although all three resins showed similar behavior at the smallest 50 J impact energy applied, BRE311W and DION9160 resins performed better with energy increase.

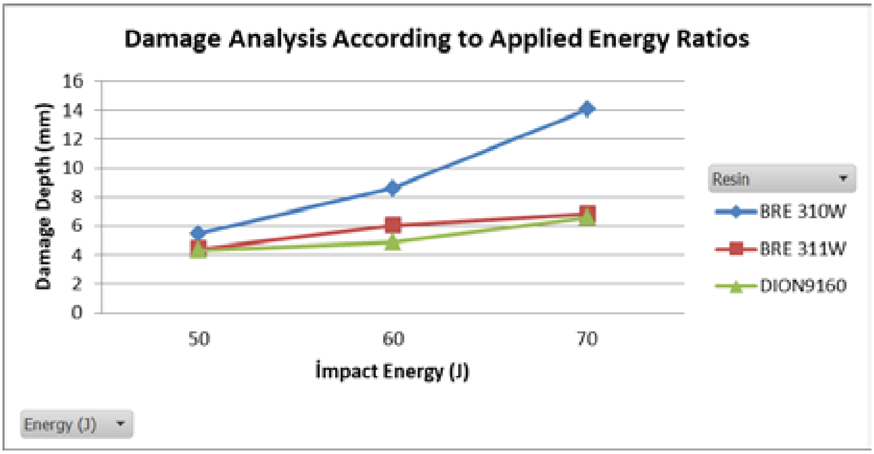

Figure 9. *Damage analysis graph*

The hardness values of the composite materials are given in Figure 10. Due to the increase in hardness, the impact energy damping property also increases.

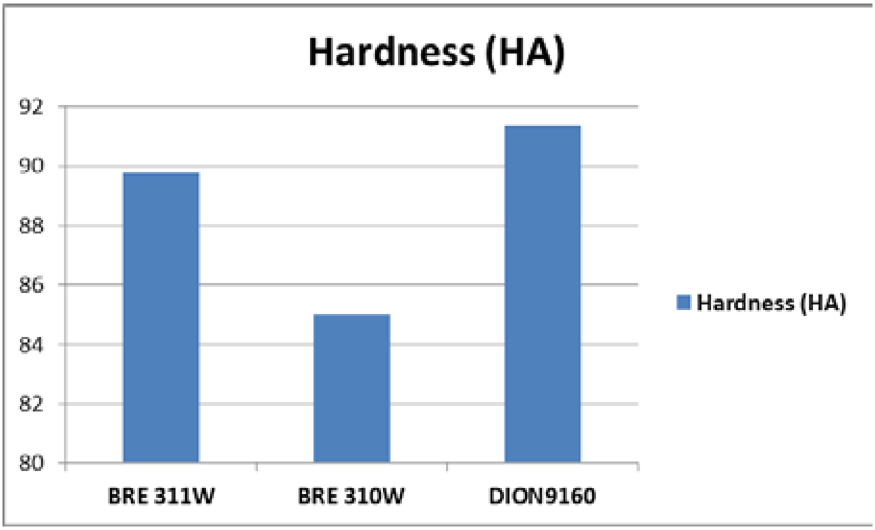

Figure 10. *Hardness measurement results*

4. CONCLUSION

In this study, two types of resin types (BRE 310W (orthophthalic), BRE 311W (isophthalic) and DION9160 (vinylester) were used in experimental study. The numerical data obtained and the results of the image analysis and evaluation results are presented below with recommendations.

1. As a result of hardness measurements, the highest hardness value was obtained in DION9160 vinyl ester resin.
2. Although the three resins showed similar behavior at the smallest 50 J impact energy applied, the BRE311W and DION9160 resins performed better with the increase in energy.
3. Although BRE311W and DION9160 resins have similar performance, due to the low% elongation of the BRE311W resin, the tensile stress on the fibers resulting from the spread of the damage area over a large area has caused fiber breakage.
4. BRE 310W resin performance decreases significantly at high impact energies.
5. It is suggested that it is useful to search for inserts with different profile geometries and composite production variables.

REFERENCES

Aytaç, A., & İlivan, M. (2018). Scientific Studies in the Area of Mechanical Engineering: A Descriptive Analysis Related To Researches in Turkey. *American Journal of Engineering Research*, *7*(12), 87–96.

DION® Corrosion Guide—Reichhold—PDF Catalogs | Technical Documentation | Brochure. (n.d.). Retrieved September 22, 2019, from https://pdf.directindustry.com/pdf/reichhold/dion-corrosion-guide/37855-629859-_9.html

Global Research Report, Materials Science and Technology. (n.d.). Retrieved September 22, 2019, from Studylib.net website: https://studylib.net/doc/9739988/global-research-report--materials-science-and-technology

Gül, F., & İlivan, M. (2016). SiO2 takviye edilmiş Al kompozitlerin abrasiv aşınma davranışını etkileyen faktörlerin istatistiksel analizi. *Proceeding Book*, 1799–1809. Antalya.

Hebert, M., Rousseau, C.-E., & Shukla, A. (2008). Shock loading and drop weight impact response of glass reinforced polymer composites. *Composite Structures*, *84*(3), 199–208. https://doi.org/10.1016/j.compstruct.2007.07.002

Kaya, D. (2011). *Effect of resin and fiber on the abrasion, impact and pressure resistance of cylindrical composite structures* (Master Thesis). Middle East Technical University, Ankara.

Manasoglu, G., Celen, R., Kanik, M., & Ulcay, Y. (2019). Electrical resistivity and thermal conductivity properties of graphene-coated woven fabrics. *Journal of Applied Polymer Science*, *136*(40), 48024. https://doi.org/10.1002/app.48024

Nash, N. H., Young, T. M., McGrail, P. T., & Stanley, W. F. (2015). Inclusion of a thermoplastic phase to improve impact and post-impact performances of carbon fibre reinforced thermosetting composites—A review. *Materials & Design*, *85*, 582–597. https://doi.org/10.1016/j.matdes.2015.07.001

Savage, N. (2012). Materials science: Super carbon. *Nature*, *483*(7389), S30–S31. https://doi.org/10.1038/483S30a

Şenel, M. C., Gürbüz, M., & Koç, E. (2017). The fabrication and characterization of graphene reinforced aluminum composites. *Pamukkale University Journal of Engineering Sciences*, *23*(8), 974–978. https://doi.org/10.5505/pajes.2017.65902

Singh, V., Joung, D., Zhai, L., Das, S., Khondaker, S., & Seal, S. (2011). Graphene Based Materials: Past, Present and Future. *Progress in Materials Science*, *56*, 1178–1271. https://doi.org/10.1016/j.pmatsci.2011.03.003

Sonnenfeld, C., Mendil-Jakani, H., Agogué, R., Nunez, P., & Beauchêne, P. (2017). Thermoplastic/thermoset multilayer composites: A way to improve the impact damage tolerance of thermosetting resin matrix composites. *Composite Structures*, *171*, 298–305. https://doi.org/10.1016/j.compstruct.2017.03.044

Thakur, V. K., Thakur, M. K., & Kessler, M. R. (2017). *Handbook of Composites from Renewable Materials, Physico-Chemical and Mechanical Characterization*. John Wiley & Sons.

MODELING OF PARAMETERS AFFECTING THE PERFORMANCE OF S833 AIRFOIL BY ARTIFICIAL NEURAL NETWORK METHOD

CHAPTER

13

Burak ÇANAKÇI[1]
Emre AYTAV[2]
Murat BAKLACI[3]
Murat ŞAHİN[4]

1 National Defence University, Military Academy, Department of Mechanical Engineering, Ankara-Turkey. bcanakci@kho.edu.tr
2 National Defence University, Military Academy, Department of Mechanical Engineering, Ankara-Turkey. eaytav@kho.edu.tr
3 National Defence University, Military Academy, Department of Mechanical Engineering, Ankara-Turkey. mbaklaci@kho.edu.tr
4 National Defence University, Military Academy, Department of Mechanical Engineering, Ankara-Turkey. msahin@kho.edu.tr

1. INTRODUCTION

Fossil fuels are the largest source of energy consumed. In order to meet the energy needs of fossil fuels due to the damages to the environment and the sources of these resources, they are looking for alternative energy sources. When future plans in energy production are examined, it is predicted that petroleum-derived fuels will no longer be the main energy source (Aytaç et al., 2019a). Among the alternative energy sources, thermal batteries with their robust structures are remarkable for their use in weapon systems (Aytaç et al., 2019b). Because it is easy to convert to utilizable energy, windenergy used widely since ancient times It was found Conversion of wind energy to electrical wind turbines through. The aerodynamic properties of the airfoil to be selected play an important role on the performance of wind turbines. When deciding the airfoil to be selected,basic aerodynamic properties; lift force (L), drag force (D), pitching moment (M) and these forces/moment are calculated without dimension, lift coefficient (C_L), drag coefficient (C_D), pitching coefficient (C_M) are taken into consideration. C_L/C_D ratio is used for performance comparison and analysis of airfoil. Determination and calculation of aerodynamic parameters can be done experimentally by wind tunnel tests or theoretically by computational fluid dynamics analysis. Another method by which the effect of parameters such as wind speed, angle of attack and wing surface condition on performance and the interaction between these parameters can be examined is a full factorial experimental design method (Çanakçı et al., 2018). In addition to these methods, ANNs are emerging as an alternative method for aerodynamic investigations of wing profiles. However, in the application of all these scientific analysis methods; In addition to revealing the problem that is desired to be solved, it is more important to implement the solution and reach the right result (Aytaç and İlivan, 2018).

An artificial neural network is called an algorithm that can perform the operations of the brain, make decisions, draw conclusions, reach the result from the existing information in case of insufficient data, accept continuous data input, learn and remember. The artificial nerve cell is an information processing technology developed by simulating the way the biological nervous system works, inspired by the information processing technologies of real nerve cells. ANNs are complex systems that are formed by connecting artificial neurons to each other with different connection geometries (Oztemel, 2012).

ANN differs from computational techniques that require special processing. It is widely used in the solution of nonlinear problems. ANN, similar to the information processing method of the brain, collects information, stores and generalizes the information with the connection weights between cells. The concept of generalization can be defined as the fact that ANN generates similar responses for entries that it does not encounter during education or learning. McCulloch and Pitts developed the first cell model and studied the interconnection of several cells. Hebb suggested the first learning rule to adjust cell connections (Yalcin et al., 2005). The studies on ANN have gained widespread use in the fields of industry, finance, defense and health.

ANNs can learn key examples of information from a multidimensional database rather than complex mathematical methods and algorithms (Kalogirou, 2000). ANN is a model system based on the human brain. ANN try to solve problems that cannot be solved by classical methods, similar to the brain's working system (Dorvlo et al., 2002)

In the recent years, ANN's applications in aerodynamics have become very popular due to the ease of complex calculations, cost and time savings. The ANN method can be used very efficiently in estimating optimum wing geometry and reducing costs. In a study, lift and drag force data were processed based on the estimation on wing geometry. It was stated that the validation test results after modeling were in the range of 0,61-0,59% (Sun et al., 2015). For the analysis of aerodynamic loads of unmanned aerial vehicles, finite element analysis (FE) and computational fluid dynamics (CFD) analysis can be utilized in the design process. In a study using the results obtained from this study, ANN was used for the examination of pressure points. It has been observed that the use of ANN is much more reliable than other regression techniques (Mazhar et al., 2013)

The biggest problem that decreases the efficiency of wind power systems is the change in wind speed and the discontinuity of the wind. So, the continuity of the energy produced becomes an important problem in wind power facility. Pitch control appears to be a useful method for power regulation above the nominal wind speed. In studies conducted to model the inclination angle controller with multi-layer artificial neural networks, it has been observed that turbine power output can be obtained adequately at variable wind speeds and overloads can be prevented (Yilmaz and Özer, 2009).

In this study, airfoil performance analyzes were carried out with a ANN based model using Matlab program. Verification experiments of the neural network model established differently from the literature were performed and compared with Matlab Simulink results. With the ANN model, the performance of the S833 aitrfoil can be estimated at different wind speeds and angle of attack, rather than long experiments in the laboratory.

2. MATERIALS AND METHODS

The S833 airfoil selected for the study was modeled in computer environment using the coordinates developed by NREL and manufactured from ABS material with the size of 200x200 mm Fortus 250 MC 3D Printer (Figure 1.a,b). The produced airfoil was tested at different wind speeds and angle of attack in the TecQuipment AF 100 subsonic wind tunnel (Figure 2.a) with a maximum wind speed capacity of 37 and a test cabinet (Figure 2.b) size of 300x300x600 mm. During the experiments, three-component balancer (Figure 2.c) integrated in the wind tunnel was used to measure lift, drag forces and pitch moments.

As a result of the experiments, the data were recorded with the data collection software prepared according to the wind tunnel type and C_L, C_D and C_M coefficients and C_L/C_D ratio to be going to used in ANN model were calculated.

a. Fortus 250 MC 3D printer

b. Manufactured airfoil

Figure 1. *Manufacturing of the S833 airfoil*

a. Subsonic wind tunnel

b.Wind tunnel workspace

c. Force measurement balancer

Figure 2. *Wind tunnel used in experimental studies*

2.1 Aerodynamic Performance Parameters of Airfoils

Since the flow on airfoil is often close to two-dimensional, in the examination of the flow properties, it is sufficient to examine the flow around a single section as the flow properties remain the same across all sections of the wing opening. The aerodynamic efficiency in a wing profile is related to the buoyancy, drag force around the wing profile and the ratio of these two forces to each other (Seifert et al., 2004) Increasing the camber of the airfoil increases the area on the top surface of the airfoil, which increases the speed of the air passing over the airfoil. As a result, the increase in pressure difference between the lower surface and the upper surface of the blade increases the lift forceand performance increase. S833 airfoil geometry is shown in Figure 3.

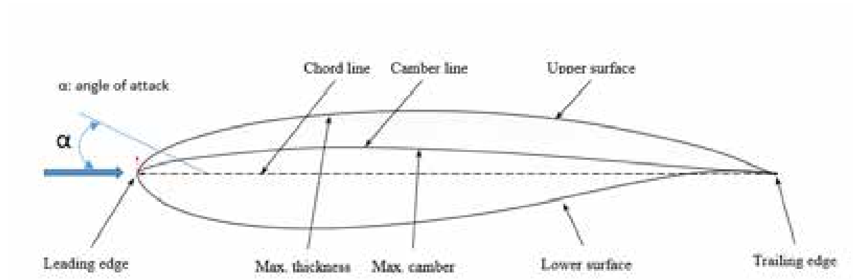

Figure 3. *S833 Airfoil geometry*

Two forces (drag and lift) components and a moment (pitching) component affect on the airfoil (Rajadurai et al., 2008). The lift force and pitching moment are generally dependent on the pressure distribution along the airfoil surface. Drag force depends on the pressure and friction distribution across the surface.

Wing profiles have been developed for various purposes in a wide variety of shapes and sizes. Dimensionless coefficients are taken into consideration in comparisons and evaluations C_L (Eq.1) and C_D coefficients (Eq.2) which are considered in performance evaluation of wing profiles are calculated in two dimensions as follows. After calculating these coefficients without dimension, C_L/C_D ratio can be used in comparisons. Also, the moment component acting in the profile lift-drag plane is defined as the pitching moment coefficient (Eq.3) (Houghton and Carpenter, 2003).

$$c_L = \frac{L}{(1/2)\rho V^2 S} \qquad \text{Eq. (1)}$$

$$c_D = \frac{D}{(1/2)\rho V^2 S} \qquad \text{Eq. (2)}$$

$$c_M = \frac{M}{(1/2)\rho V^2 S_C} \qquad \text{Eq. (3)}$$

In equations, L lift force, D drag force, M moment, V wind speed, ρ fluid density, S airfoil surface area and Sc shows the multiply of the airfoil surface area with the cord length of the airfoil.

2.2 ANN Structure and Levenberg-Marquardt Algorithm

ANN consists of an input layer, one or more intermediate layers and an output layer. Neurons in all layers except the output layer are bound to all of the neurons in the next layer, and all of these connections have a weight value. The working structure of neurons in the network is generally presented in Figure 4. Each neuron produces its output by transferring the total input to the activation function (Demuth and Beale, 2000). The total input is the sum of all the inputs to a neuron multiplied by their own weight values. ANN is trained with sample data to learn the relationship between inputs and outputs. Learning or training is performed by updating the weight values of the links. The training of ANN is carried out through a cyclical process (Haykin, 1994) (Schalkoff, 1997).

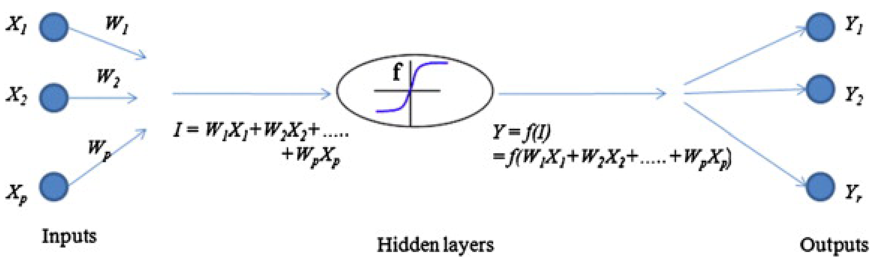

Figure 4. *Working of neural network (Mazhar et al., 2013)*

In ANN, when transition between layers in, the data passes through the threshold functions The output ranges of these threshold functions are in the range [-1,1] or [0,1]. The use of raw data on ANNs is dependent on the traction of data into these ranges. In many applications, the actual value needs to be normalized between “0” and “1”. Normalization is one of the most basic preprocessing methods. In this way, the education and learning performance of ANN can be improved (Visalakshi and Kuttiyannan, 2009).

In this study, Levenberg-Marquardt learning algorithm, which can learn fast and has good convergence feature, was used to train ANN. Basically, this algorithm is a method of calculating least squares based on the idea of maximum neighborhood. This method is not affected by the problem of slow convergence (Saranya and Manikandan, 2013). In the calculations, sigmoid activation function was used for ANN modeling. All inputs and outputs are normalized in the [0 1] range. A multilayer feed forward (Multilayer Perceptron with feed forward, FF-MLP) ANN network structure; It contains 2 input data (wind speed, angle of attack), 1 hidden layer, 4 output data (C_L, C_D, C_M, C_L/C_D).

Wind tunnel tests of S833 airfoil were performed at angle of attack between -10° and +29° in corresponding to the wind speeds ranging 5 m/s to 37 m/s . Experimental design matrix is presented in Table 1.

Table 1. *Experimental design matrix*

Exp. Nu.	Angle of Attack	Wind Speed	C_M	C_L	C_D	C_L/C_D
1	-10°	5 $m.s^{-1}$	0,000	-0,111	0,030	-3,703
2	-8°	7 $m.s^{-1}$	0,000	-0,238	0,069	-3,454
3	-5°	37 $m.s^{-1}$	0,020	-0,332	0,068	-4,894
4	-3°	8 $m.s^{-1}$	0,059	-0,183	0,050	-3,660
5	0°	12 $m.s^{-1}$	0,070	-0,100	0,048	-2,100
6	3°	15 $m.s^{-1}$	0,090	0,005	0,058	0,085
7	6°	8 $m.s^{-1}$	0,082	0,162	0,061	2,661
.	.	.	.	.	.	.
.	.	.	.	.	.	.
396	10°	20 $m.s^{-1}$	0,134	0,294	0,087	3,384
397	12°	25 $m.s^{-1}$	0,151	0,407	0,100	4,070
398	15°	6 $m.s^{-1}$	0,048	0,350	0,114	3,070
399	20°	15 $m.s^{-1}$	0,199	0,937	0,275	3,433
400	29°	30 $m.s^{-1}$	0,158	1,410	0,664	2,124

Of the 400 data obtained as a result of the experimental design, 65% were randomly selected as training data, 20% as validation data and 15% as test data.In the analysis performed using Matlab program, sigmoid was selected for the input layer and linear activation functions were selected for the output layer. In order to determine the most suitable network structure, experiments were conducted with a large number of different network structures and neurons. As a result of the experiments, the most suitable network structure was determined for the output data (C_L, C_D, C_M, C_L/C_D). In the ANN model with the most appropriate network structure, a single hidden layer of 25 neurons was used. The internal structure diagram of the designed ANN is presented in Figure 5.

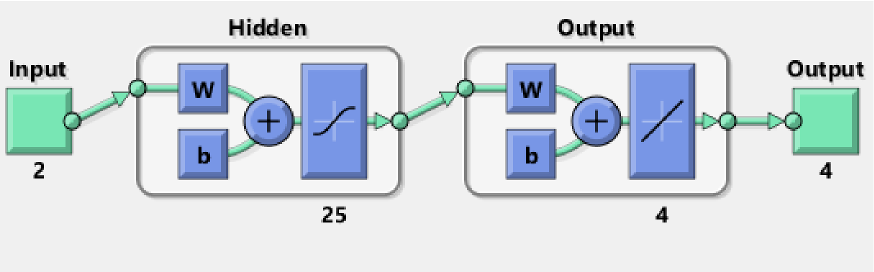

Figure 5. *Diagram of the internal structure of the ANN designed*

The ANN model performance was calculated by means of mean square error (MSE) and regression coefficient (R). MSE (Eq.4) is used to determine the error rate between the estimated value and the actual value. The MSE value should be close to zero for the model to have high predictive capabilities.

In the equation, n is the number of data, y_i is the estimated value obtained from the neural network model, y_{di} is the actual value. The degree of conformity of the ANN model shows the R (Eq.5) value. The fact that the values obtained from the model are close to the actual values depends on the fact that R value is close to 1 value.

In the equation y_m is the average of the actual values.

3. RESULTS AND DISCUSSION

3.1. Neural Network Optimization

The regression coefficients, which show the convergence of the model to the real values, yielded values quite close to 1 for training, estimation and test values (Figure 6.a;c). In the graphs, the horizontal axis shows the expected output values and the vertical axis shows the values given by the neural network. R=0,99058 value was obtained for the model. In this case, it is possible to obtain values very close to the actual values with the established model. 60 iterations in total were performed and the MSE of 0,09207 for training, verification and test data was achieved in the 54th iteration, which is the best verification performance (Figure 7). This value indicates that the established model has a high validation capability. As a result, it is expected to obtain very close to reality results from the model for the different wind speed and angle of attack values to be given to the ANN model which has successfully completed the learning process.

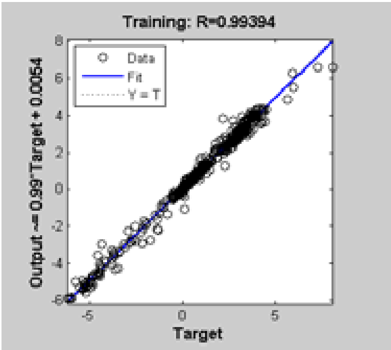

a. Regression coefficient for training data

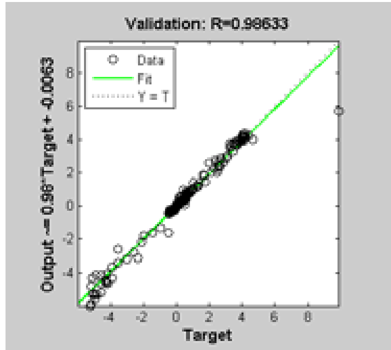

b. Regression coefficient for verification data

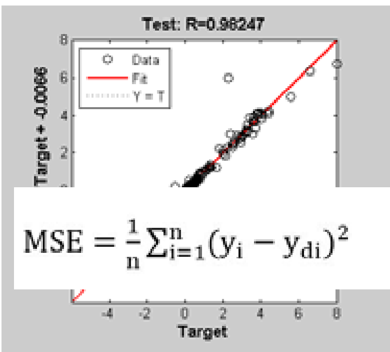

$$MSE = \frac{1}{n}\sum_{i=1}^{n}(y_i - y_{di})^2 \qquad \text{Eq. (4)}$$

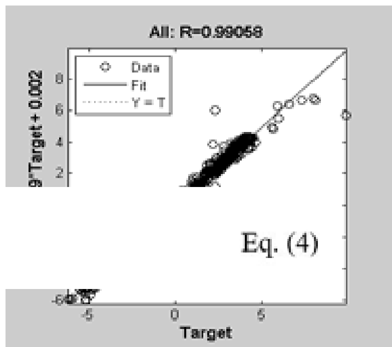

c. Regression coefficient for test data

d. Regression coefficient for all model

Figure 6. *Performance data of ANN model*

$$R = \sqrt{1 - \frac{\sum_{i=1}^{n}(y_i - y_{di})^2}{\sum_{i=1}^{n}(y_{di} - y_m)^2}} \qquad \text{Eq. (5)}$$

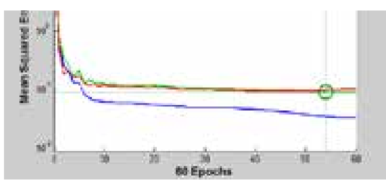

Figure 7. *MSE value of the model*

3.2 Verification of ANN Model

The appropriateness of the ANN model established at this stage of the study was questioned. Matlab based Simulink module was used for this process. First of all, 40 input values (wind speed: in the range of 8 m/s to 37 m/s, angle of attack: in the range of -10° to +29°) are selected which are different from the data entered into the ANN model for teaching purpose. By using this input data, simulink module has been used to estimate the C_L, C_D and C_L/C_D values which are the basic criteria used in the performance evaluation of airfoil. Afterwards, verification tests were performed in the wind tunnel with these input data and experimental results were obtained. The comparison of verification test data and Simulink estimation results is shown in Figure 8.

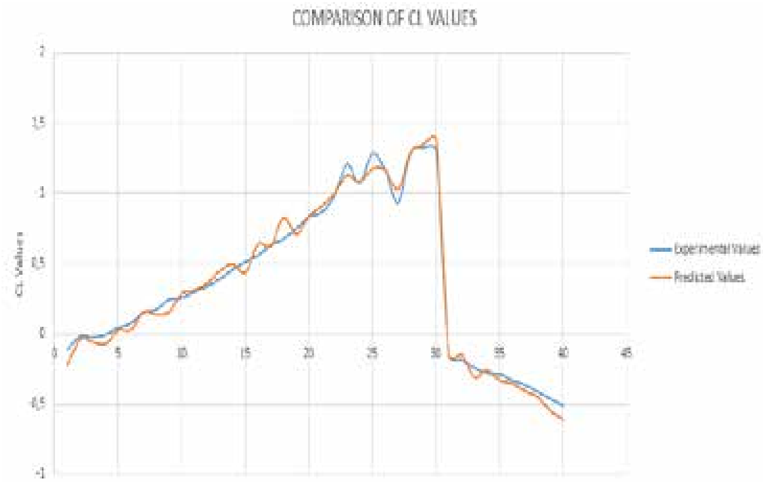

a. Comparison of C_L

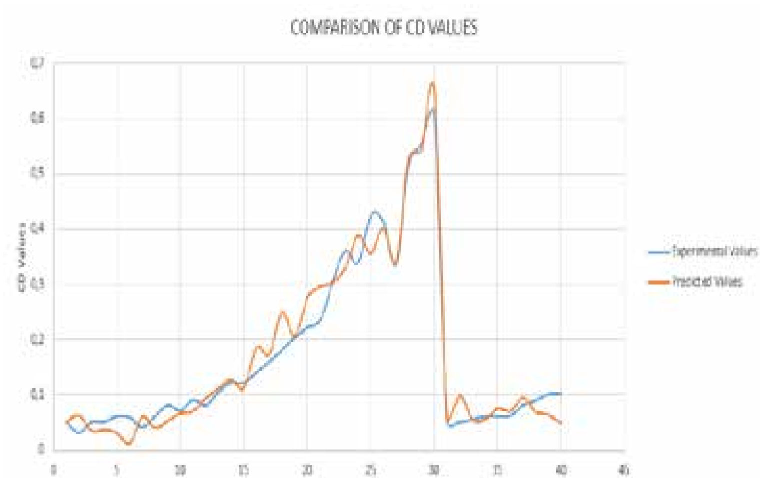

b. Comparison of C_D

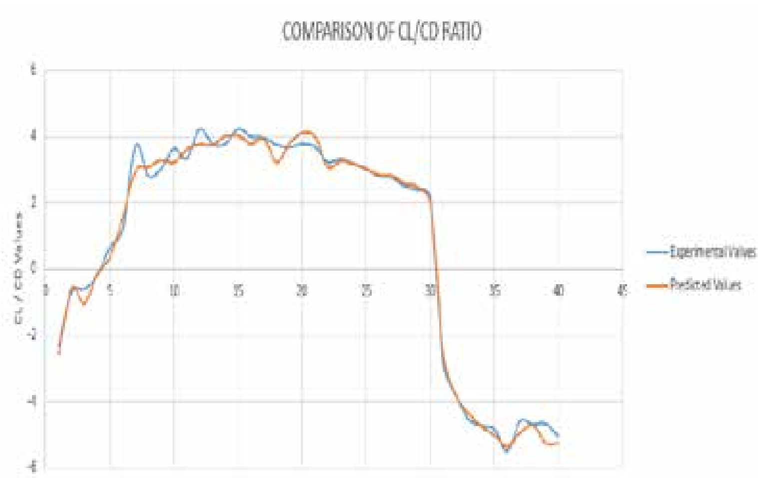

c. Comparison of C_L/C_D

Figure 8. *ANN verification results*

As expected from the ANN model performance data, the verification test results coincide with the estimation data. The ANN model for C_L, C_D, C_L/C_Dvalues were able to make very good estimates (Figure 8.a;c). This shows that the established model can also accurately estimate different input values.

4. CONCLUSIONS

Production of the S833 airfoil, which was selected for aerodynamic performance review, was productedwith a 3D printer. The produced airfoil was tested at different speeds (range 5 m/s to 37 m/s) and anglesof attack (range -10° to +29°) in the subsonic wind tunnel to obtain the data needed for the training of the ANN model. As a result of the experiments, the ANN model was established in Matlab program by using 400 result data obtained for C_L, C_D, C_M and C_L/C_D performance criteria. The performance parameters of the ANN model established wereobtained as R=0,99058 and MSE=0,09207. These values show that the model can make realistic predictions.

For the verification, C_L, C_D, C_L/C_D output data were estimated from the Simulink module using 40 different input data not used in ANN training. With the same input data, verification experiments performed in the wind tunnel proved that the model gives realistic results.

REFERENCES

Aytaç, A., Aytav, E., Aztekin, K., Aksu, S. B. (2019). Turkey's Renewable Energy Sources and Policies. In *Multidisciplinary Studies in the World of Science* (pp. 152–167). Berikan Publishing.

Aytaç, A. and İlivan, M. (2018). Scientific Studies in the Area of Mechanical Engineering: A Descriptive Analysis Related To Researches in Turkey. *American Journal of Engineering Research (AJER)*, *7*(12), 87–96.

Aytaç, A., Kuşcu, R., Aytav, E., Çanakçı, B. (2019). Thermal Batteries: Investigation of Current Technology and its Future Directions. In *Multidisciplinary Studies in the World of Science* (pp. 181–203). Berikan Publishing.

Çanakçı, B., Çakır, U., Aytaç, A., Özdemir, T., Aztekin, K., Işık, M. S. (2018). Determination of Parameters Affecting Aerodynamic Performance in S833 Airfoil (pp. 29–41). Presented at the International Congress on New Trends in Science, Engineering and Technology (ICONTRENDS 2018), Rome, Italy.

Demuth, H. and Beale, M. (2000). Neural Network Toolbox for use with MATLAB, *9*.

Dorvlo, A. S. S., Jervase, J. A., Al-Lawati, A. (2002). Solar radiation estimation using artificial neural networks. *Applied Energy*, *71*(4), 307–319. https://doi.org/10.1016/S0306-2619(02)00016-8

Haykin, S. (1994). *Neural Networks: A Comprehensive Foundation* (1st ed.). Upper Saddle River, NJ, USA: Prentice Hall PTR.

Houghton, E.L., Carpenter, P.W. (2003). *Aerodynamics for Engineering Students (5th ed.)*. Butterworth-Heinemann.

Kalogirou, S. (2000). Applications of artificial neural-networks for energy systems. *Applied Energy*, *67*, 17–35. https://doi.org/10.1016/B978-0-08-043877-1.50005-X

Mazhar, F., Khan, A. M., Chaudhry, I. A., Ahsan, M. (2013). On using neural networks in UAV structural design for CFD data fitting and classification. *Aerospace Science and Technology*, *30*(1), 210–225. https://doi.org/10.1016/j.ast.2013.08.005

Oztemel, E. (2012). *Artificial Neural Networks (3 rd ed.)*. Istanbul: Papatya puplication.

Rajadurai, J. S., Christopher, T., Thanigaiyarasu, G., Rao, B. N. (2008). Finite element analysis with an improved failure criterion for composite wind turbine blades. *Forschung Im Ingenieurwesen*, *72*(4), 193–207. https://doi.org/10.1007/s10010-008-0078-8

Saranya, C. and Manikandan, G. (2013). A study on normalization techniques for privacy preserving data mining, *5*, 2701–2704.

Schalkoff, R. J. (1997). *Artificial neural networks* (International ed). New York ; London : McGraw-Hill.

Seifert, A., Greenblatt, D., Wygnanski, I. J. (2004). Active separation control: an overview of Reynolds and Mach numbers effects. *Aerospace Science and Technology*, *8*(7), 569–582. https://doi.org/10.1016/j.ast.2004.06.007

Sun, G., Sun, Y., Wang, S. (2015). Artificial neural network based inverse design: Airfoils and wings. *Aerospace Science and Technology*, *42*, 415–428. https://doi.org/10.1016/j.ast.2015.01.030

Visalakshi, N. K. and Kuttiyannan, D. T. (2009). Impact of normalization in distributed K-means clustering. *International Journal of Soft Computing*, *4*, 168–172.

Yalcin, M. E., Suykens, J. A. K., Vandewalle, J. P. L. (2005). *Cellular Neural Networks, Multi-Scroll Chaos and Synchronization*. World Scientific. https://doi.org/10.1142/5753

Yilmaz, A. S.and Özer, Z. (2009). Pitch angle control in wind turbines above the rated wind speed by multi-layer perceptron and radial basis function neural networks. *Expert Systems with Applications*, *36*(6), 9767–9775. https://doi.org/10.1016/j.eswa.2009.02.014

OPTIMIZATION OF PARAMETERS AFFECTING ON MACHINABILITY IN SUPER-TIX® 51 AF TITANIUM ALLOY WITH RESPONSE SURFACE METHODOLOGY (RSM)

CHAPTER

14

Muhammed İLİVAN[1]
Ayhan AYTAÇ[2]
Kadir AZTEKİN[3]
Mehmet Arif SALTAN[4]

1 Dumlupınar University, Pazarlar Vocational School, Kutahya, Turkey. muhammed.ilivan@dpu.edu.tr

2 National Defence University, Military Academy, Department of Mechanical Engineering, Ankara-Turkey. aytac@kho.edu.tr, aaytac2001@gmail.com

3 National Defence University, Military Academy, Department of Mechanical Engineering, Ankara-Turkey. kaztekin@kho.edu.tr, kadiraztekin@yahoo.com

4 National Defence University, Military Academy, Department of Mechanical Engineering, Ankara-Turkey. masaltan@kho.edu.tr

1. INTRODUCTION

It is becoming more and more essential to make a difference in terms of design with increasing competition conditions. To obtain the same strength with lighter structures, however, more efficient use of energy resources can be achieved by selecting the right material and fully utilizing the machinability properties. At this point, titanium alloys are the most prominent materials in defense, medical products, aerospace, and aerospace industries.

One of the important parameters of chip removal in machining is the cutting forces acting on the cutting tool. Cutting forces; It varies depending on cutting parameters such as feed rate, cutting speed, chip angle, depth of cut, the material of the workpiece. To calculate the part production cost, it is necessary to know the effect of the cutting parameters on the cutting force. In this way, important operations such as determining the required power and correct dimensioning of the machine can be realized.If the stresses caused by force and strain are analyzed well, it is possible to increase the production quality and the longevity of the machines (Yussefian et al., 2017).

During chip removal from materials, the life and machining time of the cutting tool is very important due to the wear of the cutting tool. Selected suitable cutting tool and cutting parameters; quality production, excellent surface quality, the most appropriate machine power to determine the best results in terms of achieving great importance. Hard metal cutting tools are used to work at high cutting speeds and increase production. A wide range of investigations have been carried out on the performance of these tools and are still underway. Today, about 80% of all machining operations are done with coated cutting tools (Sarwar and Haider, 2009). These coated cutting tools; Titanium carbide (TiC), Titanium Nitride (TiN), Titanium Carbon Nitride (TiCN), Aluminum Oxide (Al_2O_3) etc. It is covered with different coating materials. Chemical Vapor Deposition (CVD) and Physical Vapor Deposition (PVD) methods are commonly used for coating (Rech, 2006).

To improve the quality of a product, it is necessary to consider all the factors that affect the product quality and to determine the level of these factors. Quality-factor number-levels equation is one of the most important problems for companies. Because in determining the appropriate factor levels, the designer has to analyze a lot of data and take into account many factor levels. The situation becomes even more complicated when these factors give different results when combined or individually. With the increase in the number of factors and levels, although classical experimental design techniques allow for healthier data analysis, they are far from being a cost effective solution. The increase in the number of experiments leads companies to easy solutions in terms of time, labor and cost.In this case, developing and applying appropriate scientific approaches for the solution of the problem can provide important facilities to the designer.

Experimental Design can be defined as the determination of the factors and levels affecting the result of the experiment, determination of the number of repetitions for each factor, analysis, and interpretation of the experimental data results. In other words, it can be defined as observing, obtaining and interpreting the variability caused by the changes made in the input variables of any process on the result (Besterfield et al., 1995). Different studies were carried out using the full factorial experimental design method to determine the factors affecting the machinability of AISI 4140 steel (Işık et al., 2018; Aztekin et al., 2018). In addition, parameters of 7000 series Aluminum alloys can be determined by optimizing with CYM to obtain the best surface quality (Çakır et al., 2018).

Titanium alloys are difficult to process due to their low elasticity, high formability and tendency to break.In hole drilling operations of Ti-6Al-4V alloy, drill bits are exposed to vibration, resulting in poor surface quality and tool failure. In a study, the effect of drill parameters such as speed, helical angle, feed rate on surface roughness, side wear and drill vibration was investigated by the RSM. Laser doppler vibrometer was used to measure the vibration of the drill bit. These signals were converted into time domain at different time intervals using a high-speed Fourier converter. A multiple response optimization was performed to optimize drill parameters such as minimum surface roughness and side wear, drill vibration. 26,16° helical angle, 10,0 mm/min feed rate and 600 rpm speed were found to be the optimum cutting parameters (Balaji et al., 2018).

Mechanical properties are an important criterion in material selection. The effect of different alloy steels such as AISI 1008-1040-4140 on the mechanical properties of carbon content and alloying elements can be investigated experimentally (Aytaç et al., 2018). Titanium and its alloys are attractive materials with high strength-to-weight ratios and exceptional corrosion resistance at high temperatures. The main application of titanium is the aerospace industry. However, the trend has been reported from military to commercial and from space to industry. Titanium and its alloys are renowned for their poor thermal properties and are classified as difficult to process materials. These properties have limited the use of these materials, especially in industries where cost is more important than the space industry.

Processing is an important production process. Due to the low machinability of alloys, the choice of processing conditions and parameters is critical. The range of cutting and feeding speeds that provide satisfactory tool life is limited. However, adequate tools, coating, geometry and cutting flow materials must be used, otherwise, possible tolerance errors and high tool wear will result in unacceptable defects in parts requiring high accuracy. Turning tests with conventional uncoated carbides on Ti-6Al-4V were carried out (Ribeiro et al., 2003).

The application of the Taguchi method for the optimization of surface roughness in the machining of titanium alloy in nano-coated carbide-tipped continuous turning is discussed. The use of conventional tools in the machining of titanium alloy increases the tool wear rate. In a research, nano-coated carbide tip was used for titanium alloy processing analysis. Considered cutting parameters are cutting speed, feed, corner radius and depth of cut. The effect of machining parameters on surface quality was determined and optimum cutting conditions were determined using the S/N ratio to minimize surface roughness. Analysis of variance was used to find the most effective parameter affecting the surface roughness. From the results, it was found that feed speed was the most effective parameter, followed by cutting speed, corner radius and cutting depth. Chip formation during machining of titanium alloy tested with different cutting parameters. Tool wear and surface quality of the workpiece were studied using SEM (Nithyanandam et al., 2014).

In this study, it is aimed to optimize the parameters which are effective on machinability by CYM in turning process which is one of the most applied methods in chip removal of Super-TIX® 51 AF titanium alloy. For this purpose, surface roughness was chosen as the dependent response variable. First of all, the surface roughness values of the Super-TIX® 51 AF test specimens were investigated by using 2^k full factorial test design and effective factors were evaluated depending on the feed rate, cutting speed and tip radius parameters. Convergence to the optimum point using contour graphics. Then, a new experimental design was made with CYM using central composite design. As a result of the study, mathematical models and optimum experimental parameters were determined. The consistency of the predictions made with the model and the results of the experiment and the optimum experimental parameters were examined. As a result, it was seen that the model created with CYM can be used to estimate the actual values and the optimum turning process conditions have been determined.

2. MATERIALS AND METHODS

In the study, it was tried to reach the optimum surface roughness value by optimization of the parameters affecting the surface roughness value during the turning process of Super-TIX® 51 AF material. Factors to be investigated on the effect of roughness; cutting speed, feed speed and cutting tool tip radius. Super-TIX® 51 AF is a Ti-5% Al-1% Fe based alloy with an O addition for fine-tuning hardness.This alloy can be compared to the most popular titanium alloy Ti-6% Al-4 V with extra-low brittleness to a standard degree.It is light and strong, and in addition to its hot formability, Young's modulus is superior to Ti-6% Al-4% V (Fujii and Saga, 2011).

2.1 Material

35 mm diameter Super-TIX® 51 AF was used in the experiments. Chemical composition of this material is given in Table 1 and tensile properties are given in Table 2.

Table 1. *Chemical Compositions of Super-TIX® 51 AF AFM (%)*

Material	H	O	N	Fe
Super-TIX® 51 AF	0,003	0,16	0,002	1,05
	C	**Al**	**Mo**	**Ti**
	0,001	5,19	-	Bal.

Table 2. *Mechanical Properties of Super TIX 523 AFM*

Material	0.2% Proof Strength (MPa)	Tensile Strength (MPa)	Elongation (%)	Reduction of Area (%)
Super-TIX® 51 AF	795	961	16,0	36,3

2.2 Average Surface Roughness and Surface Roughness Measurement

The average surface roughness is the arithmetic mean of the changes in height measured from the mean line.

$$Ra = \frac{1}{l}\int_0^1 |Z(x)|dx \qquad \text{Eq. (1)}$$

Ra values (Eq.1) are calculated automatically by the device to be used in the experiment. Surface roughness was measured with TMTeck TMR200 moving surface roughness tester (Figure 1). Three measurements parallel and perpendicular to the cutting direction were made. The average of three surface roughness (Ra) measurements were used to show the roughness of the sample surface.

2.3 Selection of Cutting Parameters and Test Conditions

Titanium alloys are difficult to process due to low modulus of elasticity or plastic deformation. In spite of increased usage and titanium production, titanium and its alloys can be expensive to process compared to other metals due to problems during manufacturing and processing. Experimental studies on turning operations were carried out on a CNC lathe which can rotate with a maximum power of 1,5 kW and 2000 revolutions. Cylindrical titanium alloy was machined with Al_2O_3 coated Cemented Carbide cutting tools under dry cutting conditions with three different feed and cutting speeds. The cutting zone layout is shown in Figure 2. The factors and levels used in processing were determined by the user experience and were indicated in Table 3.

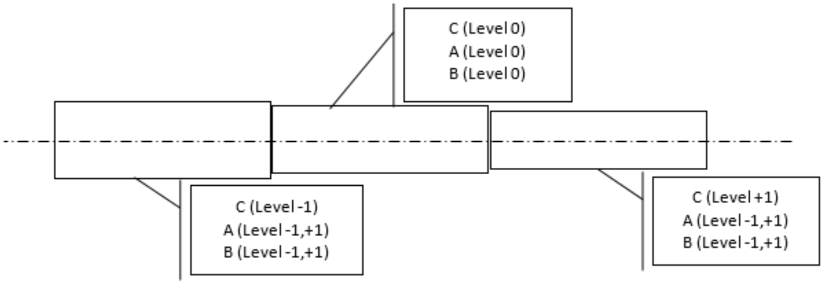

Figure 1. *Cutting Sections*

Figure 2. *Surface Roughness Measuring Device and Measuring Process*

Table 3. *Cutting Parameters Levels*

Factor	Unit	Symbol	Lower Level	Center Point	Upper level
Cutting Tool Tip Radius	mm	A	0,4	0,8	1,2
Cutting Speed	m/min	B	25	30	35
Feed Speed	mm/rev	C	0,025	0,05	0,075
Cutting Depth	mm	-	0,5	0,5	0,5

2.4 Factorial Experimental Design

The choice of optimum process conditions is of most importance as it determines the surface quality and dimensional accuracy of the manufactured parts. In machine design, it is aimed to process the contact surfaces of the working machine elements with a certain roughness. Sometimes, sensitive surfaces are required, and sometimes rough surfaces are suitable for proper machine operation. For this reason, it is important to determine the surface roughness at the design stage and control it at the production stage. The surfaces can then be operated at the desired roughness (Karayel, 2009). To process the machine parts by the environment in which they will work, it is necessary to optimize the surface quality and determine the optimum cutting parameters. For this purpose, in this study; cutting speed, feed speed, cutting tool tip radius were determined as the parameters to be used. Experiments were performed according to the full factorial experimental design method. Experimental design matrix is given in Table 4.

Table 4. *Full Factorial Experimental Design Matrix*

Experiment Number	Factors and Levels		
	A	B	C
1	-1	-1	-1
2	+1	-1	-1
3	-1	+1	-1
4	+1	+1	-1
5	-1	-1	+1
6	+1	-1	+1
7	-1	+1	+1
8	+1	+1	+1
9	0	0	0
10	0	0	0
11	0	0	0

3. RESULTS AND DISCUSSION

At the end of the experiments, according to the roughness (Ra) values, a Pareto graph was created with $\alpha = 0{,}15$ significance (confidence) level as a result of the analysis performed using the Minitab-18 program. In the Pareto graph analysis given in Figure 3.a, the main factors and the factors exceeding the 1,650 line, which is the threshold value for binary/triple interactions, are the most influential factors on surface roughness. As can be seen from the graph, the first important factor is cutting speed, the second important factor is the Cutting Tool Tip Radius-Cutting Speed-Feed Speed triple interaction. The main factors of cutting tool tip radius and feed speed have no effect on surface roughness. A linear model adaptation is needed for optimization with CYM. For this reason, the distortion of the linearity was prevented by the addition of a center point to the designed modelIn. 2^k design, the central points do not affect the usual impact estimates. The effects of the main factor and factor interactions on the response (surface roughness) were given in Figure 3.b. Increased cutting speed increases surface roughness. The increase in the triple interaction of Cutting Tool Tip Radius-Cutting Speed-Feed Speed also increases the surface roughness.

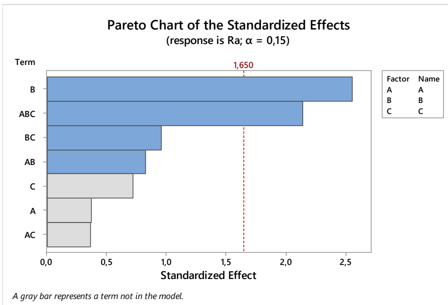

(a)

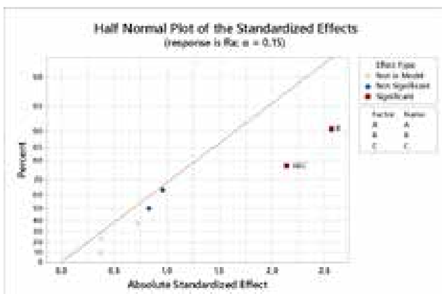

(b)

Figure 3. *a. Pareto graph showing factor effects, b. Main factors impact graph*

As can be seen from the main effects and dual interaction graph in Figure 4, the Cutting Tool Tip Radius and feed speed alone did not affect surface roughness. In the dual interaction of these two factors; while the roughness value remains the same for all the cutting tool tip radius at low feed rates, the increase in the tip radius at a high feed speed reduces the roughness. Cutting tool tip radius-cutting speed in binary interaction; The increase in cutting tool tip radius increases the roughness at low cutting speed, while the roughness decreased with increasing tip radius at high cutting speed. Feed speed-cutting speed in binary interaction; the increase in feed speed at low cutting speed decreases the roughness, while the increase in feed speed at high cutting speed was increased the roughness.

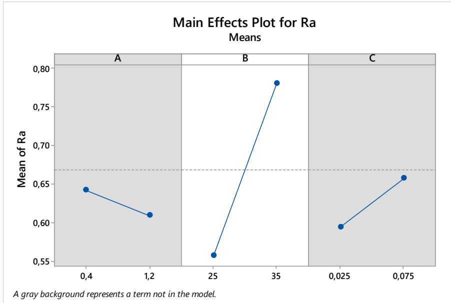

(a)

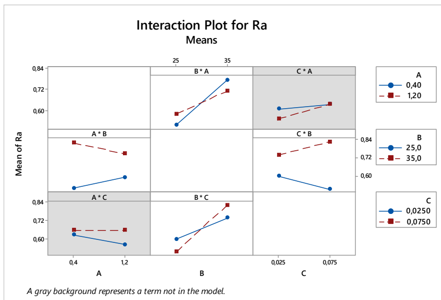

(b)

Figure 4. *a. Main factor effects graph, b. Binary factor effects graph*

In Figure 5, the contour plots of the cutting speed-cutting tool tip radius double interaction are given. It is seen that the lowest surface roughness can be achieved with high cutting speed and medium selected cutting tool tip radius. Using the steepest exit method (descent to the minimum response point) for the selected region, a line is drawn through the center of the region and perpendicular to the matched surface contours. Experiments are repeated for the new working points determined and a new model is created, which defines the optimum working area. According to the new model, the optimum values of the independent variables investigated are determined.

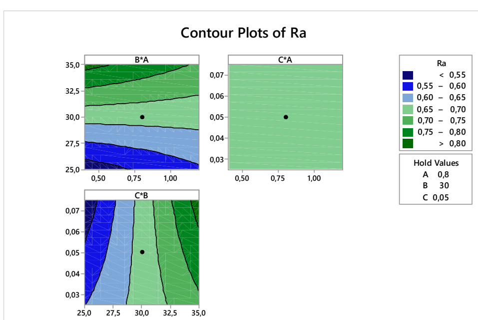

Figure 5. *Cutting speed-Tool tip radius (B*A), Feed Speed-Tool tip radius (C*A), Feed Speed-Cutting Speed (C*B) Contour plots of binary interactions*

The lowest roughness was reached in the tip values between 0,4-1,2 mm, the median value of 0,8 mm was chosen as the tip radius value. According to the contour plot of the feed speed-cutting speed binary interaction, the selected 0,8 mm tip radius value is suitable for achieving low surface roughness at high feed speed values.

3.1. Analysis of Variance and Regression Equation

In multiple regression analysis; The roughness values obtained from the experiments performed for two levels of each parameter with the backward elimination method were used. In the regression analysis, it is aimed to explain the relationship between variables functionally and to define this relationship with a model. In the analysis of variance, the significance of factors contribution to the model at α=0,15 significance level is investigated. Variance analysis results were presented in Table5. At the significance level α = 0,15, it can be concluded that the main effects or interactions are significant for cases where the probability value p is less than 0,15. In addition, for the lack of fit of the model, since the p value (0,809) was greater than 0,15, it can be said that the mathematical form of the model was appropriate. The ratio of explaining the relationship between variables (regression determination coefficient) of the model was R^2=67,94% (R^2 (adjusted)=46,57%). When the contribution of factors to the model is examined; cutting speed factor had the biggest effect with 34,95%, the second most crucial contribution was with triple interactions of factors with 24,45%.

Table 5. *Variance analysis results*

Source	DF	Seq SS	Contr.	Adj SS	Adj MS	F-Val.	P-Val.
Model	4	0,19333	67,94%	0,1933	0,04833	3,18	0,100
Linear	1	0,09946	34,95%	0,0994	0,09945	6,54	0,043
B	1	0,09946	34,95%	0,0994	0,09945	6,54	0,043
2-Way Interactions	2	0,02431	8,54%	0,0243	0,01215	0,80	0,492
A*B	1	0,01037	3,64%	0,0103	0,01036	0,68	0,440
B*C	1	0,01394	4,90%	0,0139	0,01394	0,92	0,375
3-Way Interactions	1	0,06956	24,45%	0,0695	0,06956	4,58	0,076
A*B*C	1	0,06956	24,45%	0,0695	0,06956	4,58	0,076
Error	6	0,09121	32,06%	0,0912	0,01520		
Curvature	1	0,05475	19,24%	0,0547	0,05475	7,51	0,041
Lack-of-Fit	3	0,01210	4,25%	0,0121	0,00403	0,33	0,809
PureError	2	0,02436	8,56%	0,0243	0,01218		
Total	10	0,28455	100,00%				

S	R-sq	R-sq(adj)	PRESS	R-sq(pred)
0,123298	67,94%	46,57%	0,239182	15,94%

In order to determine the coefficients of the regression equation, t-test was applied. The T-test results and the coefficients obtained were presented in Table 6 and the empirical formula Eq.2 obtained from the T-test. The effects of the factors in the model were clearly visible. The regression equation was obtained for the mean surface roughness value including center point (CtPt) addition.

Table 6. *T-test results and regression equation coefficients*

Term	Effect	Coef	SE Coef	95% CI	T-Val.	P-Val.	VIF
Constant		0,6685	0,0372	(0,5775; 0,7594)	17,98	0,000	
B	0,2230	0,1115	0,0436	(0,0048; 0,2182)	2,56	0,043	1,00
A*B	-0,0720	-0,0360	0,0436	(-0,1427; 0,0707)	-0,83	0,440	1,00
B*C	0,0835	0,0418	0,0436	(-0,0649; 0,1484)	0,96	0,375	1,00
A*B*C	0,1865	0,0933	0,0436	(-0,0134; 0,1999)	2,14	0,076	1,00

Ra	=	0,6685 + 0,1115 B - 0,0360 A*B + 0,0418 B*C + 0,0933 A*B*C

Eq. (2)

3.2 Optimization with RSM

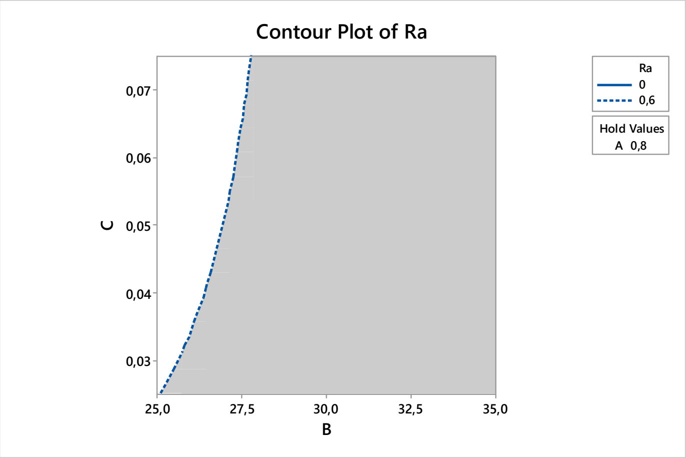

Figure 6. *Contour plot of feed speed-cutting speed interaction*

Optimization was made on the region where the surface roughness took the lowest value (0-0,6) (Figure 6). Movements between upper and lower levels of factors may have different consequences on response. To determine the desired value from the response (surface roughness) and the factor values to be optimized, optimization was performed. According to the contour plot of feed speed-cutting speed binary interaction; to achieve the lowest surface roughness; It is seen that the cutting speed in the range of 25-27,5 m/min versus the feed speed in the range of 0,03-0,07 mm/rev should be selected. In this context, optimum region and optimum surface roughness were investigated with the newly designed experimental design. The newly prepared experimental design matrix is shown in Table 7. In the experiments, the center value of 0,8 mm was chosen as the cutting edge radius for the lowest roughness according to the surface graph of the feed speed-cutting speed binary interaction.

Table 7. *Full Factorial Experimental Design Matrix for Optimization Experiments*

Experiment Number	Factors and Levels		
	A (Cutting Speed)	Tool tip radius	B (Feed Speed)
1	-1	+1	-1
2	+1	+1	-1
3	-1	+1	+1
4	+1	+1	+1
5	-1,41	+1	0
6	+1,41	+1	0
7	0	+1	-1,41
8	0	+1	+1,41
9	0	+1	0
10	0	+1	0
11	0	+1	0
12	0	+1	0
13	0	+1	0

In Figure 7, according to the results of the new analysis performed using the Minitab 18.0 program; α=0,10 significance (confidence) level was given pareto graph. In the pareto graph analysis, the factors that exceed the threshold value 1,833 are the most influential factors for surface roughness. As can be seen from the graph, the first important factor is the feed speed-cutting speed binary interaction, the second factor is the cutting speed, the third factor is the feed speed. According to the results obtained, it is seen that a new linear regression model will be found defining the optimum working region. Optimum values of independent variables (feed speed and cutting speed) of the model created by CYM are wanted to be determined.

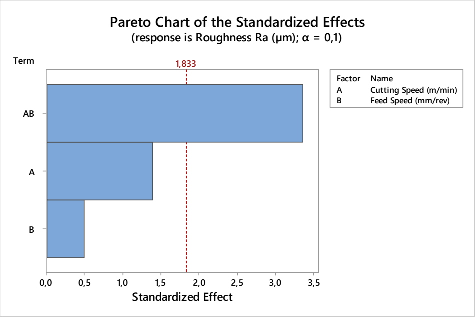

Figure 7. *Pareto graph showing factor effects of optimization region*

The graphs of the effects of the main factors (feed speed, cutting speed) on the response (surface roughness) examined in the optimization zone are given in Figures 8.a and 8.b. Both factors showed linear change. Roughness increases with increasing cutting speed while increasing feed speed decreases roughness. According to binary interaction graphs; it is seen that the optimum value for roughness can be achieved by selecting the feed rate in the range of 0,069-0,105 mm/rev in response to the cutting speeds in the range of 24,48-28,02 m/min.

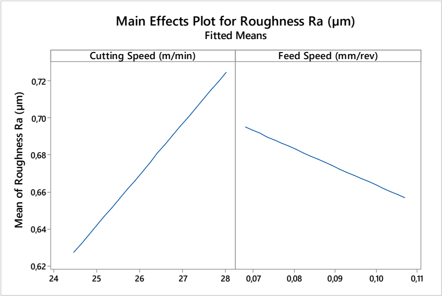

(a)

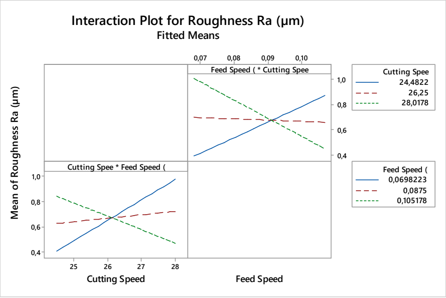

(b)

Figure 8. *a. Main factors impact graphs, b. Binary interaction graphs*

In Figure 9.a.b, the feed speed-cutting speed binary interaction contour plots of the new model created as a result of CYM were given. From the curves, it can be seen that for optimization (the region where the roughness value changes in the range of 0,4-0,5 µm) can be studied in two regions. When the surface graph (Figure 9.c) and contour graphs are evaluated together; because allowing a wider range of operation, 24,5-25 m/min cutting speed and 0,060-0,078 mm/rev feed speed were chosen as the optimum working zone.

The optimization results for the feed speed and cutting speed at which the best value can be obtained from the response are given in Figure 10. Multipurpose optimization method; For each response to be optimized, for the singular satisfaction function (d) and combined satisfaction function (D) levels are investigated in which combination of factors the best values can be achieved. The singular satisfaction function (d) evaluates the optimum point that the factors can reach individually. Combined Satisfaction function (D) of the whole system shows how close the result can be with the obtained factor values. Satisfaction level is between 0 and 1. A value of 1 indicates ideal, while a value of 0 indicates that one or more values are outside acceptable limits. In the analysis, the combined satisfaction function was obtained as D=1. In other words, it was found that the ideal state can be reached with the determined factor value ranges. Since there was only one answer, the combined satisfaction function (D) and the singular satisfaction function (d) of the system had been the same value.

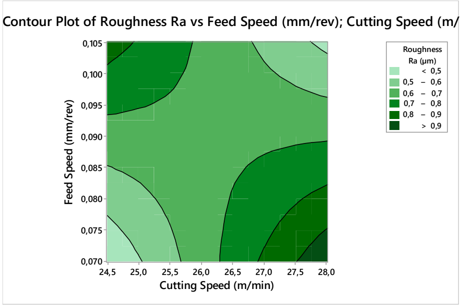

(a)

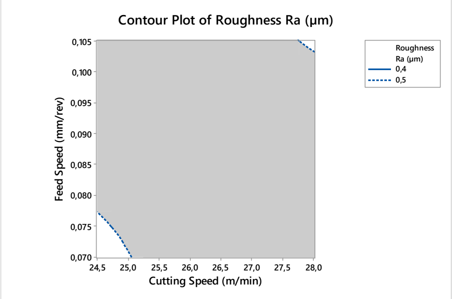

(b)

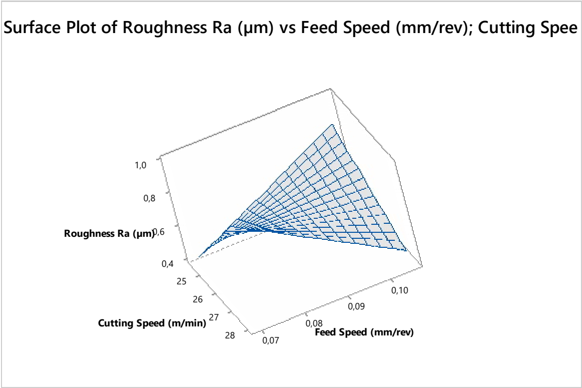

(c)

Figure 9. *Contour Plots of the feed speed-cutting speed binary interaction for the optimization zone (a-b), c. Three-dimensional surface plot*

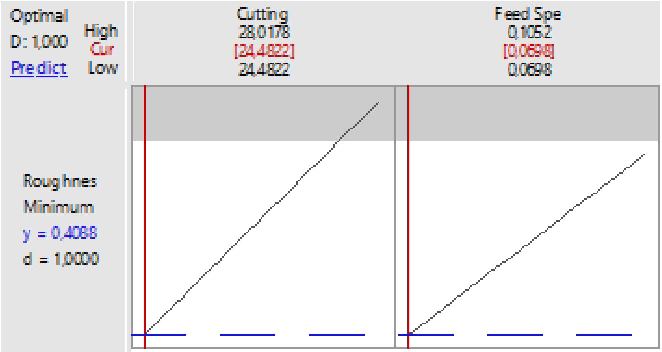

Figure 9. *Optimization Results*

By applying the best factor values, the response (y) value that can be reached was found to be Ra = 0,4088 µm. The response optimization resulted in an improvement of approximately 45% relative to the roughness value (Raort = 0,910 µm) obtained from the initial factor values.

3.3 Analysis of Variance and Regression Equation After Optimization

In the variance analysis given in Table 8, linear and binary effect values were evaluated at α=0,10 significance level. The most effective factor (contribution value 50,20%), cutting speed-feed speed was the binary interaction. The second effective factor (contribution value 8,57%) was the cutting speed, the least effective factor was the feed speed (contribution value 1,10%). The ratio of explaining the relationship between variables (regression determination coefficient) of the model was R^2=59,87% (R^2 (adjusted)=46,49%).

Table 8. *Variance analysis results after optimization*

Source	DF	Seq SS	Contr.	Adj SS	Adj MS	F-Val.	P-Val.
Model	3	0,06641	59,87%	0,0664	0,02213	4,48	0,035
Linear	2	0,01072	9,66%	0,0107	0,00536	1,08	0,379
Cutting Speed	1	0,00950	8,57%	0,0095	0,00950	1,92	0,199
Feed Speed	1	0,00121	1,10%	0,0012	0,00121	0,25	0,632
2-Way Interactions	1	0,05569	50,20%	0,0556	0,05569	11,26	0,008
Cutting Speed* Feed Speed	1	0,05569	50,20%	0,0556	0,05569	11,26	0,008
Error	9	0,04452	40,13%	0,0445	0,00494		
Lack-of-Fit	5	0,03707	33,41%	0,0370	0,00741	3,98	0,103
PureError	4	0,00745	6,72%	0,0074	0,00186		
Total	12	0,11094	100,00%				

S	R-sq	R-sq(adj)	PRESS	R-sq(pred)
0,0703368	59,87%	46,49%	0,130453	0,00%

In order to determine the coefficients of the regression equation, t-test was applied. T-test results and obtained coefficients were given in Table 9. The empirical formula obtained from optimization was presented in Equation 3. The effects of the factors in the model can be seen here.

Table 9. *T-test results and regression equation coefficients after optimization*

Term	Coef	SE Coef	95% CI	T-Val.
Constant	0,6761	0,0195	(0,6319; 0,7202)	34,66
Cutting Speed	0,0488	0,0352	(-0,0308; 0,1283)	1,39
Feed Speed	-0,0174	0,0352	(-0,0970; 0,0621)	-0,50
Cutting Speed* Feed Speed	-0,2360	0,0703	(-0,3951; -0,0769)	-3,36

Ra (µm)	=	-17,31+ 0,688 Cutting Speed (m/min) + 197,3 Feed Speed (mm/rev) - 7,55 Cutting Speed (m/min)*Feed Speed (mm/rev)

Eq. (3)

3.4 Verification Test

Verification test was performed to check the accuracy of the regression equation obtained according to the optimization result. Verification test results were given in Table 10. The surface roughness value of 0,561 μm found in the verification test was within the estimation limits.

Table 10. *Verification Test Predict Values*

Variable		**Setting**	
Cutting Speed (m/min)		24,8	
Feed Speed (mm/rev)		0,073	
Fit	**SE Fit**	95% CI	95% PI
0,491605	0,0654542	(0,343537; 0,639672)	(0,274255; 0,708955)

4. CONCLUSIONS

Findings obtained as a result of the study were given below.

- The regression model, which was formed by adding the center point at α=0,15 confidence level, explained the change in surface roughness as 46.57%.
- The most effective factor on surface roughness was the cutting speed, the second important factor was the triple interaction of Cutting Tool Tip Radius-Cutting Speed-Feed Speed. The main factors of cutting tool tip radius and feed speed had no effect on surface roughness.
- For the selected optimization region (cutting speed in the range of 24,5-25 m/min, feed speed in the range of 0,060-0,078 mm/rev), the regression determination coefficient of the new regression model was determined to be R^2 (adjusted)=46,49%.
- According to the new experimental design after optimization, the most effective factor on surface roughness was the feed speed-cutting speed binary interaction, the second important factor was the cutting speed, and the third factor was the feed speed.
- The optimization results in a 45% improvement compared to the 0.8 mm tip radius test result, where the highest roughness was measured.
- Verification test was performed to determine the accuracy of the regression model obtained as a result of optimization. As a result of the test, the results obtained from the regression model were consistent with the estimated value.

ACKNOWLEDMENT

We would like to thank NIPPON STEEL-Japan for providing the Super-TIX 51® AF material used in the experiments.

REFERENCES

Aytaç, A., Işık, M. S., Çanakçı, B., Özdemir, T., Aztekin, K., İpek, H. (2018). Investigation of Microstructure and Mechanical Properties of Heat Treatment, Carbon Ratio and Alloying Elements in AISI 1008, 1040 and 4140 Steels. The Journal of Defense Sciences, 17(2), 139–167.

Aztekin, K., Işık, M. S., Aytaç, A., Özdemir, T., Çakır, U., Çanakçı, B. (2018). Effects of Heat Treatment Conditions and Surface Roughness on Fatigue Strength of AISI 4140 Steel (pp. 298–311). Presented at the International Multidisciplinary Congress of Eurasia-IMCOFE 2018, Barcelona, Spain.

Balaji M., Venkata Rao K., Mohan Rao N., Murthy, B.S.N. Optimization of drillin gparameters for drilling of TI-6Al-4V based on surface roughness, flank wear and drill vibration. Measurement 114 (2018) 332–339.

Besterfield, D.H., Besterfield, C., Besterfield, G.H., Besterfield, M. (1995). Total quality management, New Jersey: Prentice Hall Inc.

Çakır, U., Çanakçı, B., Aytaç, A., Işık, M. S., Özdemir, T., Aztekin, K. (2018). Optimization of Machining Parameters of 7000 Series Aluminum Alloys by Response Surface Method (pp. 482–489). Presented at the International Multidisciplinary Congress of Eurasia-IMCOFE 2018, Barcelona, Spain.

Fujii, H., Saga, M. Nippon Steel Tech. Rep., 391 (2011), pp. 169-174.

Işık, M. S., Aytaç, A., Aztekin, K., Özdemir, T., Çakır, U., Çanakçı, B. (2018). The Effect of Cooling Environment and Tempering Temperature on Wear Resistance of AISI 4140 Steel (pp. 550–560). Presented at the International Science and Technology Conference-ISTEC 2018, Paris, France.

Karayel, D., "Prediction and control of surfaceroughness in CNC lathe using artificial neural network", Journal of Materials Processing Technology, 209, 7, 3125–3137, 2009.

Nithyanandam J., Sushil Lal Das, K. Palanikumar. Surface Roughness Analysis in Turning of Titanium Alloy by Nano coated Carbide İnsert. Procedia Materials Science 5 (2014) 2159-2168.

Rech J., Influence of cutting tool coatings on the tribological phenomena at the tool/chip interface in orthogonal dry turning, Surface Coating Technolgy, vol. 200 pp. 5132-5139, July 2006.

Ribeiro M.V., Moreira M.R.V., Ferreira J.R. Optimization of titaniumalloy (6Al–4V) machining. Journal of Materials Processing Technology 143–144 (2003) 458–463.

Sarwar M. and Haider J., Development of advanced surface engineering technologies for the benefit of multi point cutting tools, Advanced Materials Research, vol. 83-86, pp. 1043-1050, December 2009.

Yussefian N.Z., Hosseini A., Hosseinkhani K., Kishawy H. A., "Design For Manufacturing of Variable Microgeometry Cutting Tools" Journal Manufacturing Scienceand Engineering vol. 1, pp. 15-17, 2017.

ANALYSIS OF PARAMETERS AFFECTING SURFACE ROUGHNESS IN TURNING OF SUPER-TIX 523 AFM TITANIUM ALLOY BY TAGUCHI METHOD

CHAPTER

15

Muhammed İLİVAN[1]
Ayhan AYTAÇ[2]
Kadir AZTEKİN[3]
Tayyar Salih ADIGÜZEL[4]

1 Dumlupınar University, Pazarlar Vocational School, Kutahya, Turkey. muhammed.ilivan@dpu.edu.tr
2 National Defence University, Military Academy, Department of Mechanical Engineering, Ankara-Turkey. aytac@kho.edu.tr, aaytac2001@gmail.com
3 National Defence University, Military Academy, Department of Mechanical Engineering, Ankara-Turkey. kaztekin@kho.edu.tr, kadiraztekin@yahoo.com
4 National Defence University, Military Academy, Department of Mechanical Engineering, Ankara-Turkey. tsadiguzel@kho.edu.tr

1. INTRODUCTION

The selection of suitable materials is important in the design of engineering products and it is made considering the environmental conditions and loading conditions to which the machine parts are exposed. For example, for a helicopter propeller, vibration and variable loads may be important, while corrosion and impact resistance may be prominent for a submarine armour (Aytaç et al., 2019).

Titanium alloys are one of the most interesting materials these days. Due to its high mechanical and corrosion properties, it is the most suitable material for the human body for biomedical applications. (Gepreel et al., 2013 and Geetha et al., 2009). Titanium alloys are used as fracture fixation, artificial joints, artificial bones and complex parts as medical products (Okada et al., 2004). Titanium alloys are widely used in the aerospace industry, defence industry and medical instruments due to their low weight, high corrosion resistance and strength (Ma et al., 2015).

Titanium and its alloys have low machinability due to some microstructural properties. Titanium is very reactive with chemically and therefore tends to weld to the cutting tool during machining. This leads to poor chip formation and tool breakage. The low thermal conductivity of Titanium increases the temperature at the tool-work piece interface, which adversely affects tool life. (Ezugwu et al., 2005).

In spite of increasing usage and Titanium production, Titanium and its alloys can be expensive to machine due to the problems that arise during manufacturing and machining compared to other metals (Li et al., 2012).

Although many factors are affecting the machinability of a material, the type of material, machining type, cutting tool material and geometry, chip formation and desired surface quality are the main factors. Turning is widely used to machine materials with the desired surface quality and finish product. Therefore, it is economically important to optimize important factors such as cutting speed, feed rate and tool geometry when turning a difficult material, such as titanium, to the desired surface quality. The surface quality of a machined material is an important factor. A machined material with good surface quality offers a variety of performance and high resistance to engineering failures (Ezugwu et al., 2005).

In order to improve the quality of a product, it is necessary to consider all the factors that affect the product quality and to determine the level of these factors. Quality, the number of factors and the level equation is one of the most important problems for companies. Because in determining the appropriate factor levels, the designer has to analyse a lot of data and take into account many factor levels. The situation becomes even more complicated when these factors give different results when combined or individually. With the increase in the number of factors and levels, although classical experimental design techniques allow for healthier data analysis, they are far from being a cost effective solution. The increase in the number of experiments leads companies to easy solutions in terms of time, labor and cost. In this case, developing and applying appropriate scientific approaches for the solution of the problem can provide important facilities to the designer. It has become possible to achieve the same results with fewer experiments and with a very small margin of error, rather than expensive experiments where all the factor possibilities that require high costs are made. Especially in engineering applications, Taguchi method, full and fractional factorial experimental design, Response Surface Method (RSM), Artificial Neural Networks (ANN), etc. are widely used. Which of these methods is the most suitable method varies according to the engineering application (Aytaç et al., 2018; Aztekin et al., 2018; Çakır et al., 2018; Işık et al., 2018)

Taguchi method, developed by Dr.Taguchi, using the principles of experimental design, has become one of the important statistical tools of Total Quality Management to design a quality system at a low cost. Taguchi Method provides an effective and systematic way to optimize experimental designs in terms of performance, quality and cost. This method has been used successfully in the design of reliable and high-quality products at low cost in areas such as automotive, aviation and consumer electronics (Hasçalık et al., 2008).

To design experiments in process development research in the industry, various methods have been developed that obtain the most information in the shortest time, with the lowest cost and labor. The difficulties of some methods, which can be considered as classical for experimental design, have led to new studies being done in this research area. Taguchi Method, which is used especially in product development in 1980 and later, is one of these studies. In Taguchi design, better predictions can be obtained for some designs since the visuality of the orthogonal array shows, which interaction components derive from the deviation (Şirvancı, 1997).

In the literature, it is seen that the studies made with the machinability of Titanium material (Sartori et al., 2017; Ghani et al., 2013; Kumar et al., 2017) are mainly focused on the optimization of cutting factors, but there is a need for studies on Titanium alloys because there are a lot of machining methods and cutting factors.

In engineering research and development studies, getting desired tolerances requires controlling many factors. Surface quality is an important measure of machinability and optimization of the effects of tool type, cutting speed and feed rate is required to improve.

The aim of this research is to investigate the effects of cutting parameters (feed rate, cutting speed and tool geometry) on surface roughness, which is an important machinability criterion, by making turning experiments on Titanium alloys used in machine manufacturing industry. In this study, after the literature review, the factors affecting the surface roughness in turning were evaluated and Titanium alloy sample was subjected to three different nose radius, feed rates and cutting speeds. The results of Taguchi Method were evaluated in terms of optimization and the concordance of the findings with the literature.

2. MATERIALS AND METHODS

2.1 Material

15 mm diameter SUPER TIX 523 AFM Titanium alloy was used in the experiments. The chemical composition of this material is given in Table 1 and its mechanical properties are given in Table 2. Super-TIX® 523 AFM can be further strengthened by suitable heat treatment. In addition, a yield stress of 0.2% permits a reduction from about 950 MPa to about 420 MPa by ordinary heat treatment. However, it is also possible to regain the old strain ratio. In addition, this alloy allows for some unique functions, such as reducing the normal Young module from 110 GPa to 70 GPa to facilitate cold processing (Fujii et al., 2011).

Table 1. *Chemical Compositions of Super TIX 523 AFM (%)*

Material	**H**	**O**	**N**	**Fe**
Super-TIX 523 AFM	0.006	0.17	0.003	1.91
	C	**Al**	**Mo**	**Ti**
	0.003	5.33	2.99	Bal.

Table 2. *Mechanical Properties of Super TIX 523 AFM*

Material	**0.2% Proof Strength (MPa)**	**Tensile Strength (MPa)**	**Elongation (%)**	**Reduction of Area (%)**
Super-TIX 523 AFM	1044	1069	13.0	40.0

2.2 Surface Roughness Measurement

Surface roughness was measured with TIME TR 200 surface roughness tester. Three measurements parallel and perpendicular to the cutting direction were made. The average of three arithmetic mean surface roughness (Ra) measurements in and along the cutting direction was used to show the roughness of the sample surface.

2.3 Selection and Levels of Cutting Parameters

Experimental studies in turning operations were carried out on a CNC lathe which has a maximum power of 1,5 kW and speendle speed 2000 rev/min, respectively. revolutions. Titanium alloys are difficult to process due to low modulus of elasticity, or plastic deformation. Despite the increasing use and the production of Titanium, Titanium and its alloys can be expensive to machine compared to other metals due to problems arising during manufacturing. The cylindrical Titanium test specimen was machined under dry cutting conditions, with Al_2O_3 coated cemented carbide cutting tools with three different nose radiuses and three different feed and cutting speed combinations.

The cutting pattern which applied to the test specimen is shown in Figure 1. The factors and their levels used in machining are determined by the user experience and are shown in Table 3.

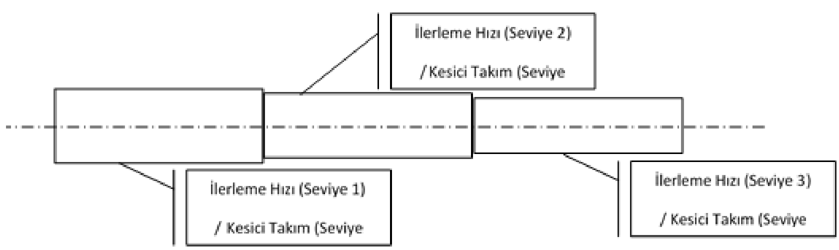

Figure 1. *Cutting Sections*

Table 3. *Cutting Factors and Levels*

Faktör	Birim	Sembol	Level 1	Level 2	Level 3
Nose Radius	mm	A	0.4	0.8	1.2
Cutting Speed	m/min	B	25	30	35
Feed Rate	mm/rev	C	0.02	0.04	0.06

2.4 Taguchi Design Experiment

The choice of optimum process conditions is an important issue as they determine the surface quality and dimensional accuracy of the manufactured parts.The contact surfaces of the working machine elements must be finished with a certain surface quality.In order for a machine to operate at the desired performance, low surface roughness in some parts of the machine and rough surface roughness in other parts may be required. For this reason, it is important to determine the surface roughness at the design stage and control it at the production stage. The surfaces can then be operated at the desired roughness (Karayel, 2009).

To manufacture the machine parts under the environment in which they will work, there is a need to optimize the surface quality and determine the optimum cutting parameters. For this purpose, Cutting speed, feed rate, cutting tool nose radius are determined as the parameters to be used. In the experiments, the L9 orthogonal array in Taguchi method was used for 3 factors, all having 3 levels. The L9 orthogonal array is given in Table 4.

Table 4. *Taguchi L9 Orthogonal Array*

Experiment Number	**Control Factors**		
	Nose Radius (A)	**Cutting Speed (B)**	**Feed Rate (C)**
1	1	1	1
2	1	2	2
3	1	3	3
4	2	1	2
5	2	2	3
6	2	3	1
7	3	1	3
8	3	2	1
9	3	3	2

2.5 Calculation of of S/N Ratios

Experimental results were analyzed in the Minitab 16.1 statistical software program. As it is known, Taguchi has presented 3 methods for converting experimental results to S/N ratios. These are “Smaller is better”, “Nominal is best” and “Larger is better” respectively. Since the smaller values of surface roughness are better, “Smaller is better” formula stated in Equation 1 was used in the calculation of S/N ratios.

$$\frac{S}{N} = -10 * \log \left[\sum_{i=1}^{n} \frac{{Y_i}^2}{n}\right] \qquad \text{Eq. (1)}$$

3. RESULTS AND DISCUSSION

3.1. Results of Experiments

In the machining tests of SUPER TIX 523 AFM Titanium alloy according to Taguchi L9 Orthogonal array, S/N ratios were calculated using "Smaller is better" equation according to the surface roughness values. The surface roughness values measured after machining and calculating S/N ratios is given in Table 5.

Table 5. *Surface Roughness Values and S/N Ratios after Machining*

Exp. Num.	Control Factors			Surface Roughness (Ra) (µm)	S/N Ratios (dB)
	Nose Radius (mm) (A)	Cutting Speed (m/min) (B)	Feed Rate (mm/rev) (C)		
1	1	1	1	0,348	9,16842
2	1	2	2	0,397	8,02419
3	1	3	3	0,591	4,56825
4	2	1	2	0,559	5,05176
5	2	2	3	0,401	7,93711
6	2	3	1	0,481	6,35710
7	3	1	3	0,416	7,61813
8	3	2	1	0,368	8,68304
9	3	3	2	0,425	7,43222

The degree of effect (rank) of control factors on surface roughness was analyzed using S/N ratios response table. Table 6 shows the S/N ratios response table and ranks of factors for surface roughness. Table 6, which was created by Taguchi method, shows the optimum level as well as the degree of factor effect (rank).

The graph of the mean values of the factor effects is shown in Figure 2 and the graph of the S/N values obtained from the mean values is shown in Figure 3.

Figure 2 and Figure 3 show that the optimum level of nose radius, cutting speed and feed rate for surface roughness are 0,4 mm, 35 m/min and 0,04 mm/rev respectively. The surface roughness value measured at this level is 0,368 µm.

Table 6. *S/N Ratios for Surface Roughness*

Level	Nose Radius (A)	Cutting Speed (B)	Feed Rate (C)
1	7,254	7,279	8,070
2	6,449	8,215	6,836
3	7,911	6,119	6,708
Delta	1,462	2,096	1,362
Rank	2	1	3

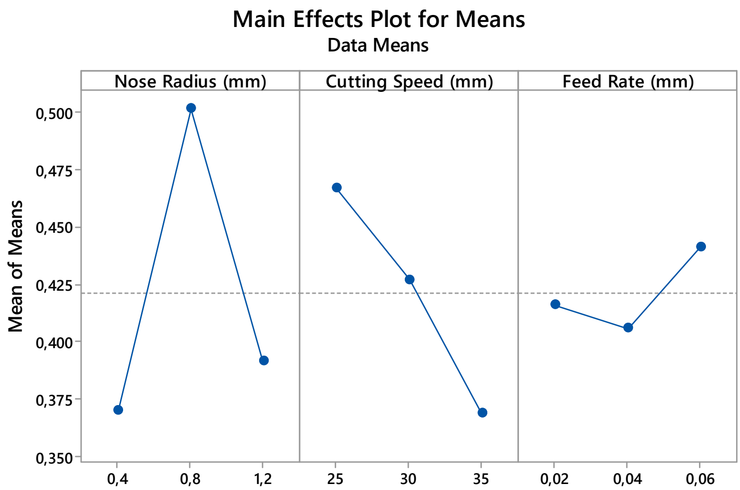

Figure 2. *Main Effects of Means of Surface Roughness*

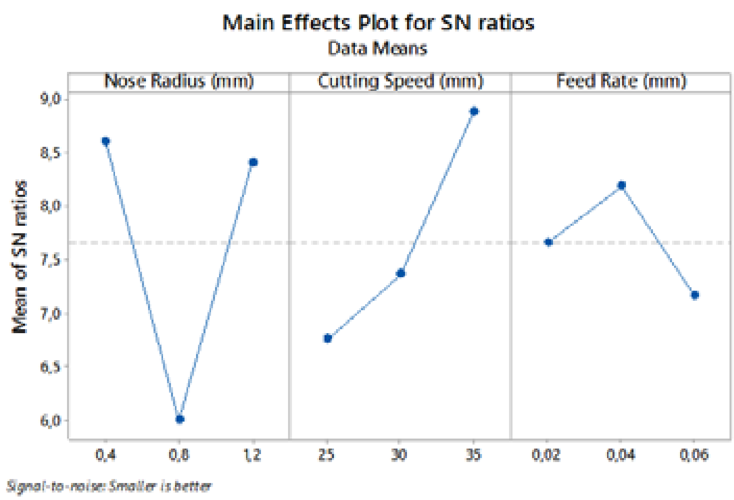

Figure 3. *Main Effects of S/N Ratios Surface Roughness*

The main effects of cutting factors on surface roughness are shown in Figure 4. According to Figure 4, the surface roughness decreases as the nose radius increases from 0,4 mm to 0.8 mm and increases as the nose radius increases from 0,8 mm to 1,2 mm. The surface roughness tends to decrease with increasing of cutting speed. The surface roughness decreases as the feed rate increases from 0,02 mm/rev to 0.04 mm/rev and increases as the feed rate increases from 0,04 mm/rev to 0,06 mm/rev.

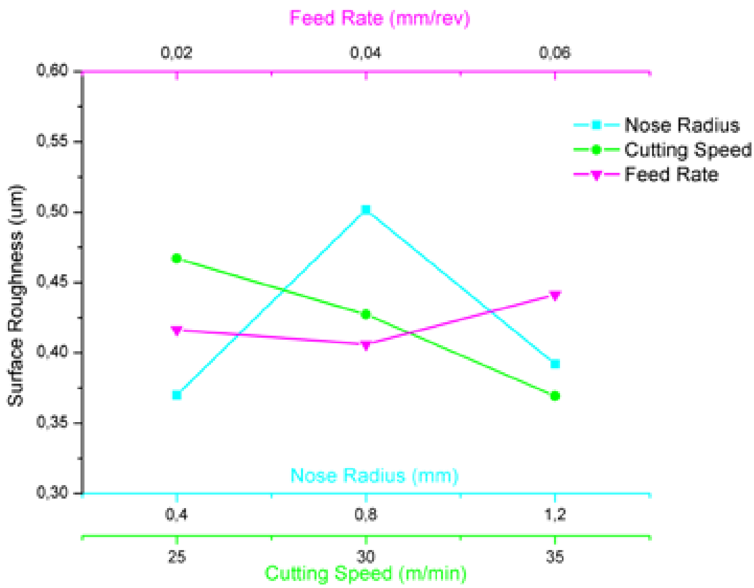

Figure 4. *Effects of Cutting Factors on Surface Roughness*

3.2 Evaluation and Discussions of Results

3.2.1 Evaluation of the Effects of Cutting Factors

As can be seen from Table 6, the cutting speed is the most important factor on surface roughness. The effects of nose radius and feedrate on surface roughness are close to each other. When the literature is reviewed, it is known that the nose radius and feedrate are the most important factors in affecting the surface roughness in most traditional metals. However, this situation may change in Titanium alloys which are difficult to machine due to their internal structure and mechanical properties. In this study, it was seen that cutting speed affects surface roughness more than nose radius and feed rate. It can be said that this causes the bad chip formation, extremely high temperatures on tool and material interface and the weldment tendency of the material to tool. It is useful to investigate these subjects in future academic studies.

3.2.2 Evaluation of Optimum Factor Levels

When Table 1, Figure 2 and Figure 3 are considered together, it will be seen that experiment 1 has the lowest surface roughness. In this experiment, the cutting speed is 35 m/min, the nose radius is 0,4 mm, the feedrate is 0,04 mm/rev and measured surface roughness is 0,348 μm. In the literature and theoretical calculations, low surface roughness is obtained with high nose radius, low federate and suitable cutting speeds. Nose radius and feedrate yields the lowest surface roughness at their medium level. The effect of cutting speed on surface roughness was obtained at the highest value of 35 m/min and it would be beneficial to investigate the effects of higher cutting speeds effects on surface roughness in future academic studies. As mentioned in the above paragraph, Titanium alloy is difficult to machine and the results obtained from the cutting of conventional metals may not be used for Titanium alloys.

3.2.3 Evaluation of Nose Radius and Feed Rate

For both cutting factors, the lowest surface roughness value was obtained in the middle values. While low surface roughness is achieved with high nose radius and high feed rate in most conventional metal materials low surface roughness may not be obtained in Titanium alloys. It can be said that due to the difficult machinability of Titanium alloys, low surface roughness cannot be obtained in these values. At low feed rates, it can be said that adverse machining conditions between the cutting tool and the material cause these results.

3.2.4 Evaluation of Cutting Speed

As the cutting speed increases, the surface roughness tends to decrease and no turning point can be achieved in this curve. Cutting speed is one of the most important cutting factors affecting chip formation which directly affects the surface roughness. In the light of these informations, it is useful to investigate the optimum cutting factors in another research where a turning point in surface roughness values will be determined by increasing the cutting speed values. Furthermore, the possibility of changing the optimum nose radius and feedrate values at the optimum cutting speed value should be kept in mind.

4. CONCLUSIONS

In this study, optimization of cutting factors affecting the machinability of Titanium alloy was done by Taguchi method and the following conclusions were obtained.

- The degree of effect of the three cutting factors on the surface roughness was determined as cutting speed, nose radius and feedrate respectively.
- With Taguchi method optimization, the lowest surface roughness value was obtained 0,348 μm in experiment 1, where the cutting speed was 35 m/min, the nose radius was 0,4 mm and the feed rate was 0.04 mm/rev.
- Low surface roughness was obtained at medium values where the feedrate was 0,04 mm/rev and the nose radius was 0,8 mm. Due to the difficult machinability of Titanium alloys, it was evaluated that lower surface roughness could not be obtained with low feedrate and big nose radius values.
- It was found that surface roughness decreased with increasing cutting speed. In the graphs, since a turning point could not be obtained, it was considered that it would be beneficial to study higher cutting speed values with other cutting factors in future studies.

ACKNOWLEDMENT

We would like to thank NIPPON STEEL-Japan for supplying the Super-TIX® 523 AFM material used in the experiments.

REFERENCES

Aytaç, A., Işık, M. S., Çanakçı, B., Özdemir, T., Aztekin, K., İpek, H. (2018). Investigation of Microstructure and Mechanical Properties of Heat Treatment, Carbon Ratio and Alloying Elements in AISI 1008, 1040 and 4140 Steels. The Journal of Defense Sciences, 17(2), 139–167.

Aytaç, A., Çanakçı, B., Aslan, B., Aytav, E. (2019). An Analysis of The Reasons That Create Helicopter Vibrations and Vibration Reduction Techniques. In Multidisciplinary Studies in the World of Science (pp. 203–223). Berikan Publishing.

Aztekin, K., Işık, M. S., Aytaç, A., Özdemir, T., Çakır, U., Çanakçı, B. (2018). Effects of Heat Treatment Conditions and Surface Roughness on Fatigue Strength of AISI 4140 Steel (pp. 298–311). Presented at the International Multidisciplinary Congress of Eurasia-IMCOFE 2018, Barcelona, Spain.

Çakır, U., Çanakçı, B., Aytaç, A., Işık, M. S., Özdemir, T., Aztekin, K. (2018). Optimization of Machining Parameters of 7000 Series Aluminum Alloys by Response Surface Method (pp. 482–489). Presented at the International Multidisciplinary Congress of Eurasia-IMCOFE 2018, Barcelona, Spain.

Ezugwu, E.O., (2005). Key Improvements in the Machining of Difficult to-Cut Aerospace Super Alloys. International Journal of Machine Tools and Manufacture. 45 (12–13) 1353–1367.

Fujii, H., Saga, M. Nippon Steel Tech. Rep., 391 (2011), pp. 169-174

Geetha M., Singh A.K., Asokamami R., Gogia A.K. (2009). Ti Based Biomaterials, The Ultimate Choice for Orthopaedic Implants – A Review. Progress Materials Science, 54 397–425.

Gepreel, M.A.H., Niinomi, M. (2013). Biocompatibility of Ti-Alloys for Long-term Implantation. Journal of the Mechanical Behavior of Biomedical Materials, 20 407–415.

Ghani J.A., Haron,C.H.C., Hamdan, S.H., Said, A.Y.M., Tomadi, S.H. (2013). Failure Mode Analysis of Carbide Cutting Tools Used for Machining Titanium Alloy. Ceramics International 39 4449–4456.

Hasçalık, A., Çaydaş, U. (2008). Optimization of turning parameters for surface roughness and tool life based on the Taguchi method. The International Journal of Advanced Manufacturing Technology. 38 (9–10) 896-903.

Işık, M. S., Aytaç, A., Aztekin, K., Özdemir, T., Çakır, U., Çanakçı, B. (2018). The Effect of Cooling Environment and Tempering Temperature on Wear Resistance of AISI 4140 Steel (pp. 550–560). Presented at the International Science and Technology Conference-ISTEC 2018, Paris, France.

Karayel, D. (2009). Prediction and Control of Surface Roughness in CNC Lathe Using Artificial Neural Network. Journal of Materials Processing Technology., Vol. 209, No.2, pp. 3125–3137.

Kumar, S.M.R., Kulkarni, S.K. (2017). Analysis of Hard Machining of Titanium Alloy by Taguchi Method. Materials Today: Proceedings 4 10729–10738

Li, A., Zhao, J., Luo, H., Pei, Z., Wang, Z. (2012). Progressive Tool Filure in Highspeed Dry Milling of Ti–6Al–4V Alloy with Coated Carbide Tools. The International Journal of Advanced Manufacturing Technology. 58 (5–8) 465–478.

Ma J., Andrus P., Condoor S., Lei, S. (2015). Numerical Investigation of Effects of Cutting Conditions and Cooling Schemes on Tool Performance in up Milling of Ti-6AL-4V Alloy. The International Journal of Advanced Manufacturing Technology. 78 361–383.

Okada, A., Uno, Y., Yabushita N., Uemura, K., Raharjo, P. (2004). High Efficient Surface Finishing of Bio-Titanium Alloy by Large-Area Electron Beam Irradiation. Journal of Materials Processing Technology 149 506–511.

Sartori, S., Moro L., Ghiotti, A., Bruschi, S. (2017). On the Tool Wear Mechanisms in Dry and Cryogenic Turning Additive Manufactured Titanium Alloys. Tribology International 105 264–273

Şirvancı, M. (1997). Kalite için Deney Tasarımı: Taguçi Yaklaşimi, (pp.12-100), İstanbul:Literatür Yayıncılık.

A LITERATURE REVIEW ON TIRE NOISE AND DESIGN CONCEPTS FOR REDUCING TIRE NOISE

CHAPTER

16

Merve KÜÇÜKALİ ÖZTÜRK[1]
F. Banu NERGİS[2]
Cevza CANDAN[3]

[1] Istanbul Technical University, Faculty of Textile Technologies and Design, Istanbul- Turkey kucukalim@itu.edu.tr
[2] Istanbul Technical University, Faculty of Textile Technologies and Design, Istanbul- Turkey
[3] Istanbul Technical University, Faculty of Textile Technologies and Design, Istanbul- Turkey

1. INTRODUCTION

In recent years, with the growth and improvement in the automotive industry, expectations of people from automobiles has been changed. Previously mechanical properties of vehicles such as endurance or safety, were the important ones for people. But nowadays more than mechanical properties, comfort is at the forefront. Part of this comfort is provided by the reduction of in-cabin noise (Gloerfelt, 2009).

The noise emission of cruising vehicles essentially consists of tire/road noise, drivetrain/motor noise (engine with intake and exhaust system etc.) and aerodynamic noise (Gloerfelt, 2009; Li, 2018). Figure 1 shows external noise sources on road vehicles.

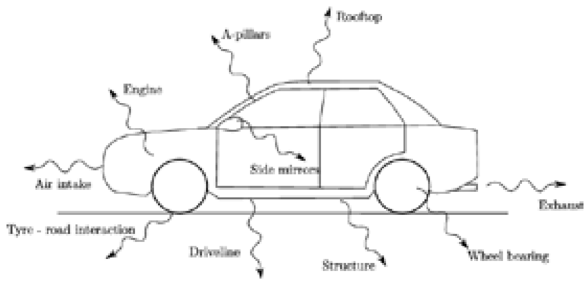

Figure 1. *External noise sources on road vehicles (Pignier, 2017).*

Before 1970's engine was the dominant noise source, however, as engine and exhaust became less noisy, and the aerodynamic design of vehicle body was optimized (Dechipre et al., 2010). Nowadays, the tire-pavement interaction noise has become more and more dominant, as shown in Figure 2. The curves indicate how the limits and the sources engine, intake, exhaust and tire have developed over time (Sandberg, 2001).

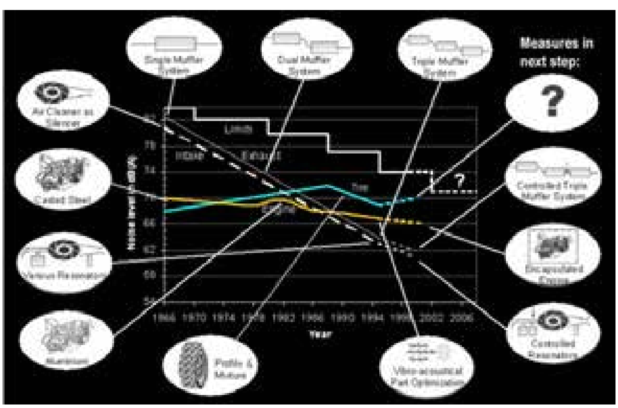

Figure 2. *The most important reduction measures employed in a common car in order to satisfy the various steps in tightened noise emission limits in Germany and the EU (Sandberg, 2001).*

Sandberg (2001) further claimed that usually tire noise dominates during almost all types of driving for vehicles, as shown in Figure 3 (Bernhard and Wayson, 2005).

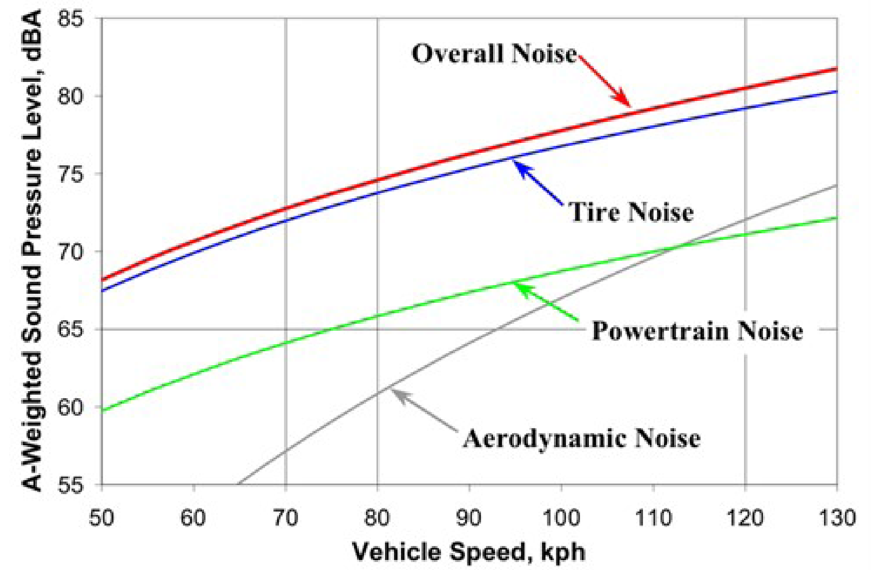

Figure 3. *Contributions of various sub-sources of highway traffic noise (Bernhard and Wayson, 2005).*

Several factors can lead to tire noises when driving and there are ways to avoid them. This survey comprises common causes of tire noise and design concepts for reducing tire noise.

2. TIRE STRUCTURE

Tyre is a complex structure which contains rubber, and rubber is not stable and can not resist against stresses so auxiliary materials are necessary. Conventional tyres have many layers and each of them has different functions. Generally, there are reinforcing materials as one of the layers of a tyre that ensure its stable shape and protection against dynamic stresses. In addition, reinforcing materials are related with loading capacity, abrasion resistance, and other properties of the product (Kumar, 2013). Cross section of a high performance passenger tire is shown in Figure 4.

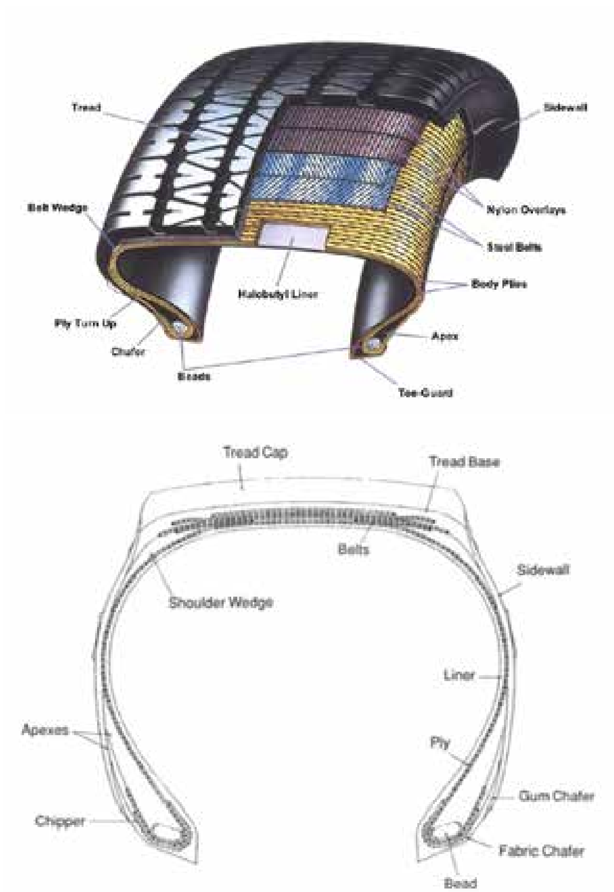

Figure 4. *Cross Section of High Performance Passenger Tire (Rodgers and Waddell, 2005).*

On a tire, tread is the surface where tyre meets with the road. It is the wear resistance component of the tire and must generate minimum noise and heat. Tread shoulder affects tread heat distribution, where tread base is the rubber part that supports adhesion between belts and tread. Tread base also affects heat distribution like tread shoulder and has low rolling resistance. Sidewall is a rubber composite material that protects the tyre against side frictions and controls tire ride characteristics. Curb guard is a rubber offset in the sidewall that protects the tyre from friction on curbs. Plies are the main reinforcing materials of a tyre which might be textile based or steel cord.

The rigid steel wire loops that immobilize the plies and connect tire onto the wheel are beads. (Rodgers and Waddell, 2005).

3. TIRE NOISE GENERATION MECHANISMS

3.1 Tread impact

At the entrance of the interface between the tire and pavement an impact occurs as the tread hits the pavement. This impact causes vibration of the car shaft (Bernhard and Wayson, 2005).

The tread design may energize noise vibrations that pass through the rigid sidewalls of the tire to the vehicle itself, where it is damped, isolated, amplified or conducted, based on the structure of the car. When the tread components are evenly spaced around the tire's circumference, they create a clearly identifiable note that rises in frequency as the speed increases. Any accurately repeated pattern will generate a particular note, or combination of notes, and harmonics that will vary according to the speed of the vehicle (Ball, 1995).

3.2 Air pumping

Air pumping refers to a collection of acoustic sources, which are all characterized by rapid displacement of air, in or near the contact patch (Winroth et al., 2013). Within the contact patch, the passages and grooves in the tire are compressed and distorted. The air entering these passages will be compressed and pumped in and out of the passages. Therefore, aerodynamically generated sound is created (Ohiduzzaman, 2016).

3.3 Stick-Slip

One noise excitation mechanism results in stick-slip vibrations of the tread block during longitudinal acceleration or braking as well as severe cornering of the vehicle. The longitudinal or horizontaL slip of the tire causes friction actuated self-excited vibrations of the tread blocks. The frequencies of the stick-slip vibrations depend on the geometry of the tread block, on the material and contact properties as well as on the process parameters like sliding velocity or normal load (Kröger, 2010).

During the passage through the contact patch the tread block first sticks on the road and in the second part of the contact the tread block slides. However, for some contact conditions, especially for certain slip and normal load conditions, the tread block causes self-excited stick-slip vibrations which are too loud (Kröger, 2010).

3.4 Stick-snap (adhesion)

The contact between the tread block and the pavement causes adhesion between the tread block and pavement. When the tread block exits the contact patch, the adhesive force holds the tread block. The release of the tread block causes both sound energy and vibration of the tire carcass (Bernhard and Wayson, 2005).

4. DESIGN CONCEPTS TO REDUCE TIRE NOISE

Research on design concepts for reducing tire noise has been on the focus of researchers for a couple of decades.

According to the results of a research tyre noise has become distracting for the drivers with the speed of over the 80 km/h, structure-borne noise arises at low frequencies under the 500 Hz and, airborne noise arises at high frequencies from 500-2000 Hz (Lopez et al., 2007). But according to another study, tyre/road noise dominates over power unit noise for all speeds and gears except when driving on the first gear. In practice, it means that at constant-speed driving tyre/road noise always dominates (Zhou, 2013). For reducing vehicle interior noise, the structural-acoustic finite element method is frequently used which is effective for low frequencies (Hambric et al., 2016).

The modification has been applied to tire tread, tread pattern, tire cavity, and rim. However, few of these design concepts are commercially viable due to manufacturing complexities and costs, safety and durability; the sound absorbing materials attached inside the tire cavity to reduce the cavity resonance noise might be the most successful so far (Li,2018).

Iwao and Yamazaki (1996) aimed at reducing the vibration by the mass effect and reduction of the noise was tried by local modification of the tire construction, by attaching a rubber ring on the inside surface of the center part of the tread surface. (Iwao and Yamazaki, 1996). Saemann (2011) applied seal and foam absorber to the inside surface of tread band in order to reduce tyre noise. Zhou (2013,2014) tried to reduce tyre noise by using the bypass structure and bionic tread groove. The result of the study showed that the circumferential grooves with bypass not only lower pipe resonance noise of circumferential grooves but also reduce far-field radiated noise of tire. Cusimano (1992) made modification on tread pattern by using a low noise pneumatic tire tread and minimized the total amount of acoustic energy produced by tire's tread by strategic placement of grooves in a tread design. In an another study on modification in the rim design, Kühl type lightweight steel rim was developed (Fitz and Heck, 2001). Modifications on the tire rim or tire cavity can decouple these resonances by shifting the natural frequency outside of the 200 – 250 Hz range to reduce the audible noise levels (Sainty et al., 2012). A Helmholtz resonator, which would form a part of the rim structure was tested to selectively remove the tire cavity resonance mode, creating the audible noise peak. It was found that the Helmholtz resonator has clearly reduced the noise levels within the 205 – 240 Hz range as expected (Fernàndez, 2006). The geometric shape of the tire cavity was changed by introducing three strips of rubber, which extended into the cavity from the tire, to shift the modal frequency of the tire cavity. Polyurethane foam (PU) as sound absorbing material was placed in tire to fill the tire cavity. The results showed that the PU foam was able to absorb the standing waves of the sound travelling throughout the tire cavity (Yukawa et al., 2004). Moreover, a novel model of a tire including the dynamics of the acoustic cavity has been developed in order to quantify the effect of the cavity resonances on the tire response as well as the transmitted force and moment at the spindle (Molisani et al., 2003). In another study, a thin, light weight plastic resonator was developed for tire cavity noise and this on-wheel resonator is able to reduce tire cavity noise by 10 dB (Kamiyama, 2014). In another one, a trim layer was inserted onto the inner surface of the tire tread. It was found that the absorbent trim material inserted on the inner surface of the tyre tread plate is capable to reduce the sound pressure amplitude of the cavity resonance. The reduction depends on the material and thickness of the trim layer (Mohamed and Wang, 2015).

5. MARKET RESEARCH

Continental- ContiSilent™

ContiSilent™ is a tire noise-reducing technology developed by Continental. It is designed to reduce interior noise on all road surfaces. ContiSilent™ tires are equipped with an inner tire absorber, a polyurethane foam, attached to the inner surface of the tread area with an adhesive. ContiSilent™ helps reduce interior vehicle noise up to 9 dB(A), depending on the type of vehicle, its speed and the road surface (Continental 2014).

GOODYEAR- Dunlop Noise Shield Technology

A tyre technology that cuts interior sound levels by up to 50%. It works by bonding an advanced polyurethane foam layer to the tyre's inner surface to reduce interior vehicle noise, without compromising performance capabilities (Goodyear 2017).

GOODYEAR- SoundComfort Technology

Goodyear's new "SoundComfort" technology features an open-cell polyurethane foam element attached to the inner surface of the tire. The technology dampens the Tire Cavity Resonance (TCR) sound peak, generated when the tire rolls over a surface, by up to 11dBA and enables an vehicle interior noise reduction of up to 4dB, making the vehicle cabin significantly quieter across a large range of vehicle speeds (Goodyear 2018).

MICHELIN® Acoustic Technology®

Acoustic Technology effectively reduces vibrations caused by the road resulting in a significant reduction of interior noise by approximately 20%*. A custom designed polyurethane foam solution muffles noise resonance (Michelin 2016).

PIRELLI- Noise Cancelling System™ (PNCS)

Pirelli's sound absorbing sponge reduces the frequency filtering through the car, providing superior comfort compared to traditional tyres. The Pirelli Noise Cancelling System reduces noise by between two or three decibels, which on average reduces the perceived noise by half, with a consequent improvement in driving comfort (Pirelli 2013).

TOYO TIRES- Toyo Silent Technology

They focused on reduce noise by utilizing the flow of air. Using the flow of air when sound passes through the hole further increases the noise-reduction effect so they arranged a porous film to face the flow of air (the pathway of the air) that they ascertained from visualization, and studied disposing a structure through which generated sound can pass (Toyo Tires 2018).

6. CONCLUSION

Automobile owners demand ever-increasing levels of refinement and silent driving conditions. There are three different kinds of noise source disturbing driver; aeroacoustic noise, engine noise and road noise. The term tyre/road noise denotes the noise emitted from a rolling tyre as a result of the interaction between the tyre and the road surface. Active and passive noise control approaches can be adopted for noise control in different means of transport. Active noise control is the process of reducing the total noise using a secondary sound source, whereas passive noise control is provided by sound-absorbing and sound-isolating materials. This survey includes common causes of tire noise, design concepts to reduce tire with market research.

REFERENCES

Ball, C.A. (1995). Tread design plays major role in tire noise. Tire Business.

Bernhard, R., Wayson, R. L., Haddock, J., Neithalath, N., El-Aassar, A., Olek, J., ... & Weiss, W. J. (2005). An introduction to tire/pavement noise of asphalt pavement. Institute of Safe, Quiet and Durable Highways, Purdue University.

ContiSilent™. Continental AG, 2014, https://www.continental-tyres.ie/car/technology/contisilent.

Dechipre, H., Hartmann, M., Ewert, R., & Delfs, J. (2010). Assessment of Numerical Methods for Computation of Automotive Rain Gutter Wind Noise. In 16th AIAA/CEAS Aeroacoustics Conference (p. 3755).

Dunlop expands winter line-up equipped with Noise Shield technology for a comfortable winter performance drive. Goodyear 2017, https://news.goodyear.eu/dunlop-expands-winter-line-up-equipped-with-noise-shield-technology-for-a-comfortable-winter-performance-drive/

Fitz, F., & Heck, T. (2001). Development of tooling for a light weight steel Kühl wheel (No. 2001-01-0750). SAE Technical Paper.

Gloerfelt, X. (2009). Noise from automotive components. Aerodynamic noise from wall-bounded flows, 9-13.

Hambric, S. A., Sung, S. H., & Nefske, D. J. (Eds.). (2016). Engineering Vibroacoustic Analysis: Methods and Applications. John Wiley & Sons.

Iwao, K., & Yamazaki, I. (1996). A study on the mechanism of tire/road noise. JSAE review, 17(2), 139-144.

Kamiyama, Y. (2014). Development of a new on-wheel resonator for tire cavity noise (No. 2014-01-0022). SAE Technical Paper.

Kröger, M., & Moldenhauver, P. (2010). Influences on the vibration frequencies of tire tread block. In Proceedings of ISMA (pp. 4015-4021).

Kumar, R. S. (2013). Chapter 10: Textiles in Automobiles. In R. S. Kumar, Textiles for Industrial Applications(Vol. 1st edition, pp. 245-292). CRC Press.

Li, T. (2018). Literature review of tire-pavement interaction noise and reduction approaches. Journal of Vibroengineering, 20(6), 2424-2452.

Lopez, I., Blom, R. E. A., Roozen, N. B., & Nijmeijer, H. (2007). Modelling vibrations on deformed rolling tyres—a modal approach. Journal of Sound and Vibration, 307(3-5), 481-494.

MICHELIN® Acoustic Technology®. Michelin, 2016, https://www.michelinman.com/acoustic-technology.html

Mohamed, Z., & Wang, X. (2015). A study of tyre cavity resonance and noise reduction using inner trim. Mechanical Systems and Signal Processing, 50, 498-509.

Molisani, L. R., Burdisso, R. A., & Tsihlas, D. (2003). A coupled tire structure/acoustic cavity model. International journal of solids and structures, 40(19), 5125-5138.

Ohiduzzaman, M. D., Sirin, O., Kassem, E., & Rochat, J. (2016). State-of-the-art review on sustainable design and construction of quieter pavements—Part 1: traffic noise measurement and abatement techniques. Sustainability, 8(8), 742.

Pignier, N. (2017). Predicting the sound field from aeroacoustic sources on moving vehicles: Towards an improved urban environment (Doctoral dissertation, KTH Royal Institute of Technology).

Pirelli Noise Cancelling System. Pirelli, 2013, https://www.pirelli.com/tyres/en-ww/car/pncs-technology

Rodgers, B., & Waddell, W. (2005). Tire engineering. In Science and Technology of Rubber (pp. 619-II). Academic Press.

Ronneberger, D. (1984). Experimentelle und theoretische Untersuchungen spezieller Mechanismen der Rollgeräusche. Mitteilungen des Instituts für Straßen,-Eisenbahn-und Felsbau an der ETH Zürich, 55-57.

Sainty, S., Tawaf, A., Richard, J., Mohamed, Z., & Wang, X. (2012, August). Analysis of potential solutions to audible tire cavity and rim coupling resonance noise. In ASME 2012 Noise Control and Acoustics Division Conference at InterNoise 2012 (pp. 15-21). American Society of Mechanical Engineers.

Sandberg, U. (2001). Noise emissions of road vehicles effect of regulations: Final Report 01-1. Noise News International, 9(3), 147-203.

SoundComfort Technology. Goodyear, 2018, https://www.goodyear.eu/content/gy-master-en/en/consumer/why-goodyear/soundcomfort-technology.html

Torra i Fernàndez, È. (2006). The influence of tyre air cavities on vehicle acoustics (Doctoral dissertation, KTH).

Toyo Silent Technology. Toyo Tires, 2018, https://toyotires.eu/news/item/id/9881

Winroth, J., Hoever, C., Kropp, W., & Beckenbauer, T. (2013). The contribution of air-pumping to tyre/road noise. In Proceedings of AIA-DAGA 2013 (pp. 1594-1597).

Yukawa, N., Nishikawa, M., Nakajima, T., Aoki, C., & Sugihara, H. (2004). U.S. Patent No. 6,726,289. Washington, DC: U.S. Patent and Trademark Office.

Zhou, H. (2013). Investigate into Influence of Tire tread Pattern on Noise and Hydroplaning and Synchronously Improving Methods (Doctoral dissertation, Ph. D. Dissertation, Jiangsu University, China).

Zhou, H., Wang, G., Yang, J., & Ying, S. (2014). Simulation and analysis of the bypass influences on tire noise. Research Journal of Applied Sciences, Engineering and Technology, 7(3), 576-580.

CLASSIFICATION WITH DEEP LEARNING: MALARIA IMAGES EXAMPLE

CHAPTER

17

Mohanad Mohammed QANBAR[1]
Sakir TASDEMIR[2]

1 Department of Information Technology Engineering, Selcuk University, Konya Turkey
2 Department of Computer Engineering, Selcuk University, Konya Turkey

INTRODUCTION

Rapid changes in technology generated and important effects on human life. With these developments, technology and physical computer systems are indispensable to human life continuously. Computers, their hardware-software and supported devices serve and assist the humans almost in the whole life. It is possible to see the utilization from this technology in worksites, homes, schools, in short, at any field of the life. One of these fields is the health sector and medicine. Such systems are commonly used in diagnosis, classification and treatment phase of the diseases (for the purpose of decision-support). Reasons such as high number of diseases, needing quite a few data in diagnosis and treatments, incremental costs in collection and processing of these data turned the use of computer systems in medicine into a necessity. Early diagnosis is of great importance in treatment of many diseases for medical scientists. Researches oriented to the early diagnosis are in a privileged position. IT scientists working in relation with the medicine in parallel with this are striving to develop different functions and libraries in order to overcome the difficulties encountered in data collection and image processing aspects, notably deep learning algorithms. In such way, the computer systems may be used for the purpose of decision-support for allowing the medical scientists to take more accurate and faster decisions (Bergsland, 2017) .

Malaria is a type of disease borne by mosquitoes and affecting humans and animals. Fever, fatigue, vomiting and headache are among the typical symptoms of the malaria. Serious malaria cases lead to yellow skin, seizures and serious outcomes going up to death. Such symptoms generally start to develop about 10-15 days after the bite of a mosquitoes carrying the malaria. If the disease was not properly treated, the infection may develop again. In case of inadequate disinfection in those who recover from the infection, symptoms may develop again. In 2016, it was encountered with 216 million of malaria cases all over the World and as a result of this, thousands of people lost their life. There may be increase in health expenses, decrease in labor force and negative effects on tourism and trade sectors (due to the contagiousness of the disease) depending on this disease. The malaria seen in Turkey progresses mildly and does not directly lead to death based on the disease. These circumstances lead to the diseases being neglected. However, whereas the malaria disease seen in Turkey does not directly lead to deaths, it leads to death at highly important amounts by leading to spontaneous abortion, stillbirth, low birth weight infant and maternal mortalities. To make classification with Deep Learning for a disease having such important impacts is of great importance in terms of facilitating the procedures pertaining to patient and assisting the medical science (WHO, 2014) .

Today, the deep learning algorithms are being commonly used in the medical field. Likewise, the accuracy share of the artificial intelligence is high and its predictions are better. Besides these, the role in the activities of disease prevention and the fact that it reduces the medical costs are seen. It is applied in the health and medical fields for its positive impacts such as diagnosis programs, development of treatment protocol, drug development, customized medicine, patient follow-up and care. In this context, one of the objectives in the study is the expectation regarding that it may reduce the manpower ad medical costs for the diagnosis of the malaria disease. Operation of Convolutional Neural Networks with a big data set will realize a more accurate, faster and cost-efficient diagnosis. Such positive outcomes may present the importance of the study (LeCun, Bengio, & Hinton, 2015; Litjens et al., 2017).

Another contribution of the Deep Learning approach is that it can provide a positive impact on the treatment process by noticing any minor details which may not be noticed between the symptoms seen in the patient and disease. It may be provided with such artificial learning algorithms to make both procedures to be faster and more economic. In such way, it may have contributions both into the patient comfort and the national economy. (Şeker, Diri, & Balık, 2017).

The importance of the study may develop clearly in such way. Due to such negative conditions, diagnosis and treatment processes of the malaria are of importance. Using of computer-aided algorithms and approaches which can support the procedures which any medical doctor performs in the diagnosis and treatment process and may lead to a fast decision-making process in this field reveals the aim and importance of the study in a clear way 4(Toha & Ngah, 2007).

In the literature review, it can be seen that different computer-based studies have been conducted for the malaria. Image processing, machine learning and deep learning algorithms are some of these. Developments in the deep learning approach in the recent years have been placed among the alternatives as an applicable method for the diagnosis of malaria disease. The literature reviews support this study. There are different literature studies oriented to this aim.

In this study, a deep learning approach will be developed for classification and diagnosis of the Malaria disease. For this purpose, Residual Attention Network that is a deep learning Convolutional Neural Networks (CNN) may be used with a previously classified data set. It is aimed to design a computer-aided software in order to classify the malaria on parasite-infected blood cell images (blood samples). A such decision-support system would have been performed by the deep learning approach. In this study, the reason why "Residual Attention Network" that is a Convolutional Neural Network is used is that it may have the capacity which will yield better results in the image processes compared with other algorithm types. At the end of this study, it will be determined that whether images examined are infected with parasite or not, thus, such a classification may be made as infected or non- infected (Dong et al., 2017).

LITERATURE SEARCH

In the literature research examined, results such as classification, diagnosis have been drawn by using the different algorithms of Deep Learning, different software and libraries related with the Malaria disease. It can be seen that the accuracy rate of the results of these studies which were mainly conducted over diagnosis, is between 80-90%.

In an article written by (Quinn et al., 2016) named "Deep Convolutional Neural Networks for Microscopy-Based Point of Care Diagnostics", a care diagnosis using the microscopy and computer-aided vision method was applied on many practical problems and it was noted that it was particularly related with low-income, high disease load areas. Besides, the sensitivity and specificity of the vision methods with these computers used are subjected to restrictions. Generally, it was explained that the deep learning has the features of revolution in the computer vision exceeding the human performance for duties of other object recognition in some cases recently. Evaluating the performance of the deep convolutional neural networks in three different microscopy duties, to establish diagnosis of malaria in thick blood stains and to determine tuberculosis in sputum samples and intestinal parasite eggs in stool samples are among the aims of the article. In any case, it was argued that it has a very high accuracy rate and is much better than an alternative approach representing the traditional medical imaging techniques. As an example, there are 1.72 microscopes for a population amounting to 100.000 in a national study conducted in Ghana; but, there are only 0.85 trained laboratories for a population of 100.000. Consequently, it was said that tests are frequently performed in basis of clinical symptoms and symptoms, this is open to error and it leads to higher mortality, drug resistance and the economic burden of purchasing unnecessary drug. An accuracy rate of 96% was obtained at the end of the disease identification studies performed with CNN.

In an article titled "Evaluations of Deep Convolutional Neural Networks for Automatic Identification of Malaria Infected Cells", (Dong et al., 2017) automatically defined the malaria infected cells by using deep learning. For compiling the used data cluster, all slide images of thin blood stains were labelled with four pathologist groups of the malaria-infected red blood cells and non-infected cells. The well-known convolutional neural networks are divided into three as: "*LeNet*", "*AlexNet*" and "*GoogLeNet*". According to the data which the results of the simulation performed in the show, the success of all these dee convolutional neural networks makes classification above 95%. The approximate value which can be obtained in the method in which support vector whose sensitivity is higher is 92%. Also, the deep learning methods have other advantages: since it enters the features automatically, it reduces the necessary number and power of human.

In a study conducted by (Rajaraman et al., 2018) titled "Pre-Trained Convolutional Neural Networks as Feature Extractors Toward Improved Malaria Parasite Detection In Thin Blood Smear Images", the microscopes generally examine the thick and thin blood stains for diagnosing the diseases and calculating the parasitemia. The computer-aided diagnosis (CADx) methods applied on the microscopic images of smears by using the artificial intelligence properties, using the machine learning (ML) techniques and being based on the computer-aided diagnosis (CADx) methods entail specialty in the analysis of morphological, tissular and spatial variations. On the contrary, the Convolutional Neural Networks (CNN) that are the deep learning class (DL) models promise highly scalable and superior results with the end-to-end feature extraction and classification. For this reason, the automatic malaria screening by using the DL techniques may be used as an effective diagnosis assistant. In this article, we evaluate the performance of CNN-based DL models as the feature extractors for the classification of parasite-infected and non-infected cells in order to assist the developed disease screening. The most proper model layers were experimentally determined for the feature extraction from the basic data.

In a book named "Classification of Malaria-Infected Cells Using Deep Convolutional Neural Networks", (Pan, Dong, & Wu, 2018).mentioned of the use of machine learning Technologies for the automatic diagnosis of the malaria. Some of the recent studies over the classification of the malaria-infected cell deeply in an exceptionally correct way were presented: Convolutional Neural Networks (CNN). Firstly, the image processing methods used for the segmentation of red blood cells from whole slide were explained: Images. Data augmentation methods used for augmenting the size of data set significantly under the light of extreme conformity problem related with the deep convolutional networks' training were explained as well as the procedures of compiling the image data set under the curatorship of pathologist for training the deep neural network. Then, the accuracy of classification which the deep convolutional neural networks obtained was compared with various combinations of data sets by way of training, confirming and testing. These datasets contain the dataset increased significantly obtained by using the original dataset and direct interpolation. A result in rate of 95.5% was obtained at the end of the study.

MATERIAL AND METHOD

A deep learning approach that facilitates the detection of the disease will be conducted for the purpose of competing with Malaria disease better, assisting the medical staff, reducing the cost related with disease diagnosis and minimizing the cases which may be overlooked by the specialist or entail an experience spread for a very long time.

In the aimed study, primarily a ready data set may be used for the deep learning algorithms. The dataset is consisted of infectious and healthy subject images taken from the blood samples by using a microscope. The dataset used by SMEAR images containing infected and uninfected blood samples of malaria disease that used in this study were obtained from (Arunava, 2019) and also benefited from the website of the National Medical Library (Jaeger, 2019). With these data, a deep learning approach which can perform the diagnosis and classification of the malaria disease is aimed. In such way, also this dataset may be compared with the other literature which used this dataset. If required in the next stages of the study, a ready dataset from other libraries may be used or data will be supplied from hospitals.

In this study, primarily images of healthy and infected individuals will be classified. The classified images will be used in training and testing of the network. "Residual Attention Network" that is a Convolutional Neural Network which uses the attention mechanism that may be brought together with an advanced feed network architecture having the cutting-edge technology in a form of end-to-end training, is used for detecting the features in the Images. The working principle of the Residual Attention Network is given as example in the Figure 1 (Wang et al., 2017).

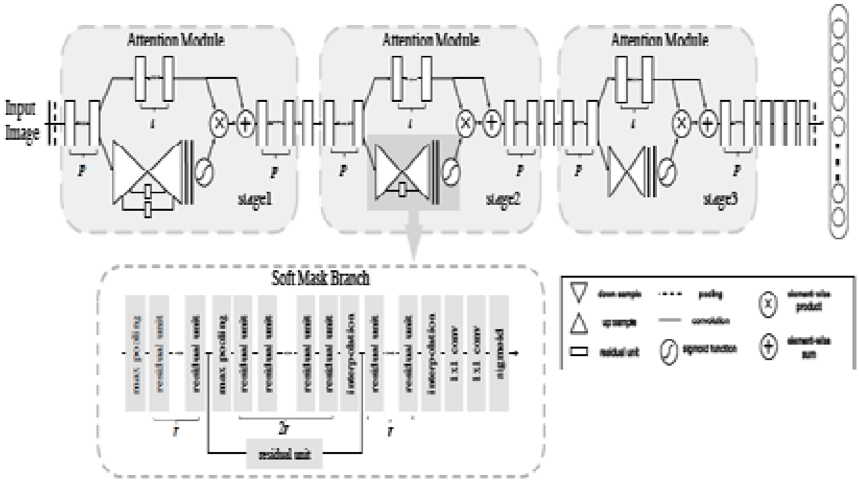

Figure 1. *Working Principle of Residual Attention Network*

Also, unlike the Convolutional Neural Network (CNN), the results could be compared statistically by using different classification algorithms like Support Vector Machine (SVM). It will be determined that what the difference from SVM is, whether it is better or not by comparing the obtained classification results with "Residual Attention Network" that is a Convolutional Neural Network (CNN), that is, it may be used as a provider of CNN. According to the course of the study, other different deep learning algorithms may be also used.

In this study; the software to be used for examination and classification of SMEAR images belonging to the Malaria disease will be written by using Python programming language. For this purpose, it will be utilized from TensorFlow, Keras and Scikit-learn that are the developed "Machine Learning" and "Deep Learning" algorithms.

Within this scope;

- Keras algorithms included within TensorFlow 2.0 library will be used for the classification of SMEAR images with the Convolutional Neural Network (CNN).

- Vector Classification (Support Vector Classification – SVC) algorithms will be used for the classification of SMEAR images with the technique of Support Vector Machine (SVM).

In this study's process, proper software and libraries may be used by taking the useable hardware units and working environments into account for the purpose of facilitating and accelerating the procedures. Once the size of data set to be used in this study is considered, a computer whose hardware features (like CPU, new generation GPU, RAM) are strong may be needed. In such way, it will be able to analyze and process many data and images and yield fast and correct results. In the event that such a specific-equipped computer is not found, the study may also be completed with alternatively equipped computers.

In this study, it was tried to develop tools which may be used for detection, diagnosis and classification procedures of the malaria disease in a fast and correct way and to determine the superiorities of the used methods by using the deep learning approach and big data structures containing image information.

GENERAL DESCRIPTION OF MALARYA DISEASE

In our present World, two billion populations are under the risk of malaria, 160 – 200 million of people from this population catch malaria disease. Together with the former patient, annual total patient number amounts to 300-500 million. Of these patients, about two million of people die every year. One million of died people is constituted by the children who are below five years old. As will be understood from these figures, the Malaria disease is placed in the top ranks within all diseases seen all over the World and death reasons (Akdur, 2001). For this reason, a conceptual framework was drawn by giving general info about the malaria disease.

DEFINITION OF MALARIA

Malaria is an infectious disease which develops with parasitism of *Plasmodium s*pecies contaminating to human with bite of Anopheles type female mosquitos, starting with shivering and fever seizures at varying intervals and progressing with seizures ending with shivering, characterized by secondary anemia, splenomegaly and hepatomegaly and occurs with accumulation of a pigments in internal organs and that is also known as Malaria, Paludisma, Remittent fever, Paludismus, Marsh miasma (Unat, Yücel, Altaş, & Samastı, 1995).

Parasite principally involves the liver cells and red blood cells. It is migrated to healthy people by taking from the infected or those carrying parasite by mosquitos fed by human blood and it causes the healthy people to get infected. The malaria parasite has four different types as vivax, malaria, falciparum and oval. Of these, vivax is a type which leads to seizure in every three days (the tertian malaria). It is the malaria whose fatality is least. For this reason, it is also called as benign malaria. A type seen locally in Turkey is this type. Malaria progresses with seizures coming at every four days (the quartan malaria). In the falciparum, the seizures are not apparent (Akdur, 2001) The malaria developed with falciparum is the most fatal type. For this reason, it is called as malign malaria. It is mostly common in tropical regions such as Africa, Far East and South America. Hence, it is called as tropical malaria. Quartan malaria and tropical malaria are not locally seen in Turkey. However, it is seen in cases coming from abroad. Oval is only seen in West Africa (Akdur, 2001).

MALARIA VECTORS

Only *Anopheles* species of the mosquitos contaminate the *Plasmodium* that is the malaria agent to human. The contamination source for Anopheles is human having gametocyte in their blood. Anopheles serve as developer-producer biological carrier (vector) to *Plasmodium. Plasmodiums* undergo a sexual reproduction stage in the body of them. Sporozoites accumulated in salivary glands of Anopheles are transferred to the human blood during the bite (Merdivenci, 1984). Each *Anopheles* species does not contaminate the malaria agents; there is the impact of factors such as tendency of anopheles to bite the human, blood sucking habit, lifetime, the possibility of *Plasmodium* to settle in anopheles, efficiency and period of anopheles. Thus, although there are many anopheles' species in each region, only some of these serve as vector to *Plasmodiums* (Merdivenci, 1984).Vectors of the malaria in our country are *Anopheles sacharovi, Anopheles superpictus* and *Anopheles maculipennis* which plays a lesser role. The primary one among the reasons of increasing malaria cases in 1977 is that because *Anopheles sacharovi* gained resistance against D.D.T, they reproduced rapidly and started to spread the malaria again (Özcel, 1993; Özcel & Özbilgin, 1995).

In our country, the following species are available; A. sacharovi, A. maculipennis, A. melanoon subalpinus, A. algeriensis, A. plumbeus, A. hyrcanus, A. hyrcanus mahmudi, A.superpictus, A. claviger, A. marteri, A. sinensis, A. sergentii, A. multicolor (Özcel, 1993; Özcel & Özbilgin, 1995).

DIAGNOSIS OF THE MALARIA

Besides there are many diagnoses in the diagnosis of the malaria disease, we can examine these by classifying as direct and indirect diagnosis methods.

Direct Diagnosis Methods

The best, cheapest and fastest methods used in diagnosis of the malaria leading to such a clinic Picture extending from the important clinic symptoms to death is direct microscopy. In the microscopy, diagnosis is established with parasites seen in the erythrocytes. The most commonly used methods in the diagnosis is preparation of thick drop and thin smear preparade. While preparing the preparade, Wright, Giemsa or Wright-Giemsa staining methods are used. Giemsa is more superior than the other staining methods in monitoring of some morphological structures belonging to the parasite. In these preparade prepared, trophozoite (Figure 2), schizont and gametocyte shapes of *Plasmodium are monitored and diagnosis is established* (Altıntaş, 2002; Saygı, 1998).

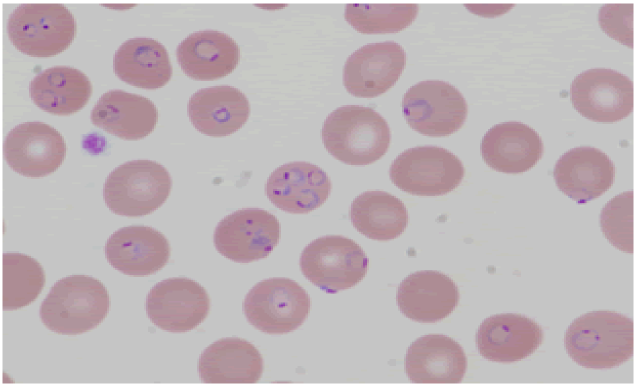

Figure 2. *Trophozoites in Erythrocytes, http://health.mo.gov/lab/bloodparasites.php (01.09.2019).*

Indirect Diagnosis Methods

IFAT, IHA, Immunoprecipitation and ELISA are being used, particularly antibodies formed against the infections in the erythrocytic stage are detected. Also, malaria diagnosis may be established with molecular biology diagnosis methods, Polymerase chain reaction (PCR), Quantitative Buffy Coat Method (QBC), Rapid Diagnosis Tests (Kocaçiftçi, 2008)

Types of the rapid diagnosis test are OptiMAL test, ICT Malaria test, MAKROmed Rapid Malaria Test, ParaSight-F Test (Taşkın, 2010) .

Rarely used diagnosis methods in the malaria are as follows (Girginkardeşler, 2015).

Quantitive Buffy Coat (QBC, Becton Dickonson) Methods: *"Heparin, acridine – orange", "Fluorescent microscope*".

Culture methods: Demanding vaccination studies, Culture plates, SCMI 612, RPMI 1640

Serological methods: Transfusion-based, retrospective, ELISA, IFAT

Studies conducted by World Health Organization (WHO) over Malaria

While the number of malaria cases all over the World in 1954 was about 250 million, the number of people died due to malaria was 2.5 million. Today, while 300-350 million of new malaria cases are seen every year, the number of people died is 1.5-2.7 million. Annual clinic case number totally exceeds 500 million. 90% of these cases are seen in tropical Africa. Deaths originating from the malaria in the World in 1997 were ranked in 6th and 8th among the all death reasons (according to the estimated figures). Besides, the estimated highest figure is considered (2.7 million) among the deaths seen following the fatal contagious diseases based on malaria, the malaria is ranked third following acute lower respiratory tract infection and tuberculosis. The number of deaths seen in children who are below five years old is 1 million, this rate constitutes 9% of the death of child who is below five years old (Yıldırım & Yıldırım, 2000).

Objective of the Global Malaria Strategy applied by the World Health Organization (WHO) was to reduce the deaths based on malaria in at least 75 of the countries affected from the disease at a rate of 20% until 2000 compared with the figures in 1995. In line with this strategy, 90% of the countries affected from the malaria achieved this objective. WHO developed a malaria control program particularly for 24 countries located in Africa which could not achieve this objective and put into practice starting from the year 1997. When the status of malaria in the World is considered by six WHO regions, Africa Region, Southern East Asia region and Western Pacific Region are of great importance in terms of malaria (Yıldırım & Yıldırım, 2000).

Examination of SMEAR Images of Blood Samples Infected and Not Infected with Malaria Parasites

The dataset used by SMEAR images containing infected and uninfected blood samples of malaria disease that used in this study were obtained from (Arunava, 2019) and also benefited from the website of the National Medical Library (Jaeger, 2019).

SMEAR images to be used in this study were divided into two different classes as parasitic and non-parasitic and they were resized in form of pictures in dimensions of 32x32 for convenience in the study.

SMEAR pictures of sample carrying Malaria parasite are shown in Figure 3. and SMEAR pictures of sample not carrying Malaria parasite are shown in Figure 4.

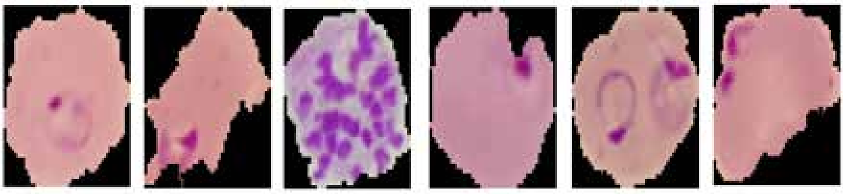

Figure 3. *SMEAR blood samples carrying Malaria parasite*

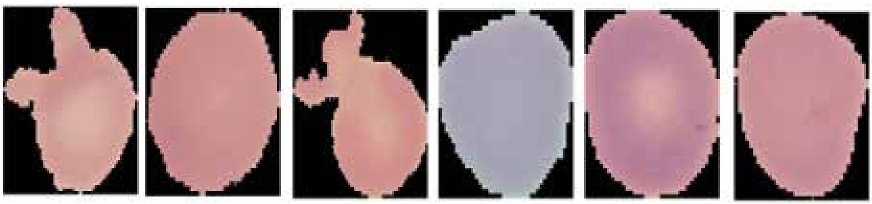

Figure 4. *SMEAR blood samples not carrying Malaria parasite*

Of these sample SMEAR images; it was grouped in the software in the following way: 11.500 images in deep learning training (training), 1.500 images in deep learning validity control (validation) and the remaining 100 images in deep learning control (test).

Experiments and Results

The following information regarding data availability was provided: *https://www.kaggle.com/iarunava/cell-images-for-detecting-malariaAccess*.

The dataset contains a total of 27,558 cell images including equal instances of infected and uninfected cells. A sample from the malaria is shown in the figure 5.

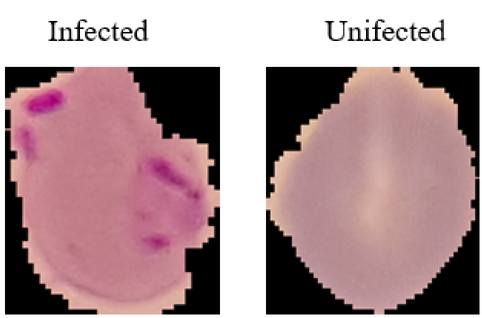

Figure 5. *Sample images of the dataset show the difference between infected and uninfected cells.*

In this study; Python programming language was used for examining the SMEAR images of the Malaria Disease. For this purpose, it was utilized from "Machine Learning" and "Deep Learning" algorithms and from TensorFlow, Keras and Scikit-learn libraries.

In this study, malaria from the dataset was classified as infected or non-infected. The data was divided into groups. In this context, 20658 image training and 6900 image tests were used (60 epoch). The data was then converted to a file for correct training. The following results were obtained; 95.78% in the training of Residual Attention Network that is a Convolutional Neural Network (CNN) (Figure 6) and 95.89% in test process (Figure 7). The training process, used time, algorithm, materials, result and Matrix are shown in the Figure. This program is powered with a computer that is Nvidia GPU. This study is a Deep Learning study.

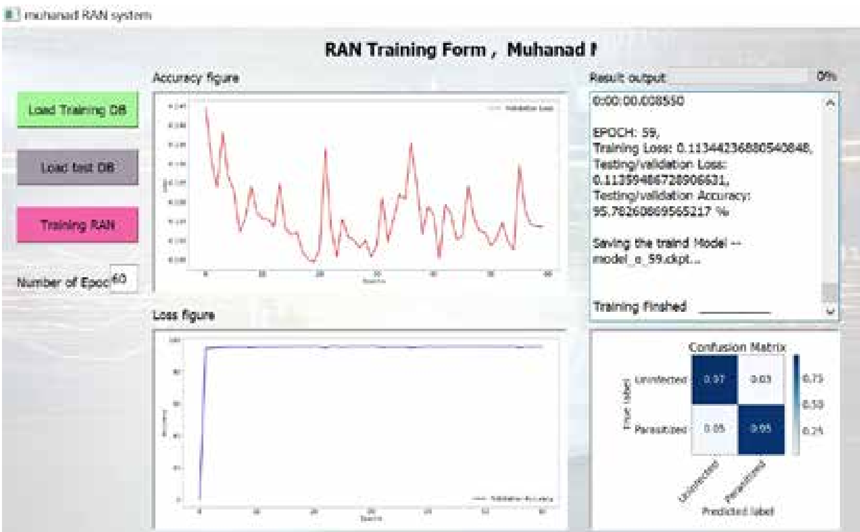

Figure 6. *The training of Residual Attention Network that is a Convolutional Neural Network (CNN).*

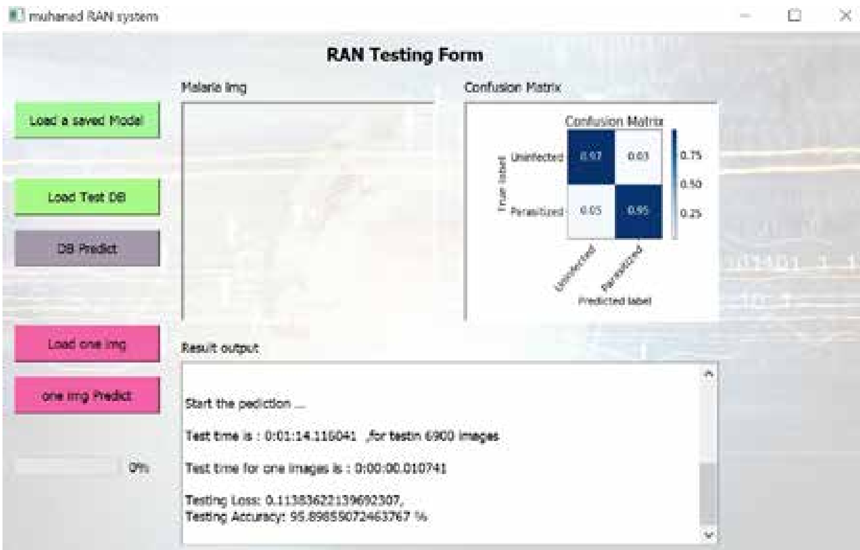

Figure 7. *The Testing of Residual Attention Network that is a Convolutional Neural Network (CNN)*

In such way, Malaria was classified with the Support Vector Machine (SVM) of the Machine Learning and a result of 83% was obtained (Figure 8).

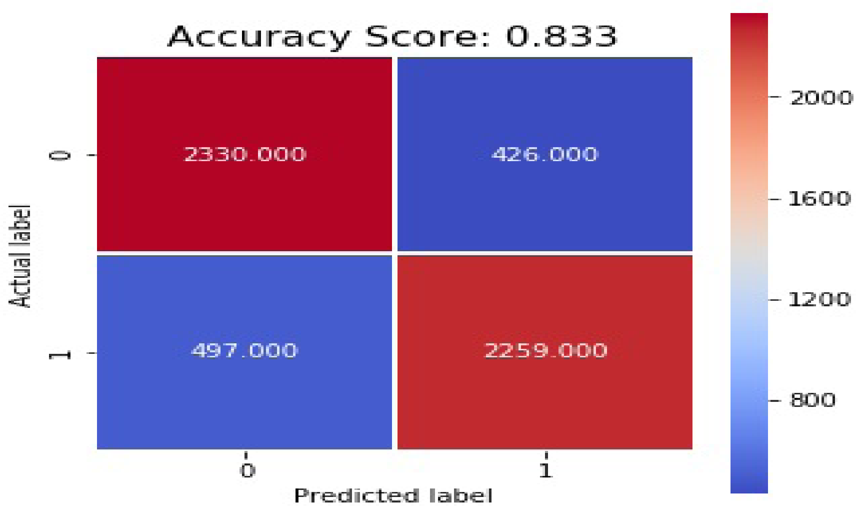

Figure 8.*Classfied Support Vector Machine (SVM)*

CONCLUSION

Today, information systems are effectively used in many scientific studies. Particularly, Convolutional Neural Network (CNN) and Support Vector Machine (SVM) are distinguished with the advantages they provided in the artificial intelligence and deep learning systems. Within this scope, different methods have been developed for increasing the efficiency of the CN method and increasing the accuracy rate in the estimation process. The most common of these methods is Residual Attention Network (RAN).

In this study in which the diagnosis of the Malaria disease by using Deep Learning Techniques was investigated, it was based on the use of CNN methods. In this context, the following points were investigated in this study;

- The usability of SVM method of the deep learning techniques, its advantages and disadvantages compared with other methods,
- The usability of RAN of the CNN methods and layer models such as VGG16, Resnet50 and MobilenetV2 known as the pre-trained methods and commonly used in the scientific research and their advantages to each other,
- The usability of SVM and CNN methods together.

In the study, 20658 Malaria SMEAR images prepared by World Health Organization for being used in the academic and scientific researches were used in the training process of the model. Images which have different dimensions as of their original nature were turned into 32 x 32 dimensions in introduction of each model for the purpose of providing the standardization.

At the end of the study conducted; while the accuracy rate in the estimation processes performed by using Residual Attention Network (RAN) deep learning model yielded 96.05%, the accuracy rate in the estimation processes performed with Support Vector Machine (SVM) model yielded 83%. Accordingly, it is considered that the use of “Residual Attention Network” (RAN) model in the diagnosis of the Malaria disease with deep learning methods yielded more effective results and preference of this model in the studies conducted in this context would be proper.

Within the scope of the study, it was concluded that VGG16, Resnet50 and MobilenetV2 models that are the pre-trained CNN methods have advantages and disadvantages compared to each other; however, they could not generate completely effective results in the Malaria SMEAR images used within the scope of the study. Of these models, VGG16 had a higher accuracy rate than the other models in terms of accuracy with an accuracy rate of 68.6%. MobileNetV2 completed the training process in a shorter period than the other models with 14.67 minutes. Data pertaining to these models are shown in Table 1.

Table 1. *Comparison of pre-trained CNN models*

Model Type	Epoch Number	Training Time	Model Loss Ratio	Model Accuracy Ratio
VGG16	60	20.89 minutes	0.5895	0.6863
Resnet50	60	23.88 minutes	0.6933	0.4989
MobileNetV2	60	14.67 minutes	0.6834	0.5517

According to another result of the study, it was found out that CNN and SVM methods of deep learning methods may be combined through proper methods. Too many calculations are needed in respect of the dimensions of SMEAR images for making the required calculations in SVM model. Also, due to dimension differences of images, a previous image sizing process is needed. In this context, it was determined that features belonging to SMEAR images to be used as input data in SVM model could be obtained by combining the CNN and SVM models and by using CNN method and thus, the process may be performed in a shorter period and a higher estimation accuracy rate would be obtained.

In conclusion, improving the result of the deep learning model training is of great importance in terms of affecting the training data of the system developed. The deep learning model established has a position of a specialist determining whether the collected data are adequate for the training data or not.

At the end of the study conducted, it is considered that it is possible to combine the accumulation of knowledge and experience which the persons who specialized in the field of medicine have with the deep learning-based systems and a model efficiency and diversity may be developed through the academic studies to be carried out in this regard.

REFERENCES

Akdur, R. (2001). Sıtma. In T. S. B. S. S. D. B. v. S. P. G. Koordinatörlüğü (Ed.), (Vol. 1. Basım): Ankara.

Altıntaş, K. (2002). *Tıbbi parazitoloji*. Kozan Ofset, 1. Baskı: Nobel Tıp.

Arunava. (2019). Malaria Cell Images Dataset. *https://www.kaggle.com/iarunava/cell-images-for-detecting-malariaAccess*.

Bergsland, R. (2017). The human/wearable technology engagement and its embodied effects on self-trackers.

Dong, Y., Jiang, Z., Shen, H., Pan, W. D., Williams, L. A., Reddy, V. V., . . . Bryan, A. W. (2017). *Evaluations of deep convolutional neural networks for automatic identification of malaria infected cells.* Paper presented at the 2017 IEEE EMBS International Conference on Biomedical & Health Informatics (BHI).

Girginkardeşler, N. (2015). Sıtmada Rutin Ve İleri Tanı Yöntemleri. Celal Bayar Üniversitesi Tıp Fakültesi Tıbbi Parazitoloji AD, https://www.klimik.org.tr/wp-content/uploads/2015/10/S%C4%B1tmada-Rutin-ve-%C4%B0leri-Tan%C4%B1-Y%C3%B6ntemleri-Nogay-G%C4%B0RG%C4%B0NKARDE%C5%9ELER.pdf, Erişim Tarihi: 15.08.2019. Retrieved from https://www.klimik.org.tr/wp-content/uploads/2015/10/S%C4%B1tmada-Rutin-ve-%C4%B0leri-Tan%C4%B1-Y%C3%B6ntemleri-Nogay-G%C4%B0RG%C4%B0NKARDE%C5%9ELER.pdf

Jaeger, S. (2019). Malaria Datasets, https://lhncbc.nlm.nih.gov/publication/pub9932, Erişim tarihi: 04.09.2019. Retrieved from https://lhncbc.nlm.nih.gov/publication/pub9932

Kocaçiftçi, İ. (2008). Plasmodium Vivax'ın Tanısında kalın Damla İle İmmünokromatografik Yöntemlerin Karşılaştırılması. *Uzmanlık Tezi, Çukurova Üniveristesi Tıp fakültesi Parazitoloji Anabilim Dalı, https://docplayer.biz.tr/18954718-Uzmanlik-tezi-tez-danismani-doc-dr-i-soner-koltas.html, Erişim tarihi: 04.09.2019*.

LeCun, Y., Bengio, Y., & Hinton, G. (2015). Deep learning. *nature, 521*(7553), 436.

Litjens, G., Kooi, T., Bejnordi, B. E., Setio, A. A. A., Ciompi, F., Ghafoorian, M., . . . Sánchez, C. I. (2017). A survey on deep learning in medical image analysis. *Medical image analysis, 42*, 60-88.

Merdivenci, A. (1984). *Türkiye sivrisinekleri:(Yurdumuzda varlığı bilinen sivrisineklerin biyo-morfolojisi, biyo-ekolojisi, yayılışı ve sağlık önemleri)*: İÜ Cerrahpaşa Tıp Fak.

Özcel, M. (1993). GAP ve parazit hastalıkları. *Türkiye Parazitoloji Derneği Yayını*(11), 29-52.

Özcel, M., & Özbilgin, A. (1995). Güneydoğu Anadolu Projesini Tehdit Eden Parazit Hastalıkları. *Ege Ünv. Basımevi, İzmir*.

Pan, W. D., Dong, Y., & Wu, D. (2018). Classification of Malaria-Infected Cells Using Deep Convolutional Neural Networks. *Machine Learning: Advanced Techniques and Emerging Applications*, 159.

Quinn, J. A., Nakasi, R., Mugagga, P. K., Byanyima, P., Lubega, W., & Andama, A. (2016). *Deep convolutional neural networks for microscopy-based point of care diagnostics.* Paper presented at the Machine Learning for Healthcare Conference.

Rajaraman, S., Antani, S. K., Poostchi, M., Silamut, K., Hossain, M. A., Maude, R. J., . . . Thoma, G. R. (2018). Pre-trained convolutional neural networks as feature extractors toward improved malaria parasite detection in thin blood smear images. *PeerJ, 6*, e4568.

Saygı, G. (1998). *Temel tıbbi parazitoloji*: Esnaf ofset matbaacılık, 1. Baskı, Sivas.

Şeker, A., Diri, B., & Balık, H. H. (2017). Derin Öğrenme Yöntemleri ve Uygulamaları Hakkında Bir İnceleme. *Gazi Mühendislik Bilimleri Dergisi (GMBD), 3*(3), 47-64.

Taşkın, A. (2010). *Sıtma hastalarında lökositlerin oksidatif stresinin araştırılması/ Investigation of Leukocytes' oxidative stress in patients with malaria.*

Toha, S., & Ngah, U. (2007). *Computer aided medical diagnosis for the identification of malaria parasites.* Paper presented at the 2007 International Conference on Signal Processing, Communications and Networking.

Unat, E. K., Yücel, A., Altaş, K., & Samastı, M. (1995). Unat'ın Tıp parazitolojisi. *Baskı Cerr Tıp Fak. Vakfı Yay, 15*, 206-208.

Wang, F., Jiang, M., Qian, C., Yang, S., Li, C., Zhang, H., . . . Tang, X. (2017). *Residual attention network for image classification.* Paper presented at the Proceedings of the IEEE Conference on Computer Vision and Pattern Recognition.

WHO, A. (2014). Global Brief on Vector-Borne Diseases. *World Health Organization, Geneva*.

Yıldırım, R., & Yıldırım, U. D. (2000). Türkiye'yi tehdit eden bir hastalık: Sıtma. *Sürekli Tıp Eğitimi Dergisi, 9*(8), 17-19.

A ROBUST FUZZY MODEL FOR WIND ENERGY POTENTIAL ESTIMATION

CHAPTER

18

Onur İNAN[1]
Kazım KUMAŞ[2]
Ali Özhan AKYÜZ[3]
Afşin GÜNGÖR[4]

1 Mehmet Akif Ersoy University, Bucak Emin Gulmez Vocational School of Technical Sciences
2 Mehmet Akif Ersoy University, Bucak Emin Gulmez Vocational School of Technical Sciences
3 Mehmet Akif Ersoy University, Bucak Emin Gulmez Vocational School of Technical Sciences
4 Mehmet Akif Ersoy University, Bucak Technology Faculty

INTRODUCTION

Energy has become an indispensable element with the rapid increase of the population in the world and the use of technology. Continuous increase in energy consumption causes negative environmental problems. Therefore, the demand for energy and environmental problems cause research on renewable energy sources to intensify [1]. The geographical structure of Turkey is advantageous in terms of the use of renewable energy sources. It is inevitable to increase the share of renewable energy sources in energy consumption rapidly for both environmental pollution and sustainable development [2]. Renewable, environmental, located in clean and cheap energy category, wind energy, which is one of the unlimited energy sources, has an important value in our country. Wind energy is the fastest developing and most promising resource among renewable energy sources.

The wind energy potential of Turkey with a wind speed of 6.5-7 m/s at an altitude of 50m is 83906.96 MW. The wind energy potential at 7-7.5 m/s wind speed is 29259.36 MW and the areas with 7.5-8 m/s wind energy potential is 12994.32 MW. Although areas with high wind energy potential are located in coastal areas, there are also regions with moderate wind potential in inland areas away from the sea. As of 2016, the total installed wind power in Turkey is 45240 MW [3].

Wind speed is a very significant parameter for determining wind energy potential. The installation location and design of the wind turbines are determined according to the average wind speed. 1% error in wind speed measurements results in an error of about 2% at the energy output. The chaotic nature of the wind is a major obstacle to predictability in energy production. In spite of this chaotic structure and uncertainty, there are some estimation methods developed for forward forecasts [4].

Wind speed estimation studies are important for the efficiency of wind energy use. In addition to statistical methods, artificial intelligence methods such as time series analysis models, ARMA and ARIMA method, artificial neural networks, radial based function and fuzzy logic have been begun to use in wind speed estimation [5, 6]. In their study, Damousis et al built a fuzzy logic model that predicts the wind speed required for electricity generation. They used genetic algorithm based learning in the training of the model. They observed that the estimation values of the model were in agreement with the actual values [7]. In their work, Jursa and Rohrig estimated short-term wind power with artificial neural networks and nearest neighbor search method. As a result of their study, they stated that the model created with particle swarm optimization gave the best results in power estimation [8]. In their study, Yayla et al. determined the wind energy potential of Van Yüzüncü Yıl University campus area. Data for 2004-2005 years were obtained from a 30 m high measuring mast. The data were used in the WASP program and the average wind speed of the region and the wind power density were found as 3.87 m/s and 87 W/m^2 respectively. They stated that if the most suitable turbine selection is made, the energy to be produced will be 237 MWh [9]. In his study, Yağcı estimated the wind speed at 50 meters altitude by using wind speed data of 10, 30 and 50 meters of a region. Estimated wind speeds and actual values were compared and error analyzes were performed. Power and energy quantities to be obtained from seven different wind turbines were determined. As a result of the error analysis made between the estimated speed and the measured speed values, it was stated that the errors were acceptable [10]. In their study, Özcan et al estimated the wind speed of Isparta by utilising Adaptive Network based Fuzzy Inference System (ANFIS) and Artificial Neural Networks (ANN). They used Tansig function in their estimation by ANN method and obtained the best result with LM12 algorithm. They compared the results achieved from ANN and ANFIS statistically and determined that R^2 value achieved by ANFIS method is higher than the value achieved by ANN method. Therefore, they stated that ANFIS method is more suitable for wind speed estimation [4]. In his study, Zorlu estimated the wind speed by using the temperature, humidity and pressure values of the province of Kırşehir between 1975 and 2010. In this work, as a method of analysis, Feed Forward Back Propagation Artificial Neural Networks and findings obtained from two different algorithms were compared. Levenberg-Marquardt (LM) and Resilient Back Propagation (RBP) algorithms were compared according to criteria such as Root Mean Square Error (RMSE), Mean Absolute Error (MAE), and Mean Absolute Percentage Error (MAPE). As a result, it was stated that Resilient Back Propagation learning algorithm gave relatively better results although the performance of both algorithms was very close to each other [11]. In their study, Kaya et al built two different models using various wind turbine data and estimated the wind power potential of Kastamonu province. Nordex 50, Vestas V66, Neg Micon 1000/60, Bonus 2MW, Vestas V90 and Power Wind 90 turbines were selected for creating models. The data for the turbines were achieved from the power-wind speed curves in the turbine manufacturer catalogs. For the power estimation, daily maximum wind speed data of Kastamonu province of 2015 were obtained from General Directorate of State Meteorological Services (DMI). Maximum power values that can be produced according to the turbine type were estimated by utilising Adaptive Network based Fuzzy Inference System (ANFIS) and Artificial Neural Networks (ANN) methods. As a result, it was stated that the wind potential of Kastamonu is pretty good and high capacity energy could be produced with efficient turbines [12]. In their study, Dikmen and Örgen have established a meteorological weather station to determine the wind potential of an area in the region of Burdur-Ağlasun. Between January and December 2013, they recorded the wind speed data at a height of 2 meters with the measuring station. The wind speeds at the hub heights of the wind turbines (60, 65, 73 and 75 meters) were estimated by different extrapolation methods and the most suitable turbine was determined for the region [1].

In this work, a fuzzy logic model to find monthly average wind speed was created by using meteorological data measured between 2000 and 2016 in Burdur, Isparta and Antalya within Turkish Lakes Region. Based on this model, a linear equation system was established to find the monthly average wind speed in this district.

Obtaining Fuzzy Rules from Subtractive Fuzzy Clustering Method

Subtractive Fuzzy Clustering (SPC) is an efficient method for direct fuzzification of data. Clustering clusters data in order to increase processing speed and allows the system to be handled more clearly. SFC uses the distances between the data to determine the most appropriate cluster centers that represent data sets. Firstly, input and output data are generated from DMI measurements to determine cluster centers. SFC algorithm starts with the normalization of the data set. After normalizing the N number of data, the potential for each data point of the data set is calculated as follows:

$$P_i = \sum_{j=1}^{N} e^{\left(-\frac{4}{r_a^2}\|x_i - x_j\|^2\right)}, i = 1, \ldots, N \tag{1}$$

where r_α is a positive constant representing the neighborhood radius. The data point with the maximum amount of neighboring is then chosen as the first cluster center. Briefly, the data point with highest potential is initial cluster center. The highest potential can be symbolized by $P_{(1)*}$ and first cluster center could be notated by $x_{(1)*}$. The potentials of all other data points are then recomputed to exclude the effect of the first cluster center:

$$P_i' = P_i - P_{(k)*} e^{\left(-\frac{4}{\eta r_a^2}\|x_i - x_{(k)*}\|^2\right)}, i = 1, \ldots, N \tag{2}$$

Here η is another positive constant that prevents the cluster centers from being close together. This process goes on till an adequate number of cluster centers are achieved by considering the relevant criteria [13].

In expert systems, IF-THEN logical connectors form the basis of fuzzy rules. These rules logically set input-output relationships and control the system. Sugeno type Fuzzy Inference System (FIS) is utilized in SFC method. FIS consists of precursor and posterior units. Thus, a large number of inputs and outputs could be expressed by the following rule mechanism [14]:

$$\begin{aligned} &IF\ y_1\ is\ A_1^k\ \&\ y_2\ is\ A_2^k\ \&\ldots THEN \\ &z_1\ is\ B_1^k\ \&\ z_2\ is\ B_2^k\ \ldots \end{aligned} \tag{3}$$

where k corresponds to the rule number while y_j is the jth input and z_j is the jth output. Here, B_j^k is a first order equation which can be defined as a linear output of the input variables:

$$B_j^k = a_0 + a_1 y_1^k + a_2 y_2^k + \ldots \tag{4}$$

A sufficient number of cluster centers have already been obtained by applying SFC on meteorological data ($x_{(1)*}, x_{(2)*}, \ldots, x_{(k)*}$). FIS kth rule corresponds to the respective cluster center. The membership function A_j^k is calculated for kth rule as follows:

$$\mu_{A_j^k}(y) = e^{-\frac{4}{r_a^2}\left\| x_i - x_{(k)*} \right\|^2} \tag{5}$$

Finally, FIS outputs are found by taking the weighted average of each rule output. By changing the parameters such as neighborhood radius r_α and compression factor η, it is tried to find the most suitable FIS. As a result of the optimization process, the coefficients of the linear equation system are found and the application of the SFC method is completed. By using SFC, the relationship model between input and output data pairs can be practically established. This method is well suited for complex calculations and higher accuracy could be achieved by increasing the number of inputs.

Fuzzy Logic Model Design for Wind Speed Estimation

A fuzzy logic model based on SFC method was built to find monthly average wind speeds in Burdur, Isparta and Antalya cities within Turkish Lakes Region. The fuzzy model has four inputs and one output shown in Fig. 1. Year, month, monthly average air temperature and monthly average relative humidity were used as input parameters. Monthly average wind speed data was evaluated as output parameter. In order to establish our fuzzy model and confirm its accuracy, data pairs for Turkish Lakes Region were produced from DMI measurement data. The data obtained were divided into two groups as training and control. Each group data pairs are completely distinct. Training data was utilized to establish our fuzzy model and control data was used to confirm the validity of the model. For the installation and verification of the model 500 training data pairs and 112 control data pairs were evaluated.

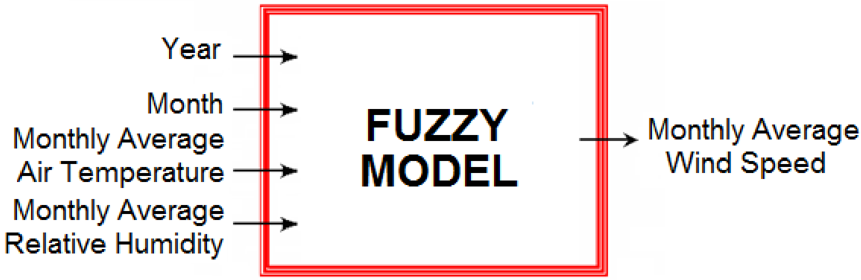

Fig. 1. *Model proposed for estimating monthly average wind speed in Turkish Lakes Region*

The results of the designed model have been compared with the meteorological wind speed data. For each province in May, model results are given in Fig. 2. together with the wind speed data measured by DMI. The model results have high accuracy. RMSE (Root Mean Square Error) and MAE (Mean Absolute Error) values were taken as criteria for training and control data pairs. In order to obtain the most suitable model, r_α and η parameter values were tested. The wind speed error variation due to the neighborhood radius of the fuzzy model can be seen in Fig. 3. The r_α value, where the training and control data pairs have the closest error values, was taken as the optimum value for the fuzzy model. Table 1 shows the neighboring radius, compression factor and number of rules corresponding to the optimum results. RMSE and MAE values of training and control data corresponding to the most appropriate neighborhood radius are also given in Table 2.

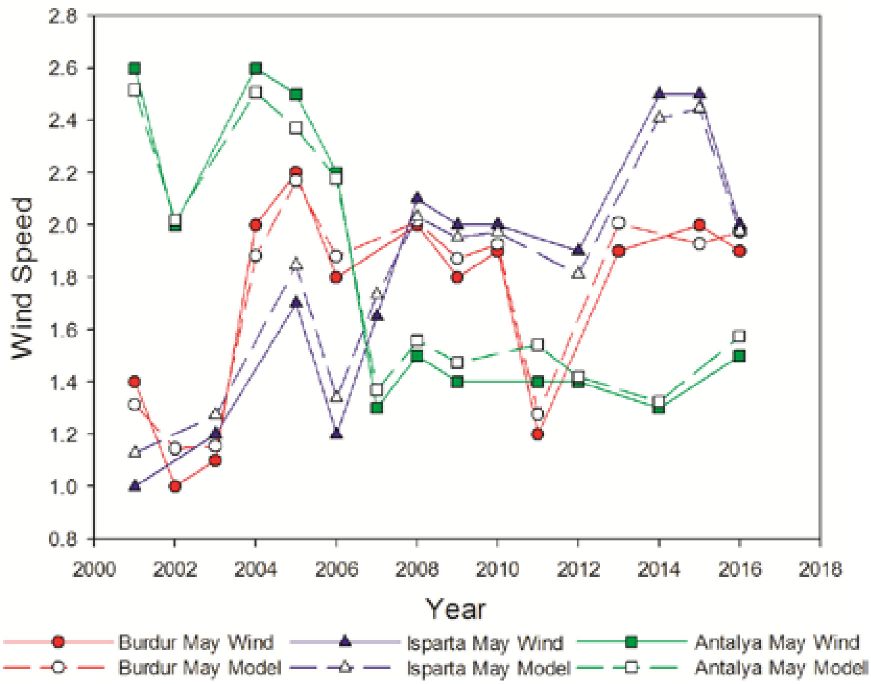

Fig. 2. *Fuzzy Model Results & DMI Measurement Data*

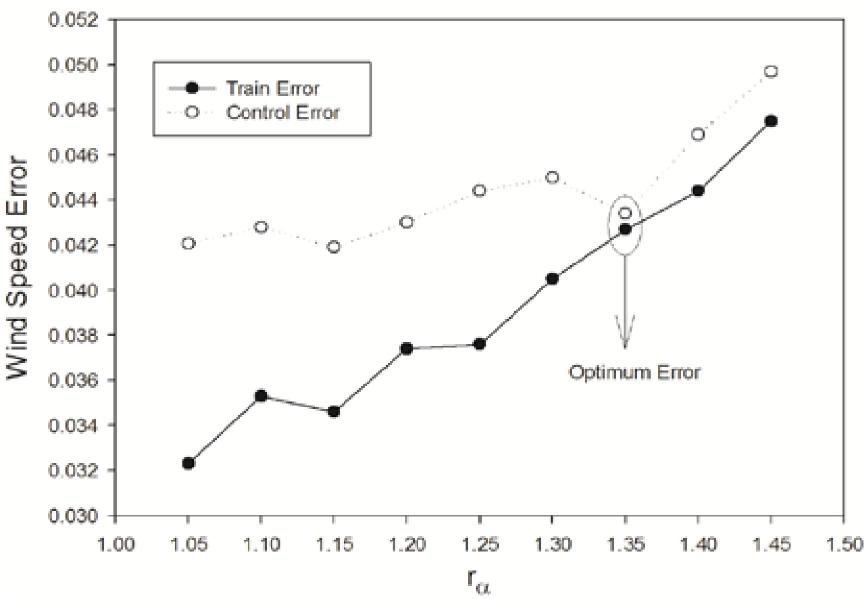

Fig. 3. *Fuzzy Model Wind Speed Training & Control Data Error Distribution*

Table 1. *Optimal Parameter Values and Number of Rules*

r_a	η	Number of rules
1.35	1.4	7

Table 2. *Error Values Corresponding to Optimal Radius*

Training		Control	
RMSE	MAE	RMSE	MAE
0.0407	0.0166	0.0434	0.0211

RESULTS

In this study, Turkey Lakes Region monthly average wind speed estimation was performed successfully using the SFC method. With SFC-based modeling, data sets are classified according to cluster estimation, cluster centers are generated and fuzzy rules are achieved from these centers. Thus, system complexity was significantly reduced and a rapid calculation was obtained. As a result, it is envisaged that this method, which has the ability to calculate in a practical way, can be preferred as an alternative to classical methods in geographical and meteorological applications.

REFERENCES

Dikmen, E., Örgen, F. K. (2018). Ağlasun Bölgesi İçin Rüzgâr Hızı Tahmini ve En Uygun Türbin Tespiti, Omer Halisdemir University Journal of Engineering Sciences, 7(2), 871-879.

Önal, E. ve Yarbay, R. Z., (2010). Türkiye'de Yenilenebilir Enerji Kaynakları Potansiyeli ve Geleceği, İstanbul Ticaret Üniversitesi Fen Bilimleri Dergisi, 9(18), 77-96.

Şenel, M. C., Koç, E. (2015). Dünyada ve Türkiye de Rüzgar Enerjisi Durumu-Genel Değerlendirme, Mühendis ve Makine, 56, 663, 46-56.

Özcan, İ., Şahin Şencan, A., Dikmen, E., Bayram, G. (2013). Isparta İlinde Rüzgâr Hızı Değerlerinin Belirlenmesi, Suleyman Demirel University Journal of Natural and Applied Science, 17(1), 109-112.

Philippopoulos, K., Deligiorgi D. (2012). Application of artificial neural networks for the spatial estimation of wind speed in a coastal region with complex topography, Renewable Energy, 38, 75-82.

Cadenas, E., Rivera, W. (2010). Wind speed forecasting in three different regions of Mexico, using a hybrid ARIMA ANN model. Renewable Energy, 35, 2732-2738.

Damousis, I. G., Alexiadis, M. C., Theocharis, J. B., Dokopoulos, P.S. (2004). A fuzzy model for wind speed prediction and power generation in wind parks using spatial correlation. ,Energy Conversion, IEEE Transactions on, 19(2), 352-361.

Jursa, R., Rohrig, K. (2008). Short-term wind power forecasting using evolutionary algorithms for the automated specification of artificial intelligence models, International Journal of Forecasting, 24(4), 694-709.

Yayla, S., Yumak, H., Bayram, A. (2010). Yüzüncü Yıl Üniversitesi Kampüs Alanının Rüzgâr Enerjisi Potansiyelinin Belirlenmesi, Yüzüncü Yıl Üniversitesi, Fen Bilimleri Enstitüsü Dergisi, 15(1),17-23.

Yağcı, E. (2013). Rüzgâr Hızı Yükseltmelerinde Kullanılan Farklı Yöntemlerin Karşılaştırılması ve Hata Analizleri, İstanbul Teknik Üniversitesi, Enerji Enstitüsü, Enerji Bilim ve Teknoloji Anabilim Dalı, Yüksek lisans tezi, 91s, İstanbul.

Zorlu, E. (2015). İç Anadolu Bölgesi İçin Modern Kontrol Yöntemleri ile Rüzgâr Hızı Tahmini: Kırşehir Bölgesi Örneği, Kırıkkale Üniversitesi Fen Bilimleri Enstitüsü, Yüksek Lisans Tezi,58s.

Kaya, Ü., Caner, M., Oğuz, Y. (2016). Wind Energy Potential Estimation Via Artificial Neural Networks, Technological Applied Sciences (NWSATAS), 11(3), 65-74.

S. L. Chiu,(1994). Fuzzy Model Identification Based On Cluster Estimation, Journal of Intelligent and Fuzzy Systems, 1994, 2, 267-278.

M. Sugeno and T. Takagi,(1985). Fuzzy identification of systems and its application to modeling and control, IEEE Trans. on Systems, Man & Cybernetics, 1985, 15, 116-132.

MULTISTAGE AXIAL INDUSTRIAL COMPRESSOR 13CR4NI (UNS S42400) BLADE SRUCTURAL EVALUATION AND PRESSURE FLOW FINITE ELEMENT ANALYSIS

CHAPTER

19

Özdoğan KARAÇALI[1]

[1] Department of Mechanical Engineering, Faculty of Engineering, Istanbul University - Cerrahpaşa, Avcılar, Istanbul, Turkey, 34320
ozdogank@istanbul.edu.tr

1. INTRODUCTION

A compressor is simply a mechanical unit that raises the pressure, volume, or speed of gas [1]. Compressors are divided into two main groups as positive displacement and dynamic compressors according to gas pressure increasing method. The compressor types and subcategories are shown in Figure 1.

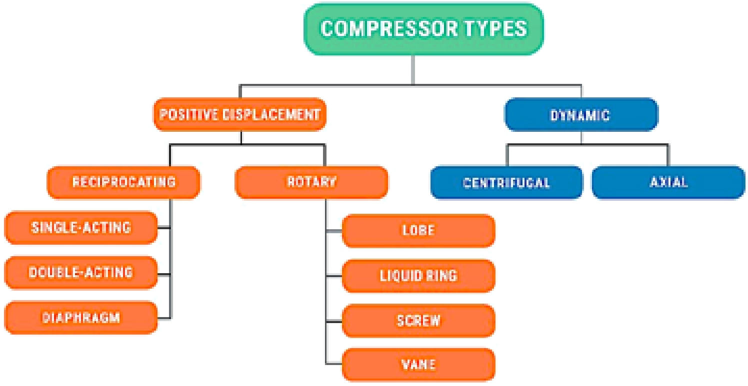

Figure 1: *Types of compressor*

The evaluation of the flow in multistage axial centrifugal compressors with 3-dimensional flow and full analysis is very complex compare to positive displacement compressor [2]. Therefore, approximate solutions are researched by simplifying the flow model. For example, for situations where the flow is stable, one-dimensional flow approach can be used in certain sections.

Multistage axial centrifugal compressors are composed of a fixed number of rotating impellers that provide high speed to the air and a certain number of expanding passages that increase the pressure by slowing down the air [3]. Diffusion and expanding passages of the compressor are also called diffusers. Implants can be single, double or closed type. But in basic theory they are all the same. The air sucked into the impeller chamber is rotated at high speeds by the fins on the disc as shown in Figure 2.

In normal practice, the compressors are designed in such a way that half of the pressure increase is in the impeller and the other half is in the diffusers. The MAC is characterized by radial discharge flow. The air is drawn into a rotating turbine with a radial blade and is pushed around the turbine by centrifugal force. As a result of the radial movement of the air, pressure increases at the same time and kinetic energy is produced. The air passes through a diffuser and a coil where kinetic energy is converted to pressure before being directed to the center of the turbine of the next compressor stage. Each stage contributes to the total pressure increase of the compressor unit. In industrial machines, the maximum pressure ratio of a centrifugal compressor stage is usually no greater than three. Higher-pressure ratios reduce the efficiency of the stage. Low-pressure single stage applications are used, for example, in wastewater treatment plants. Multi-stage applications provide intercooling to reduce power requirements. Multiple stages can be arranged in series on a low speed shaft. This concept is mainly used in the oil and gas or process industry. The pressure ratio per stage is low, but multiple compressor sets operating in series and / or in series are used to achieve the desired outlet pressure. For air compression applications, a high-speed gearbox is integrated in the compressor stages to rotate the turbines on high-speed pinions as shown in Figure 2.

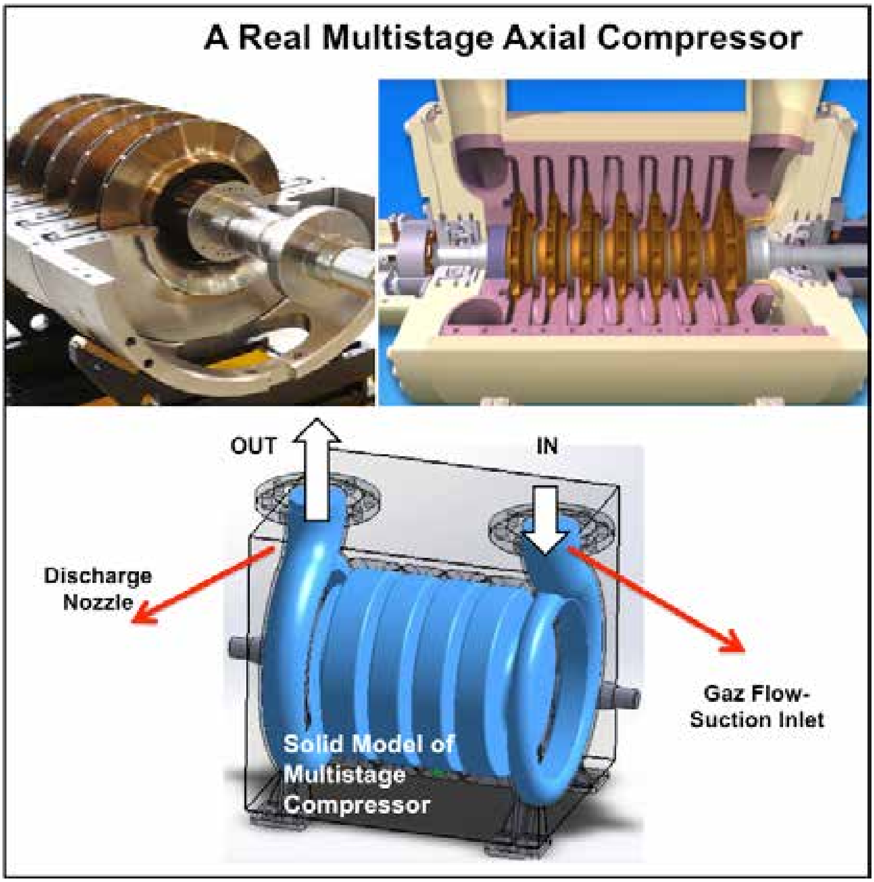

Figure 2: *Centrifugal compressor*

Compressor is a general name given to machines used to increase the pressure of a compressible fluid. In the gas turbine engine, air must be compressed before expanding along the turbine. This compression is done using one of two basic compressor types. One of them is centrifugal compressor and the other is axial compressor. Although the use of axial compressors is much more common, they are also available in hybrid form including both centrifugal and axial compressors as given in Figure 3.

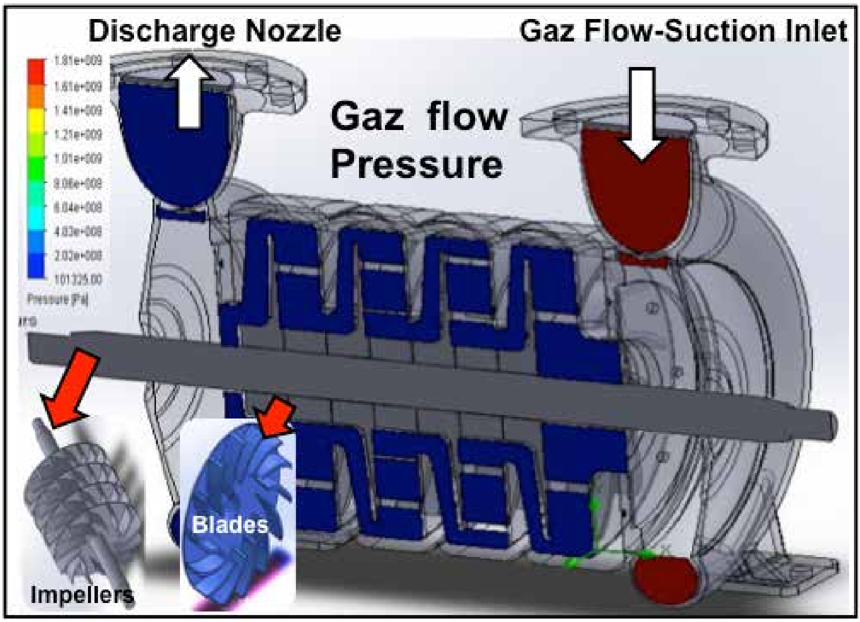

Figure 3: *Gas pressure and velocity in MAC*

Multistage axial compressors (MAC) with high speed are dynamic compressors in which a rotating impeller or blade transfers kinetic or potential energy to air. As of the rigorous design circumstances of the gas turbine sections and the great rotational speed they operate, a component failure can cause serious destruction to the complete unit [4]. In the meantime, the rotating and immobile parts of the turbine unit, such as discs and blades, tend to operate in a harsh situation under an excessive heat gas stream with a higher-pressure increase [5]. A gas turbine for MAC used to generate electrical power is a multifaceted system with a large number of rotating and stationary components operating under fully controlled operating conditions as shown in Figure 3.

The incoming rotating air in a gas turbine section is compressed a few steps ahead of the fixed and rotating blades. This air will later be reused in the chamber of combustion and cooling. Compressed air entering the combustion chamber in the centrifugal compressor, high pressure and high heat gas flow and high pressure, which may operate shaft of the turbine at high momentums, are assorted with ignited fuel. This high pressure causes distortion von Mises stresses and displacements on the blades and discs. This activates the static strain energy of the blade and disk. The fatigue caused by these alternative impacts creates metal in the fatigue. [3-6]. The effects of liquid and air pressure require an increase in compression and redesigning geometry of blade. Numerous scientific reseraches [4-9] performed on CrNiMoV fault analysis of turbine blades as shown in Figure 4. Typical errors analysis concluded in the steel parts of various stages of modern aircraft gas turbine engines [10-13].

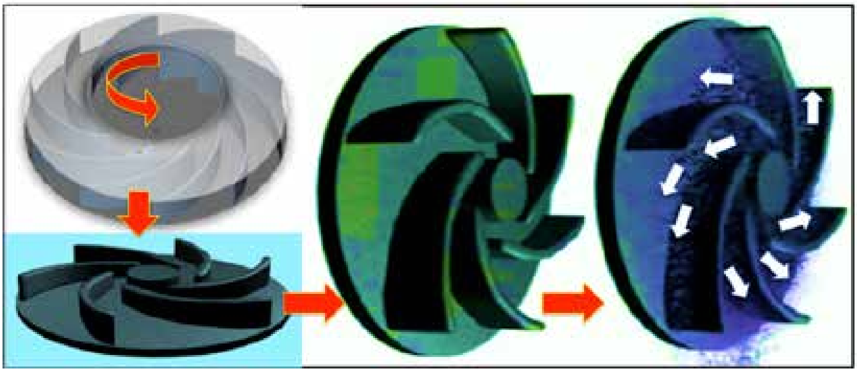

Figure 4: *Solid models of multistage axial compressor blades and gas flow*

The blade geometry is modified by designers using conventional engineering tools based on their past experience until a desired flow field, as predicted by CFD analysis, is achieved as given in Figure 4. The blade loading is evaluated numerically through the relative velocity difference between the blade suction and pressure surface. The blade loading profiles are linked to local flow features therefore impact the overall compressor performance envelope.

In order to avoid excessive flow deceleration, designers typically use self-developed criteria for the maximum allowable loading derived from streamline curvature analysis or full three-dimensional Navier-Stokes analysis [8]. Also, flow deceleration along the impeller shroud is considered as the dominant factor for the impeller performance. Therefore, in the conventional direct approach, smooth flow deceleration along the impeller shroud is judged based on the resulting loading distribution. Discussions of blade loading impacts on the compressor performance have been seen in many open literatures [13-16].

For this research, the baseline impeller was designed through a typical hierarchy of time-mean and fidelity aerodynamic modeling approach, i.e. from the mean-line analysis to the three-dimensional CFD analysis as given in Figure 4. In order to examine the impact of blade loading profile and magnitude on compressor performance and stability, it was redesigned with a different loading profile and a reduced blade count using an in-house blade generation ANSYS-LSDYNA [17]. The simulation is sort of combined inverse and optimization design tool in the limits of the quasi-3D in viscid flow. As alternative to the conventional direct design approach, it allows direct control over local blade loading profiles that might be linked to flow features associated with good performance. A mid-loading distribution at the impeller hub and shroud along with geometrical constraints of the impeller and the requirement of impeller work input was used for the redesign. With the reduced blade count, the redesigned mid-loading impeller results in a much higher blade loading than the impeller, exceeding conventionally hold criteria of maximum blade loading according to CFD analysis.

To validate the design results, three impellers were manufactured, and the details of the flow and performance were measured at the aero test facility of turbines compressor. This facility has been used to obtain detailed flow and performance information for product improvement and new compressor stages. The extensive experimental activities greatly enhanced state-of-the-art design of compressor components [17-20]. In the present work, the main objective is to experimentally quantify the three impellers and understand the blade loading effect on compressor performance and stability.

The results achieved was presented that instable simulations remarkably increase the correctness of the centrifugal compressor blade performance evaluations explained in later section of this chapter. This research is to study gas pressure and velocity effect on the surface of MAC blade as shown in Figure 4. General equations were developed for the calculation of flow parameters in the turbomachinery, regulated to include the increase in entropy flow [5]. The maximum yield for impellers with backward tilted wings may be between 0.705 and 1.018 of the specific speed [6]. A general design procedure was developed for centrifugal compressors and turbines [7]. On the wheel, he defined a loss coefficient for enthalpy losses to shift from ideal flow to real flow. He introduced this loss coefficient as a multiplier on the right side of the dimensionless mass flow parameter and developed a design for one-dimensional flow including losses.

The results of measurements was made in a high-pressure centrifugal compressor during operation was examined in the turbulence zone. It showed how turbulent flow occurs in the impeller and then the pressure fluctuation [8]. A design procedure based on estimation of entropy loss for non-design operating conditions was analyzed after design point calculations for turbocharging applications using centrifugal compressors and turbines [9]. The appropriate operating conditions were determined by showing engine speeds on turbine performance curves [10].

The preliminary design calculations of the centrifugal compressor were achieved [11]. The effect of the power shortage factor was investigated on the pressure edge diameter [13]. The suction edge showed the effect of relative Mach number, suction edge geometry and critical flow conditions. A preliminary design procedure was presented for the centrifugal compressor using a finned and finless diffuser.

An experimental study was conducted on the pressure distribution of high pressure compressors during operation. During the operation, the pressure distributions of a 5-stage high-pressure compressor under various conditions were determined. By comparing the pressure distributions obtained as a result of the experiments, information was obtained about the behavior of the compressor and gas at high pressures [7]. High-pressure compressor development for internal combustion engines has been made. The high-pressure ratio causes over-sound flows and changes the compressor design [8]. The performance of multistage high-pressure compressors has been investigated. The cooling of the fluid between the stages and the behavior of the fluid at high pressures were investigated. Losses occurred between stages were examined and ideas were put forward about the methods to minimize these losses [9]. In high-pressure compressors, the behavior of the compressor equipment and the pressure characteristics are determined numerically by finite element analysis in case the high-density fluid is compressed. High-pressure gas compressor design conditions as 425 bar pressure, gas temperature range - 50, 160 ° C designed for 16 days, the results of various tests are given [10].

Dry gas sealing solution methods of centrifugal compressors used at extremely high pressures for gas injections were investigated [11]. The sealing elements of high-pressure natural gas compressors are designed in computer environment and analyzed with computer programs. The studies have been carried out on sealing elements that provide optimum safety and efficiency at high pressures [11]. In this study, 3-dimensional flow analysis in a centrifugal compressor is investigated and numerical analysis of flow is accepted as stable, incompressible and viscous flow. In addition to understanding the physics of flow in a compressor, the ways to get rid of these losses have been examined. 3-dimensional measurements were made and the importance of turbulence modeling in compressor and diffuser having unstable flow structure was emphasized. The results obtained in the study were compared with the existing experimental data and their parallelism was investigated and the agreement between them was observed [12]. Optimization of the production of a compressor body was developed by applying powder metallurgy and diffusion welding methods. The effects of temperature rise on the shear strength and hardness values of the weld seam were investigated [13].

The pressure and temperature of the fluid in the compressor must operate in wide ranges and the materials must be resistant to high temperature and high tensile strength. It must also be resistant to fatigue, cracking and oxidation. Alloy metals are used, as no material will have these properties by itself. Alloys that can withstand very high temperatures are called super alloys nickel, cobalt-based alloys. Aluminum and titanium alloys are preferred for durability and added to the alloy. Titanium can be used for stator vanes in the low-pressure area, but is not suitable for smaller stator vanes in the compression system for high temperature and pressure encountered in the internal stages of the compressor. Because of any excessive scrubbing that may occur between rotating and static components as a result of other mechanical failures, titanium ignites. This can lead to expensive repair costs and possible airworthiness hazard.

One of the biggest problems of gas turbines is low thermal efficiency and there are two basic methods to solve this problem by increasing thermal efficiency [14-18]. These methods are to increase the compression ratio and combustion temperature in the compressors. Therefore, the compression ratio obtained in the compressor of the gas turbine is extremely important in terms of thermal efficiency. In the use of axial flow compressors in gas turbines, a shaft turns the compressor rotor by the gas-generating turbine. Such applications are known as single shaft gas turbine applications if there is no turbine rotated by a separate shaft. In this type of gas turbines where axial flow compressors are used, around 55-65% of the power generated in the turbine is consumed by the compressor. The axial flow compressors used today consist of 17 to 25 steps and provide high compression ratios.

Nowadays, it can be said that the designs of the new engine, hence the compressor, have a common tendency.

Since natural energy resources become less accessible every day, fuel consumption is an important goal. In recent years, important studies have been carried out on issues such as carbon dioxide emission directly related to fuel consumption with increasing environmental awareness, as well as noise.

Another important feature for airline operators is the maintenance costs. The selection of the compressor to be designed at the initial stage of engine design is an important issue. A consensus should be reached between many parameters such as yield targets, number of stages, fluctuation range in flight envelope, stress limits, mechanical factors. Having fewer steps in the compressor zone means reducing engine length and thus weight and cost, but with higher aerodynamic loads. Although increasing the amount of work done at each stage often leads to a decrease in efficiency, studies on compressor aerodynamics in recent years have minimized this decrease in efficiency [20-12].

In the design of the compressor, a stable operation should be provided for every point of the envelope as well as for discontinuity conditions. Existing solutions for a non-perpetual, compressible, viscous flow are still open to development, although their programs are largely solution-oriented. After the design of pal geometry, the preliminary mechanical design of the compressor is realized. The pal disk connection and related parameters are agreed. Then, the base of the palette radius is determined by structural analysis and necessary changes are made to the palette geometry. Disc design and housing design are also performed simultaneously [22]

When literature studies on compressors are examined, it is seen that limited number of studies have been done on this subject [13-16]. The reason for this is that the importance of compressors has recently begun to be understood. Although compressors are used in many countries of the world, academic studies and information flow on this subject is very low [5-8].

Although literature studies on almost all components that make up compressors are possible, these studies are limited in part to form a whole for the compressor.

Next section explains finite element method, the material and method related to CFD and structural modeling to present new research area for the MAC blade.

2. FINITE ELEMENT METHOD (FEM)

Due to the complexity of many variables, the processes that occur in nature are mostly expressed in mathematical models. With these mathematical expressions, it is aimed to simplify various processes and distributions in fields such as economics as well as positive sciences such as physics, chemistry and biology. In order to understand the compressors mechanical and gas flow effect behaviors in compressor engineering problems, the finite element method (FEM) is used. Finite element analysis has become widespread in parallel with the development of compressor software simulations tools.

Finite element method is a numerical method that provides general solution by subdividing various engineering problems. The mathematical model to be used is determined according to the nature of the problem. For example; in mechanical problems involving solids, stress analysis and displacement are generally expected to be solved. In this case for compressors, approximate solution is obtained with second order partial differential equations.

Continuing on the stress analysis sample when a structure or system is subdivided, a large number of equilibrium equations are obtained at the junction points of the parts. The use of computer software has gained importance at this point and finite element analysis (FEA) studies have been developed with CAE software. In the past, the experiments carried out at high costs for analysis were replaced by computer-aided structural analyzes that can be performed while still in design [9].

Finite element analysis of compressors is applied in three basic stages; mesh generation: after the mathematical model is established, the structure formed by the sub-elements and connection points is like a network. Increasing the network density is usually better. Determining the forces acting on (load application): The forces acting on the system are determined, especially the mass forces, single and spreading forces.

Boundary conditions: A system has naturally occurring or artificially created boundary conditions. For example, in structural analysis, elastic displacements can be calculated by reference to boundary conditions. These steps will be explained in coming parts.

3. COMPUTATIONAL FLUID DYNAMICS (CFD) MODELING

Computational Fluid Dynamics (CFD) analysis for compressors is the modeling of fluid passing around pipe channel structure. Mathematical modeling is used for determination of fluid properties by numerical solution for compressors.

CFD is the simulation ability to analyze complex problems involving the interaction of liquid-solid, liquid-liquid, or liquid-gas fluids. The CFD analysis, which is frequently used in engineering areas, can be modeled as a sample of how a centrifugal compressor is working with gas and creating a fluid flow and model pressure effect.

CFD analysis and simulations are very important as they save time in the design process [17]. Thus, cheaper and faster results can be obtained compared to conventional tests to obtain data. In fact, the required tests can be carried out in any number of different parameters using CFD analysis.

4. DETERMINATION OF DESIGN PARAMETERS

Some parameters that have a direct impact on performance, yield, size and geometry need to be decided at the first stage of the design [25]. Perhaps the most important of these is the step pressure ratio. It is one of the most important factors determining the number of stages and thus the length of the compressor. In recent years, step pressure ratios have increased in parallel with the increase in environmental speed. Increasing the aerodynamic loading has made it more difficult to achieve higher-pressure rates due to the boundary layer on the pal surface [26].

Furthermore, pal tip speed is one of the most important limiting factors in compressor sizing. Increasing the pal tip speeds (Tip) in formula (1) and (2) is possible by increasing either the outer diameter (tip) or the rotational speed (N). In both cases, it is clear that the pal-tip increases aerodynamic losses as well as stresses due to greater centripetal forces [27].

$$U_{Tip} = 2\pi r_{Tip} N \quad (1)$$

$$m = \rho V_a A = \rho V_a \pi (r_{Tip} - r_{root}) \quad (2)$$

Since the housings of the compressor are cylindrical structures operating under high pressure, they can be considered as pressure vessels. They usually consist of a cylindrical or conical shell. Other enclosures on the front and rear of the enclosure, or there are two flanges that allow them to be attached to other frames by means of bolts. Furthermore, they have one or more flanges in the tangential direction called the split flange.

When a housing is viewed from the outside, there are holes used for a large number of leak air, protrusions of the pallet rotating mechanism, and openings used for inspection. In addition, the housing shell is viewed axially or circumferentially in the form of panels with a plurality of rings attached to increase the strength of the housing. Enclosures may be single- or double-layer, depending on the thermal behavior of the environment in which they work.

The split housings have T-shaped slots to which pals or pal-end shields can be connected along their circumference. The housings are often referred to by the name of the motor component they enclose, such as the high-pressure compressor housing, the fan housing, or the turbine housing.

The high-pressure housing determines the external flow path of the high-pressure compressor. It acts as a connection point for variable angle stator pallets and their components. It is usually composed of two halves to ensure easy access during maintenance and inspection. It forms the main body of the load flow path between the fan frame and the compressor rear frame or between the combustion chamber emitter and the nozzle housing.

It constitutes the structural backbone of the compressor and transfers the loads on the frames to the bearings. Although it is a thin structure that works under high pressure and high pressure, it has very low deformations. It has a critical function in terms of operation and protection of pal tip opening by providing thermal coupling with the rotor. Provides a fixed location for ports and sensors. It is a structure that is secured against mistakes [28].

Another important task of the compressor housing is to provide safe protection of broken pal and pal particles as a result of bird impact, high cycle fatigue of the fins or high-low cycle fatigue of the pigeon tail joint. The safe protection of the pals is related to the capacity of the housing shell to absorb energy and the kinetic energy at the moment of the break [29].

The bolted connections on the housing shall be able to function in extreme pressure conditions without causing any breakage or air leakage. Also these connections must be able to withstand the loads resulting from basic rotor damage. The circumferential bolt connections have tight fittings to ensure that the housings are centered and aligned relative to each other.

The casing material should be soft enough not to cause the pal tip to break during rubbing, but also hard enough to not peel off by rubbing. However, the material used should allow for easy processing of the shapes of the complex housing structures, and the weldability should be high as a plurality of parts are welded onto the housing.

5. MATERIALS AND METHODS

In this research, CFD analysis of rotating systems at high speeds is carried out to bring the design parameters to the most efficient working conditions. Pump CFD analysis, Compressor CFD analysis systems are important for examining the effect of fluid pressure and velocity values on the existing surfaces in the working environment.

CFD-Computational Fluid Dynamics models have the interaction between fluid analysis and geometrical environment in working environment. These interactions are predominantly dependent on understanding the design code to correctly predict energy loss models [7-8]. CFD determines how severely reduced energy loss on performance due to improper geometric constraints. The surface friction was caused by energy losses. The overpressure recovery, flow recirculation; vortex incidence and blade tip leakage also was result of energy escapes.

The centrifugal compressor has a fixed case with a rotating impeller, which gives the air a high speed. The impeller is sucked in the air and rotated at high speed by the blades on the centripetal disc. The first measured performance was static pressure amount. The static pressure ratio was at the outlet to the total pressure in the inlet. Figure 3 displays the static pressure ratio as an inlet utility corrected and exit improved mass flow. From this study for the physics of the turbine blade, the CFD analysis may be affected and found an improved resolution. The pressure ratio plots versus exit improved mass flow rate presented in Figure 4 were found as a useful tool in off-design operation for MAC. The corrected mass flow exit graph in Figure 4 is valuable as for jet or MAC engines. The new compressor design is to provide a steady airflow into the combustion chamber.

The contribution of this paper to scientific research was to determine the design and better performance of a centrifugal compressor that could be computer-generated virtually simulation correctly using CFD software. The design analysis was developed by ANSYS-CFD to produce high quality results.

6. RESULTS

To simulate the internal flow of liquid correctly in a MAC, the Navier-Stokes equations were resolved by commercial software–ANSYS/CFD. Centrifugal compressor surface model was generated using commercial software SOLIDWORKS. In addition, existing network production and computer aided engineering ANSYS CFD were employed to identify the geometry and behavior of the blade and disc material as shown in Figure 5.

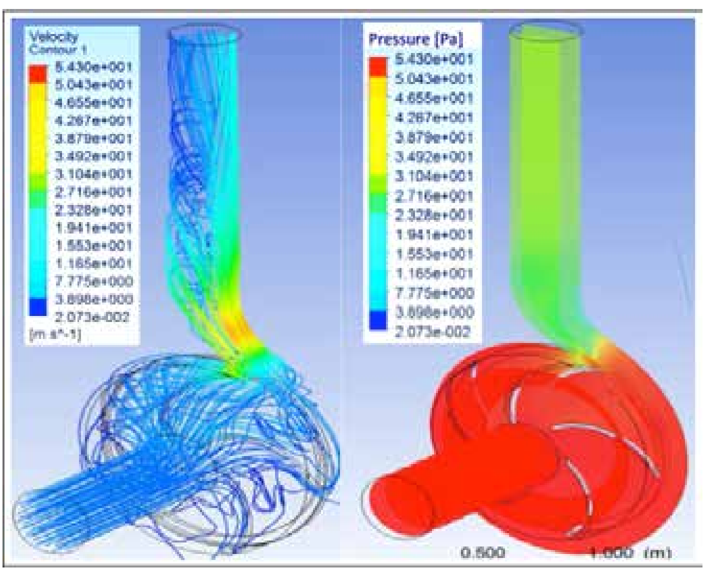

Figure 5: *Velocity and pressure analysis of gas turbine engine blade*

Figure 5 shows the impeller blade pressure loading profile obtained from LS-DYNA ANSYS analysis, according to CFD analysis, the impeller had overall higher head rise and extended impeller stall margin. Blade Modeler provides the essential link between blade design and advanced simulation including computational fluid dynamics and stress analyses. Blade Modeler contains a rich set of tools and functions for designing a turbo machinery blade from scratch, using industry-specific tools, workflow, and language that the blade designer expects. The user can re-design existing blades to achieve new design goals or create completely new blade designs from scratch. When either re-designing or evaluating an existing blade design, ANSYS facilitates the import of blade geometry interactively or through user supplied files.

ANSYS allows sculpted or ruled element blades with linear or compound lean leading or trailing edges. Over/under-filing can be applied and leading and trailing edge shapes are easily specified as a full radius, an ellipse ratio, or a simple cutoff. Blade modeler represents a pivotal link between blade design, advanced analysis and manufacturing. Used in combination with ANSYS analysis software, users can rapidly evaluate the performance of a component. ANSYS blade model files can be imported into design modeler using the blade editor feature. Blade editor provides a seamless path to both structural and fluid analysis, which enables the user to efficiently transition from preliminary blade design, to full 3- D viscous flow analysis, and finally to the users native CAD system for pressure loading distribution on the compressor blade as given in Figure 6.

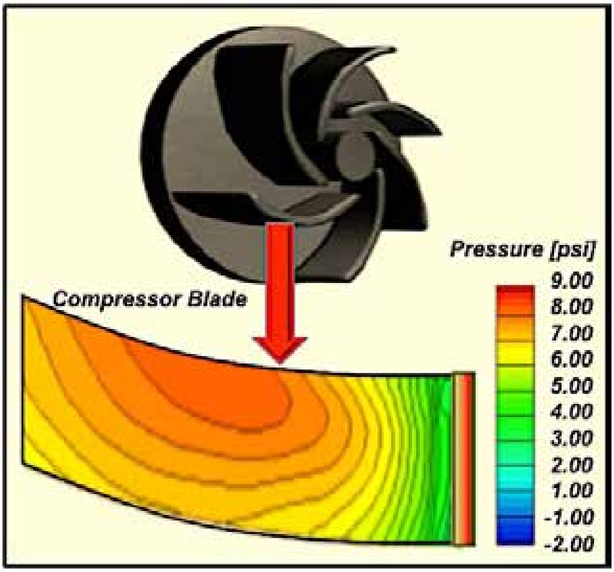

Figure 6: *Pressure loading distribution on the compressor blade*

The difference between the maximum radial displacement value and the minimum radial displacement value is considered as a measure of in the angular radial displacement values section of the housing inner surface.

The propeller part was simulated, and then an inclusive fluid flow analysis and a turbulence model revision were accomplished to identify the magnitude of possible errors from mathematical models. After the entire MAC working phase, the design was virtually realized. Various simulation parameters were chosen to perform the test setup accurately and to increase the speed of digital convergence.

Finally, a number of studies were performed, ranging from 60 to 93% of the design speed to non-design work. The results were analyzed for better understanding of flow physics under suitable working conditions after comparison with experimental measurements for velocity analysis on single MAC as shown in Figure 7 and Figure 8.

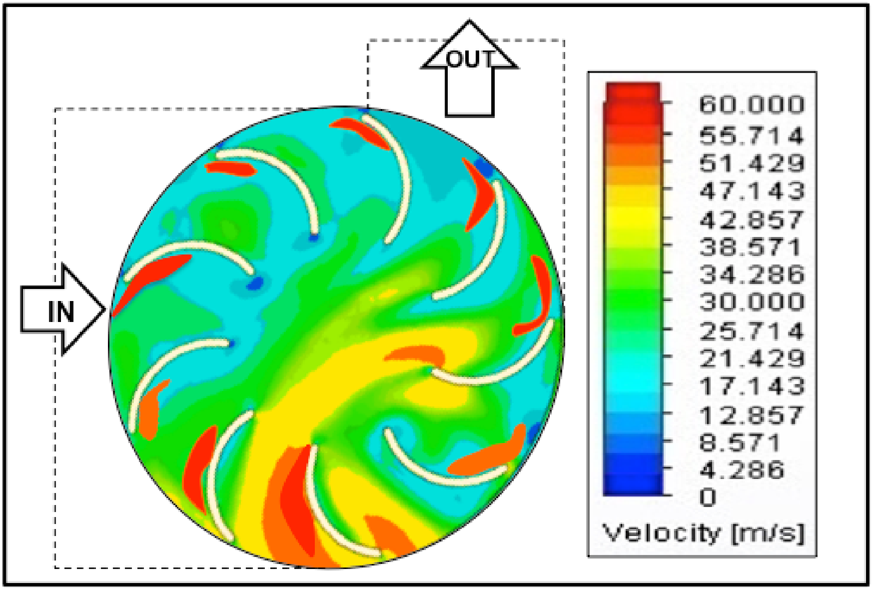

Figure 7: *Velocity airfoil analysis*

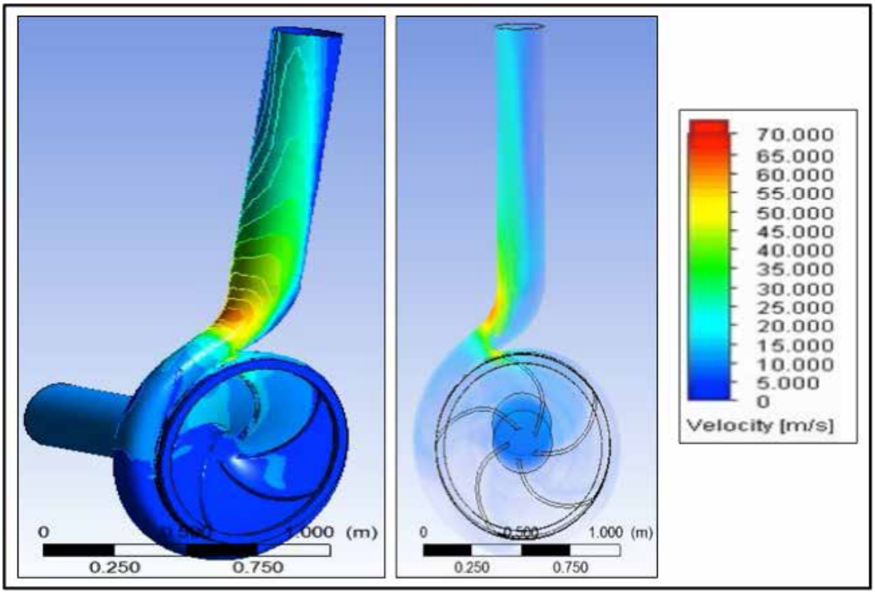

Figure 8: *Velocity analysis on single MAC*

In the evaluation of the results, the stresses were compared with the maximum and minimum radial deformations, which are a measure of stress and pressures. In addition, the weight of the housing and axial deformation is considered.

Examining the contact pressure, engagement and spacing between the contact surfaces compared the condition of the contact surfaces.

A new approach for MAC blade stress-strain was applied to evaluate by the finite element method. The aerodynamic and power supplies were analyzed by computing the strength and strain and the life of the blade at the beginning of the design process in this research.

The variety of dynamic loads is mainly due to the centrifugal force, vibration and aerodynamic forces on the blade. This MAC blade modeling was carried out for static strain (ESTRN) analysis as shown in Figure 8. Finally, 3D blade disc was demonstrated with equivalent von Mises analysis of gas turbine engine at the measured time on the surface of blade and disc, as shown in Figure 9.

The σ_v as von Mises stress, pointed in axis direction in x,y,z. In the design process, the purpose of the von Mises stress analysis that meets the aerodynamic criteria is to calculate and model the real stress as given in Figure 9. So, it is achievable to predict the possible destruction. In von Mises stress calculation, 24% of the stress was more on the blade than on the blade disc. Figure 6 displays the stress distribution of the MAC with high rotational speed. Maximum stresses occur at the base of the blade of the compressor disc. 235.72 MPa, which is below the yield stress of AISI 403 steel of 310 MPa. Therefore, the compressor design is safe.

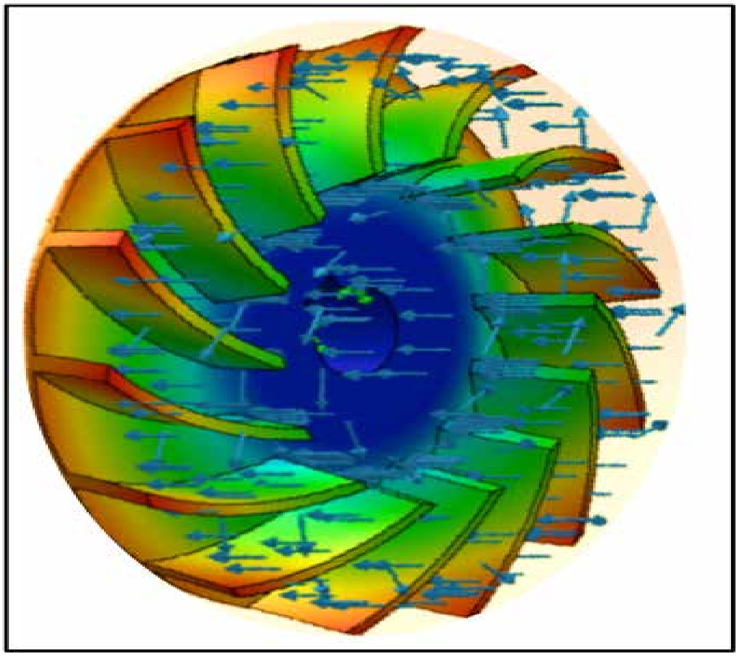

Figure 9: *Displacement of gas turbine engine blade*

Another parameter is to analyze occupational health and safety measures. Multi stage compression is essential not only for saving compressor energy, but also for occupational safety and health. Especially in piston compressors, oil is used to reduce the friction between piston and cylinder. These oils break down at high temperature to form explosive and toxic compounds and the resulting gases and oil residues mix into the compressed air. In order to avoid hazards, it is desirable that the compressed air temperature is at most 40 ° C below the ignition temperature of the oil used. It is envisaged that the ignition temperature of the oil that can be used in compressors should be at least 200 ° C.

7. DISCUSSIONS AND CONCLUSION

Given the wide variety of loss mechanisms and models available in the literature, an analysis aimed at establishing an appropriate set of these loss models, which is crucial for the proper assessment of centrifugal compressor efficiency, was developed.

From structural analysis we conclude that von-Mises stress induced in the turbine blade is 63.62 MPa. This value of stress gives maximum value of factor of safety for structural analysis.

From modal analysis and Harmonic analysis shows that the first natural frequency is far higher than maximum operating frequency, this gives clear indication that turbine is safe against resonance phenomenon. Also harmonic response within specified range is also acceptable, as maximum value of displacement is far lesser than static displacement.

This research determined a set of systematic correlation loss in centrifugal compressors; however, for certain situations, additional models should be included to consider certain characteristics.

For the prediction of complex non-design MAC performance, CFD analysis software has been used to analyze speed and pressure on the gas turbine wing surface. 13Cr4Ni (UNS S42400) stainless steel material was used for the Blades.

This research offers a new approach to von Mises computational modeling for the MAC-tipped disk. Important results of difficult and unbalanced MAC calculations suggest that completely unbalanced flow analyses can provide better performance forecasting, especially for high rotational speeds and pressure impact. MAC computational analysis results show that fully unstable fluid flow phenomena can produce better application accounts, especially at high rotational speeds. Verification of commercial ANSYS / CFD software to predict complex non-design MAC operation has been successful in understanding a better MAC physics.

8. ACKNOWLEDGMENTS

Istanbul University- Cerrahpaşa financially sponsored this research, BAP (Scientific Research Projects) project no: 48281, Avcılar, İstanbul, Turkey.

9. REFERENCES

Botha BW, Moolman A. Determining the impact of the different losses on centrifugal compressor design. Res Develop J 2005;21 (3):23–31.

Japikse D. Centrifugal compressor design and performance. White River Junction: Concepts Eti; 1996.

Boyce MP. Centrifugal compressors: A basic guide. Tulsa: Pennwell Books; 2003.

Forsthoffer WE. Forsthoffer's best practice handbook for rotating machinery. Oxford: Butterworth-Heinemann; 2011. p. 93–228.

Barsi, D., Perrone, A., Qu, Y., Ratto, L., Ricci, G., Sergeev, V. and Zunino, P. (2018) Compressor and Turbine Multidisciplinary Design for Highly Efficient Micro-Gas Turbine. Journal of Thermal Science, 27, 259-269. https://doi.org/10.1007/s11630-018-1007-2

Xiang, J., Schulter, J. and Duan, F. (2015) Effects of Tip Clearance on Miniature Gas Turbines Compressor Performance: A Numerical Approach. Proceedings of 33rd AIAA Applied Aerodynamics Conference, Dallas, 22-26 June 2015. https://doi.org/10.2514/6.2015-2412

Wen- Guang Li (2011) ,Inverse design of impeller blade of centrifugal pump with a singularity method, Jordan Journal Of mechanical and industrial engineering Volume5, Number2, April 2011 ISSN 1995- 6665 Pages 119-128.

Swamy, S. and Pandurangadu, V. (2013) Effect of Tip Clearance on Performance of a Centrifugal Compressor. IJRET: International Journal of Research in Engineering and Technology, 2, 447-453.

Perrone, A., Ratto, L., Ricci, G., Satta, F. and Zunino, P. (2016) Multi-Disciplinary Optimization of a Centrifugal Compressor for Micro-Turbine Applications. Pro- ceedings of ASME Turbo Expo 2016: Turbine Technical Conference and Exposi- tion, Seoul, 13-17 June 2016, V008T23A025. https://doi.org/10.1115/GT2016-57278

Barsi D., Perrone A., Ratto L., Simoni D., Zunino P. Radial inflow turbine design through Multidisciplinary optimization technique. ASME Turbo Expo 2015: Turbine Technical Conference and Exposition GT2015 Montreal, Canada, June 15–19: 2015.

Perrone A., Ratto L., Ricci G., Satta F., Zunino P. Multi-Disciplinary Optimization of a Centrifugal Compressor for Micro-Turbine Applications. ASME Turbo Expo 2016: Turbine Technical Conference and Exposition GT2016, Seul, South Corea, June 13–17, 2016.

Geuzaine C., Remacle J. F. Gmsh: a three-dimensional finite element mesh generator with built-in pre- and postprocessing facilities. International Journal for Numerical Methods in Engineering, 2009, 79(11): 1309–1331.

Gao Xing, Liu Baojie, Effects of Circulation Spanwise Distribution on High Specific Speed Mixed Flow Impellers, J. Journal of Engineering Thermophysics, 2008, Vol 29

Mert Cevik, Design and Optimization of a Mixed Flow Compressor Impeller Using Robust Design Methods, D. 2009.

Ji Guofeng, Gui Xingmin, A Blade Design Method for Axial/Centrifugal Compressor Airfoils Using Arbitrary Camber Lines, J. Journal of Aerospace Power, 2009(1):24-1

Mangani L, Casartelli E, Mauri S. Assessment of Various Turbulence Models in a High Pressure Ratio Centrifugal Compressor With an Object Oriented CFD Code. ASME. J. Turbomach. 2012, 134(6).

Ji Guofeng, The Apply of General Blade Design System for Axial/Centrifugal Compressors, D. 2009

Bourgeois JA, Martinuzzi RJ, Savory E, Zhang C, Roberts DA. Assessment of Turbulence Model Predictions for an Aero-Engine Centrifugal Compressor. ASME. J. Turbomach. 2010, 133(1).

Baskharone A. E. (2006). Principles of Turbomachinery in Air-breathing Engines. Texas A&M University, Cambridge University Press, U.K..

Mert Cevik, Oguz Uzol, Design Optimization of a mixed Flow compressor Impeller for a small turbojet engine, J. Aircraft Engineering andAerospace Technology, 2011.

Verstraete, T., Alsalihi, Z., Van den Braembussche R., 2010, “Multidisciplinary Optimization of a Radial Compressor for Microgas Turbine Applications”, Journal of Turbomachinery, Volume 132

Suanne Kruger, Nicolas Martin and Philippe Dupont (2010) “Assessment of wear erosion in pump impeller”, Proceeding of the Twenty- Sixth International Pump Users Symposium, 51-56

Mueller, L., Alsalihi, Z., Verstraete, T., 2013, “Multidisciplinary Optimization ofa Turbocharger Radial Turbine”, Journal of Turbomachinery, Volume 135

REN Neifei, CHEN Mingmin, JIANG Jie and CHENG Li (2011) “Flow Numerical Simulation of Centrifugal Pump with Splitting Blades based on Reverse Engineering”, Applied Mechanics and Materials, 43: 691-694

SowjanyaVijiapurapu, Jie Cui. (2010) “Performance of turbulence models for flows through rough pipes”, Applied Mathematical Modelling. 34 : 1458–1466

A Mittal, B K Gandhi, and KM Singh (2009) “Improvement in the design of a centrifugal impeller for an oil cooling blower system using computational fluid dynamics”, Power and Energy, 223: 981 -989.

M. Casey, C. Robinson, A method to estimate the performance map of a centrifugal compressor stage, ASME J. Turbomachinery 135 (2013). R.N.Brown, Compressors: SelectionandSizing,thirded.,ElsevierInc,USA,2005.

D. Vittorini, R. Cipollone, Financial analysis of energy saving via compressor replacement in industry, Energy 113 (2016) 809–820, https://doi.org/10.1016/ j.energy.2016.07.073.

Brown N. R. (2005). Compressors: Selection and Sizing. Third Edition, Gulf Professional Publishing, U.S.A.

ENGINEERING PROPERTIES OF GROUND-GRANULATED BLAST FURNACE SLAG MORTARS ACTIVATED WITH VARIOUS ALKALIS

CHAPTER

20

Bekir ÇOMAK[1]
Özlem SALLI BİDECİ[2]

1 Düzce University, Faculty of Technology, Department of Civil Engineering, 81620 Düzce, Turkey
E-mail:bekircomak@duzce.edu.tr
2 Düzce University, Faculty of Art, Design and Architecture, Department of Architecture, 81620 Düzce, Turkey
E-mail address: ozlembideci@duzce.edu.tr

1. INTRODUCTION

Concrete is among the most important construction materials because of its economic and technological advantages compared to other building materials (Gomez-Zamorano, Vega-Cordero, & Struble, 2016; Rostami & Behfarnia, 2017). Concrete industries through the world use 1.6 billion tons of Portland cement (PC) per year, producing approximately 12 billion tons of concrete each year. Cement production is increasing by about 3% per year (Hardjito & Rangan, 2005). As a matter of fact, for 1 tonne of cement production, approximately 0.94 tonnes of CO_2 gas is released into the atmosphere (Rashad, 2013). The cement industry is responsible for 6-7% of CO_2 gas emissions released into the atmosphere (Rashad, 2013). Increased PC production requires many natural resources and at the same time, PC production is a comprehensive process in terms of energy. For this reason, in recent years, researchers are continuing to work on the construction industry in order to promote sustainability, to preserve natural resources and to produce alternative materials to replace cement due to environmental degradation concerns (Guades, 2016; Saha & Rajasekaran, 2017). Development of alkaline activated new bonding materials as an alternative to PC has been the center of interest of the researchers recently.

Alkali-activated material (AAM) is the broadest classification, encompassing essentially any binder system derived by the reaction of an alkali metal source with a solid silicate powder (Provis & van Deventer, 2013). AAMs can be produced from waste materials, such as metallurgical slag, natural pozzolan, fly ash or bottom ash and mine tailings. AMMs are made by mixing rich silica-alumina material with an alkaline activator (alkali hydroxides, silicates, carbonates, sulfates, aluminates or oxides) (Provis & van Deventer, 2013; Simatupang, 2017; Yliniemi, Kinnunen, Karinkanta, & Illikainen, 2016). AAMs compared to binders prepared from PC that it could designed to have superior properties. That is, they could be exhibited higher strength, better heat resistance, lower drying shrinkage and creep and better resistance to acids and sulfate (Luukkonen, Abdollahnejad, Yliniemi, Kinnunen, & Illikainen, 2018)

The most common cementitious material for Alkali Activated Slag (AAS) is Ground-Granulated Blast Furnace Slag (GGBFS). GGBFSs obtained from the iron-steel production has various usage opportunities in cement and concrete sector due to their binding properties as such (Dorum, Koçak, Yılmaz, & Uçar, 2009). GGBFS has an amount of hydraulic properties. When it the reaction with water, its hydraulic properties are very slow and less on effect than the hydraulic properties of Portland cement. For this reason, GGBFS's should be activated by alkaline activators such as NaOH, Na_2CO_3, KOH etc. (El-Didamony, Amer, El-Sokkary, & Abd-El-

Aziz, 2013; Praveen, Senthilkumar, Sridhar, & Nickson, 2015; Universit & Benbouali, 2009).

Studies on activating GGBFS using alkaline have continued for more 70 years (Altan & Erdoğan, 2012) . AASs have used in production alkali-activated cement, alkali-activated mortar, and alkali-activated concrete. These products have been commercially produced and used in limited construction projects in some countries. They have been used in a variety of applications areas such as transportation, industrial, residential, agricultural, mining, oil well cements, in waste management, including radioactive wastes management, immobilization of toxic metals, high-volume applications and so on (Aydın & Baradan, 2014; C. Li, Sun, & Li, 2010).

There are numerous studies present in the literature: investigating the effect of type and amount of the activator used on AASs (Aydın & Baradan, 2014; Bernal, 2015; Shi, Shi, Wan, & Ou, 2017; Shi, Shi, Wan, & Zhang, 2018), the effect of different curing temperatures (Altan & Erdoğan, 2012; Dhruva Narayana Katpady, 2017; Zhang, Li, Ma, & Wang, 2016), mechanical properties (Fang, Ho, Tu, & Zhang, 2018; M.S. Midhun, 2018; Ramezanianpour & Moeini, 2018; Saad Al-Rawi, 2018), durability (Ahmet Emin Kurtoglu, 2018; Chi, 2012; El-Didamony, Amer, & Abd Ela-ziz, 2012; Law, Adam, Molyneaux, & Patnaikuni, 2012; Rostami & Behfarnia, 2017), resistance to chlorine and acids (Lee & Lee, 2016), resistance to carbonation (He, Gao, Wu, He, & Pu, 2018), effect of high temperatures (H.M. Khater, 2015; T. Li, Zhang, & Dai, 2017; Pan, Tao, Cao, Wuhrer, & Murphy, 2018; Rovnaník, Bayer, & Rovnaníková, 2013; W.-C. Wang, Wang, & Lo, 2014), microstructures (Gu, Fang, You, Gong, & Zhu, 2015; N. Li, Farzadnia, & Shi, 2017; Sakulich, Miller, & Barsoum, 2010) etc. The use of alkali-activated cements is already included in the legislation in some countries (Luukkonen et al., 2018). However, supply chains for raw materials, suitable admixtures for alkali-activated materials, and testing protocols are still inadequate (Luukkonen et al., 2018). For this reason, AAS has been and continues to be the focus of researchers.

In this study, it was aimed to produce Alkali-activated slag mortars (AASMs) by the use of alkaline activators that are obtained by mixing sodium hydroxide (NaOH) and sodium silicate (water glass) (Na_2SiO_2) in different proportions with ground granulated blast furnace slags (GGBFS). The physical characteristics of fresh AASMs such as flow diameter and density, and physical characteristics (water absorption, porosity, capillary absorption and density) and mechanical characteristics (compressive strength, flexural strength) with microstructure characteristics (SEM-EDS, FTIR, and XRD) were examined.

2. MATERIALS AND METHODS

2.1. Materials

Cement: CEM III/A (S) 32.5N type Blast Furnace Slag Cement (TS EN 197-1 [45]) was used in this study.

Silica Sand: In the tests, commercially available 40-45 AFS silica sand (Celiktas Industrial Sand Industry Trade and INC, Turkey) was used. It is used in the construction chemicals sector. Silica Ratio is minimum 99%. The particle size distribution of silica sand are given in Fig 1.

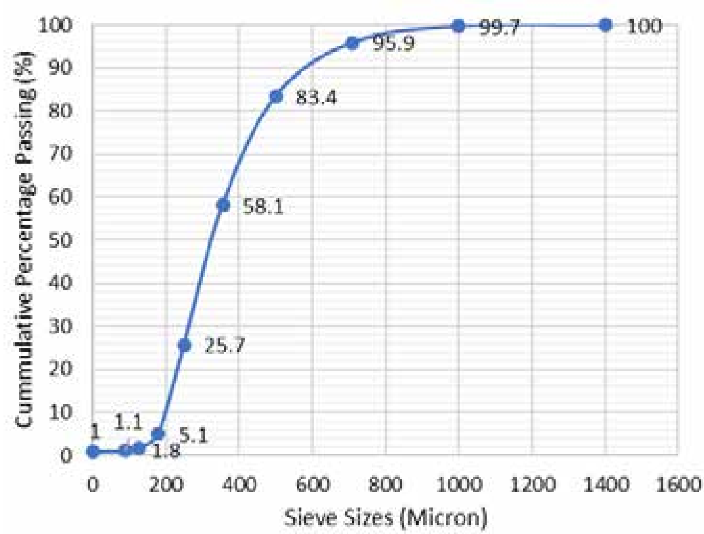

Fig 1. *Particle size distribution of silica sand*

Ground-Granulated Blast Furnace Slag (GGBFS): Chemical and technical characteristics of GGBFS produced in accordance with the TS EN 15167-1 (TS EN 15167-1 2006) standart by Bolu Çimento A.Ş. are given in Table 1. It contains, 90% particles sized lower than 45 µm. It is neutral with the basicity coefficient [$K_b = (CaO + MgO)/(SiO_2 + Al_2O_3)$] of 0.75. As can be seen from Table 1, the hydration modulus HM = $(CaO + MgO + Al_2O_3)/S_iO_2$ of slag is 1.38.

Table 1. *Chemical characteristics of ground granulated blast furnace slag (Oyak Bolu Cement Inc, 2019)*

Technical Properties		**Chemical Composition (%)**					
Activity, 7 days (%)	50	**SiO_2**	40.52	**Al_2O_3**	14.59	**Na_2O**	0.58
Activity, 28 days (%)	75	**Fe_2O_3**	1.10	**CaO**	34.18	**K_2O**	1.1
Specific Surface (cm^2/g)	4800	**TiO_2**	0.98	**MgO**	7.29	**SO_3**	0.16

Activators: Sodium silicate solution (water glass) and sodium hydroxide (NaOH) were used as activators in the production of the samples. By calculating the molarity, mixtures of 12 M, 16 M and 20 M sodium hydroxide were prepared and used after waiting 1 day. Activator was prepared by adding sodium silicate solution (water glass) in different proportions (sodium hydroxide solution/sodum silicate solution: 1/2, 2/1, 3/0) to the sodium hydroxide mixtures prepared. The characteristics of the sodium silicate solution (water glass) and sodium hydroxide (NaOH) used in the study are given in Table 2.

Table 2. *Characteristics of the sodium silicate solution (water glass) and sodium hydroxide (NaOH)*

Characteristcs		
	Sodium Silicate	**Sodium Hydroxide**
Physical State	Liquid	Solid
Specific Density	1.4 g/cm^3	2.1 g/cm^3
Molecular weight	-	39.9971 g/mol
Chemical formula	$Na_2O(SiO_2)x. (H_2O)x$	NaOH
Composition	Composed of 40% Sodium Metasilicate, Pentahydrate and 60% H_2O by mass	

Water: As water, potable water from the municipal water system was used in the mixture.

2.2. Method

2.2.1. Preparation of AASMs

AASMs were produced from ground granulated blast furnace slag, activator and silica sand without cement. The materials used in the mixture and codes given to the samples are listed in Table 3.

M in the coding of samples, represents mixture; numbers such as 12-16-20 represent molar value of NaOH, 1/2, 2/1, 3/0 ratios represent sodium hydroxide solution/ sodium silicate solution ratios.

Table 3. *Amounts of materials in the mixture for AASMs*

	Cement (g)	Water (ml)	GGBFS (g)	Silica Sand (g)	Activator (ml)			Sodium Hydroxide Solution/ Sodium Silicate Solution
					Mol	Sodium Hydroxide Solution (NaOH)	Sodium Silicate Solution (Water glass)	
Ref (reference)	450	225	0	1350	0	0	0	0
M-12-1/2	0	0	450	1350	12	75	150	1/2
M-12-2/1	0	0	450	1350	12	150	75	2/1
M-12-3/0	0	0	450	1350	12	225	0	3/0
M-16-1/2	0	0	450	1350	16	75	150	1/2
M-16-2/1	0	0	450	1350	16	150	75	2/1
M-16-3/0	0	0	450	1350	16	225	0	3/0
M-20-1/2	0	0	450	1350	20	75	150	1/2
M-20-2/1	0	0	450	1350	20	150	75	2/1
M-20-3/0	0	0	450	1350	20	225	0	3/0

In preparation of mixtures, mixing procedure in TS EN 196-1 standard was applied (TS EN 196-1 2016). In preparation of mixtures, firstly activator and GGBFS were added to the mixing container. The mixture was started to be mixed at low speed, and after 30 s sand was continuously added for 30 s. The mixer was adjusted to high speed and mixing was continued for 30 s. more. The mixer was stopped after 1 min. 30 s. and the mortar that adhered to the walls and base of the container were scraped by rubber scraper and gathered towards the middle part of the container. Mixing was continued for 210 s. at high speed. Obtained mortar samples were placed into cubical 50×50×50 mm and 40×40×160 mm dimensioned molds. Three samples were produced for each batch. AASM samples that were unmoulded after 48 hours from moulding process were air-cured at laboratory environment. No thermal processing was applied on the samples.

2.2.2. Tests on AASMs

Consistency and density of fresh AASMs were determined in according to TS EN 1015-3 (TS EN 1015-3/A2, 2007) and TSE EN 12350-6 (TS EN 12350-6, 2010) standarts, respectively. Physical (density (TS EN 12390-7) (TS EN 12390-7, 2010), water absorption (ASTM C642 (ASTM C 642-13, 2013), capillary water absorption (ASTM C1585 - 04, 2004) and porosity) and mechanical (compressive strength (TS EN 196-1), flexural strenght) tests were performed on the samples of hardened AASMs.

Microstructure characteristics of AASMs with the reference sample, which have low, moderate and high compressive strengths for 28 days, were examined by performing SEM-EDS, FT-IR and XRD analyzes.

3. RESULTS

3.1. Consistency and processability values of fresh AASM samples

Flow diameters and fresh density values obtained by the samples in the study are given in Table 4.

Table 4. *Flow diameters and densities of fresh AASMs*

	Ref	M-12-1/2	M-12-2/1	M-12-3/0	M-16-1/2	M-16-2/1	M-16-3/0	M-20-1/2	M-20-2/1	M-20-3/0
Flow diameter (cm)	11.7	10.0	10.1	12.9	12.9	11.2	11.3	10.8	11.8	12.9
Change %	0	-15	-14	10	10	-4	-4	-8	1	10
Density (kg/m^3)	2195	2259	2270	2307	2323	2320	2317	2279	2268	2166
Change %	0.0	2.9	3.4	5.1	5.9	5.7	5.6	3.8	3.3	-1.3

When Table 4 is examined, M-12-3/0, M-16-1/2 and M-20-3/0 mixtures was found to have the same value (12.9 cm) and also valid for M-20-2/1 mixture (11.8 cm), as this four mixture had greater values of flow diameter than the reference sample (11.7 cm), consistency of this four samples are better than the reference sample. The consistency of the remaining mixtures are observed to be lower than the reference sample. The consistency of the 12 M and 16 M batches increase with the increasing amount of NaOH. However, there is no such relationship in the 16 M batches. It is clear from Table 4 that the different ratios of activator mixtures affect the consistency of AASMs.

When density of the AASMs are examined; it is observed that the values vary from 2166 kg/m3 to 2323 kg/m3. The highest increase in denstiy was in 16 M batches whereas the lowest density values was in 20 M batches. Except the batch M-20-3/0; it is observed that density values increase when compared to the reference sample. This situtaion is thought to be due to the fact that density of activator included in the mixture is higher than the density of water.

3.2. Density, water absorption and capillary water absorption values of hardened AASMs

Mean density and mean absorption values of AASMs for 28 days are given in Table 5.

Table 5. *Mean density and mean water absorption test results*

	Ref	M-12-1/2	M-12-2/1	**M-12-3/0**	**M-16-1/2**	**M-16-2/1**	**M-16-3/0**	**M-20-1/2**	**M-20-2/1**	**M-20-3/0**
Density (kg/m^3)	2144	2187	2211	2214	2253	2234	2201	2216	2218	2216
Water Absorption (%)	9.0	6.5	3.9	3.8	4.3	2.8	2.3	4.3	2.1	2.5
Porosity %	17.8	13.4	8.3	8.1	9.3	6.1	5.0	9.1	4.5	5.4
Water absorption / Porosity	0.51	0.49	0.47	0.47	0.46	0.46	0.46	0.47	0.46	0.46

According to Table 5, it is observed that sample densities were between 2144 kg/m^3 and 2253 kg/m^3. When compared to reference sample, it is observed that density values increased in all of the series (for 12 M series mean 2.8%, for 16 M series mean 4%, for 20 M series mean 3.4%). The highest increase in density was in the batch M-16-1/2 with 5.1% increase. It is thought that the increase in density in all batches was caused by increase in the resulting resistance products of polymerisation reactions in the mortar.

The amount of water absorbed by AASMs are related to their porosity ratio. If the pores in the AASM or sand particles are open, they will absorb water due to their porosity ratio; otherwise, if the pores are semi-open or completely closed, mortars will absorb less water. When porosity values are examined, it is seen that the produced AASMs had values ranging between 4.5% and 17.8%. As it can be seen, water absorption ratios are 50% of the porosity values. In this case, it can be concluded that half of the pores are semi open or completely closed. It can be said that in all molar compositions, the batches with NaOH / water glass ratio of ½ have higher water absorption rates and porosity values than the other batches.

Capillary water permeability tests were performed according to ASTM C 1585 (ASTM C1585 - 04, 2004). The initial rate capillary permeability coefficients of the mortars were found by capillary permeability tests that were carried out on 3 samples. (Fig 2).

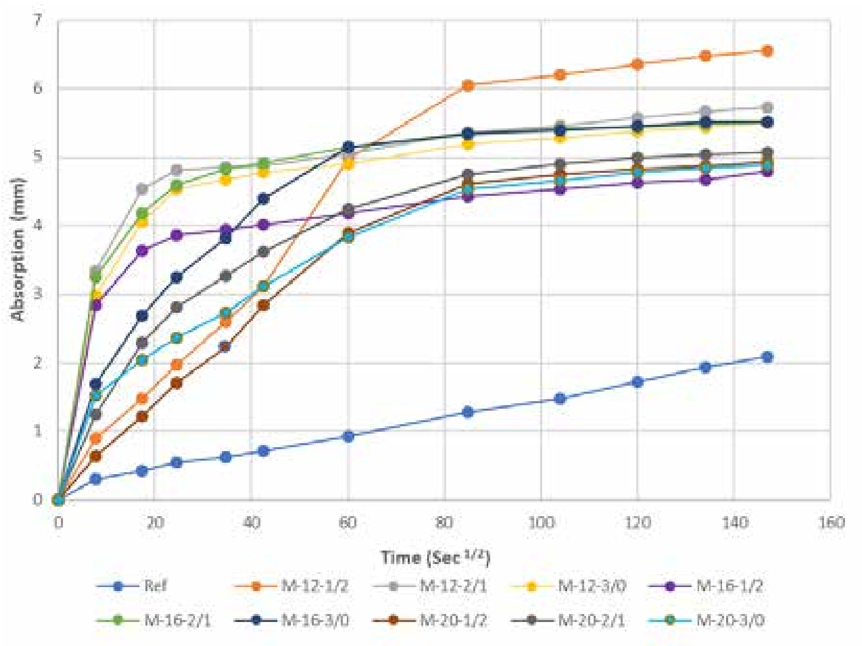

Fig 2. *Initial rates of water absorption of AASMs*

Table 6. *Capillary water absorption correlation coefficients*

	Ref	M-12-1/2	M-12-2/1	M-12-3/0	M-16-1/2	M-16-2/1	M-16-3/0	M-20-1/2	M-20-2/1	M-20-3/0
R^2	0.998	0.899	0.741	0.713	0.814	0.695	0.764	0.876	0.833	0.907

In the related standart, it is stated that in determination of initial rate capillary water permeability coefficient, if a linear correlation can not be found for the data between 1 minute to 6 hours (a correlation coefficient smaller than 0.98) and a systematic curve is demonstrated, the initial absorption rate can not be determined (ASTM C1585 - 04, 2004). Therefore, as none of the batches could provide the correlation coefficient condition (0.98) of the standart, initial rate capillary water permeability coefficients could not be determined (Table 6). The initial rate capillary water permeability coefficient of the reference sample is found as 1.28×10^{-2}) When Fig 2 is examined, it can be observed that the batches except reference and M-12-1/2 reach nearly saturation at 120 minutes and the curve progresses as a straight line. When the batches M-12-2/1, M-12-3/0, M-16-2/1 and M-16-1/2 are examined in Fig 2, it can be seen that they absorbed more water in one minutes when compared to the others. Therefore, it can be concluded for these series that, they have greater diameters of capillary water channels and the air voids captured in the samples are connected to each other with the capillary channels.

3.3. Compressive stregth of hardened AASMs

In accordance with TS EN 196-1, graphical demonstrations of 7, 28 and 180 days of mean compressive strength values of 50×50×50 mm dimensioned AASMs are given in Fig 3.

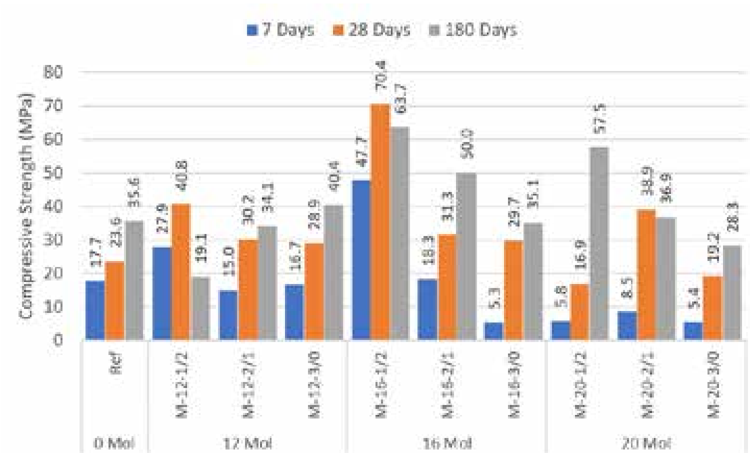

Fig 3. *Compressive strength values of AASMs for 7, 28 and 180 days*

When Fig 3 is examined, the compressive strength values are observed to increase with the sample age correspondingly. When 7 days compressive strength values are examined, it can be seen that, with the 169% increase, M-16-1/2 (47.7 MPa) batch had the highest strength value compared to the reference sample (Ref) and M-12-1/2 and M-16-2/1 batches keep up with the strength increase 57% (27.9 MPa) and 4% (18.3 MPa) correspondingly. In the other batches lower values were obtained compared to reference (Ref). When 28 days compressive strength values are examined, compared with the reference sample, M-16-1/2 (70.4 MPa) batch had the highest strength value with 198% strength increase and M-20-1/2 had the mimimum strength value (16.9 MPa). Compared to reference sample, the compressive strength variance of the batches for 28 days were determined as 73%, 28%, 23%, 198%, 33%, 26%,-28%, 65% and 19% respectively. When percentage changes are examined, except M-20-1/2 and M-20-3/0 batches, better results were obtained when compared to the reference sample. When 180 days of compressive strength are examined, compared to reference sample, batches M-16-1/2 (79%), M-20-1/2 (61%), M-16-2/1(40%), M-12-3/0 (13(%) and M-20-2/1(%4) had better stregths with compressive strength values 7%, 61%, 40%, 13% and 4% respectively. Similar or smaller values than the reference batch were obtained by other batches. When batches M-12-1/2, M-16-1/2 and M-20-2/1 are examined, it can be seen that 180 days compressive strength values are smaller than the 28 days compressive strength. Alkali-activated binders that contain sodium-based activators more vulnerable to efflorescence. This is due to an increase in Na_2O/Al_2O_3 ratio. When Na_2O exists in an unreacted state increases, it can be accelerated the relatively easy movement of sodium ions in the alumino-silicate structure, which is a product of the alkali-activated binder. The internal alkalis are able to diffuse towards the surface until an equilibrium (saturation) condition between the pore solution and the crystals is reached. The crystallization pressure due to the precipitation of sodium carbonates in the pores of the binder may also introduce inner stress, and affect the mechanical properties of the alkali-activated binder. Therefore it is evident that efflorescence has a negative influence on strength development (Hyeok-Jung, Kang, & Choe, 2018; Zhang, Provis, & Wang, 2015). It is thought that this decrease in compressive strength is due to efflorescence. Examples of AASMs that had extensively efflorescence are shown in Fig 4.

Fig. *Examples of AASMs that efflorescence had arisen*

When compressive strenth ratio of 7/28 days of AASMs are examined, the compressive strength values were found as 0.75, 0.68, 0.50, 0.58, 0.68, 0.58, 0.18, 0.34, 0.22 and 0.28 respectively, from the reference batch to the M-20-3/0 batch. It can be observed that for the batches M-16-3/0, M-20-1/2, M-20-2/1 and M-20-3/0, the first 7 days strength values are 35% lower than their 28 days final strength. It is thought that this condition is the result of increase in NaOH concentration, in another words, it is caused by the NaOH concentration included in the mixture. This ratio is above 49% in the other batches.

When the results obtained are examined, the importance of the activator used in the AASM, the amount of the activator in the mixture and the mixing ratio of the activator species has been revelaed. Although the amount of the substances except the activator is the same, the strength values are very different due to the activator. NaOH/ water glass ratio and molar concentration of NaOH have the most influence on the compressive strength and this change is not linear.

It has been observed that there are different color changes in the samples resulting from polymerisation of prepared activators and GGBFS (Fig 5).

Fig 5. *AASM samples fractured after compressive strength test*

Due to this color change, it can be seen that different hidration products are formed and due to these different hidration products, it can be concluded that different stregths can be obtained.

3.4. Flexural stregth values of hardened AASMs

7 and 28 days of mean compressive and flexural strength values of AASMs are given in Fig 6.

Fig 6. *Mean flexural strength values of AASMs*

When 7 days flexural strength values of the AASMs are examined; batches M-12-3/0 (4.7 MPa), M-16-1/2 (4.4 MPa) and M-16-2/1 (4.0 MPa) had better strength values with the 30%, 21% and 12 % increase, respectively. Other batches had lower results than the reference. Flexural strength values of M-16-3/0, M-20-1/2, M-20-2/1 and M-20-3/0 batches demonstrated similar results with their compressive strength values and had the lowest values. When 28 days of flexural strength is examined, M-12-1/2 (95%) and M-12-2/1 (98%) batches demonstrated similar flexural strength characteristics, whereas M-20-1/2 (2.3 MPa) sample had the lowest strength value. The other batches showed better flexural strength values, while M-12-3/0 and M-16-1/2 batches had the highest strength with the value 5.4 MPa.

3.5. Scanning Electron Microscopy (SEM) with Energy Dispersive Spectroscopy (EDS) Analysis

SEM and EDS analyzes of 28th day hydrated blast furnace slag cement (ref) and AASM batches M-12-2/1, M-16-1/2 and M-20-1/2 are given in Fig 7, Fig 8, Fig 9 and Fig 10.

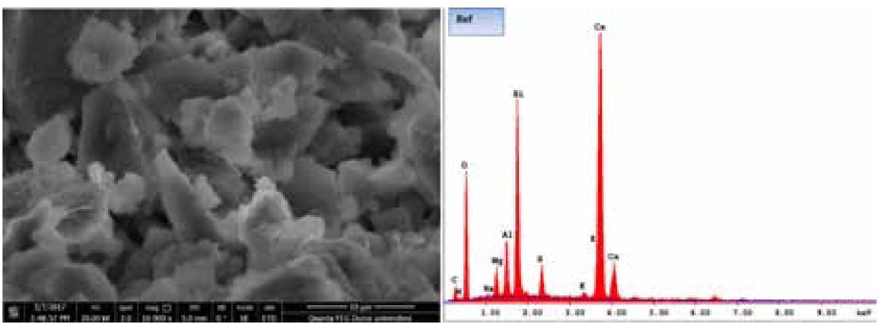

Fig 7. *SEM and EDS results of reference batch.*

The main structure of blast furnace slag cement paste (ref) was mainly consisted of crystalline and partly acicular C-S-H phase. The amorphous gel formed the dominant phase in the whole structure, bonded between hydration products, tried to fill up the voids, but though there were seen local voids having lengths of 1-5 microns. EDS spectrum on the surface of blast furnace slag cement paste had shown that the composition of surface layer was consisted of mainly Si and Ca (Fig 7).

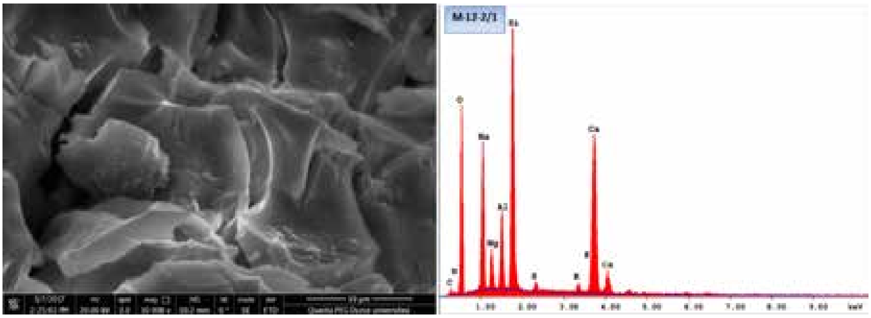

Fig 8. *SEM and EDS analysis of M-12-2/1 batch*

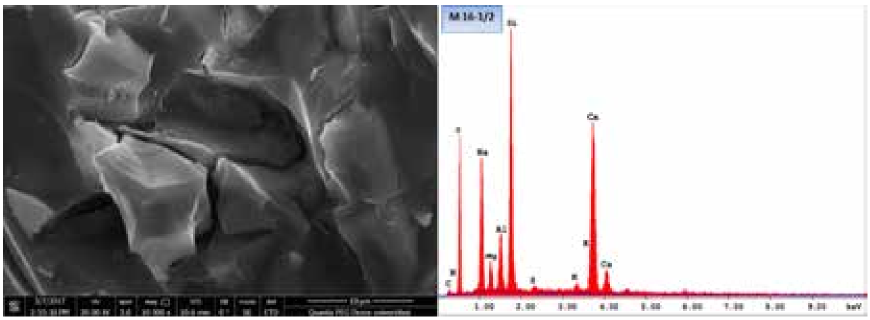

Fig 9. *SEM and EDS analysis of M-16-1/2 batch*

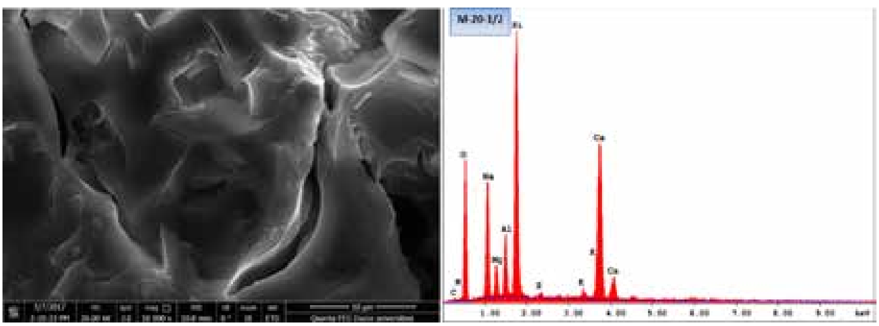

Fig 10. *SEM and EDS analysis of M-20-1/2 batch*

In Fig 8, Fig 9 and Fig 10, C-S-H phase, which dominates to the structure was seen. This phase tried to fill up the voids, but though there were local voids having lengths of 1-7 microns in the paste M-12-2/1, there were local voids having lengths of 1-3 microns in the paste M-16-1/2 and there were local voids having diameters of 5 microns in the paste M-20-1/2 and more dense voids having lengths of 15 microns. The situation in the M-20-1/2-coded paste suggests that the bond structure between the dominant phases is weakening. EDS spectra had shown that the composition of surface layer was consisted of mainly Si, Ca and Na, respectively.

The hydration of the reference has a characteristic morphology with a relatively dense and compact structure compared to CSH gel crystals (Fig

7). The compact structure is observed in the M-16-1/2 batches at 28 days of hydration, although a few small cracks were observed in those made of sodium hydroxide and sodyum silicate, which are due to the high drying-shrinkage that this specimen normally suffer (Fig 9). As a result, M-16-1/2 batches can be crosslinked the forming cracks and restrain its extension effectively, thus increase strength and improve toughness.

3.6. Fourier Transform Infrared spectroscopy (FT-IR)

FT-IR spectra of 28th hydration day of blast furnace slag cement (ref) and AAS paste batches M-12-2/1, M-16-1/2 and M-20-1/2 are given in Fig 11.

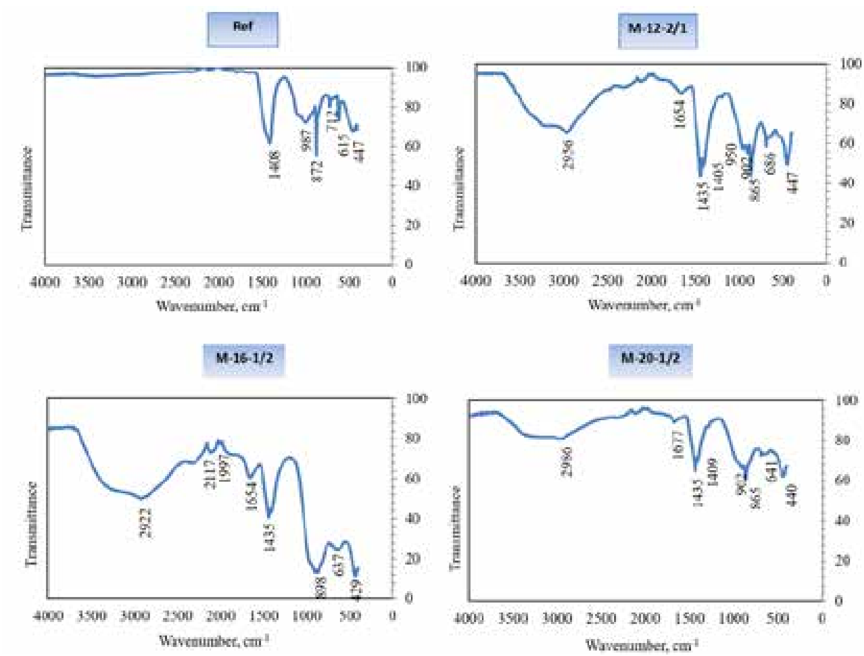

Fig 11. *FT-IR spectra*

The fundamental O–H bond in the water, the references wide bands are formed between 3500 and 3350 cm^{-1} in the spectra. Also AAS samples wide bands are formed between 1654 and 1677 cm^{-1} in the spectra. The Si–O bond (v3) of the produced C-S-H or C-A-S-H gel of alkali-activated geopolymer or modified specimen's characteristic strongest vibration can be form at wave numbers between 902 and 987 cm^{-1}, on the other hand may be form at higher wave numbers (1050 cm^{-1}) because of on the precursor. The reference and AAS mixtures Si–O–Si bond (weakest) vibration formed at 615–686 cm^{-1}. The Si-O-Si bond (v1) also has a band corresponding to 429-447 cm^{-1}. Calcite characteristic of the C-O bond observed in different mixtures in different wave numbers (v3 at 1405–1435 cm^{-1}, v2 at 865-898 cm^{-1}). Two bands of low density (Fig 11) are formed to be between 2922 and 2986 cm^{-1} wave numbers attributed to the harmonics produced by carbon in calcite (Angulo-Ramírez, Mejía de Gutiérrez, & Puertas, 2017; Chen, Zhu, Wang, & Chen, 2018; Kocak, Tascı, & Kaya, 2013; Sakulich et al., 2010). The paste carbonation can be controlled by the alkaline content of the pore solution and the high pH; the presence of NaOH and the alkaline pH increases the content, so use accelerate the carbonation rate and thus increases the depth in the sample (Angulo-Ramírez et al., 2017).

3.7. XRD Analyses

X-ray diffractograms of 28th hydration day of blast furnace slag cement (ref) and AAS paste batches M-12-2/1, M-16-1/2 and M-20-1/2 are given in Fig 12.

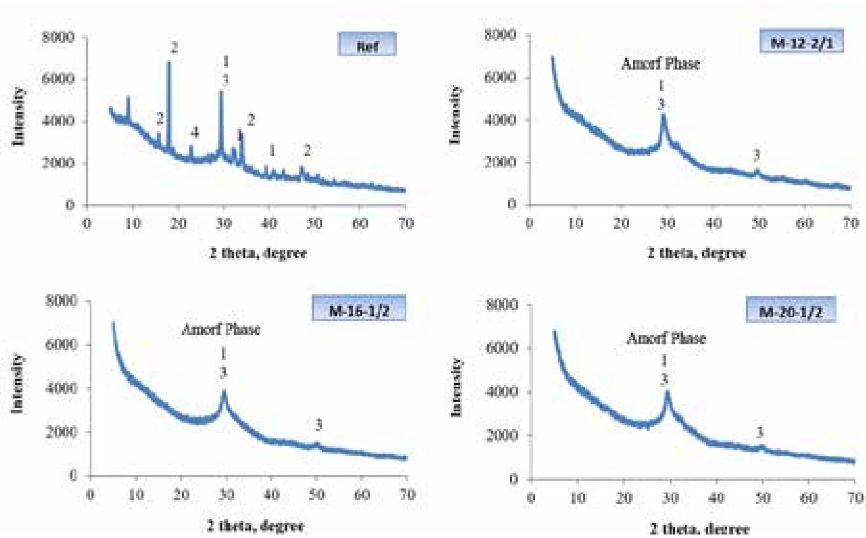

Fig 12. *X-ray diffractograms of 1: C-S-H, 2: C-H* ($Ca(OH)_2$*, 3: Calcite* ($CaCO_3$*), 4: Quartz* (SiO_2*).*

After AAS at curing ages of 28 days, new crystalline reaction products are identified (Fig 12), whose peak intensity is dependent on the GGBFS ratio, sodium hydroxide and sodium silicate. In AAS (Fig 12 - ref), the main reaction product is shown near 29° 2 theta, resembling the diffraction pattern of a poorly ordered C–S–H with a river sideite type structure (approximately $2CaSiO_3.3H_2O$), long with traces of calcite. C–S–H type gel has previously been reported as the main reaction product in AAS. Calcite peaks do not show differences in intensity suggesting that this compound is a residue of the anhydrous GGBFS (Ismail et al., 2014; Kocak & Nas, 2014; S.-D. Wang & Scrivener, 1995; Yang, Yao, Zhang, & Wang, 2012).

4. RESULTS

In this study, physical, mechanical and microstructural characteristics of AASMs obtained by using alkaline activators, that are obtained by mixing sodium hydroxide (NaOH) and sodium silicate ($Na_2O(SiO_2)x. (H_2O) x$) in different ratios, with ground granulated blast furnace slag (GGBFS) were investigated. The following results can be summarized as an outcome of this study;

- The consistencies of the AASMs vary with the activator usage. The flow diameter of batches M-12-3/0, M-16-1/2, M-20-3/0 and M-20-2/1 increased, where the flow diameter values of the other batches decreased to 15%.
- AASMs had fresh density values ranging from 2166 kg/m3 to 2323 kg/m3. When compared to reference sample, there exists density increase except M-20-3/0 batch. This situation is attributed to be the outcome of the activator density in the mixture.
- The densities of the AASMs in hardened phase were higher than the reference sample. Density values increased av. 2.8 % in 12 M batches, av. 4% in 16M batches and av. 3.4% in 20 M batches. The highest density increase occured in M-16-1/2 batch with the value 5.1%.
- Water absorption ratios of AASMs are about 50% of the porosity values. In another words, structure consists of semi-open or completely closed pores.
- When compared to reference sample, 28 days compressive strength was obtained in M-16-1/2 (70.4 MPa) batch with 198% strength increase, whereas the lowest compressive strength was obtained in M-20-1/2 (16.9 MPa) batch with 28% strength decrease.
- When compared to reference, except for M-20-1/2 and M-20-3/0 batches, 28 days of compressive strength values were obtained to be better than the reference with 73%, 28%, 23%, 198%, 33%, 26%, 65% increase in strength respectively.
- When compared to reference sample, better values had been obtained in 180 days compressive strength test for the batches; M-16-1/2 (79%), M-20-1/2 (61%), M-16-2/1(40%), M-12-3/0 (13%) and M-20-2/1 (4%) respectively. Other batches had similar or smaller values sthan the reference sample.
- It could be observed that for the batches M-16-3/0, M-20-1/2, M-20-2/1 and M-20-3/0, the first 7 days strength values were 35%

lower than their 28 days final strength. It was thought that this condition is the result of increase in NaOH concentration, in another words, it was caused by the NaOH concentration included in the mixture. This ratio was above 49% in the other batches.

- It was concluded that, the NaOH/water glass ratio and molar concentration of NaOH affect most to the compressive strength mechanisms of AASMs. But this change is not linear.
- There are different color changes in the resulting polymerisation samples obtained from the reaction of the prepared activators and GGBFS.
- M-20-1/2 (2.3 MPa) sample had the lowest flexural strength, whereas the other batches had similar or higher strength values. M-12-3/0 and M-16-1/2 batches had the highest strength with the value 5.4 MPa.
- When SEM images were examined, it was seen that compared to reference sample, M-16-1/2 batch had a more compact structure.
- When SEM and EDS analyzes were examined, it was observed that they had similar compositions having Si, Ca and Na and C-S-H phases were dominant.
- The results obtained from XRD, FT-IR, and SEM analyzes confirm each other.
- Providing that efflorescence defect is not ignored, it is concluded that AASM prepared by GGBFS, by its high performance can be used whereever blast furnace slag cement is used.

5. REFERENCES

Ahmet Emin Kurtoglu, R. A., Omar Aljumaili, Anil Nis, Mehmet Eren Gulsan, Ghassan Humur and Abdulkadir Cevik. (2018). Mechanical and durability properties of fly ash and slag based geopolymer concrete. *Advances in Concrete Construction, 6*(4), 345-362. doi:http://dx.doi.org/10.12989/acc.2018.6.4.345

Altan, E., & Erdoğan, S. T. (2012). Alkali activation of a slag at ambient and elevated temperatures. Cement and Concrete Composites, 34(2), 131-139. Retrieved from http://www.sciencedirect.com/science/article/pii/S0958946511001351. doi:https://doi.org/10.1016/j.cemconcomp.2011.08.003

Angulo-Ramírez, D. E., Mejía de Gutiérrez, R., & Puertas, F. (2017). Alkali-activated Portland blast-furnace slag cement: Mechanical properties and hydration. Construction and Building Materials, 140, 119-128. Retrieved from http://www.sciencedirect.com/science/article/pii/S0950061817302945. doi:https://doi.org/10.1016/j.conbuildmat.2017.02.092

ASTM C1585 - 04. (2004). Measurement of rate of absorption of water by hydraulic- cement concretes. In (Vol. ASTM C 1585 - 04, pp. 6). West Conshohocken, PA,: ASTM International.

ASTM C 642-13. (2013). Standard test method for density, absorption, and voids in hardened concrete. In (Vol. ASTM C642-13). West Conshohocken, PA,: ASTM International.

Aydın, S., & Baradan, B. (2014). Effect of activator type and content on properties of alkali-activated slag mortars. Composites Part B: Engineering, 57, 166-172. Retrieved from http://www.sciencedirect.com/science/article/pii/S1359836813005660. doi:https://doi.org/10.1016/j.compositesb.2013.10.001

Bernal, S. A. (2015). Effect of the activator dose on the compressive strength and accelerated carbonation resistance of alkali silicate-activated slag/metakaolin blended materials. Construction and Building Materials, 98, 217-226. Retrieved from http://www.sciencedirect.com/science/article/pii/S0950061815302300. doi:https://doi.org/10.1016/j.conbuildmat.2015.08.013

Chen, X., Zhu, G. R., Wang, J., & Chen, Q. (2018). Effect of polyacrylic resin on mechanical properties of granulated blast furnace slag based geopolymer. Journal of Non-Crystalline Solids, 481, 4-9. Retrieved from http://www.sciencedirect.com/science/article/pii/S0022309317303472. doi:https://doi.org/10.1016/j.jnoncrysol.2017.07.003

Chi, M. (2012). Effects of dosage of alkali-activated solution and curing conditions on the properties and durability of alkali-activated slag concrete. Construction and Building Materials, 35, 240-245. Retrieved from http://dx.doi.org/10.1016/j.conbuildmat.2012.04.005. doi:10.1016/j.conbuildmat.2012.04.005

Dhruva Narayana Katpady, K. T., Toshinobu Yamaguchi. (2017). Development of slag based Shirasu geopolymer. Computers and Concrete, 20(1), 077-084 doi:http://dx.doi.org/10.12989/cac.2017.20.1.077

Dorum, A., Koçak, Y., Yılmaz, B., & Uçar, A. (2009). The effects of blast furnace slag on the cement surface properties and hydration. Journal of the Institute of Science and Technology of Dumlupinar University, 19, 47-58.

El-Didamony, H., Amer, A. A., & Abd Ela-ziz, H. (2012). Properties and durability of alkali-activated slag pastes immersed in sea water. Ceramics International, 38(5), 3773-3780. Retrieved from http://www.sciencedirect.com/science/article/pii/S0272884212000272. doi:https://doi.org/10.1016/j.ceramint.2012.01.024

El-Didamony, H., Amer, A. A., El-Sokkary, T. M., & Abd-El-Aziz, H. (2013). Effect of substitution of granulated slag by air-cooled slag on the properties of alkali activated slag. Ceramics International, 39(1), 171-181. Retrieved from http://www.sciencedirect.com/science/article/pii/S0272884212005238. doi:http://doi.org/10.1016/j.ceramint.2012.06.007

Fang, G., Ho, W. K., Tu, W., & Zhang, M. (2018). Workability and mechanical properties of alkali-activated fly ash-slag concrete cured at ambient temperature. Construction and Building Materials, 172, 476-487. Retrieved from http://www.sciencedirect.com/science/article/pii/S0950061818307980. doi:https://doi.org/10.1016/j.conbuildmat.2018.04.008

Gomez-Zamorano, L. Y., Vega-Cordero, E., & Struble, L. (2016). Composite geopolymers of metakaolin and geothermal nanosilica waste. Construction and Building Materials, 115, 269-276. Retrieved from <Go to ISI>://WOS:000376833400029. doi:10.1016/j.conbuildmat.2016.03.002

Gu, Y.-m., Fang, Y.-h., You, D., Gong, Y.-f., & Zhu, C.-h. (2015). Properties and microstructure of alkali-activated slag cement cured at below- and about-normal temperature. Construction and Building Materials, 79, 1-8. Retrieved from http://www.sciencedirect.com/science/article/pii/S0950061814013701. doi:https://doi.org/10.1016/j.conbuildmat.2014.12.068

Guades, E. J. (2016). Experimental investigation of the compressive and tensile strengths of geopolymer mortar: The effect of sand/fly ash (S/FA) ratio. Construction and Building Materials, 127, 484-493. Retrieved from <Go to ISI>://WOS:000388047400048. doi:10.1016/j.conbuildmat.2016.10.030

H.M. Khater, H. A. A. E. G. (2015). Effect of firing temperatures on alkali activated Geopolymer mortar doped with MWCNT. Advances in Nano Research, 3(4), 225-242 doi: http://dx.doi.org/10.12989/anr.2015.3.4.225

Hardjito, D., & Rangan, B. V. (2005). Development and properties of low-calcium fly ash-based geopolymer concrete. Retrieved from Research report GC-1, Faculty of Engineering, Curtins University of Technology,Perth, Australia:

He, J., Gao, Q., Wu, Y., He, J., & Pu, X. (2018). Study on improvement of carbonation resistance of alkali-activated slag concrete. Construction and Building Materials, 176, 60-67. Retrieved from http://www.sciencedirect.com/science/article/pii/S0950061818309231. doi:https://doi.org/10.1016/j.conbuildmat.2018.04.117

Hyeok-Jung, K., Kang, S.-P., & Choe, G.-C. (2018). Effect of red mud content on strength and efflorescence in pavement using alkali-activated slag cement. International Journal of Concrete Structures and Materials, 12(1), 18. Retrieved from https://doi.org/10.1186/s40069-018-0258-3. doi:10.1186/s40069-018-0258-3

Ismail, I., Bernal, S. A., Provis, J. L., San Nicolas, R., Hamdan, S., & van Deventer, J. S. J. (2014). Modification of phase evolution in alkali-activated blast furnace slag by the incorporation of fly ash. Cement and Concrete Composites, 45, 125-135. Retrieved from http://www.sciencedirect.com/science/article/pii/S0958946513001340. doi:https://doi.org/10.1016/j.cemconcomp.2013.09.006

Kocak, Y., & Nas, S. (2014). The effect of using fly ash on the strength and hydration characteristics of blended cements. Construction and Building Materials, 73, 25-32. Retrieved from http://www.sciencedirect.com/science/article/pii/S0950061814010642. doi:https://doi.org/10.1016/j.conbuildmat.2014.09.048

Kocak, Y., Tascı, E., & Kaya, U. (2013). The effect of using natural zeolite on the properties and hydration characteristics of blended cements. Construction and Building Materials, 47, 720-727. Retrieved from http://www.sciencedirect.com/science/article/pii/S0950061813004315. doi:https://doi.org/10.1016/j.conbuildmat.2013.05.033

Law, D. W., Adam, A. A., Molyneaux, T. K., & Patnaikuni, I. (2012). Durability assessment of alkali activated slag (AAS) concrete. Materials and Structures, 45(9), 1425-1437. Retrieved from https://doi.org/10.1617/s11527-012-9842-1. doi:10.1617/s11527-012-9842-1

Lee, N. K., & Lee, H. K. (2016). Influence of the slag content on the chloride and sulfuric acid resistances of alkali-activated fly ash/slag paste. Cement and Concrete Composites, 72, 168-179. Retrieved from http://www.sciencedirect.com/science/article/pii/S0958946516302347. doi:https://doi.org/10.1016/j.cemconcomp.2016.06.004

Li, C., Sun, H., & Li, L. (2010). A review: The comparison between alkali-activated slag (Si+Ca) and metakaolin (Si+Al) cements. Cement and Concrete Research, 40(9), 1341-1349. Retrieved from http://www.sciencedirect.com/science/article/pii/S000888461000089X. doi:https://doi.org/10.1016/j.cemconres.2010.03.020

Li, N., Farzadnia, N., & Shi, C. (2017). Microstructural changes in alkali-activated slag mortars induced by accelerated carbonation. Cement and Concrete Research, 100, 214-226. Retrieved from http://www.sciencedirect.com/

science/article/pii/S0008884617301175. doi:https://doi.org/10.1016/j.cemconres.2017.07.008

Li, T., Zhang, Y., & Dai, J.-G. (2017). Flexural behavior and microstructure of hybrid basalt textile and steel fiber reinforced alkali-activated slag panels exposed to elevated temperatures. Construction and Building Materials, 152, 651-660. Retrieved from http://www.sciencedirect.com/science/article/pii/S0950061817313922. doi:https://doi.org/10.1016/j.conbuildmat.2017.07.059

Luukkonen, T., Abdollahnejad, Z., Yliniemi, J., Kinnunen, P., & Illikainen, M. (2018). One-part alkali-activated materials: A review. Cement and Concrete Research, 103, 21-34. Retrieved from http://www.sciencedirect.com/science/article/pii/S0008884617306877. doi:https://doi.org/10.1016/j.cemconres.2017.10.001

M.S. Midhun, T. D. G. R., T.Chaitanya Srikrishna. (2018). Mechanical and fracture properties of glass fiber reinforced geopolymer concrete. Advances in Concrete Construction, 6(6), 29-45. doi:http://dx.doi.org/10.12989/acc.2018.6.1.029

Oyak Bolu Cement Inc. (2019). Ground blast furnace slag. Retrieved from http://www.bolucimento.com.tr/documents/bolu-ogutulmus-yuksek-firin-curufle.html

Pan, Z., Tao, Z., Cao, Y. F., Wuhrer, R., & Murphy, T. (2018). Compressive strength and microstructure of alkali-activated fly ash/slag binders at high temperature. Cement and Concrete Composites, 86, 9-18. Retrieved from http://www.sciencedirect.com/science/article/pii/S0958946516303961. doi:https://doi.org/10.1016/j.cemconcomp.2017.09.011

Praveen, J. A., Senthilkumar, P., Sridhar, J., & Nickson, S. (2015). A comparative study of alkali activated slag and fly ash-based geopolymer concrete. International Journal of Innovative Research in Science, Engineering and Technology, 2001, 10151-10156. doi:10.15680/IJIRSET.2015.0410063

Provis, J. L., & van Deventer, J. S. J. (2013). Alkali Activated Materials: State-of-the-Art Report, RILEM TC 224-AAM: Springer Netherlands.

Ramezanianpour, A. A., & Moeini, M. A. (2018). Mechanical and durability properties of alkali activated slag coating mortars containing nanosilica and silica fume. Construction and Building Materials, 163, 611-621. Retrieved from http://www.sciencedirect.com/science/article/pii/S0950061817324650. doi:https://doi.org/10.1016/j.conbuildmat.2017.12.062

Rashad, A. M. (2013). A comprehensive overview about the influence of different additives on the properties of alkali-activated slag - A guide for Civil Engineer. Construction and Building Materials, 47, 29-55. Retrieved from <Go to ISI>://WOS:000325232600004. doi:10.1016/j.conbuildmat.2013.04.011

Rostami, M., & Behfarnia, K. (2017). The effect of silica fume on durability of alkali activated slag concrete. Construction and Building Materials, 134, 262-268. Retrieved from <Go to ISI>://WOS:000393726700029. doi:10.1016/j.conbuildmat.2016.12.072

Rovnaník, P., Bayer, P., & Rovnaníková, P. (2013). Characterization of alkali activated slag paste after exposure to high temperatures. Construction and Building Materials, 47, 1479-1487. Retrieved from http://www.sciencedirect.com/science/article/pii/S0950061813005886. doi:https://doi.org/10.1016/j.conbuildmat.2013.06.070

Saad Al-Rawi, N. T. (2018). Performance of self-compacting geopolymer concrete with and without GGBFS and steel fiber. Advances in Concrete Construction, 6(4), 323-344 doi:DOI: http://dx.doi.org/10.12989/acc.2018.6.4.323

Saha, S., & Rajasekaran, C. (2017). Enhancement of the properties of fly ash based geopolymer paste by incorporating ground granulated blast furnace slag. Construction and Building Materials, 146, 615-620. Retrieved from <Go to ISI>://WOS:000403120600066. doi:10.1016/j.conbuildmat.2017.04.139

Sakulich, A. R., Miller, S., & Barsoum, M. W. (2010). Chemical and microstructural characterization of 20-month-old alkali-activated slag cements. Journal of the American Ceramic Society, 93(6), 1741-1748.

Shi, Z., Shi, C., Wan, S., & Ou, Z. (2017). Effect of alkali dosage on alkali-silica reaction in sodium hydroxide activated slag mortars. Construction and Building Materials, 143, 16-23. Retrieved from http://www.sciencedirect.com/science/article/pii/S0950061817305135. doi:https://doi.org/10.1016/j.conbuildmat.2017.03.125

Shi, Z., Shi, C., Wan, S., & Zhang, Z. (2018). Effects of alkali dosage and silicate modulus on alkali-silica reaction in alkali-activated slag mortars. Cement and Concrete Research, 111, 104-115. Retrieved from http://www.sciencedirect.com/science/article/pii/S0008884618302047. doi:https://doi.org/10.1016/j.cemconres.2018.06.005

Simatupang, P. H. (2017). Characteristics of Alkali Activated Material (Geopolymer) in Sulfuric Acid Solution. AIP Conference Proceedings, 1887(1), 020028. Retrieved from https://aip.scitation.org/doi/abs/10.1063/1.5003511. doi:10.1063/1.5003511

TS EN 196-1 (2016). Methods of testing cement - Part 1: Determination of strength. In (pp. 35): Turkish Standards Instituion.

TS EN 1015-3/A2. (2007). Methods of test for mortar for masonry - Part 3: Determination of consistence of fresh mortar (by flow table) In (pp. 5): Turkish Standards Instituion.

TS EN 12350-6. (2010). Testing fresh concrete - Part 6: Density In (pp. 12): Turkish Standards Instituion.

TS EN 12390-7. (2010). Testing hardened concrete - Part 7: Density of hardened concrete. In (pp. 11): Turkish Standards Instituion.

TS EN 15167-1 (2006). Ground granulated blast furnace slag for use in concrete, mortar and grout - Part 1: Definitions, specifications and conformity criteria. In (pp. 23): Turkish Standards Instituion.

Universit, B., & Benbouali, H. (2009). Some Parameters Affecting the Heat of Hydration of Blast-Furnace Slag. SBEIDCO – 1st International Conference on Sustainable Built Environment Infrastructures in Developing Countries ENSET(Durability of materials and structures), 8-16.

Wang, S.-D., & Scrivener, K. L. (1995). Hydration products of alkali activated slag cement. Cement and Concrete Research, 25(3), 561-571. Retrieved from http://www.sciencedirect.com/science/article/pii/000888469500045E. doi:https://doi.org/10.1016/0008-8846(95)00045-E

Wang, W.-C., Wang, H.-Y., & Lo, M.-H. (2014). The engineering properties of alkali-activated slag pastes exposed to high temperatures. Construction and Building Materials, 68, 409-415. Retrieved from http://www.sciencedirect.com/science/article/pii/S0950061814006291. doi:https://doi.org/10.1016/j.conbuildmat.2014.06.016

Yang, T., Yao, X., Zhang, Z., & Wang, H. (2012). Mechanical property and structure of alkali-activated fly ash and slag blends. Journal of Sustainable Cement-Based Materials, 1(4), 167-178.

Yliniemi, J., Kinnunen, P., Karinkanta, P., & Illikainen, M. (2016). Utilization of mineral wools as alkali-activated material precursor. Materials, 9(5), 312. Retrieved from http://www.ncbi.nlm.nih.gov/pmc/articles/PMC5503039/. doi:10.3390/ma9050312

Zhang, Z., Li, L., Ma, X., & Wang, H. (2016). Compositional, microstructural and mechanical properties of ambient condition cured alkali-activated cement. Construction and Building Materials, 113, 237-245. Retrieved from http://www.sciencedirect.com/science/article/pii/S0950061816303294. doi:https://doi.org/10.1016/j.conbuildmat.2016.03.043

Zhang, Z., Provis, J. L., & Wang, H. (2015). Critical Thinking On Efflorescence In Alkali Activated Cement (Aac). Paper presented at the International Conference on Performance-based and Life-cycle Structural Engineering, School of Civil Engineering, The University of Queensland.

THE USE OF METALLIC PIGMENTS IN OLD AND NEW PAPER

CHAPTER

21

Öznur ÖZDEN[1]
Sinan SÖNMEZ[2]

[1] Assist. Prof. Dr., Corresponding author, İstanbul-Cerrahpaşa University, Faculty of Forest, Department of Forest Product Chemistry and Technology, İstanbul, Turkey
ozdeno@istanbul.edu.tr

[2] Prof. Dr., Marmara University, School of Applied Sciences, Department of Printing Technologies, İstanbul, Turkey
ssonmez@marmara.edu.tr

INTRODUCTION

Pigment is the name given to organic or inorganic substances that change the color of reflected or transmitted light according to the selective absorption of its wavelength.

In other words, the pigment; is a colorant in the form of particles that are insoluble in an environment but which may be dispersed to change color.

Pigments of very different structures and colors are generally applied to objects by two different methods.

a) As surface coating. This is a modern term for traditional painting methods. In this method, the pigment ground and colored to make a dye or printing ink is applied to the surface of the object.

b) With Mass coloring. This method is used to color plastics before extruding. It is applied by adding pigment into the solution of man-made textile fibers such as viscose or cellulose (McLaren, 1986).

Natural pigments were used in the first years of use. Nowadays, although predominantly synthetic pigments are used, the tendency to use natural pigments has increased in recent years.

Most of the inks contain colored pigments. Natural pigments processed to be sand free are sometimes used in printing inks. For example, umber, ocher, sienna, Indian red and iron yellow. However, most of the colored pigments are synthetic organic and inorganic pigments (Bajpai, 2015). Some of these are iron blues, chrome greens, vermillion (mercury sulfide), cadmium red, cadmium yellow, zinc yellow, calcium, barium or aluminum lakes of acid dyes, insoluble azo dyes, phosmolybdic or phosphotungstic lakes of basic dyes and white pigments (titanium dioxide, lithopone, zinc white and white lead) (Casey, 1983).

Metallic pigments (aluminum, copper, or brass powder) are special inks used for printing brochures, advertising leaflets and labels (URL1). The important point in such inks is that they have high foliation (sheet-foil forming) value which increases the brightness of the film. Size, shape, surface conditions of pigment flakes are factors in determining leafing quality. Although aluminum powders are very stable, the bronze pigment is not stable (Wyatt, 1988). The inks formed by adding bronze pigment should be used immediately as soon as they are prepared. Otherwise, they form dullness due to their tendency to react with weak acids in the medium. For printing with metallic inks, dense ink films should be applied under minimum pressure to achieve maximum foliage. Neutral or alkaline solutions are used to prevent blackening of bronze in lithographic printing with metallic inks (Casey, 1983).

Additives or fillers are sometimes added to printing inks to reduce the price and increase ink volume. Some of the common volume boosters are; barytes, clay, blanc fixe, whiting and silica. Increased ink pigmentation increases the color value and improves print quality. In practice, however, pigmentation is limited by the operating characteristics of the ink in pressure and absorption during printing. High pigmentation reduces ink brightness (Casey, 1983).

Metallic pigments have been used for many years in printing or painting on paper and similar products. In the past years, the pigments used in the dyeing and printing of papyrus, parchment and paper products are more common in manuscripts. Today, the use of metallic pigments is found during printing on special papers and labels.

THE USE OF METALLIC PIGMENTS IN MANUSCRIPTS

Manuscripts

The printed works that have survived until today are called manuscripts. The papers and inks used in manuscripts were produced according to the conditions of that day and general knowledge of paper production. Those who are under protection have survived to the present day. Turkey is the owner of a rich collection of works of a hand writing on this subject. The factors that increase the deterioration of these works are heat, light and moisture depending on the environment in which they are found. In addition, inks used in manuscripts also cause deterioration in paper due to the effect of environmental conditions over time due to the metallic pigments they contain.

Throughout human history, many materials such as stone, metal, baked or unbaked clay, bone, wax tablet, textile, papyrus, palm leaf, bark, wood, bamboo strips, leather, parchment and paper have been used as writing, painting or painting surfaces. The preferred dye or ink varies depending on the material used as the surface, or the material used as the substrate. With the discovery of paper, the use of paper as a writing surface has replaced other materials. Papyrus was used as the fiber source in the first years of the paper, and then, especially in the production of so-called Islamic paper, linen (*usitatissimum*), hemp (*cannabis sativa*), which are annual plants, were used. In Japan, papermaking mulberry (kozo-*broussonetia papyrifera*), mitsumata (*edgeworthia papyrifera*), gampi (wikstroemia canescens) and hemp (*cannabis sativa*) were used for papermaking. These are plants with long fibers. In the years when the paper was discovered and after many years, handmade paper was made by the traditional method. With the advancement of technology, when the Fourdinier brothers found the paper machine, the paper began to be produced in the machine. Although the invention of the paper machine was effective at every stage of production, the essence of paper production remained the same.

Usually carbon black and natural dyes from plants were used to draw shapes and write on paper. Some of these paints used in the works, which we call as manuscripts that have been preserved for many years and have survived until today, have caused deterioration over time.

Due to its paper structure, it has a moisture-absorbing property. When we drop a liquid drop on a non-glued paper surface as a stain, the liquid will be absorbed by the cellulose fibers which will not evaporate and will be absorbed by the interconnected channels forming the paper. This is an important fact that helps explain the behavior of inks on paper. If the paper surface is not porous, the ink evaporates or undergoes chemical change when ink is dropped onto this surface, both of which are a slow process. As a result, pressure is quite difficult (Loveday, 2001a).

In the production of Islamic papers, no surface glue was applied initially, but after the 15th century, increasing amounts of starch glue were used. Starch is still a popular glue used for surface and internal gluing.

From the beginning of the 12th century to the 19th century, most papers had a gradual brightness in the color tone. The papers ranged from brown to dark cream. They were produced in matte, grayish and off-white appearance after the 19th century (Loveday, 2001b).

In Islamic papers, calligraphers used paintings and ornaments to create decorative images on the pages of manuscripts. They use blue; indigo or aloe, yellow; saffron and lemon, red; from the body of the mealy beetle, olive green; mixing blue and saffron, green; by mixing copper rust and saffron, violet color was obtained by mixing blue with red. According to Ibn Badis; popular colors were reddish yellow, reddish orange, mildew green, peanut green and buff color (Loveday, 2001c).

DISTORTIONS IN MANUSCRIPTS

The manuscripts, which have an important place to illuminate the past, are usually written in Arabic and are found in the archives of Islamic countries. Most Arabic manuscript collections of Islamic countries in order: Turkey, Iran, Egypt, Iraq, Saudi Arabia, Morocco, Syria, Tunisia, Yemen, Pakistan, Afghanistan and Algeria. Apart from these, there are many manuscripts in countries such as Russia, Azerbaijan, Turkmenistan, Uzbekistan, Kyrgyzstan, Kazakhstan, Tajikistan, China and India, which have been under Turkish rule for a long time. In addition, there are more manuscripts in many countries (Vural, and Irmak, 2013).

Apart from the destruction (degradation) in the works due to environmental and biological factors, there are also degradations caused by chemical factors. Here too, the structure of the paper, the type of ink and paint used, the chemicals used in gold and paint used in miniature or illumination accelerate the deterioration. The chemicals in the dyes react with oxygen or sulfur dioxide in the air to form acidity. With the increase in acidity, color darkening (blackening) and refractions occur on the pages. This reduces the durability of the works.

As for the destruction of the ink, very sooty and iron sulfide inks were used. Sooty inks do not damage the paper because they do not form acid. But because it dissolves easily in water, it disintegrates and disrupts writings. Another factor is that the lines drawn around the paintings that give the bright green color used in miniature and illumination, the amount of copper added to the composition of the gold used in the frames to decorate or clarify the writing. Over time, copper is oxidized to form acid and fractures occur in this part.

Destruction of Ink and Paper

Ink is a colloidal system in which very small pigment particles are dispersed in suspension in a solvent. The inks used for writing or printing are liquids in various colors. Inks used in manuscripts are mostly iron gall and carbon inks.

While papers using carbon or soot ink do not have deterioration problems, there are problems with papers using iron gal inks. These inks do not chemically bond with cellulosic fibers, but rather firmly adhere to the paper by mechanical bonding. The mechanical bonding here is the placement of the drying ink in the spaces between the fibers (URL2). Figure 1 shows the degradation caused by ink in a work written using iron gal ink.

Figure 1: *Example of degradation of iron gal ink (URL2)*

Deterioration of another example taken from the Museum of Islamic Art is shown in Figure 2. This work, found in the Museum of Islamic Art (Istanbul, Turkey), is an example of Damascus documents, which are accepted as the first copies of the Holy Quran and written in the early years of Islam and the first examples of Islamic book art. The sample shows deterioration caused by both iron throat ink and pigment.

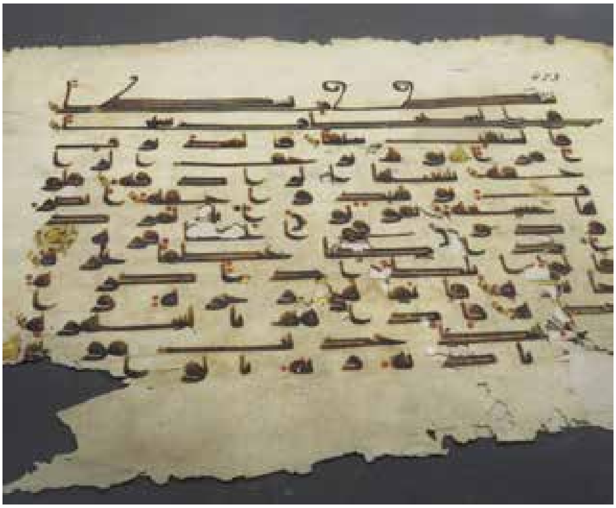

Figure 2: *Example of a distortion in a Damascus paper page from the Museum of Islamic Arts (Özden, 2019)*

Paints and Paper Destruction

After the provincial production of paper, in line with the demands and materials developed depending on the researches developed. While writing on paper, decorations have also developed. Later, calligraphers used gold and other metals in decorations and paintings. Illumination and miniature works were developed parallel to the line works. Illumination is referred to as manuscript books and decorations made with murakka paint and gold dust. Zehep (gold) is a word of Arabic origin and means gold. The term is called art of gilding and painting of handwritten works, plates and albums written with hüsn-i hat and tuğra. Red lead dust was used at the beginning of the manuscripts for ornamentation in miniature works. In addition, gilding is used in a way that does not tire the eye. Some of the metallic pigments used in decorations:

Azurit; is a greenish blue basic copper (II) carbonate pigment with a chemical formula of $2CuCO_3.Cu(OH)_2$. They were mostly used in Turkish and Armenian manuscripts in Iran and Byzantium (Orna, 2014).

Malachite green; It is a precious stone in contrast to the organic dye of the same name whose chemical formula is another copper compound $CuCO_3.2Cu(OH)_2$. While it is not found in Armenian and Byzantine manuscripts, it is found in other manuscripts.

Gypsum (Gypsum); Calcium sulfate is dehydrate ($CaSO_4\ 2H_2O$). Anhydrite is the anhydrous form of Calcium sulfate. Massicot is lead (II) oxide (PbO) in yellowish, red yellowish ortharombic form. The tetragonal form of PbO is called litharge.

The names, chemical formula and hundred years of use of some green pigments containing copper are shown in Table 1.

Table 1: *Names of some green pigments, chemical formulas and century of use (Banik, 2016)*

Pigment	Chemical Formula	Date of use
Verdigris (neutral)	$Cu(CH_3COO)_2\ H_2O$	16 th century
Malachite	$CuCO_3\ Cu(OH)_2$	15-16, 18 th century
Money-Atacamit	$Cu(OH)Cl\ Cu(OH)_2$ (Cu: 59,5% Cl: 16,7%)	11-15 th century
Copper-Chloride (unidentified)	Cu: 55% Cl: 15-16%	16 th century
Gerhardtit	$Cu(NO_3)OH\ Cu(OH)_2$	15-16 th century
Langit	$Cu_4(OH)_6SO_4\ H_2O$	16 th century
Pseudo-Malachite Chalconatronite	$Cu_5(PO_4)_2(OH)_4$	16 th century
Copper Pigment (decomposed)	9-15%	16 th century

Copper ions form historical pigments. Malachite and copper green cellulose containing copper pigments play a catalytic role in the oxidative degradation of cellulose causing the paper to become brittle. This degradation is called copper corrosion (Kocabay, 2012).

Figure 3 depicts the distortion caused by gold in manuscripts using metallic pigments, and Figure 4 shows optical microscope images of silver powders on paper.

Figure 3: *The first page of the Manuscript (Bayaz); disruption of imitation gold ingot (Mousavi et al., 2011)*

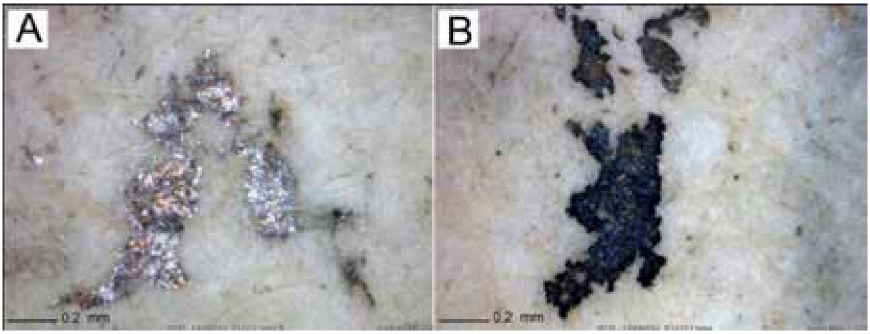

Figure 4: Optical microscope images of silver powders on paper: A: un tarnished particle; B: Blackened particle (Mousavi et al., 2011)

PROTECTION OF MANUSCRIPTS

The archives, libraries, museums and palaces are the places where the manuscripts that have survived to the present day are preserved and preserved. archives in Turkey, although there are much larger than in urban areas are densely located in Istanbul. It is the Süleymaniye Library with

67350 manuscripts, which contain the highest number of artifacts in the palaces, libraries, museums, universities, muftis and title deed cadastral spaces in İstanbul.

The first Islamic writing, Hz. It starts with Osman's copy of the Holy Quran and sending one copy to Medina and the other copies to Kufa, Basra and Damascus. These are the first manuscripts in Islam (Vural and Irmak, 2013). The manuscript shown in Figure 4 is the introduction page of Kansuh al-Ghuri to the Quran. 16 th century AD. Kansuh al-Ghuri, the world's largest Quran (Fig. 4), was repaired by CHICC Manchester in 2010 with financial support from TIMA (The Islamic Manuscript Association) (URL3).

Figure 4: *The Qur'an of Kansuh al-Ghuri, the world's largest Qur'an (URL4)*

Distortions that may occur due to inks or paints used in manuscripts can be controlled by pre-checks and by providing the conditions to protect these works. The major cause of chemical deterioration is the increased acidity of the paper. The degree of acidity as a result of all these factors is measured from the surface with the help of pH meter without damaging the artifacts. In order to protect their acidity, the artifacts are subjected to a deacidification washing system called deacidification. The aim is to react the acidic pages in an alkaline environment to create a neutral environment. In this way, the acidity of the treated frames are broken, burnt and blackened with thin Japanese paper on both sides are blocked by blocking. Figure 5 shows the repair of the damaged part of a damaged manuscript with Japanese paper.

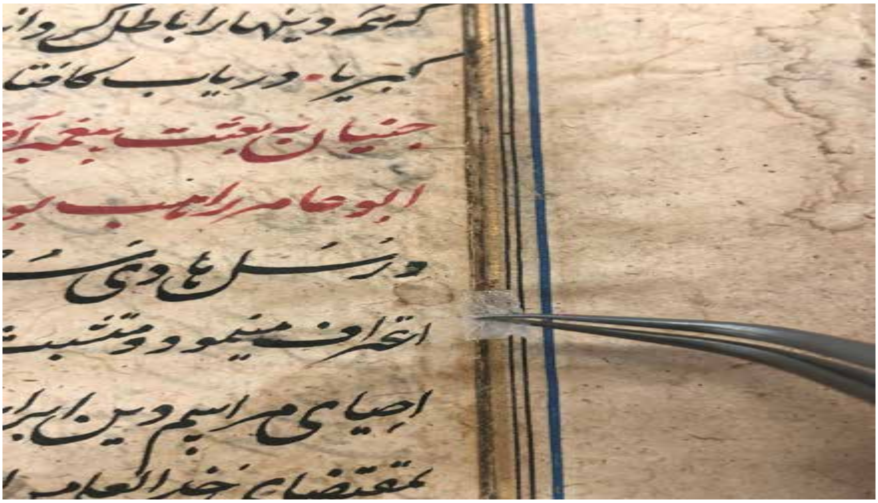

Figure 5: *Repair of a damaged work with Japanese paper (URL5)*

METALLIC PIGMENTS TODAY

More recently, until the last thirty years, the so-called acid paper is produced in the paper today, neutral or basic character papers are produced. The fact that the papers are basic increases their strength. Much more and varieties are used than inks and inks used in the past. Some inks used today also contain metallic pigments (Sönmez and Oğuz, 2017).

Such ink prints are used for some special papers that require increased visually. Metallic effect printing inks offer great possibilities for the design of a print job. It enables printers to create and produce great effects, especially in high-quality labels, brochures and packaging.

Gold effects are produced using pigments based on brass, copper and zinc alloys. They are meant to confuse people, and people wrongly talk about bronze, which is copper and tin alloys. The various nuances in the tones are the result of the ratio between the two components of the alloy. This example starts with 70 parts of copper and increases up to 100 parts of copper in a mixture of different shades of color. This mixture formed with zinc gives the golden color.

Alternatively, aluminum-based pigments may be used in combination with appropriate colored pigments together with the proportion of colored pigments which determine the actual color shade (reddish / yellowish) obtained. However, the metallic character of these variants is not as good as that obtained with the brass-based pigments mentioned above.

Metallic pigments are susceptible to corrosion. This type of corrosion causes the brass pigment to change its color tone, become a dirty brownish color and become dull during the process. This fact must be taken into consideration during printing. Therefore, the pH of the solution should not be less than 5.5 to achieve a perfect metallic effect (Huber, 2012).

Today, metallic ink pigments are increasing importance in the label and packaging industry and used in packaging and printing systems. The amount and type of metallic ink pigment present in the ink is important when using such inks. The pigment must be mixed well when preparing the ink. The binder contained in the ink must be suitable for curing. In addition, the base paper should have good absorbent properties. If the paper is too absorbent, the ink is absorbed very quickly, and if it is less absorbent, the absorption is very slow. In both cases, stains appear on the paper surface during printing (URL 5).

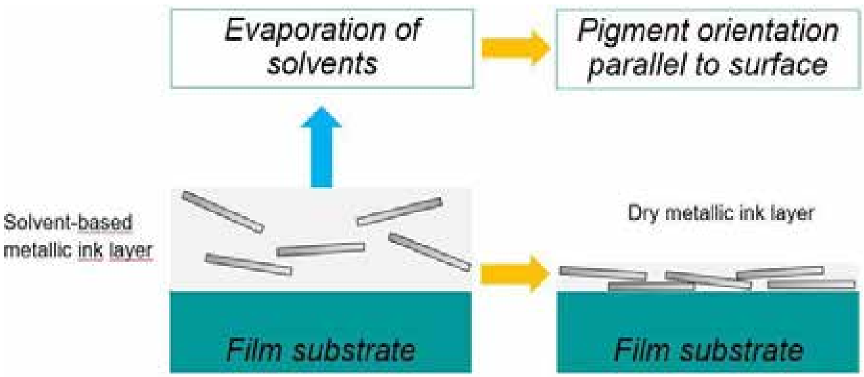

Figure 6: *Schematic drying mechanism of solvent-borne inks (URL5)*

If a solvent-based ink is applied to a smooth surface, the metallic ink should also be selected to suit this speed, as the solvent will evaporate rapidly, as shown in the figure below. The amount of binder must also be appropriate to retain the pigments in the medium.

When a small amount of binder is used, the aluminum pigment layer is very dense, resulting in high gloss, best hiding power and best color character.

Metallic pigments have been used for many years for screen printing, gravure, flexo, and offset processes.

Metallic pigments can be applied to all kinds of materials in screen printing and brightness can be achieved even with rough metals.

Gravure / flexo printing process has a high quality metallic effect. For offset printing, metallic pigments need to be very fine-grained. In this way, a good covering property is obtained.

Given the properties and effects of metallic pigments, it is not surprising that they are widely used in the graphic arts industry. They can be applied to almost any surface and can be used in all types of prints, making them very attractive for decorative and functional purposes (Tomić, et al., 2018).

CONCLUSION AND EVALUATION

Societies that cannot claim their past cannot build their future. It is not documents that we can get the best and definitive information about the past. Documents need to be preserved and protected for many years without deterioration or wear. Documents that can give us information are kept in state archives, libraries and museums under protection and maintenance.

It is easy to maintain and maintain if we know the materials on which the documents are written, the chemicals and interactions used for the text and figures written on it. If we recognize and identify the antiquities and the conditions and materials that have affected them, we also determine how we will behave in keeping the new artefacts so that they can be moved and read in the future.

It would be appropriate for the papers to be documented to be neutral in nature and to select non-distortion enhancers for the inks and dyes to be used in printing.

REFERENCES

Bajpai, P. (2015). Pulp and Paper Industry: Chemicals, Publishing Elsevier, ISBN: 978-0-12-803-408-8, USA, 141.

Banik, G. (2016). Pigments et Colorants, Green Cooper Pigments and their Alteration in Manuscripts or Works of Graphic Art, ISBN: 9782271090898, Paris, 89-102.

Casey, J. P. (1983). Pulp and Paper Chemistry and Chemical Technology, Third Edition, Volume IV, ISBN: 0-471-03175-5, eds. Michael H., Bruno and W., C., Walker., Printed by John Wiley&Sons, USA, New York 1983, 2239-2241.

Huber (2012). Technical Information, Conventional Offset Systems: Metallic Inks, Pearlescent Inks.

Kocabay, Ö. G. (2012). Yazma Eserlerde Kimyasal Bozulmalar ve Kimyasal Bozulmaların Durdurulması, Uzmanlık Tezi, T.C. Kültür ve Turizm Bakanlığı Kütüphaneler ve Yayımlar Genel Müdürlüğü, İstanbul, 80.

Loveday, H. (2001a). The Nature of Paper and its Productions, Chapter three, in Islamic Paper, A Study of the Ancient Craft ISBN 1-873132-03-4, Printed by PJ Print, UK., 29-30.

Loveday, H. (2001b). Protocol for Paper Classification, Chapter five, in Islamic Paper, A Study of the Ancient Craft, ISBN 1-873132-03-4, Printed by PJ Print, UK., 59-60.

Loveday, H. (2001c). Qualitative Characteristics of Islamic Paper, Chapter four, in Islamic Paper, A Study of the Ancient Craft, ISBN 1-873132-03-4, Printed by PJ Print, UK., 51-52.

McLaren, K. (1986). The Colour Science of Dyes and Pigments, Second Edition, ISBN: 0-85274-490-0, Published by Adam Hilger Ltd., Bristol/England, 55-57.

Mousavi, S. M., Mortazavi, M., Ahmadi, H., Karbasi, M. (2011). Identification of Imitation Gold and Silver as Metallic Pigments Used in the Illuminated Persian Manuscript by SEM-EDS and Optical Microscope, Article in Microscopy and Microanalysis, DOI: 10.1017/S1431927611009986, 1821-1823.

Orna, M. V. (2014). Artists' Pigments in Illuminated Medieval Manuscripts: Tracing Artistic Influences and Connections—A Review, Chapter 1, eds. Armitage, R. A. and Burton, H. J., ISBN: 9780841229242, Publishing American Chemical Society, USA, 11.

Özden, Ö. (2013). Medeniyet Hamuru; Kağıt ve Bir Eski Dönem Kağıthanemiz, Kağıthane-Yalakabad-, in Arşiv Kağıdı, eds. Vural, A. and Irmak, E. N., ISBN: 978-605-62350-2-3, Yalova Belediyesi 92-95.

Sönmez, S. and Oğuz, M. (2017). Investigation of Effect of Hot-Folio Printability of Mineral Pigments. Oxidation Communications, 40(2), 963-972.

Tomić, I., Pintier, I. and Dedijer, S. (2018). Pearlescent Pigments in Printing, Innovations in Publishing, Printing and Multimedia Technologies Conference, Kaunas, Lithuania

Wyatt, F. C., (1988). Flexographic Inks, Chapter 8, in The Printing Ink Manual, ed. R. H. Leach, ISBN: 978-94-011-7099-4, Published Van Nostrand Reinhold (International) Co. Ltd. and Molly Millars Lane, Wokingham, Berkshire, England, 473-474.

URL1:https://de.schlenk.com/fileadmin/editorsCMS/Medien/04_Aktuell/pdf/Mediacenter/Catalogue_Pigments_for_Printing_Inks.pdf (Accessed date: 18.09.2019)

URL1: http://blogs.bl.uk/untoldlives/2016/07/words-will-eat-themselves.html (Accessed date: 14.11.2019)

URL2: http://chiccmanchester.wordpress.com/(Accessed date: 17.09.2019)

URL3: https://gatewaytothekoran.wordpress.com/ (Accessed date: 18.09.2019)

URL4:https://standrewsrarebooks.wordpress.com/2018/09/07/reviving-art-the-process-of-conserving-a-manuscript/ (Accessed date: 18.09.2019)

URL5: https://www.eckart.net/press-events/eckart-blog/metallic-ink-pigment-guide.html (Accessed date: 15.11.2019)

MAGNETIC FIELD APPLICATORS FOR MAGNETIC HYPERTHERMIA APPLICATIONS

CHAPTER

22

Serhat KÜÇÜKDERMENCİ[1]

1 Balıkesir University Faculty of Engineering Department of Electrical and Electronics Engineering, kucukdermenci@balikesir.edu.tr

1. INTRODUCTION

Magnetic hyperthermia (MHT) is one of the newest techniques used in the fight against cancer. Unlike traditional treatments such as surgery, chemotherapy and radiotherapy, MHT has less side effects and is presented as a new alternative treatment against cancer (Hergt et al., 2008). In other words, temperature increase in the 42-45° C range causes cell damage in tumors without causing any damage to healthy tissues (Chiriac et al., 2015; Hervault et al., 2014). The heat required for temperature rise in MHT is produced by exposing the MNPs to the alternative magnetic field (AMF) (Habib et al., 2008).

In this method, biocompatible, targeted MNPs are injected directly into the tumor or into the blood stream. The magnetic energy applied to the MNPs from outside is converted into heat energy by induction. In areas of cancer cells, body tissues are exposed to temperatures of about 42-45 ° C. Cancer cells that are not resistant to thermal effects either lose their viability (thermo ablation) or become more susceptible to drug and radiation therapy. Healthy cells continue to function as they are more resistant to heat increase than cancer cells.It should be ensured that the externally applied magnetic field reaches the nanoparticles in the inner parts of the body and if possible, the magnetic field should focus on a specific area. At this stage, magnetic field generators can be classified according to different geometry and working principle. Based on the principles of magnetic field generation and shaping, magnetic field applicators can be generalized into 3 basic classes:

(a) Direct magnetic field applicators,

(b) Local magnetic field intensifiers,

(c) Magnetic field saturation applicators

2. DIRECT MAGNETIC FIELD APPLICATORS

Direct magnetic field applicators are based on the principle of supplying current to single or multiple coils. With this current, the magnetic field is induced in magnetic core or non-core coils.

In general, the 3 most common coil geometries in direct magnetic field applicators are as follows;

(a) Loop coils,

(b) Distributed plane coils,

(c) Solenoids.

Loop coils: They are the most simple geometry and are energized by current. Figure 2.1 (a) shows an example of a single cycle (Eggers & Ridihalgh 2009). As in Figure 2.1 (b), multiple loops can be used to improve the magnetic field in the target region (Tsuyama et al., 2009).

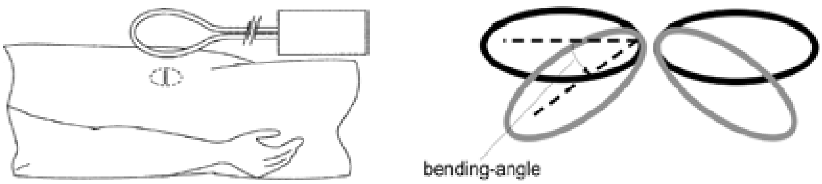

(a) (b)

Figure 2.1 *Direct magnetic field applicators (a) Single loop (Eggers & Ridihalgh, 2009) and (b) multiple loop (Tsuyama et al., 2009)*

Although structurally simple, the current loop shows limited magnetic field penetration (Huang et al., 2009). Because of this limitation, it can often be used in targets with limited depth, such as the human head region, or where the desired field strength is relatively low. Since the number of turns in this geometry is not sufficient to produce the appropriate magnetic field, this situation is tried to be closed with current. Therefore, the current given to the winding is high in the order of kA and is generally applied to the winding as a pulse (Talebinejad et al., 2011).

Distributed plane coils: It is popular in applications where a wide range of magnetic coupling is used (Bartusek and Geschiedtova 2005). However, since small distributed plane coils have shallow area penetration (Hanak et al., 2006), large distributed planar coils are required to provide deep penetration. Such geometry takes up quite a lot of space.

Solenoids: The first applications of solenoid in magnetic hyperthermia have been established by placing the target into the air core of a single solenoid. For example, in one embodiment (Storm et al., 1982), a loop is used to form the air core solenoid, as shown in Figure 2.2 (a).

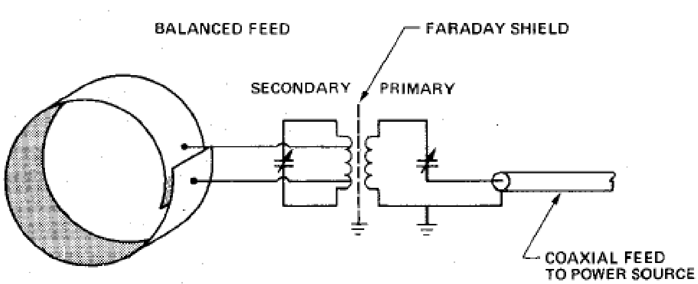

(a)

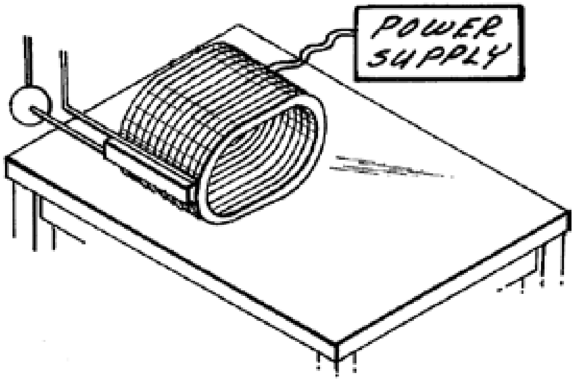

(b)

Figure 2.2 *(a) Single loop layer form (Storm et al., 1982) and (b) Single layer helix coil form (Rand 1991) solenoid magnetic field applicators*

Although this design is simple, the power loss is high as the current is concentrated on the surface due to the skin effect. To reduce this loss, the skin effect must be distributed over a larger conductive area. For this purpose, a helix-shaped coil wire is used. To cool the coil, copper pipes are used instead of wires, as shown in Figure 2.2 (b) (Rand, 1991). Cooling fluid is passed through the hollow copper pipe and unwanted heat is removed from the environment.

Placing the target zone in the air gap imposes practical restrictions on the type and size of the target. To overcome this problem, the target may be located outside the winding cavity, ie just outside the solenoid, as shown in Figure 2.3 (Sievert et al., 1993).

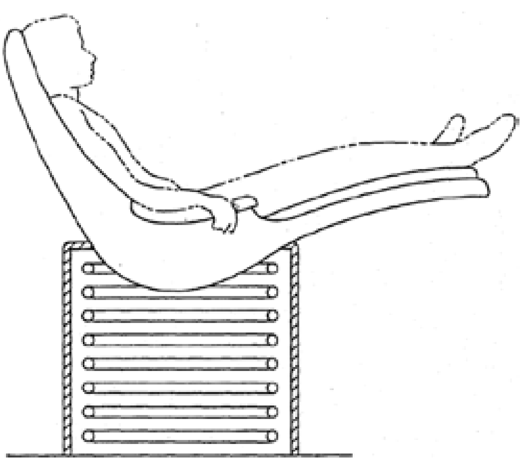

Figure 2.3 *Solenoid applicators outside the winding cavity using a single coil (Sievert et al., 1993).*

If the target is located outside the solenoid, it may be considered to use a ferromagnetic core instead of the air core to increase the magnetic field strength on the target.

The most commonly used core geometries in direct magnetic field applicators are as follows;

(a) Non-circular core,

(b) Convex, concave pole,

(c) Air-gapped core.

Non-circular core: By changing the cross-sectional geometry of the core, the magnetic field can be directed or focused in specific directions. For example, Kong (2009) showed that the focusing effect on elliptical and triangular core is beneficial in hyperthermia applications. However, no penetration effect has been demonstrated in this study.

Convex, concave pole: When the core gains a concave or convex structure in its magnetic poles, the magnetic force lines may divergent or converge around the pole. As shown in Figure 2.4 (a), Siemens' magnetic targeting applicator (Zechbauer, 2007) used the conical pole to form the field focus or the field gradient. However, it is clear from the proximity of the pole to the target that the magnetic field penetration is limited.

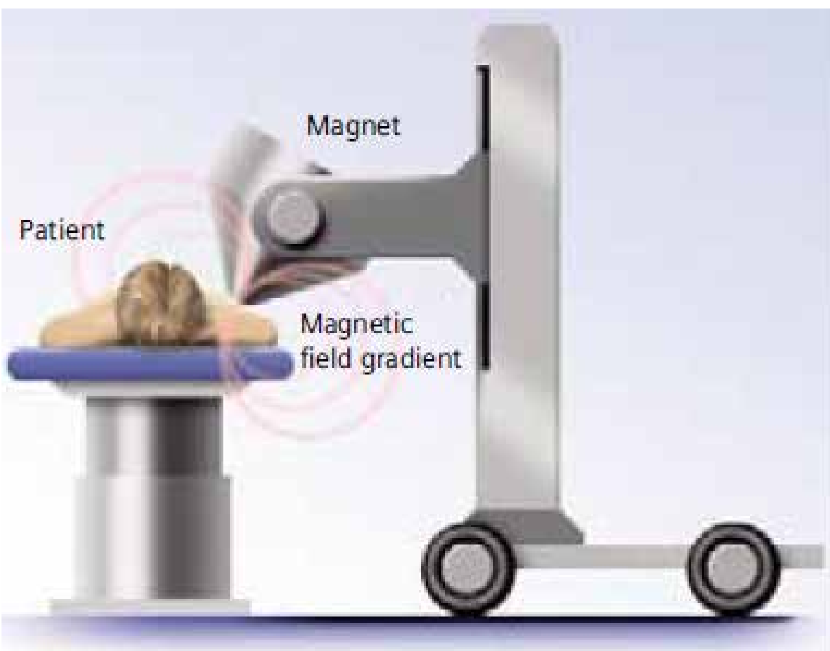

(a)

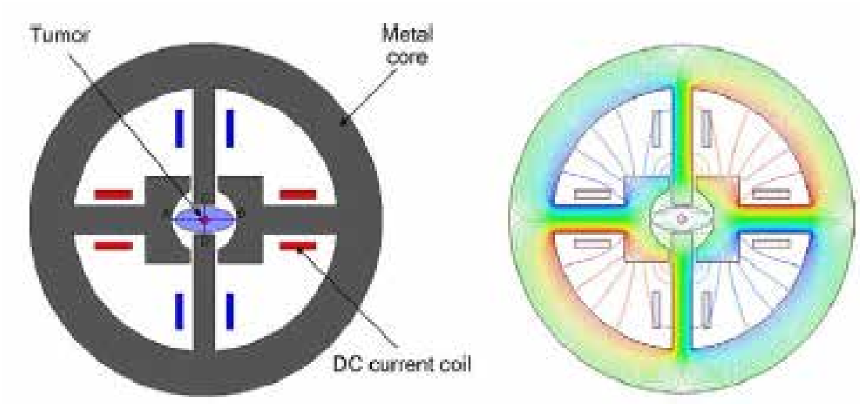

(b)

Figure 2.4 *Core(a) bent outward from the poles to intensify the magnetic field at the target (Zechbauer, 2007); and (b) to form a magnetic free field around the target that is bent inward from the poles (Ho et al., 2012a).*

Air-gapped core: One of the most widely used magnetic field applicator configurations for magnetic hyperthermia is the air gap core (Mornet et al., 2004). To ensure magnetic field penetration, the target is placed in the air gap between zone 2 opposite magnetic pole. The magnetic field in the poles may be induced by (a) ferromagnetic material induced by a single coil or (b) by different coils specific to each pole.

As shown in Figure 2.5 (a), the ferromagnetic material can also be energized with a single coil (Xu et al., 2009). Alternatively, the coil can be positioned away from both poles as shown in Figure 2.5 (b) (Handy et al., 2006). Placing the coil away from the poles protects the target against heat and electrical hazards. On the other hand, having a coil at one pole is useful when asymmetric field penetration is desired.

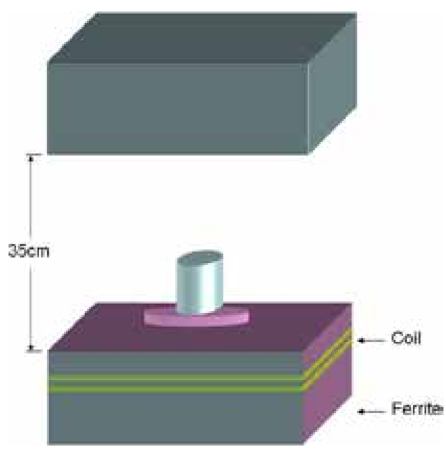

(a)

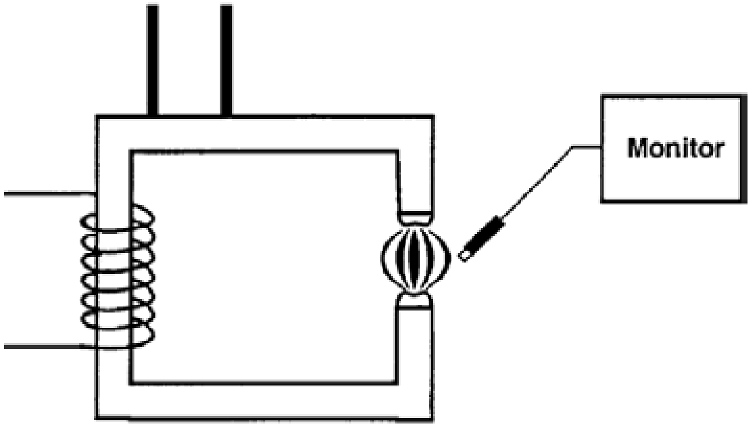

(b)

Figure 2.5 *Single coil air gap magnetic field applicators (a) coil at pole (Xu et al., 2009) and (b) coil away from the poles (Handy et al., 2006).*

For dual coil excitation, the coils are mounted on both poles facing the target area. As shown in Figure 2.6, there are also magnetic field applicators having more than one coil pair (Huang et al., 2010, Gray & Jones 2000, Ho et al., 2012a).

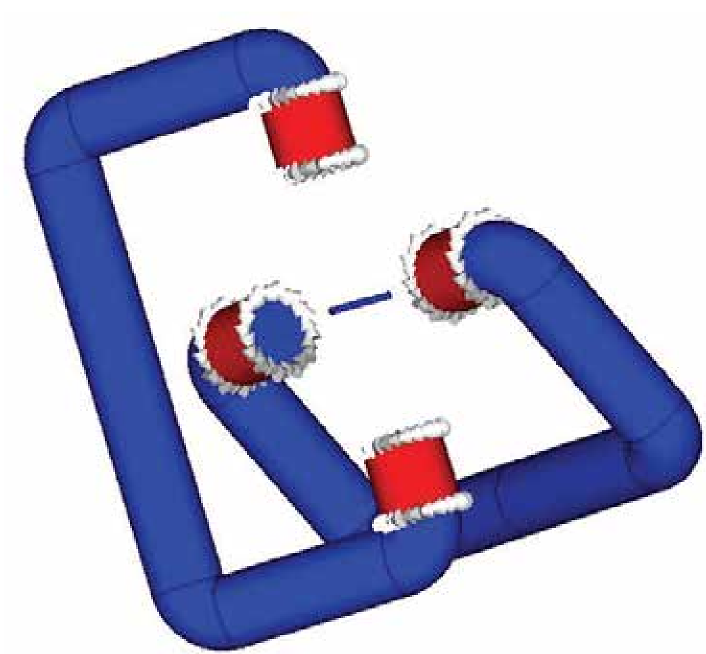

(a)

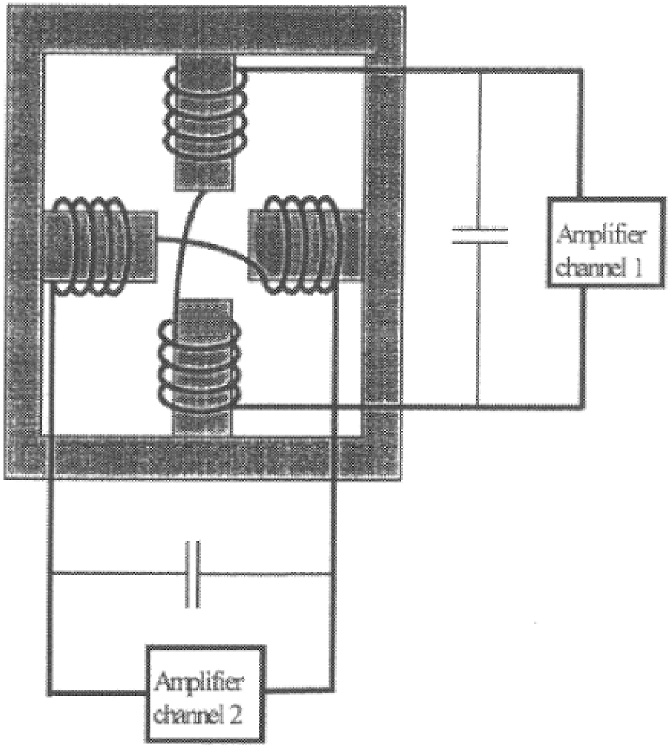
Amplifier channel 1
Amplifier channel 2

(b)

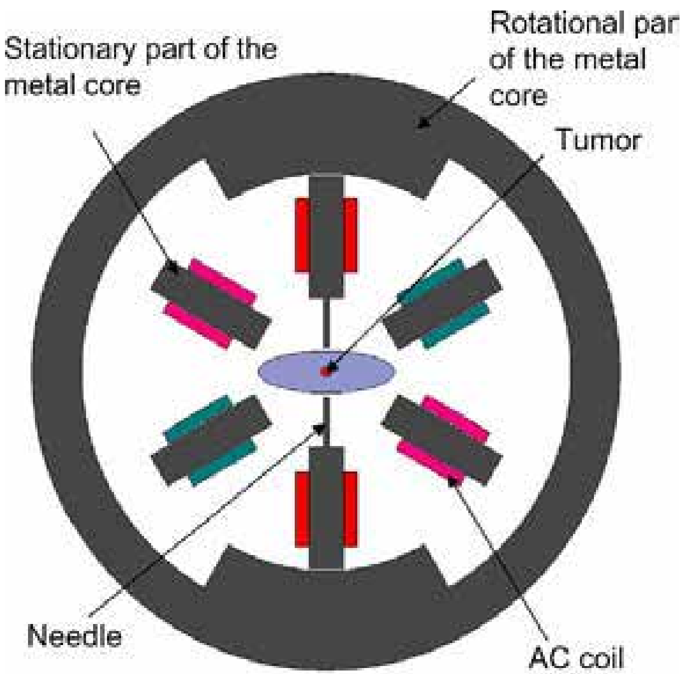
Stationary part of the metal core
Rotational par of the metal core
Tumor
Needle
AC coil

(c)

Figure 2.6 Magnetic field applicators comprising more than one coil pairs (a) energized by synchronous current sources (Huang et al., 2010), (b) current sources mutually placed (Gray & Jones, 2000) and (c) circularly placed (Ho et al. 2012A)

3. Local magnetic field intensifiers

The magnetic field acting on the ferromagnetic material can affect the magnetic dipoles to produce a net magnetic field and then amplifies the surrounding magnetic field. Therefore, by placing the ferromagnetic material near the target region, the magnetic field can be condensed in specific regions as shown in Figure 2.7 (Feucht et al., 2011).

By selecting the appropriate sized ferromagnetic concentrator, the area exposed to the high magnetic field can be limited. However, due to its short-range effect, this method does not work if the target and the ferromagnetic concentrator are placed at too much intervals from each other.

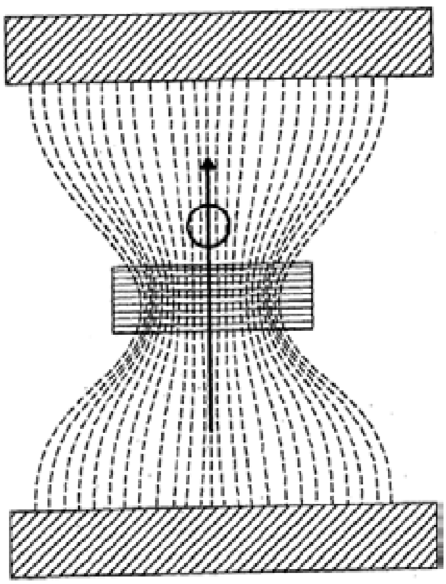

Figure 2.7 *Local magnetic field intensifiers (Feucht et al., 2011)*

4. Magnetic field saturation applicators

When a magnetic material is exposed to the AC magnetic field, it converts the magnetic energy to heat energy with hysteresis hysteresi losses and superparamagnetic losses. The heating effect is reduced as this material becomes saturated when exposed to a stronger static magnetic field at the same time. Thus, in the presence of an AC magnetic field, a strong static magnetic field may be superposed in certain regions of the working area where heating is not desired. By modulating the excitation current of 3 pairs of coils positioned perpendicular to each other, these regions can be created as shown in Figure 4.1 (a) (Gleich, 2008). In another embodiment shown in Figure 2.12 (b), 6 pairs of coils are arranged in a circular ring to produce the same effect (Ho et al., 2012b).

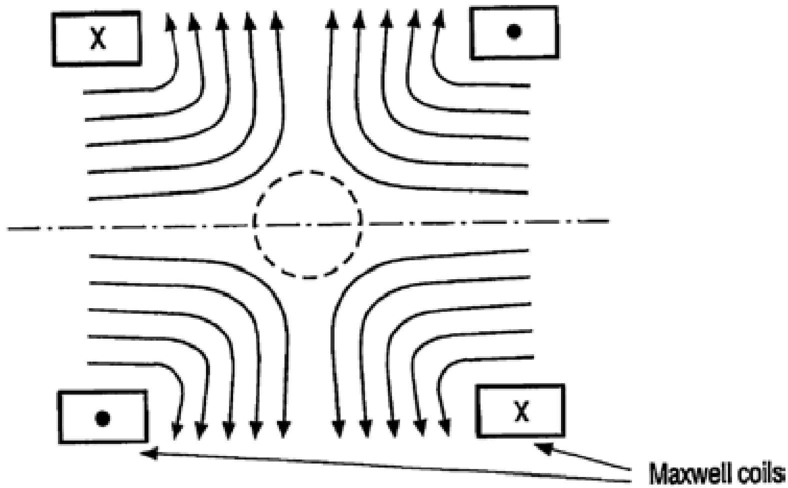

(a)

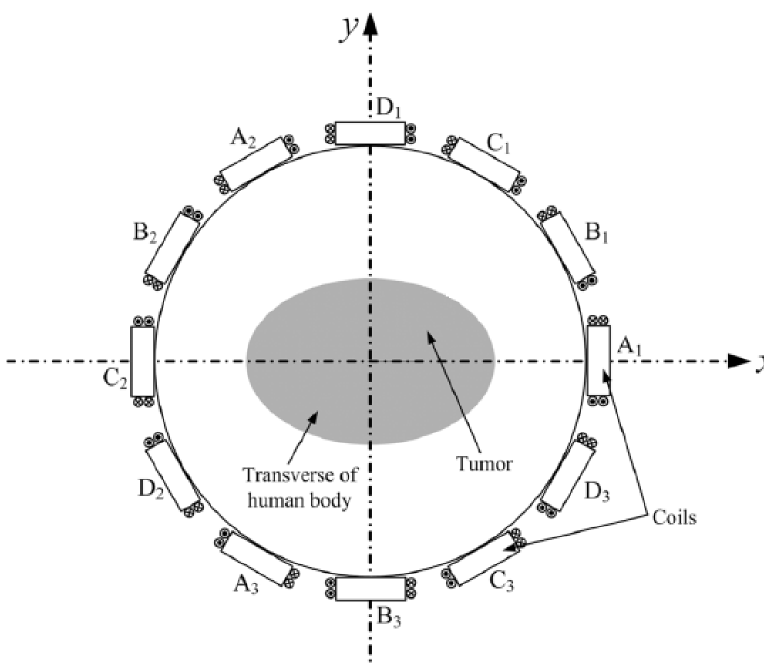

(b)

Figure 4.1 *Coils (a) at right angles (Gleich, 2008) and (b) in the form of a circular magnetic saturation applicators (Ho et al., 2012b).*

5. Customization of Magnetic Field Applicators for MHT Tests

Ability of AMF generators to produce frequency and amplitude, as well as the geometry of the generator stands out as an important feature in MHT tests. In general, air core and ferrite core inductors are used in MHT systems. Miniature versions of ferrite core systems are suitable for in vitro MHT tests with cell culture. Solenoids from air core systems are ideal for magnetic liquid tubes and small volume animals. Helmholtz coils and ferrite core large spaced inductors may be considered for applying MHT to larger volume areas of the human body.

5.1 Ferrite toroid core air cavity miniature structuresfor in vitro cell culture or MHT tests with magnetic fluids

Such toroidal structures have a small air gap. The soft core forming the toroid is magnetized with a current-carrying wire. In a sample study with in vitro cell culture (Connord et al., 2015), a miniature version of ferrite core design is presented (see Figure 5.1 (a)). MHT effects in cells were observed using confocal microscopy and 370 μm air-gapped ferrite core.

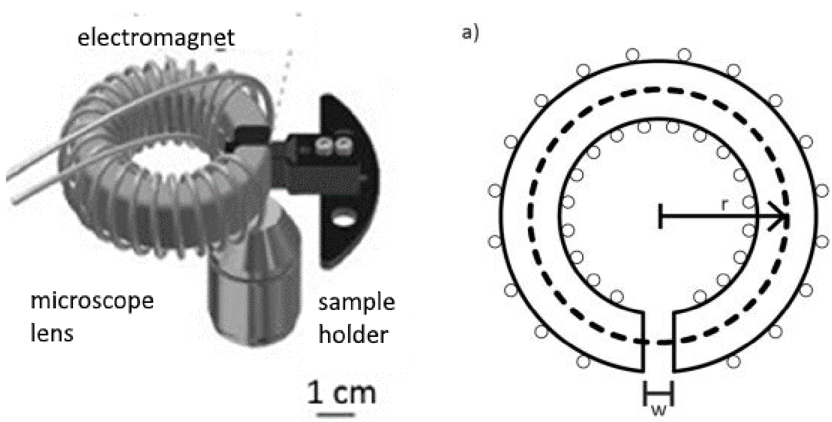

(a) (b)

Figure 5.1 *Ferrite core design (a) a miniature version (b) air-gapped toroid geometry*

The width of the cavity in the toroid constituting this structure is w, the number of windings of the wire carrying current I is N. The radius of the ampere path carrying the magnetic flux is expressed by r (see Figure 5.1 (b)). Magnetic field to be formed in the toroid cavity is expressed by Ampere's law shown in Eq. (1).

$$\oint \vec{H} \cdot d\vec{l} \approx H_g w + H_c (2\pi r - w) \quad (1)$$

Here, H_g is the magnitude of the magnetic field in the cavity and in the H_c is the magnitude of the magnetic field in the core. H_g and H_c are both considered tangential and vary only by r.

A is the cross-sectional area of the core flux conservation expression and can be expressed as in Eq. (2) and Eq. (3);

$$B_g A \approx B_c A \quad (2)$$

$$A\mu_0 H_g = \mu_c H_c \quad (3)$$

Here, μ_0 and μ_c are the permeability of cavity and core, respectively; B_g and B_c are the magnetic flux density of the cavity and core, respectively. These are can be expressed in eq. (4).

$$\frac{\mu_0}{\mu_c} H_g = \frac{1}{\mu_r} H_g = H_c \quad (4)$$

Here, the relative permeability is expressed as $\mu_r \equiv \mu_c/\mu_0$. Eq. (4) is substituted in Eq. (1) H_g can be express as in Eq. (5).

$$H_g = \frac{NI}{w\left[1 + \frac{1}{\mu_r}\left(\frac{2\pi r}{w} - 1\right)\right]} \approx \frac{NI}{w} \quad (5)$$

5.2 Air-core solenoid structures for MHT testing with magnetic fluid tubes or small animals

The use of MNPs in MHT was first attempted in 1957 (Gilchrist, 1957). Following this study, various groups investigated important operational parameters to effectively manage the use of MHT in cancer treatment (Gordon et al., 1979; Jordan et al., 1993; Atkinson et al., 2007). The air-core solenoid structures are suitable for the geometry of magnetic fluid tubes or small animals and can be used in MHT tests (see Figure 5.2).

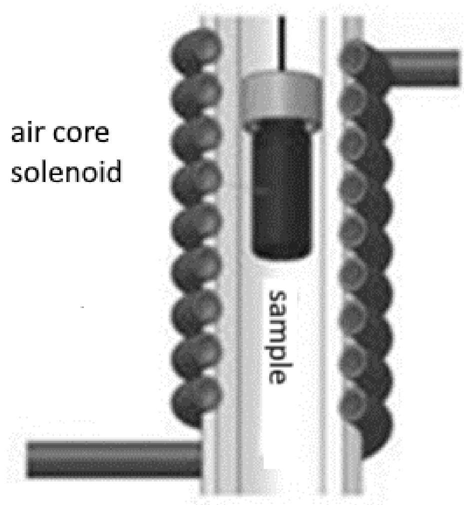

Figure 5.2 *Use of air core solenoid with magnetic nano-liquid test tubes*

İki katmanlı solenoidle sunulan bir çalışmada (Skumiel vd., 2016) solenoidin yapımı için kullanılan bakır tel kesiti 2.5 mm^2, kablonun yalıtımı ile birlikte dış çapı Δl = 3.6 mm, birinci ve ikinci katmandaki dönüş sayısı sırasıyla $n_1 = 47$ ve $n_2 = 45$, sarım katmanları çapı sırasıyla $D_1 = 44$ ve $D_2 =$ 51.5 mm'dir. Solenoid katmanların uzunlukları sırasıyla $l_1 = 170$ mm ve l_2 = 163 mm ve solenoidin indüktansı L = 93.5 µH'dir. Güç yükselteci ile 300 W'lık güç uygulandığında sağlanan akım genliği I_{max} = 15 A ve elde edilen manyetomotiv kuvvet (MMF) 1380 Amper-sarımdır. Solenoid içerisindeki manyetik alanın genliğini hesaplamak için Biot-Savart yasasından yararlanılmıştır (Huang vd., 2012). Bu yasaya göre, yarıçapın tek bir döngüsü boyunca akan akım I, eksende x noktasında H_x (bkz. Şekil 5.3) alanını üretir (bkz. Denk. (6)).

In a study presented with a two-layer solenoid (Skumiel et al., 2016), the copper wire cross-section used for the construction of the solenoid was 2.5 mm^2, with the insulation of the cable, the outer diameter Δl = 3.6 mm, the number of turns in the first and second layers $n_1 = 47$ and $n_2 = 45$, respectively. The diameter of the layers is respectively $D_1 = 44$ and $D_2 =$ 51.5 mm. The lengths of the solenoid layers are $l_1 = 170$ mm and $l_2 = 163$ mm respectively and the inductance of the solenoid is L = 93.5 µH. The current amplitude I_{max} = 15 A and the resulting magnetomotiv force (MMF) when the 300 W power is applied with the power amplifier is 1380 Ampere-winding. Biot-Savart law was used to calculate the amplitude of the magnetic field in the solenoid (Huang et al., 2012). According to this law, the flow I flowing through a single cycle of radius generates the area H_x (see Figure 5.3) at the point x on the axis (see Equation (6)).

$$H_X = \frac{I}{2r}\sin^3(\beta) \tag{6}$$

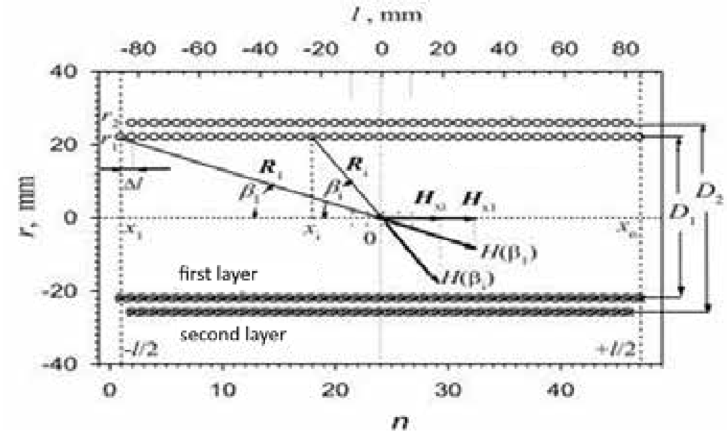

Figure 5.3 *Two-layered solenoid structure*

Where β is the angle between the winding point and the center, R is the distance vector between these points and layer diameters D_1, D_2. The magnetic field-distance graph generated under these conditions is given in Figure 5.4. According to the graph, the total amplitude of the magnetic field strength caused by the layers in the inductor center is $H_o \cong 7901\ Am^{-1}$. As you move away from the center, the field strength is damped. The usable space inside the solenoid is large enough for magnetic liquid tubes or small animals. In addition, the target sample should be placed in the inductor center in order to make maximum use of the magnetic field.

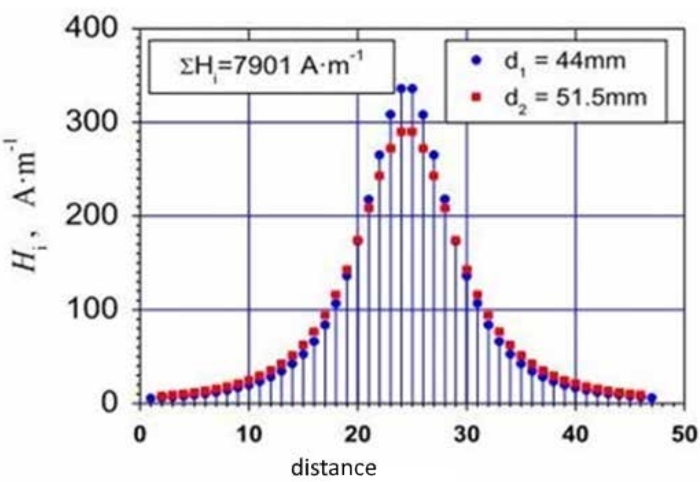

Figure 5.4 *Amplitude components of the magnetic field for a double-layer solenoid*

5.3 Helmholtz coil structures for MHT testing with large animals or human body parts

In an exemplary study with laboratory animals (Dürr et al., 2013), an AMF generator and a parallel LC circuit powered by a power amplifier were designed. In the established system, the guinea pig is placed between two flat inductors with variable distance (40-100 mm), maximum AMF density of 6.76 kAm^{-1} (~ 85 Oe) and a frequency of 200 kHz. Another example of such parallel structure inductors is Helmholtz coils. Helmholtz coils are the name given to two identical windings in series. The magnetic fields produced by the two inductors are directed in the same direction and support each other (Natividad et al., 2008). In Helmholtz coils shown in Figure 5.5, the homogeneity of the magnetic field is obtained provided that the distance from the center is *1 = r*. Where l is the distance between the windings and r is the radius of the windings.

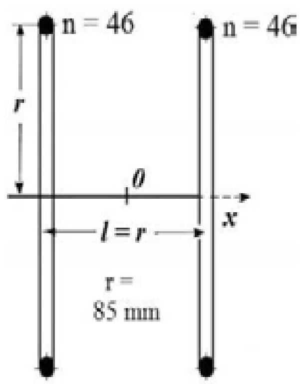

Figure 5.5 *Helmholtz coil structure*

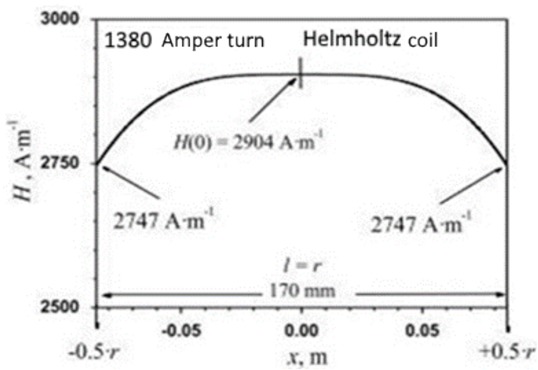

Figure 5.6 *Magnetic field distribution in Helmholtz coil*

Distribution of the magnetic field density along the x-axis of the two inductors is indicated by Eq. (7).

$$H(x) = \frac{n \cdot I}{2} \cdot r^2 \left[(r^2 + (0.5 \cdot r + x)^2)^{-3/2} + (r^2 + (0.5 \cdot r - x)^2)^{-3/2} \right] \tag{7}$$

In a study (Skumiel et al., 2016), the distance and magnetic field strength graph is shown in Figure 5.6. In this system, where the winding number is 46, the winding radius and the distance between the windings is 85 mm, the magnetic field strength in the center is 2904 Am^{-1}. In order to make maximum use of the magnetic field, the sample should be placed in the inductor center as in the solenoid sample. As we move away from the center, the field strength is seen to be damped. High currents may have to be passed through the windings to reach a certain magnetic field value. This is a problem for system stability in Helmholtz coils.

5.4 Large ferrite core air gapped structures for MHT testing with magnetic fluid tubes, animals or large parts of the human body

The first AMF applicator prototype for full- human body was made by Jordan et al., (2004).The device uses a ferromagnetic core to concentrate the magnetic field lines and produce a homogeneous AMF density in the cavity. It can operate at an AMF frequency of 100 kHz and magnetic field strength values ranging from 2.5 to 18 kAm^{-1} (32 to 226 Oe). The disadvantage of this device is its weight, cumbersome structure and lack of portable features. As an alternative to this structure, more flexible design devices with air space with ferrite core can be provided.

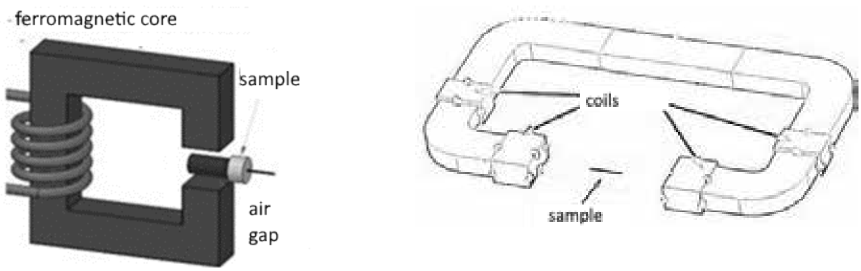

(a) (b)

Figure 7 *(a) Use of ferromagnetic cores for test tubes (b) adjustable ferromagnetic core with larger working volume*

The geometry of the large ferrite core structures can be arranged for magnetic fluid tubes as in Figure 7 (a) or for animals or larger human body parts as in Figure 7 (b). In these systems, the magnetic field depends on the number turnsi current and the width of the air gap. Soft magnetic ferrite materials can be used to easily produce magnetic field density to relatively high values (Glöckl et al., 2006; Lacroix et al., 2008; Skumiel et al., 2013; Perigo et al., 2015). Such a magnetic circuit is shown in Figure 8 (Skumiel et al., 2016). In this example, the inductance of the inductor n = 12 turns wound on the ferrite core is 100 μH. MMF = n · I, which forms the magnetic flux φ flowing through the ferrite elements and over the air gap l_g. According to these values, MMF = 180 Amper turn for I = 15A and n = 12. Magnetic flux flowing from the core can be found by magnetic circuit analysis in Eq. (8);

$$\phi = \frac{I \cdot n}{R_{Fe} + R_g} \tag{8}$$

Here, R_{Fe} and R_g are magnetic reluctances of ferrite and air gap respectively. These reluctances are defined Eq. (9) and Eq. (10).

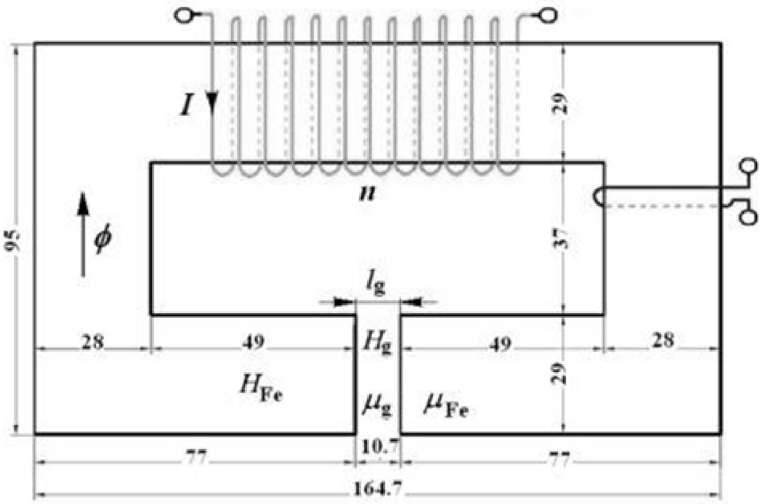

Figure 8 *Magnetic circuit with ferrite core*

$$R_{Fe} = \frac{l_{Fe}}{\mu_0 \cdot \mu_{Fe} \cdot S} \tag{9}$$

$$R_g = \frac{l_g}{\mu_0 \cdot \mu_g \cdot S} \tag{10}$$

Here, *l* is the path taken by the magnetic flux and *S* is the cross-sectional area through which the flux passes. In the sample, permeabilites are taken as $\mu_{Fe} \cong 2000$ and $\mu_g \cong 1$ These expressions refer to the relative magnetic permeability of ferrite material and air. $l_{Fe} = 0.326$ m and $l_g = 0.0107$ m are the magnetic flux path lengths in the ferrite and air space, respectively. $S_{Fe} = 17.9 \cdot 10^{-4}$ m^2 indicates the cross-sectional area through which the magnetic flux given in the sample passes. $R_{Fe} = 72.5$ kAV^{-1} s^{-1} and $R_g = 4756.3$ kAV^{-1} s^{-1} magnetic reluctance values are obtained by using Eq. (9) and Eq. (10). Magnetic flux flowing through ferrite elements and air gap is $\varphi = 37.27$ µVs calculated by Eq. (8). Therefore, the value of magnetic induction is $B = \varphi \cdot S_{Fe}^{-1} = 20.82$ mT. Thus, the magnitude of the magnetic field in the air gap is $H_g = B \cdot \mu_0^{-1} = 16.57$ kA·m^{-1}. By this example, it can be seen that a ferromagnetic core inductor can achieve a significantly higher magnetic field density than air core inductors.

6. CONCLUSION

The MHT test types and the test devices with the appropriate working volume are presented in Table 1 collectively. Many different experimental setups can be established according to the requirements of magnetic field frequency, amplitude and working area volume. Inductors capable of delivering high intensity and homogeneity magnetic field to the sample according to the MHT test type should be combined with appropriate drive circuits.

Table 1. *MHT test types and test devices with suitable working volume*

Target sample to be subjected to MHT test	**Possible test devices with suitable working volume for the test**
In vitro cell culture or magnetic fluids	Miniature structures with ferrite toroid core air gaps
Magnetic liquid tubes or small animals	Air core solenoid structures
Large animals or human body parts	Helmholtz coil structures
Magnetic fluid tubes, animals or large parts of the human body	Large ferrite core air gapped structures

7. ACKNOWLEDGMENTS

This study was supported by the Scientific and Technical Research Council of Turkey (TUBITAK), Project Number: E-EEEAG-215E107 and Balıkesir University Scientific Research Projects Unit (BAP) Project No: 2018/026 and Project No: 2018/126.

8. REFERENCES

Atkinson W. J., Brezovich I. A., and Chakraborty D. P., (2007). Biomedical Engineering, IEEE Transactions on, (1), p. 70-75.

Bartusek, K. & Gescheidtova, E. (2005). Mapping the Induction of Magnetic Field Around an Applicator for Dermato Magnetotherapy, Using Magnetic Resonance Method. Measurement Science Review, vol. 5(2), pp. 62-66.

Chiriac, H., Petreus, T., Carasevici, E., Labusca, L., Herea, D.D., Danceanu, C., Lupu N., (2015). In vitro cytotoxicity of fe–cr–nb–b magnetic nanoparticles under high frequency electromagnetic field, J. Magn. Magn. Mater. 380 13–19.

Connord, V., Clerc, P., Hallali, N., El Hajj Diab D., Fourmy, D., Gigoux V., and Carrey J., (2015). Small 11, 2437.

Eggers, P.E. & Ridihalgh, J.L. (2009). System Method and Apparatus For Localised Heating of Tissue. US Patent US7,567,843 B2.

Feucht, P., Bruss, V. & Jordan, A. (2011). Alternating Magnetic Field Application Device for Heating Magnetic or Magnetisable Substances in Biological Tissue. US Patent 2011/0160515 A1.

Gilchrist R. K., Medal, R., Shorey, W. D., Hanselman, R. C., Parrot, J. C., and Taylor C. B., (1957). J. Ann. Surg. 146, 596.

Gleich, B. (2008). Arrangement for Influencing Magnetic Particles. US Patent 7,351,194 B2.

Glöckl G., Hergt R., Zeisberger M., Dutz S., Nagel S., Weitschies W., J., (2006). Phys.: Condens. Matter 18, S2935–S2949.

Gordon, R.T., Hines, J.R., Gordon, D., (1979). Med. Hypotheses 5, 83–102.

Gray, B.N., Jones, S.K. (2000). Targeted Hysteresis Hyperthermia as a Method for Treating Tissue. US Patent US6,149,576.

Habib, A.H., Ondeck, C.L., Chaudhary, P., Bockstaller, M.R., McHenry, M.E., (2008). Evaluation of iron-cobalt/ferrite core-shell nanoparticles for cancer thermotherapy. J. Appl. Phys. 103, 07A307.

Hanak, P., Vrba, K. & Koton, J. (2006), Method of Magnetic Field Generation for Use in Dermal Magnetotherapy. Proceedings of the International Conference on Networking, International Conference on Systems and International Conference on Mobile Communication and Learning Technologies (ICNICONSMCL 2006), Apr 2006, pp. 193-97.

Handy, E.S., Ivkov, R., Ellis-Busby, D., Foreman & A., Braunhut. (2006). Thermotherapy via Targeted Delivery of Nanoscale Magnetic Particles. US Patent US7,074,175 B2.

Hergt, R., Dutz, S., Roder, M., (2008). Effects of size distribution on hysteresis losses of magnetic nanoparticles for hyperthermia, J. Phys. Condens. Matter 20 (38) 385214.

Hervault, A., Thanh, N.T.K., (2014). Magnetic nanoparticle-based therapeutic agents for thermo-chemotherapy treatment of cancer. J. Nanoscale 6, 11553-11573.

Ho, S.L., Jian, L., Gong, W. & Fu, W.N. (2012b). Design and Analysis of a Novel Targeted Magnetic Fluid Hyperthermia System for Tumor Treatment. IEEE Trans. on Magnetics, vol. 48(11), pp. 3262-65.

Ho, S.L., Niu, S. & Fu, W.N. (2012a) Design and Analysis of Novel Focused Hyperthermia Devices. IEEE Trans. on Magnetics, vol. 48(11), pp. 3254-57.

Huang, C., Lin, X., Yang, Y. (2009). Application of Magnetic Circuit and Multiple-coils Array in Induction Heating for Improving Localized Hyperthermia. World Academy of Science, Engineering and Technology, vol 58, pp. 724-27.

Huang, C., Lin, X., Yang, Y. (2009). Application of Magnetic Circuit and Multiple-coils Array in Induction Heating for Improving Localized Hyperthermia. World Academy of Science, Engineering and Technology, vol 58, pp. 724-27.

Huang, S., Wang, S.Y., Gupta, A., Borca-Tasciuc, D.A., Salon, S.J., (2012). On the measurement technique for specific absorption rate of nanoparticles in an alternating electromagnetic field, Meas. Sci. Technol. 23, 035701.

Jordan A., Gneveckow, U., Scholz, R., Bruss, V., Waldofner, N., Ricke, J., Feussner A., Hildebrandt, B., Rau B., and Wust, P., (2004). Med. Phys. 31, 1444.

Jordan, A., Wust, P., Fahling, H., John, W., Hinz, A., Feliz, R., (1993). Int. J. Hyperth. 9, 51–68.

Kong, W.B. (2009). The Design of Magnetic Nanoparticle Induction Heating Coil and Simulation of the Magnetic Effect of Focusing. MSc Thesis, National Cheng Kung University, Taiwan. URL: http://etdncku.lib.ncku.edu.tw/ETDdb/ETD-search/view_etd?URN=etd-0728109-112545

Lacroix, L.-M., Carrey, J., and Respaud, M., (2008). Rev. Sci. Instrum. 79, 093909.

Mornet, S., Vasseur, S., Grasset, F., Duguet, E. (2004). Magnetic Nanoparticle Design for Medical Diagnosis and Therapy. Journal of Materials Chemistry, vol 14, 2004, pp. 2161-75.

Perigo, E.A., Hemery, G., Sandre, O., Ortega, D., Garaio, E., Plazaola, F., (2015). Appl. Phys. Rev. 2, 041302.

Rand, R.W., Snow, H.D., Elliott, D.G. & Haskins, G.M. (1983). Induction Heating Apparatus for Use in Causing Necrosis in Neoplasm. US Patent 4,392,040.

Sievert, C., Tucker, R.D. & Loening, S. (1993). Local Application Tumor Treatment Apparatus. US Patent US5,197,940.

Skumiel A., Kaczmarek-Klinowska M., Timko M., Molcan M., Rajnak M., (2013). Int. J. Thermophys. 34, Issue: 4, 655–666.

Skumiel, A., Leszczyński, B., Molcan M., Timko M., (2016). Journal of Magnetism and Magnetic Materials 420 177–184.

Storm, F.K., Elliott, R.S., Harrison, W.H. & Morton, D.L. (1982). Clinical RF Hyperthermia by Magnetic-Loop Induction: A New Approach to Human Cancer Therapy. IEEE Trans. on Microwave Theory and Techniques, vol 30(8), Aug 1982, pp. 1149-58.

Talebinejad, M., Musallam, S. & Marble, A.E. (2011). A Transcranial Magnetic Stimulation Coil Using Rectangular Braided Litz Wire. IEEE International Workshop on Medical Measurements and Applications Proceedings (MeMeA 2011), May 2011, pp. 280-83.

Tsuyama, T. Katayama, Y., Hyodo, A., Hayami, T., Ueno, S. & Iramina, K. (2009). Effects of Coil Parameters on the Stimulated Area by Transcranial Magnetic Stimulation. IEEE Trans. on Magnetics, vol 45(10), Oct 2009, pp. 4845-48.

Xu, R. Yu, H., Zhang, Y., Ma, M., Chen, Z., Wang, C., Teng, G., Ma, J., Sun, Z. & Gu, N. (2009). Three-dimensional Model for Determining Inhomogeneous Thermal Dosage in a Liver Tumor During Arterial Embolization Hyperthermia Incorporating Magnetic Nanoparticles. IEEE Trans. on Magnetics., vol. 45(8), Aug 2009, pp. 3085-91.

Zechbauer, U. (2007). Zeroing in on Cancer. Picture of the Future, Spring 2007, pp. 62-65. Siemens AG.

SOME COMFORT PROPERTIES OF TERRY KNITTED FABRICS MADE FROM COTTON/POLYESTER BLEND

CHAPTER

23

Sena CİMİLLİ DURU[1]
Cevza CANDAN[2]

[1] Istanbul Technical University, Textile Technology and Design Faculty
[2] Istanbul Technical University, Textile Technology and Design Faculty

1. INTRODUCTION

Comfort is an important determinant of consumer satisfaction with clothing. It is a subjective response resulting from complex interactions of environmental conditions, fabric properties, garment fit, physiological factors, and the psychological state of the wearer [1]. Slater defined comfort as a state of balance between a person and their environment. Comfort involves both thermophysiological parameters [2]. Fabrics ensure both thermal and sensorial comfort of the people by providing a barrier between the skin and environment. Presence of moisture in the fabric, typically from the wearer sweating, governs not only thermophysiological but also sensorial aspects of clothing comfort. Thermophysiological parameters, like heat transfer, within a clothing system are affected by the moisture present in the system, on the other hand, feelings of dampness and fabric cling are the influential parameters on the sensorial comfort. Effective management of moisture in clothing systems could be facilitated with both moisture vapor and liquid moisture performances as well as drying capabilities of fabrics.

Terry knitted fabrics are widely used in the clothing sector such as towels, socks, baby clothes and sweatshirts etc. These fabrics belong to the group of pile fabrics which have loop piles on one or both sides covering the entire surface. These kinds of fabrics have a higher water absorption property compared to other types of textile fabrics. The amount of water absorbed, which includes the ability of material to retain a liquid in its interstice pores, [3] by terry fabrics is very important for its end use. However, this does not give any idea about how quickly a terry fabric absorbs the water or how water absorption changes with respect to time. Previous studies showed that the water absorption capacity of a terry fabric is dependent on yarn material, yarn type and fabric construction [4]. Mallikarjunan, Ramachhandran and Manohari [5] tested lyocell fabrics both pile and twill structure with different combinations for comfort properties and the results showed that lyocell pile, cotton/polyester knitted fleece and cotton/polypropylene plaited knitted fabrics can be used for cold climatic conditions. Also, they found that lyocell pile fabrics have very good water absorbency which immediately absorbs and transfers the moisture to inner layer and gives a dry feel. The study conducted by Petrulyte and Baltakyte [3] presented the investigations into the wetting phenomenon of terry fabrics which were manufactured using linen warp pile yarns. In the study made by Behera and Singh [6], yarns produced from two varieties of cotton (100% J-34 and MCU-5) and their blends with bamboo and poly vinyl alcohol (PVA) with different counts, twist and number of plies were used to prepare terry fabric of varying loop densities, loop lengths and loop shape factors. It was found that loop density is the most important parameter for water absorption rate followed by loop length and yarn twist. For the total amount of water absorbed, loop density is again the most important parameter followed by yarn twist, loop shape factor and number of ply in the pile yarn. Karahan and Eren [7] found that the type of yarns used in the production of terry fabric had the most significant effect on their static water absorption properties and added that two-ply ring-carded yarn showed a higher water absorption value than two-ply open-end yarn and single ply ring-carded yarn. They concluded their study such that an increase in weft and/or warp density reduced the percentage of static water absorption, and an increase in pile length increased the percentage static water absorption of terry fabrics. The effect of pile length on static water absorption was found to be more pronounced compared to warp and weft density. In addition, at another study of Karahan [4], the effects of same parameters on dynamic water absorption were investigated and it was found that the effect of pile length, warp and weft density on the percentage of water absorption remains limited compared to that of yarn type, and no significant effect of these parameters on water absorption is found for the last 100 seconds. Trafder et al [3] made a study about the effects of pile height, pile density, thickness, etc. on the surface water absorption characteristics and wicking phenomenon of different cotton terry fabric. The paper by Petrulyte and Velickiene [8] presented an investigation of the drying ability of terry fabrics with respect to pile height and finishing. The terry fabrics used in the experimental work were made from linen/cotton yarns, and the pile height of the samples was 6 and 12 mm. According to the results, evaporation duration time of finished ones were higher than that of grey ones and the drying of grey fabric with a low unbleached loop pile generally followed more intensively compared with a fabric a with high loop pile, while the reverse tendency was evident in finished fabrics. Krasteva et al [9] showed that higher weft density leads to greater mass of water absorbed by the terry fabrics and by increasing the loops height grows the absorbent surface, which leads to sorption of greater water quantity.

The literature survey showed that the studies conducted on water-related comfort properties of terry fabrics were generally about woven terry fabrics. In addition, in spite of the interest in the drying phenomenon of textiles, no research has been performed into the drying ability of terry knitted textiles. The aim of this study was to conduct experimental research into the drying process as well as transfer wicking terry knitted fabrics with respect to fiber type (cotton and polyester blends) and fabric tightness.

2. MATERIALS AND METHOD

2. 1 MATERIALS

For the study, terry knitted samples were produced at two different tightness factors (slack and tight) on a Sangiacomo Fantasia 1C machine. Ne 30/1 rotor yarns were used whose fiber compositions were 100% cotton, 67%/33% cotton/PET, 50%/50% cotton/PET, and 33%/67% cotton/PET. The properties of the yarns and fabric samples are given in Tables 1 and 2, respectively. First two letter indicates the fabric structure (TR- Terry), the second identification shows the fiber composition percentage; C is for cotton and PET is for Polyester, third group indicates fabric tightness (T-Tight, S- Slack).

All greige fabrics were dyed and finished under the relevant commercial production conditions. Following the dyeing and wet finishing processes the samples were squeezed, dried and then were sanforized.

Table 1: *Yarn properties*

Sample	Hairness				Yarn irregularity				Twist			
	n1	n2	n3	s3	CVm %	Thin places 50%/1000m	Thick places 50%/1000m	Neps +200%/1000m	Tour/m	CV %	Load (kgf)	Extension (%)
33% Cotton 67% PET	10688,3	1624,67	417	782,33	14,08	4	46	129	869,6	9,2	0,45731	58,555
50% Cotton 50% PET	15034	3007,33	893,67	1546	15,78	15	145	376	646,6	5,01	0,39959	50,048
67% Cotton 33% PET	20013,3	4460,33	1489,33	2695,67	14,74	7	88	220	871,4	4,13	0,35476	41,893
100 % Cotton	13566	2589,67	819	1424	12,46	0	13	80	893,6	7,56	0,33169	34,278

Table 2: *Fabric properties*

Numune	Stitch density (loop/cm^2)	Thickness (mm)	Porosity (%)	Weight (g/m^2)
TR-33/67 C/P-S	190,65	4,84	97,88	129,90
TR-33/67 C/P-T	218,55	4,85	97,65	144,24
TR-50/50 C/P-S	190,96	5,05	98,11	127,16
TR-50/50 C/P-T	224,75	5,18	97,96	140,22
TR-67/33 C/P-S	197,78	5,06	98,16	129,56
TR-67/33 C/P-T	238,24	4,94	97,93	142,86
TR-100 C-S	179,96	4,86	98,36	121,32
TR-100 C-T	251,72	4,60	97,89	147,52

2.2. METHOD

The dry relaxed fabrics were tested for some comfort-related properties: "Transfer Wicking", based on the method used by Zhuang et al. [10], but with the difference that an external pressure of 15.6 kg/m^2, which was high enough to start transfer wicking, was exerted; and "Drying Rate", based on Coplan's research [11]. Weight and thickness of the fabrics were evaluated according to the standards of TS 251 and TS 391 EN ISO 9237 respectively. The porosity values were calculated according to literature [12].

Decision-making is the art and science of choosing the best course of action or a set of preferred actions from the available alternatives [13]. TOPSIS is a decision making technique and it is a goal based approach for finding the alternative that is closest to the ideal solution. In this method, options are graded based on ideal solution similarity. If an option is more similar to an ideal solution, it has a higher grade. Ideal solution is a solution that is the best from any aspect that does not exist practically and we try to approximate it. Basically, for measuring similarity of a design (or option) to ideal level and non-ideal, it is considered distance of that design from ideal and non-ideal solution [14] The analytic hierarchy process (AHP) is the other most popular multi-criteria decision making method that deals with selection of the best alternative or ranking of alternatives under the presence of a finite number of decision criteria. [13]. The reason of popularity of AHP lies in the fact that it can handle the objective as well as subjective factors and the criteria weights and alternative scores are elicited through the formation of pair-wise comparison matrix, which is the heart of the AHP [15]. This research proposed a combined analytical hierarchy process (AHP) to calculate the weight of each risk criterion and technique for order performance by similarity to ideal solution (TOPSIS) methodology to rank. Main steps of this procedure as below [16-18]:

Step 1: The relevant objective or goal, decision criteria and alternatives of the problem are identified in this step.

Step 2: A decision matrix of criteria and alternatives is formulated on the basis of information avaible regarding the problem. The number of alternatives is M and the number of criteria is N where an element a_{ij} of the decision matrix D_{mxn} represents the actual value of the ith alternative in terms of jth decision matrix.

$$r_{ij} = \frac{a_{ij}}{\sqrt{\sum_{j=1}^{m}(a_{ij})^2}} \qquad j = 1, \ldots\ldots, m \quad i = 1, \ldots\ldots, n \tag{1}$$

Step 3: The decision matrix is converted to a normalized decision matrix. The normalized value r_{ij} is calculated as

Step 4: The relative importance of different criteria with respect to the objective of the problem is determined using AHP. To do so, a pair-wise comparison matrix of criteria is constructed using a scale of relative importance (Table 3).

Table 3: *Nine point scale of relative importance [16-18]*

Intensity of importance on a absolute scale	Definition	Explanation
1	Equal importance	Two activities contribute equally to the objective.
3	Moderate importance of one over another	Experience and judgement slightly favor one activity to another
5	Essential or strong importance	Experience and judgement strongly favor one activity to another
7	Very strongly importance	An activity is strongly favored and its dominance is demonstrated in practice
9	Extreme importance	The evidence favoring one activity over another is of the highest possible order of affirmation.

The normalized weight or importance of the ith criteria (W_i) is determined by calculating the geometric mean of the ith row (GM_i) of the above matrix and then normalizing the geometric means of rows ass:

$$GM_i = \left\{\prod_{j=1}^{N} c_{ij}\right\}^{\frac{1}{N}} \tag{2}$$

$$W_i = \frac{GM_i}{\sum_{i=1}^{N} GM_i} \tag{3}$$

To check the consistency in pair-wise comparison judgment, consistency index (CI) and consistency ratio (CR) are calculated using the following equations

$$GM_i = \left\{\prod_{j=1}^{N} c_{ij}\right\}^{\frac{1}{N}} \tag{2}$$

$$W_i = \frac{GM_i}{\sum_{i=1}^{N} GM_i} \tag{3}$$

where RCI is random consistency index and its value can be obtained from Table 3. If the value of CR is 0,1 or less than the judgment is considered to be consistent and therefore acceptable. Otherwise, the decision maker has to be reconsidering the entries of pair wise comparison matrix.

Table 4: *RCI values for different numbers of alternatives (m) [16-18]*

m	1	2	3	4	5	6	7	8	9
RCI	0	0	0,58	0,9	1,12	1,24	1,32	1,41	1,45

Step 5: The weighted normalized value υ_{ij} is calculated as

$$\upsilon_{ij} = W r_{ij} \qquad j = 1, \dots\dots, m \quad i = 1, \dots\dots, n \tag{5}$$

where W_i is the weight of the ith attribute of criterion and

Step 6: The positive ideal and negative ideal solution are determined by following formulations:

$$A^+ = \{\upsilon_i^+, \dots\dots, \upsilon_n^+\} = \{(max_j \upsilon_{ij} li \in I), (min_j \upsilon_{ij} li \in J)\} \tag{6}$$

$$A^- = \{\upsilon_i^-, \dots\dots, \upsilon_n^-\} = \{(min_j \upsilon_{ij} li \in I), (max_j \upsilon_{ij} li \in J)\} \tag{7}$$

where W_i is associated with benefit criteria and J is associated with cost criteria.

Step 7: The separation measure using the n-dimensional Euclidean distance is calculated.

$$d_j^+ = \left\{\sum_{i=1}^{n} (\upsilon_{ij} - \upsilon_i^+)^2\right\}^{1/2} \qquad j = 1, \dots\dots, m. \tag{8}$$

$$d_j^- = \left\{\sum_{i=1}^{n} (\upsilon_{ij} - \upsilon_i^-)^2\right\}^{1/2} \qquad j = 1, \dots\dots, m \tag{9}$$

Step 8: The relative closeness to the ideal solution is determined.

$$R_j = \frac{d_j^-}{(d_j^+ + d_j^-)} \qquad j = 1, \dots\dots, m \tag{10}$$

Since $d_j^- \geq 0$ and $d_j^+ \geq 0$ then clearly $R_j \in [0,1]$

Step 9: All the alternatives are arranged in a descending order according to value of R_j. The alternative at the top of the list is the most preferred one.

3. RESULTS &DISCUSSION

3.1. TRANSFER WICKING

The transfer wicking is the transmission of water through the thickness of a fabric that is perpendicular to the plane of the fabric and the mechanism of removal of liquid perspiration from the skin involves its movement through the fabric thickness [19]. In addition to Figure 1 which shows transfer wicking of the fabrics over 30 minutes, our measurements for transfer wicking of the fabrics after 30 minutes are also presented in Table 5.

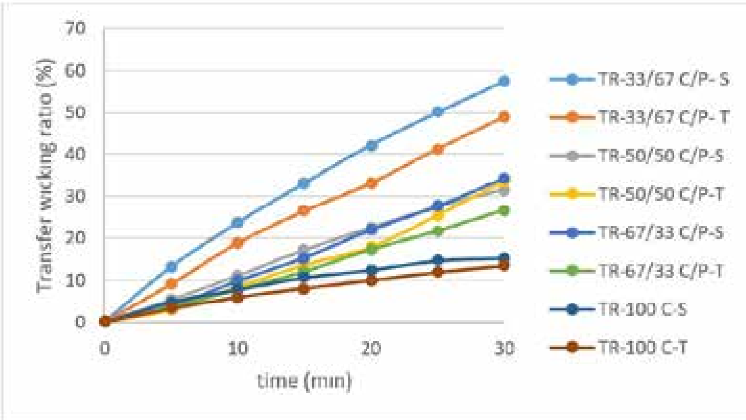

Figure 1: *Transfer wicking of the terry knitted fabrics.*

Table 5: *Transfer wicking ratios of the fabrics after 30 minutes.*

	Slack (%)	**Tight (%)**
TR-33/67 C/P	57,48	48,91
TR-50/50 C/P	31,63	33,66
TR-67/33 C/P	34,38	26,76
TR-100 C	15,26	13,48

As may be seen from Figure 1 and Table 5, within the first five minutes of the transfer wicking, the greatest wicking was observed for TR-33/67 C/P fabrics, while cotton garments gave the lowest values for the same period. Additionally, as shown in Figure 1, in the first five minutes of the test the transfer wicking ratio had a steep increase for all samples, which then became more gradual. Moreover, the terry fabrics performed such that an increase in polyester fiber percentage had a positive effect on the transfer wicking ratio, which is in agreement with the literature. As is known, liquid transport properties are significantly affected by fiber type. Also the liquid transport within a textile fabric is due to capillary action of fibers and is thus governed by the properties of fiber surface and diameter of yarn which varies with the fiber composition because of the difference in packing factor of each constituent fiber. Bearing these into mind, it may be concluded that the presence of polyester fiber having lower moisture regain and water holding capacity, in the fabrics may increase the transfer wicking ratio of the terry fabrics. The difference between the surface energies of PET and cotton fibers may also contribute this performance. It may also be noted that as the terry fabric became tighter, the transfer wicking ratio tended to decrease, irrespective of the fiber blend ratio. Literature survey showed that thickness and porosity have a sizeable effect on transfer wicking [10, 20-22]. However, as shown in Table 2, both thickness and porosity values of the samples were very close to each other and the differences between these values were not statistically significant. Therefore, this very result may partly be attributed to the differences between inter-yarn pore size as well as pore size distribution of the slack and tight terry fabrics. Also, in the tight fabrics the terry loops may be forced to randomly overlap more, which in turn may not only increase the distance taken by the liquid water, but also break the continuity of capillaries formed by the fibers, which aggravates liquid advancement through the fabric.

3.2. DRYING RATE

The drying properties of the fabrics are given in Table 6 which shows the terry fabrics with polyester fiber tended to dry faster. Due to the non-hygroscopic and highly crystalline character of polyester fibers, water molecules cannot be absorbed within the fibers and wetting occurred only on the surface of the fibers within the yarns. Thus, all the moisture of the polyester fabrics can be assumed to be free moisture, and this leads to shorter drying times. TR-50/50 C/P fabrics, on the other hand, had surprisingly the highest drying time, which is followed by TR-100 C and TR-67/33 C/P. So far as TR-100 C and TR-67/33 C/P terry fabrics are concerned, wet cellulosic fibers have a considerable amount of bound moisture due to the hygroscopic nature, and increase in hygroscopic character increases the drying time which is a good agreement with the literature [23, 24]. When it comes to TR-50/50 C/P fabrics, the relative arrangement of polyester and cotton fibers in the terry loops may create a drowning effect for the polyester fibers in the capillary channels of these loops filled with water thanks to the cotton fibers. This in turn may cause the relevant fabrics behave like cotton-intense and/or 100% cotton terry fabrics [25].

Finally, it was also found that the slack fabrics, independent of fiber blend ratio, tended to have higher drying rates and also larger water diffusion area. This is probably due to the fact that evaporation-drying ability of textiles is closely related to moisture releasing ability as well as fabric thickness, construction and fabric weight [26].

Table 6: *Drying rate and drying time of fabrics*

	Drying time (h)	Drying Rate, (g/h/m^2)
TR-33/67 C/P-S	20,005	88,04
TR-33/67 C/P-T	21,002	87,68
TR-50/50 C/P-S	25,016	115,47
TR-50/50 C/P-T	28,007	90,96
TR-67/33 C/P-S	23,005	104,62
TR-67/33 C/P-T	25,002	90,67
TR-100 C-S	25,001	84,53
TR-100 C-T	26,012	87,62

3.3. PERFORMING HYBRID AHP-TOPSIS APPROACH

With the aim of selection best sock alternative from the investigated fabrics, the relative weights of two decision criteria were determined. Drying rate and transfer wicking of the fabrics are influential and important parameters for the users to feel comfortable. Thus, these two parameters were selected as criteria. The pair-wise comparison matrix of the two decision criteria's with regard to their importance level can be observed in Table 7.

Table 7: *Pair-wise comparison matrix of criteria with regard to objective and codes*

	Transfer wicking	Drying rates	Codes
Transfer wicking	1	3	C1
Drying rates	1/3	1	C2

Then, the normalized weights, weighted normalization matrix, both positive and negative ideal solutions were calculated in turn (see Table 8).

Table 8: Weighted normalization matrix of the fabric samples

	C1	C2
W=1	0,75	0,25
TR-33/67 C/P- S	88,04	57,48
TR-33/67 C/P- T	87,68	48,91
TR-50/50 C/P-S	115,47	31,63
TR-50/50 C/P-T	90,96	33,66
TR-67/33 C/P-S	104,62	34,38
TR-67/33 C/P-T	90,67	26,76
TR-100 C-S	84,53	15,26
TR-100 C-T	87,62	13,48
Positive ideal solution	0,32	0,14
Negative ideal solution	0,24	0,03

At the next step, the separation of each alternative from the ideal solution was calculated. The relative closeness of the alternatives (R_j) to the ideal solution (A_j) was defined in terms of A^+. Based on the closeness of the coefficient to the ideal solution (R_j value), the ranking of the preference order of all the alternatives in descending order is exhibited in Table 9.

Table 9: *Preference order for the fabric samples*

Fabrics	**Pos Ideal (d+)**	**Neg Ideal (d-)**	**Relative closeness (Rj)**	**Rank**
TR-50/50 C/P-S	0,0642	0,0980	0,60	1
TR-33/67 C/P- S	0,0772	0,1097	0,59	2
TR-67/33 C/P-S	0,0650	0,0767	0,54	3
TR-33/67 C/P- T	0,0810	0,0884	0,52	4
TR-50/50 C/P-T	0,0908	0,0533	0,37	5
TR-67/33 C/P-T	0,1034	0,0372	0,26	6
TR-100 C-S	0,1362	0,0044	0,03	7
TR-100 C-T	0,1344	0,0087	0,06	8

Final ranking of hybrid AHP-TOPSIS method implied that TR-50/50 C/P-S was the best alternative based on water related comfort properties of terry socks. However, different from the subjectively expected, TR-100 C-T performed the worst alternative in the rankings.

4. CONCLUSION

This study aimed to determine the relative effects of fiber type (cotton and polyester blends) and fabric tightness (slack and tight) on drying rate and transfer wicking of terry knitted fabrics. According to the results, it was concluded that the change in cotton/polyester blend ratio from 100/0, 67/33, 50/50 to 33/67 did significantly affect positively the transfer wicking ratios of terry fabrics. Also, slack ones transported the water quickly than those of tight ones. Moreover, the experimental results revealed that the use of polyester fibers can enhance the drying rate that by increasing polyester fiber content in C/P blended fabric, the drying time of the fabric decreased and slacker ones dried faster than those of slacker ones. Due to the fact that analytic hierarchy process (AHP) and the technique for order performance by similarity to ideal solution (TOPSIS) are widely employed methodologies to facilitate this kind of processes, hybrid AHP-TOPSIS multi-criteria decision method was used in this study with the aim of select the best terry fabric. The weights for each criterion were calculated based on Analytic Hierarchy Process (AHP) and then inputted these weights to the TOPSIS method to rank alternatives. Finally, TR-50/50 C/P-S fabric was found to be the best while TR-100 C-T performed the worst one.

REFERENCES

Morris M. A., Prato H. H., White N. L. Relationship of Fiber Content and Fabric Properties to Comfort of Socks. Clothing and Textile Research Journal. 1985; 3(1): 14-19.

Furtak N. T. Socks: Correlation of Wetness Perceptions with Moisture Transport. PhD Thesis. University of Alberta. 2018.

Petrulyte S., Baltakyte R. Investigation into the Wetting Phenomenon of Terry Fabrics. Fibres & Textiles in Eastern Europe. 2008; 16, 4 (69): 62-66.

Karahan, M. Experimental Investigation of the Effect of Fabric Construction on Dynamic Water Absorption in Terry Fabrics. Fibres & Textiles in Eastern Europe. 2007; 15, 3 (62): 74-80

Mallikarjunan, K., Ramachhandran, T., Manohari, B. G. Comfort and Thermo Physiological Characteristics of Multilayered Fabrics for Medical Textiles. Journal of Textile and Apparel Technology and Management. 2011; 7(1): 1-15.

Behera B.K., Singh J.P. Factors Contributing to Absorbency Behavior of Pile Fabrics. Research Journal of Textile and Apparel. 2014; 18(3): 81-93

Karahan, M, Eren, R., Experimental Investigation of the Effect of Fabric Parameters on Static Water Absorption in Terry Fabrics. Fibres& Textiles in Eastern Europe. 2006; 14, No: 2 (56): 59-63.

Petrulyte S., Velickiene A. Investigation of Drying Phenomenon of Terry Woven Fabrics. Fibres & Textiles in Eastern Europe. 2011; 19, 6 (89): 58-63.

Germanova-Krasteva D. S., Kandzhikova G. D., Bochev A. G. Influence of Terry Fabrics Structure on Dynamic Sorption. International Journal of Clothing Science and Technology. 2013; 25(4): 243-256.

Zhuang Q., Harlock S.C., Brook D.B. Transfer Wicking Mechanism of Knitted Fabric Used as Undergarment for Outdoor Activities. Textile Research Journal. 2002; 72: 727–734.

Coplan M.J. Some Moisture Relations of Wool and Several Synthetic Fibers and Blends. Textile Research Journal. 1953; 23: 897–916.

Mukhopadhyay, A., Ishtiaque, S.M.,Uttam, D. Impact of Structural Variations in Hollow Yarn on Heat and Moisture Transport Properties of Fabrics. The Journal of the Textile Institute. 2011; 102 (8): 700–712.

Ghosh A., Mal P., Majumdar A. Advanced Optimization and Decision-Making Techniques in Textile Manufacturing. CRC Press 2019.

Sasi J. C., Digalwar A. K. Application of AHP and TOPSIS Method for Supplier Selection Between India & China in Textile Industry. International Research Journal of Engineering and Technology. 2015; 2(4): 1730-1738.

Banwet D. K., Majumdar A. Comparative Analysis of AHP-TOPSIS and GA-TOPSIS Methods for Selection of Raw Materials in Textile Industries. Proceedings of the 2014 International Conference on Industrial Engineering and Operations Management Bali, Indonesia, January 7 – 9, 2014.

Majumbar, A., Sarkar, B., Majumbar, P.K. Determination of Quality Value of Cotton Fibre Using Hybrid AHP-TOPSIS Method of Multi-Criteria Desicion-Making. Journal of Textile Institute. 2005; 96(5)- 303-309.

Moghassem, A.R., Bahramzadeh, H. Application of Multi-Criteria Analysis for Parameters Selection Problem in Rotor Spinning. Textile Research Journal. 2010; 80(20): 2176-2187.

Shyjith, K., Ilangkumaran, M., Kumanan, S. Multi-Criteria Decision Making Approach to Evaluate Optimum Maintenance Strategy in Textile Industry. JQME. 2008; 14(4): 375-386.

Mallikarjunan, K., Ramachandran T., Manohari, B.G. Comfort and Thermophysiological Characteristics of Multilayered Fabrics for Medical Textiles. Journal of Textile and Apparel Technology and Management. 2011; 7(1).

Ramachandran T., Kesavaraja N. Study on Influencing Factors for Wetting and Wicking Behavior. IE (I) J. 2004; 84: 184–186.

Nyoni A.B., Brook D. Wicking Mechanisms in Yarns—The Key to Fabric Wicking Performance. Journal of Textile Institute. 2006; 97: 119–128.

Cimilli S., Nergis B.U., Candan C. Ozdemir M., Comparative Study of Some Comfort-Related Properties of Socks of Different Fiber Types. Textile Research Journal. 2010; 80: 948–957.

Su, C.I., Fang, J.X., Chen X. H., Wu W.Y. Moisture Absorption and Release of Profiled Polyester and Cotton Composite Knitted Fabrics. Textile Research Journal. 2007; 77: 764-769.

Cay A, Gurlek G., Oglakcioglu N. Analysis and Modeling of Drying Behavior of Knitted Textile Materials. Drying Technology. 2017; 35(4): 509-521.

Yoon, H. N., Buckley A. Improved Comfort Polyester Part I: Transport Properties and Thermal Comfort of Polyester/Cotton Blend Fabrics. Textile Research Journal. 1984; May: 289-298.

Jhanji Y., Gupta D., Kothari V. K. Liquid Transfer Properties and Drying Behavior of Plated Knitted Fabrics with Varying Fibre Types. Indian Journal of Fibre & Textile Research. 2015; 40:162-169.

A SOFTWARE APPLICATION OF SERVICE ORIENTED COMPUTING

CHAPTER

24

Ali Evren GÖKSUNGUR[1]

1 Department of Computer Engineering, Nişantaşı University, İstanbul, Turkey

1. Introduction

According to developing technologies smart solutions become more important at big data operations. Since complex software operations need to be reduced to execute too many different transactions quickly. Service Oriented computing method provides to simplify computer programs operations by using associate web service solutions. Service Oriented Computing SOAP uses web services to produce any kind of complex multiple data solutions. In this paper, a software application of service oriented computing is explained in details. By using Soap method instead of too many software programs many problem may solve with quick web service solutions.

2. Service Oriented Computing - Related Literature

Previous Research on Service Oriented Computing

Service Oriented Computing method is based on web services as fundamental elements to develop software solutions to any kind of business process. By using this method complex transactions are completed easily with composite web services. (M.P. Papazoglou, 2003, p.2.) Instead of too many software program operations ; The advantage of service Oriented computing is directly to send a request and to get a response and this method provides a way to create a new architecture that will define a quick solution to software problems. (M.N. Huhns, M.P. Singh, 2005, p. 75-81.) Before to decide to use Service Oriented Computing method Organizations should consider about value of service level and quality in addition to the cost and duration of delivered services. So if any organization need to solve a big data software problem then according to its infrastructure, service needs should define and according to service needs s quick solution may develop by using Service Oriented Computing Method. (Demirkan, Delen, April 2013, p. 412-421). Servie Oriented Architecture (SOA) is an architectural style in building Web applications based on services. Also security is very important and secure connection according to trust logic of any kind of software operations it is possible to define a trust-based SOA solution based on an identified trust definition. Because trust is an important factor in successful online operations, it is a major criterion for service selection. (Zainab M.Aljazzaf, Miriam A.M.Capretz, MarkPerry, 2016, p.470-480).

For each software problem, individual solutions should develop by using web service solutions. To define a web service solution: Three basic standard is in use: These are: (Simple Object Access Protocol) SOAP: Communication: how services can be used. WSDL: Description: How services can be published. UDDI: Discovery: how services can be discovered. According to these standards effective solutions may be proceed to manage web services easily. (Nathan Griffiths, Kuo-Ming Chao, 2010, p. 24-25.)

3. Methods

Service-oriented architecture (SOA) is a style of software design where services are provided to the other components by application components, through a communication protocol over a network.

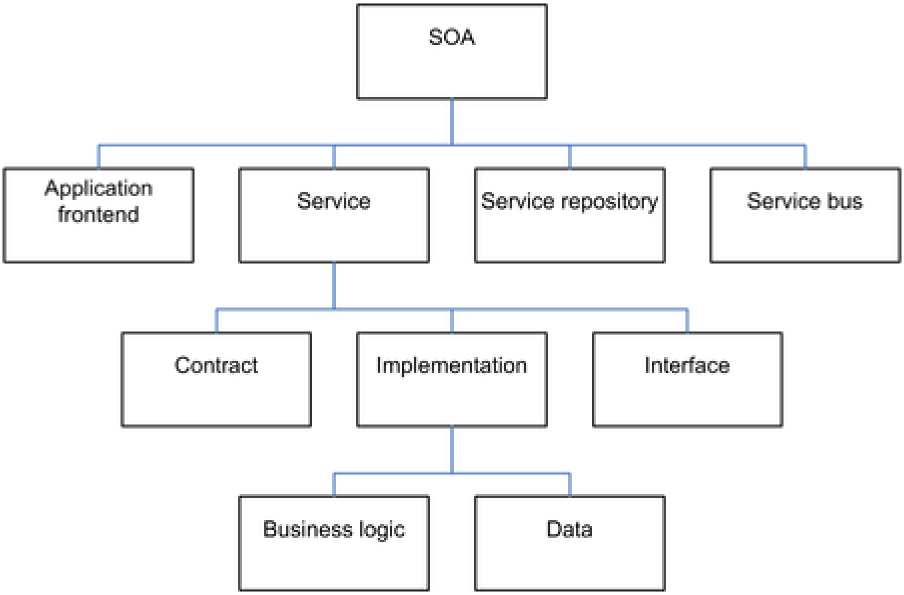

Fig. 1. *Service Oriented Architecture (SOA)*

Service Oriented Computing is also include;

- Service Based Solutions

- Uses an iterative process

- Component Based Development

- Business Process Management

- Web services composition

- API/Service Design

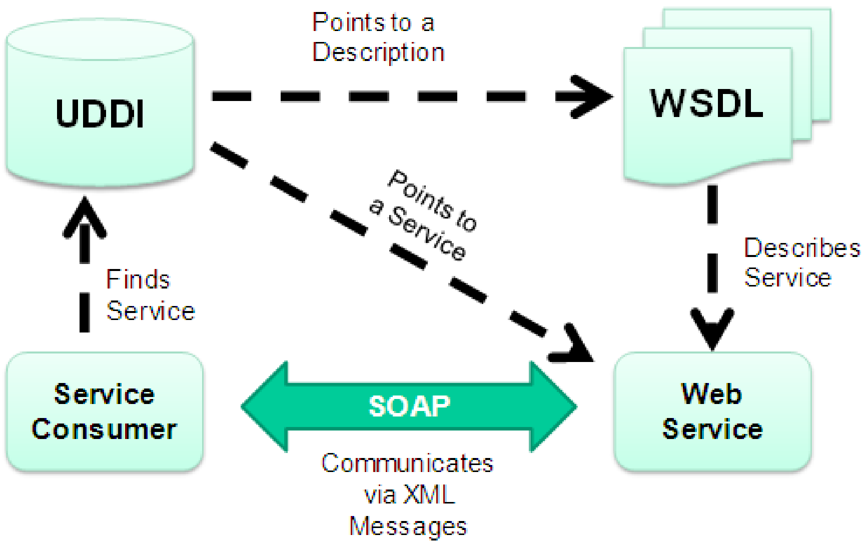

Fig.2. *Web Services - Basic Architecture (SOAP, WSDL, UDDI)*

SOAP: (Simple Object Access Protocol)

SOAP is an XML-based protocol for exchanging information between computers.

SOAP is a communication protocol.

SOAP is for communication between applications.

SOAP is a format for sending messages.

SOAP is designed to communicate via Internet.

SOAP is platform independent.

SOAP is language independent.

SOAP is simple and extensible.

SOAP allows you to get around firewalls.

SOAP will be developed as a W3C standard.

WSDL:

WSDL is an XML-based language for describing web services and how to access them.

WSDL stands for Web Services Description Language.

WSDL was developed jointly by Microsoft and IBM.

WSDL is an XML based protocol for information exchange in decentralized and distributed environments.

WSDL is the standard format for describing a web service.

WSDL definition describes how to access a web service and what operations it will perform.

WSDL is a language for describing how to interface with XML-based services.

WSDL is an integral part of UDDI, an XML-based worldwide business registry.

WSDL is the language that UDDI uses.

UDDI:

UDDI is an XML-based standard for describing, publishing, and finding web services.

UDDI stands for Universal Description, Discovery, and Integration.

UDDI is a specification for a distributed registry of web services.

UDDI is platform independent, open framework.

UDDI can communicate via SOAP, CORBA, and Java RMI Protocol.

UDDI uses WSDL to describe interfaces to web services.

UDDI is seen with SOAP and WSDL as one of the three foundation standards of web services. UDDI is an open industry initiative enabling businesses to discover each other and define how they interact over the Internet. SOAP provides a mechanism that can be used to exchange messages between Web service clients and servers.

UDDI using SOAP, and its interface is described using WSDL.

4. Results and Discussion

According to develop a Software Application of Service Oriented Computing. A health insurance software application is examined. Three basic standard is used to develop the best web service solution for this application. These three basic standards are: (Simple Object Access Protocol) SOAP: WSDL and UDDI. Also, health insurance web service is analyze with 3 method related the data structure as compute method to calculate the policy firstly. Then secondly approve method is used to approve the policy and finally print out method is used to get the pdf document of the policy.

According to develop an application of web service based solution. By using SOAP platform and WSDL methods the health insurance data set is defined as input and according to this solution.

Approve function:

Input:

```
<soapenv:Envelope xmlns:soapenv="http://schemas.xmlsoap.org/soap/envelope/" xmlns:for="ForeignersHealth">
  <soapenv:Header/>
  <soapenv:Body>
    <for:Approve>
      <!--Optional:-->
      <for:Input>
        <for:PrintType>1</for:PrintType>
        <for:IsTestMode>0</for:IsTestMode>
        <for:Channel>30806</for:Channel>
        <!--Optional:-->
        <for:Username>30806001</for:Username>
        <!--Optional:-->
        <for:TrackingCode>2019-03-22-000518-59518093</for:TrackingCode>
        <!--Optional:-->
        <for:CitizenshipNumber>0</for:CitizenshipNumber>
        <!--Optional:-->
```

```
<for:TaxNumber>6368806578</for:TaxNumber>
<for:UnitNo>11266123</for:UnitNo>
<for:PolicyNo>22756878</for:PolicyNo>
```


Output:


```
<soap:Envelopexmlns:soap=”http://schemas.xmlsoap.org/soap/envelope/” xmlns:xsi=”http://www.w3.org/2001/XMLSchema-instance” xmlns:xsd=”http://www.w3.org/2001/XMLSchema”>
  <soap:Body>
    <ComputeResponse xmlns=”ForeignersHealth”>
      <ComputeResult>
        <IsSuccess>true</IsSuccess>
        <StatusCode>status-success</StatusCode>
        <StatusDescription>Teklif alma süreci tamamlandı. (Hesaplanan Brüt Prim: 789,11 ₺)</StatusDescription>
        <TrackingCode>2019-03-22-000518-59518093</TrackingCode>
        <UnitNo>11266123</UnitNo>
        <Premium>789.11</Premium>
        <BeginDate>2019-05-01T00:00:00</BeginDate>
        <EndDate>2020-05-01T00:00:00</EndDate>
        <PolicyNo>22756878</PolicyNo>
```


5. Conclusion

To develop dynamic software applications by using service oriented computing method. Each software solution should analyze according to define firstly its service oriented architecture and then its data structure should analyze to develop effective web service solutions. In this paper, an application is analyze and according to web service standards, the problem is defined in three stage for a health insurance software application. Compute, Approve and Print web services are defined then a software program is developed to combine these web services and effective software solution is applied according to service oriented computing method.

6. References

[1] M.P. Papazoglou, Service-oriented computing: concepts, characteristics and directions, **Published in:** Proceedings of the Fourth International Conference on Web Information Systems Engineering, 2003. WISE 2003.. **Print ISBN:** 0-7695-1999-7, p.2 (https://ieeexplore.ieee.org/abstract/document/1254461)

[2] M.N. Huhns , M.P. Singh , Service-oriented computing: key concepts and principles , Published in: IEEE Internet Computing (Volume: 9 , Issue: 1 , Jan-Feb 2005), p. 75-81. https://ieeexplore.ieee.org/document/1407782

[3] Haluk Demirkan , Dursun Belen , Decision Support Systems , Published by Elsevier B.V. , Volume 55, Issue 1, April 2013, Pages 412-421https://www.sciencedirect.com/science/article/pii/S0167923612001595

[4] Zainab M.Aljazzaf , Miriam A.M.Capretz , MarkPerry, Trust-based Service-Oriented Architecture , Journal of King Saud University - Computer and Information Sciences, Volume 28, Issue 4, October 2016, Pages 470-480https://www.sciencedirect.com/science/article/pii/S1319157816300064?via%3Dihub

[5] Nathan Griffiths , Kuo-Ming Chao, Agent-Based Service-Oriented Computing , Published by Springer-Verlag London Limited 2010 , ISBN 978-1-84996-040-3 , p. 24-25 .